Edited by
Georg J. Schmitz and Ulrich Prahl

Integrative Computational Materials Engineering

Related Titles

Vaz Junior, M., de Souza Neto, E. A., Munoz-Rojas, P. A. (Eds.)

Advanced Computational Materials Modeling

From Classical to Multi-Scale Techniques

2011

ISBN: 978-3-527-32479-8

Dubois, J.-M., Belin-Ferré, E. (Eds.)

Complex Metallic Alloys

Fundamentals and Applications

2011

ISBN: 978-3-527-32523-8

Roters, F., Eisenlohr, P., Bieler, T. R., Raabe, D.

Crystal Plasticity Finite Element Methods

in Materials Science and Engineering

2010

ISBN: 978-3-527-32447-7

Breitkopf, P., Filomeno, C. R. (Eds.)

Design Optimization in Computational Mechanics

2010

ISBN: 978-1-84821-138-4

Berlioz, A., Trompette, P.

Solid Mechanics using the Finite Element Method

2010

ISBN: 978-1-84821-191-9

van Santen, R. A., Sautet, P. (Eds.)

Computational Methods in Catalysis and Materials Science

An Introduction for Scientists and Engineers

2009

ISBN: 978-3-527-32032-5

Edited by Georg J. Schmitz and Ulrich Prahl

Integrative Computational Materials Engineering

Concepts and Applications of a Modular Simulation Platform

WILEY-VCH Verlag GmbH & Co. KGaA

The Editors

Dr.rer.nat. Georg J. Schmitz
RWTH Aachen University
Access e.V.
Intzestr. 5
52072 Aachen
Germany

Dr. Ulrich Prahl
RWTH Aachen University
Department of Ferrous
Metallurgy
Intzestr. 1
52072 Aachen
Germany

Library of Congress Card No.: applied for

British Library Cataloguing-in-Publication Data
A catalogue record for this book is available from the British Library.

Bibliographic information published by the Deutsche Nationalbibliothek
The Deutsche Nationalbibliothek lists this publication in the Deutsche Nationalbibliografie; detailed bibliographic data are available on the Internet at <http://dnb.d-nb.de>.

Print ISBN: 978-3-527-33081-2
ePDF ISBN: 978-3-527-64612-8
ePub ISBN: 978-3-527-64611-1
mobi ISBN: 978-3-527-64610-4
oBook ISBN: 978-3-527-64609-8

Cover Design Adam-Design, Weinheim, Germany
Typesetting Laserwords Private Limited, Chennai, India
Printing and Binding betz-druck GmbH, Darmstadt, Germany

Contents

List of Contributors

Markus Apel
RWTH Aachen University
Access e.V.
Intzestr. 5
52072 Aachen
Germany

Tim Arping
RWTH Aachen University
Institute of Plastics Processing
Pontstraße 49
52062 Aachen
Lanxess, Germany

Markus Bambach
RWTH Aachen University
Institute of Metal Forming
Intzestr. 10
52056 Aachen
Germany

Thomas Baranowski
RWTH Aachen University
Institute of Plastics Processing
Pontstraße 49
52062 Aachen
Germany

Thomas Beer
RWTH Aachen University
Institute for Scientific Computing
Center for Computing and Communication
Seffenter Weg 23
52074 Aachen
Germany

Stefan Benke
RWTH Aachen University
Access e. V.
Intzestr. 5
52072 Aachen
Germany

now at

Cologne University of Applied Sciences

Kirsten Bobzin
RWTH Aachen University
Surface Engineering Institute
Kackertstr. 15
52072 Aachen
Germany

Patrick Fayek
RWTH Aachen University
Department of Ferrous Metallurgy
Intzestr. 1
52072 Aachen
Germany

Stephan Freyberger
RWTH Aachen University
Foundry Institute
Intzestr. 5
52072 Aachen
Germany

Thomas Gries
RWTH Aachen University
Institut für Textiltechnik
Otto-Blumenthal-Str. 1
52074 Aachen
Germany

Ario Hardjosuwito
RWTH Aachen University
Laboratory for Machine Tools and Production Engineering
Steinbachstr. 53B
52074 Aachen
Germany

Barbara Heesel
RWTH Aachen University
Institute of Plastics Processing
Pontstraße 49
52062 Aachen
Germany

Thomas Henke
RWTH Aachen University
Institute of Metal Forming
Intzestr. 10
52056 Aachen
Germany

Christian Hopmann
RWTH Aachen University
Institute of Plastics Processing
Pontstraße 49
52062 Aachen
Germany

Ulrich Jansen
Fraunhofer Institute for Laser Technology
Steinbachstr. 15,
52074 Aachen
Germany

Tatyana Kashko
RWTH Aachen University
Surface Engineering Institute
Kackertstr. 15
52072 Aachen
Germany

now at

Infineon AG

Josef Klingele
RWTH Aachen University
Institut für Textiltechnik
Otto-Blumenthal-Str. 1
52074 Aachen
Germany

Sergey Konovalov
RWTH Aachen University
Department of Ferrous Metallurgy
Intzestr. 1
52072 Aachen
Germany

Britta Kuckhoff
RWTH Aachen University
Institut für Textiltechnik
Otto-Blumenthal-Str. 1
52074 Aachen
Germany

Gottfried Laschet
RWTH Aachen University
Access e. V.
Intzestr. 5
52072 Aachen
Germany

Markus Linke
RWTH Aachen University
Institut für Textiltechnik
Otto-Blumenthal-Str. 1
52074 Aachen
Germany

now at

University of Applied Sciences
Hamburg

Wolfram Lohse
RWTH Aachen University
Laboratory for Machine Tools and
Production Engineering
Steinbachstr. 53B
52074 Aachen
Germany

Tobias Meisen
RWTH Aachen University
Institute of Information
Management in Mechanical
Engineering and Center for
Learning and Knowledge
Management
Dennewartstr. 27
52068 Aachen
Germany

Walter Michaeli
RWTH Aachen University
Institute of Plastics Processing
Pontstraße 49
52062 Aachen
Germany

Mehmet Öte
RWTH Aachen University
Surface Engineering Institute
Kackertstr. 15
52072 Aachen
Germany

Ulrich Prahl
RWTH Aachen University
Department of Ferrous
Metallurgy
Intzestr. 1
52072 Aachen
Germany

Hendrik Quade
RWTH Aachen University
Department of Ferrous
Metallurgy
Intzestr. 1
52072 Aachen
Germany

Rudolf Reinhard
RWTH Aachen University
Institute of Information
Management in Mechanical
Engineering and Center for
Learning and Knowledge
Management
Dennewartstr. 27
52068 Aachen
Germany

Eduardo Sambrano Rossiter
RWTH Aachen University
Welding and Joining Institute
Pontstr. 49
52062 Aachen
Germany

Jenny Rudnizki
RWTH Aachen University
Department of Ferrous
Metallurgy
Intzestr. 1
52072 Aachen
Germany

now at

Thyssen-Krupp Steel AG
Germany

Thomas Schläfer
RWTH Aachen University
Surface Engineering Institute
Kackertstr. 15
52072 Aachen
Germany

now at

GTV Verschleißschutz GmbH
Germany

Georg J. Schmitz
RWTH Aachen University
Access e.V.
Intzestr. 5
52072 Aachen
Germany

Preface

The idea of writing the present book about a platform for ''integrative computational materials engineering'' (ICME) evolved in the frame of a project inside the Cluster of Excellence ''Integrative Production Technologies for High Wage Countries'' being funded within the excellent initiative of the German federal government.

The initial title of the project was ''Virtual Process Chains for Processing of Materials'' and it aimed at establishing several descriptive simulation chains for different process scenarios and different materials. Almost immediately after starting the project in 2006, it turned out that a standardized, modular, open, and extendable simulation platform was mandatory for an efficient information exchange along the process chains as well as across the different length scales relevant in materials engineering.

The expertise and simulation tools of a number of institutes at the RWTH Aachen University being involved in the project provided the nucleus for setting up such a platform. This expertise covers the entire production chain from casting via hot and cold forming, heat treatments, joining, and coating to machining and comprises different materials such as metallic alloys (especially steels), composites, and polymers. It is complemented by the RWTH infrastructure and expertise in scientific computing and information management.

In detail, the following RWTH institutes have been involved: Foundry Institute (GI), Institute for Ferrous Metallurgy (IEHK), Welding and Joining Institute (ISF), Surface Engineering Institute (IOT), Institute for Metal Forming (IBF), Institute for Plastics Processing (IKV), Institute for Scientific Computing (SC), Department of Information Management in Mechanical Engineering (ZLW/IMA), Institute for Textile Technology (ITA), Fraunhofer Institute for Lasertechnology (ILT/NLD), and ACCESS.

During the course of the project, ICME has emerged as a new discipline integrating the ''computational materials'' research – dealing with length scales from atomistic up to the mesoscopic continuum scale of a microstructure – into engineering applications at the component or process scale. As the platform concept being developed in our view will be highly valuable for the emerging discipline of ICME and because it is hard to publish the details of a standardization scheme

along with examples of its applications in individual journal articles, we decided to summarize the concept for a ''Platform for Integrative Computational Materials Engineering'' within the present book. May it be useful and inspiring when reading it the first time and helpful when looking up details of the platform standard later.

Aachen, Germany
July 2011

Georg J. Schmitz
Ulrich Prahl

Part I
Concepts

Integrative Computational Materials Engineering: Concepts and Applications of a Modular Simulation Platform,
First Edition. Edited by Georg J. Schmitz and Ulrich Prahl.

1
Introduction

Georg J. Schmitz and Ulrich Prahl

1.1
Motivation

The production of increasingly complex and valuable goods requires highly advanced, knowledge-based, tailored materials and components. In general, production goes along with planning and design activities to elaborate suitable process chains, leading to the desired functionality of the component while simultaneously meeting reasonable cost targets. This leads to a dilemma where efforts spent in planning and design have to be related to the final value of the product and, accordingly, the price a customer is willing to pay for it. The quantity any producer is interested in is the profit to be made. In a very simple view, this profit may be defined as

$$\text{profit} = \text{value} - \text{costs}$$

Value here may be interpreted as the price a third party is willing to pay for the product, while costs comprise the costs of anything needed to produce the particular product. Especially, activities for designing and planning the product and its production process on the basis of experiments and simulations have to be considered here as well. Thus, any optimization of the planning process (Figure 1.1) will lead to either a reduced effort in terms of time and costs to be spent in planning or to more reliable predictions, reducing the necessity of experimental tests for verification or even enabling a production at ''first time right.'' In particular cases, even the value of the product may be increased, for example by including a virtual documentation of its production process and its properties, which may be used by the customer to elaborate better predictions for the maintenance and life cycle when using the product. A reduction in maintenance intervals or an extended service time represents an added value for this customer. Another benefit might be drawn from extending the service life of a product by entering it into service with properties being sufficient – but not yet optimal – while expecting their further optimization under operational conditions.

A fundamental requirement to meet the ambitious objective of life-cycle modeling of products is an integrative description of the history of the component, starting

Integrative Computational Materials Engineering: Concepts and Applications of a Modular Simulation Platform,
First Edition. Edited by Georg J. Schmitz and Ulrich Prahl.

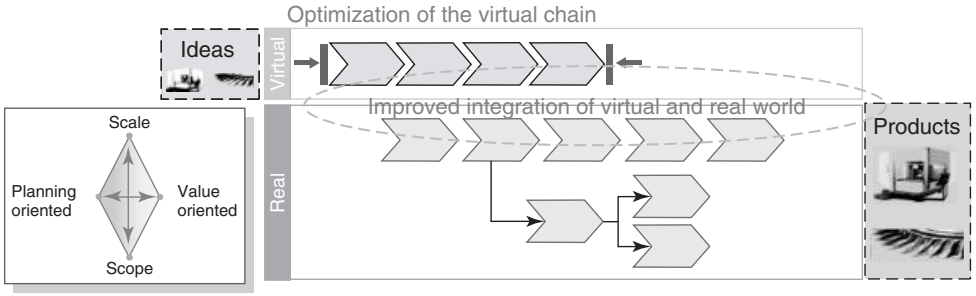

Figure 1.1 Efforts for planning production processes by simulations can be reduced by (i) optimization of individual modules and especially by (ii) improved communication between different modules. The real production process can be optimized, for example, by coupling the virtual world with on-line process control.

from the sound initial condition of a homogeneous, isotropic, and stress-free melt; continuing via subsequent processing steps; and eventually ending in the description of failure onset under operational load. The realization of such a modeling scenario is one of the key objectives of Integrated Computational Materials Engineering (ICME).

1.2 What Is ICME?

ICME or ''Integrative Computational Materials Engineering,'' as denoted in the title of this book, or ''Integrated Computational Materials Engineering,'' as used, for example, in Wikipedia – the slight differences in nomenclature already indicate that it is helpful to discuss the wording in all its aspects before entering the subject itself in more detail.

Looking at the four ingredients ''I,'' ''C,'' ''M,'' and ''E,'' materials scientists might discover an analogy with a quaternary phase diagram like for example the Fe–C–Mn–Si alloy system (Figure 1.2a–d). In order to construct a thermodynamic description of a quaternary alloy system one starts from the pure elements and continues via the binary systems. Those are then used to construct the ternary system and eventually ternary systems are used to construct the quaternary system. It is worthy to note that a ternary system might comprise information that cannot be obtained by a mere superposition of the binary subsystems.

Unveiling the complexity of the quaternary system, ICME will provide a common understanding of the wordings used in this book and best starts from exploiting the ''unaries'' I, C, M, and E first, before continuing via the ''binaries'' integrative computation (IC), integrative materials (IM), integrative engineering

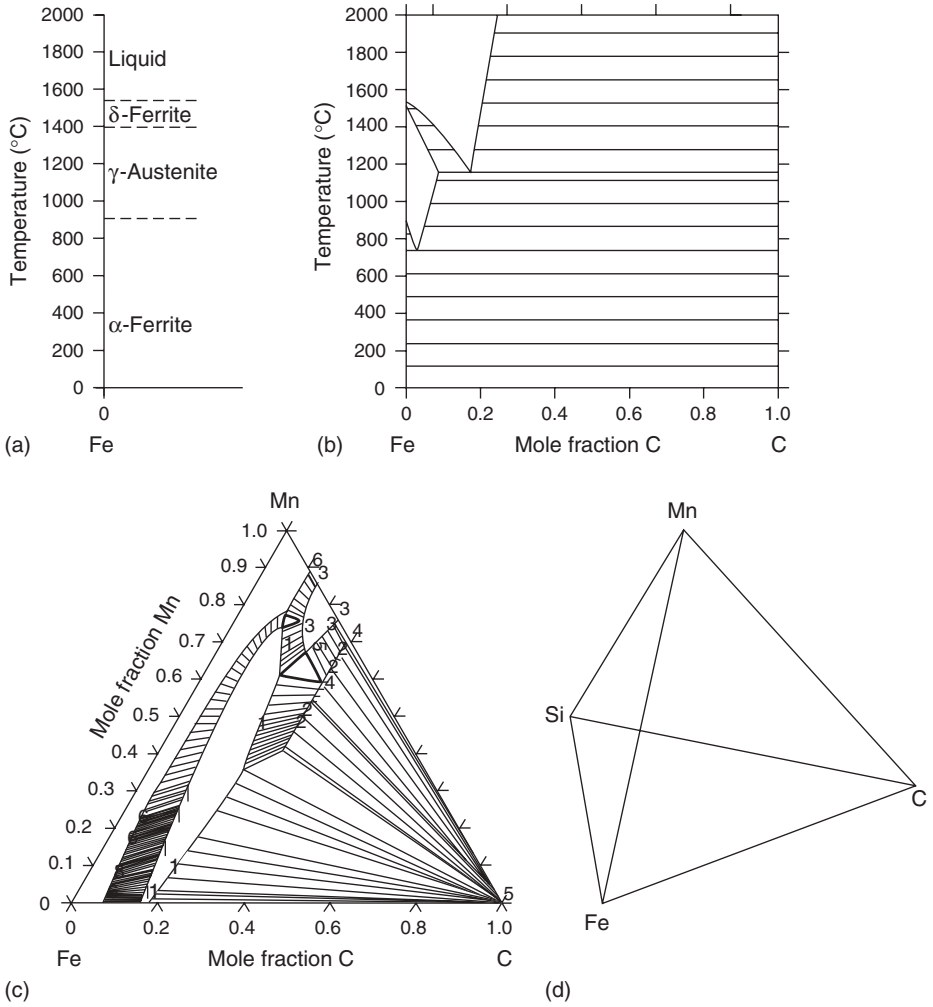

Figure 1.2 (a–d) Schematic thermodynamics of a quaternary alloy system (Fe–C–Mn–Si). (a) Unary phase diagram for pure Fe representing the left boundary for (b) the binary system Fe–C that itself for a given temperature ($T = 1200\ ^{\circ}C$) is a boundary of (c) an isothermal section of the ternary system Fe–C–Mn (calculated using Thermo-Calc). The quaternary diagram Fe–C–Mn–Si for a given temperature corresponds to a tetrahedron with four isothermal ternary sections (not shown in detail) forming the four faces of the tetrahedron (d).

(IE), computational materials (CM), computational engineering (CE), and materials engineering (ME) toward the ternaries integrated computational materials (ICM), integrative computational engineering (ICE), integrative materials engineering (IME), and computational materials engineering (CME).

1.2.1 The "Unaries": I, C, M, and E

- **"I" like integrative, integrated, integration, integr***: These expressions are found in a variety of contexts ranging from social life, mathematics, natural sciences, engineering, and others. Subjects of social integration are, for example, different cultures, and a key issue for a successful integration in social life is communication using a standard for information exchange – the common language. Integration in mathematics essentially means summing up different contributions to form a new entity – the integral. The difference between "integrated" and "integrative" may be seen in the fact that the first term implies the process of integration being already completed, while the second term considers it as still ongoing. With respect to integration in "time," the word history seems adequate, while integration of knowledge over time leads to experience. Usually, an integrative view generates additional information as compared to the mere superposition of the individual parts. Specific aspects of integration in engineering, materials, and computation are discussed in the "binaries" IE, IM, and IC.
- **"C" like computational, computers, computation, comput***: In short, anything that can be performed on a computer such as simulations, handling of large datasets, description of iterative processes, computer control and steering, storage of data and knowledge, mimicking of real processes in virtual reality, computer games, and e-learning. The computer hardware arrangements used for such purposes range from simple processors for simple control tasks to high-performance computing (HPC) for demanding simulation tasks and comprise methods such as parallel computing, grid/cloud computing, and many others. Nowadays, computer technology has reached a degree of maturity, being sufficient to handle large datasets and to tackle complex engineering tasks.
- **"M" like materials**: Classification of materials may be on the basis of different types such as plastics, rubbers, metallic alloys, ceramics, concrete, biomaterials, and wood. Other schemes hold for their individual shape such as bulk materials, thick films, thin films, coatings, or for specific functionalities such as conductors, isolators, structural materials, biocompatible materials, biodegradable materials, high-temperature materials, shape memory materials, self-healing materials, and many, many others.
- **"E" like engineering**: All activities related to design, construction, manufacture; production, assembly, operation and repair/recycling of materials, components, and systems, for example, for consumables, investment goods, public infrastructure, or exploitation of raw materials and resources. Engineering draws on fundamental understanding of phenomena in order to make them applicable for use.

1.2.2 The "Binaries" ME, IM, IE, IC, CE, and CM

The sequence of the description of the "binaries" has been selected according to the relevance for this book, meaning that those binaries without "C" are treated

first because they historically have been present before the availability of computers and thus form an initial state especially for their later ternaries comprising a ''C.''

''ME'' Like Materials Engineering or Engineering of Materials Any efforts aimed at influencing, controlling, and tailoring the properties of materials, especially for technical applications such as ''engineering materials.'' These properties are largely determined by the microstructure of the material, which itself is the result of a subtle interplay of its chemical composition and the entire history of its manufacturing process. Typical ME parameters comprise grain size, grain boundaries, local and global crystallographic orientations (''texture,''), phase fractions, precipitates, dislocations and defects, and their arrangement in the microstructure. Other relevant quantities especially are the concentrations of the individual chemical elements at the scale of the microstructure – the so-called microsegregation – and their variation across the entire component, the macrosegregation. Segregations do contribute to the mechanical properties in terms of solid solution hardening. Their major impact, however, is in their role in determining the further evolution of the microstructure such as the formation or non-formation of precipitates during heat treatment.

Besides the alloy composition itself, a number of process parameters such as heating or cooling rates, dwell times in heat treatments, application of pressure and/or special atmospheric conditions, specific deformation and recrystallization procedures are especially used to control these ME parameters. External electric or magnetic fields, ultrasound agitation, and addition of numerous seeding particles for grain refinement or the use of only a single seed when aiming at a single crystal are some other methods to influence them. It should be noted that in special cases such as for amorphous materials with special properties, the design space for respective products is restricted, for example, to products being small in at least one dimension (powders, wires, foils), because reaching the amorphous state requires extremely high cooling rates, which can only be realized for thin products.

ME – even until the end of the twentieth century – has been based on skills, experience, special recipes, and traditions. Such traditions allowed the realization of exceptional properties by a well-defined sequence of dedicated process steps leading to special microstructures, for example, in ancient damascene swords. With the beginning of the twenty-first century, the availability of sufficient computer capacities and dedicated numerical models allowed for a deeper understanding of the underlying individual processes leading to a desired microstructure in the frame of ''computational materials'' and ''integrative computational materials'' (ICM) modeling, the latter being applied in the case of several processing steps. In this context, it is worthy to note that future efforts – in terms of time and resources – to elaborate a suitable process chain, including a well-suited set of parameters, can be drastically reduced as compared to the development of the above-mentioned damascene process, which took generations to evolve.

"IM" Like Integrative Materials Integrative Materials (IM) might be interpreted as materials combining the individual properties of several materials or integrating several functionalities in a material to form a new material with improved functionalities or properties. Thus, typical examples of IM would be metal-matrix composites such as fiber-reinforced or particle-reinforced metal-matrix composites; reinforced ceramics such as cermets, textile- or steel-reinforced concrete; and reinforced polymers such as CFC, and many others.

Besides arranging one material in the bulk matrix of another material, multilayers of different materials such as laminates or coatings can be considered as another type of IM, where, for example, a coating adds a "corrosion protection" (or an optical, a tribological, or an isolating) functionality to the "structural" (or electrical) functionality of the base material.

Whether such a composite material is considered as a product created by the combination of two different materials or whether it is interpreted as a new material with new effective properties is quite diffuse and frequently depends on its final application. It seems important to note that the properties of such a composite material cannot always be estimated as a weighted average of the individual properties. An important point is that the individual materials such as a technical metallic alloy may also be considered as "composites" being combined from several phases at the scale of their microstructure. Depending on the desired application, either detailed information about the different components/phases and their spatial distribution in the composite or an "effective property of the system" may represent the necessary resp. interesting and adequate description.

"IE" Like Integrative Engineering The term *integrative engineering* might be defined in different ways. It may be interpreted as a combination of different processes ("hybrid processes"), a combination of different technologies ("hybrid systems"), or combinations of a number of components ("system engineering"). Another aspect of IE aims at integrating an increasing number of functionalities in a decreasing system size, such as downsizing concepts in the automotive industry or integrated circuits in the electronics industry.

A modern aspect of IE is integrated production engineering, which is a holistic approach to production processes comprising the engineering of process and value chains from the basic level of understanding of materials and processes up to global production networks and all related logistics.

A success story of integrated production scenarios are platform concepts being essentially characterized by modularity and standardized interfaces. Such platforms, as, for example, platforms known from car manufacture, allow creation of individualized and customized products in spite of an underlying mass production process.

"IC" Like Integrative Computation In a similar sense, software integration in informatics is the combination of different software and/or hardware tools to form a new, more complex entity. Integration in this context may extend from full in-line integration, where the different tools directly interact at each time step, to handshake protocols, enabling an easy information transfer between different tools in a serial type of coupling. Although seemingly contradictory, "distributed"

computation is a special form of integrated computation, as distributed resources are combined to form an integrated computational network. Special examples are cloud computing or ''Software as a Service'' approaches. Integrated computation also refers to special computer architectures such as shared memory architectures or special postprocessing procedures like immersed visualization.

Future developments – as already shown by present Internet browsers – increasingly will take directions of data accumulation, data integration, data retrieval, and knowledge management. Especially for ICME, such a data management is most important for both storage and retrieval of simulation parameters, particularly for a virtual documentation of the component life cycle.

''CE'' Like Computational Engineering All engineering tasks supported by computers form the area of ''CE.'' Engineering tasks, especially in the area of mechanical engineering such as design, construction, manufacture, production, assembly, and operation of components and systems, find their virtual counterparts in computational aided engineering (CAE) such as computer-aided design (CAD), computer-aided manufacture (CAM), virtual manufacturing systems (VMS), and finite element methods (FEMs).

Further aspects of production engineering such as factory planning and logistics are modeled on computers as well, for example, in the frame of condition-based factory planning (CBFP). CE of the materials-representing the basis for any production processes-and their properties proceeds in the areas of CM and CME.

''CM'' Like Computational Materials A number of keywords can be listed to describe the aspects of CM science such as *ab initio* calculations, density functional theory (DFT), molecular dynamics, CALPHAD approach, and computational thermodynamics. Most of these methods aim at descriptions of equilibrium situations or at models at the atomistic length scale. Nonequilibrium situations are tackled using cellular automata, phase-field and phase-field-crystal approaches, crystal plasticity FEM [37], and many more. Several books by now have summarized and reviewed the subject as ''computational thermodynamics'' [1] or ''computational materials'' [2]. CM science has been further extended to simulations of engineering materials [3], somehow directly bridging to the ternary CME. Note that the abbreviation ''CM'' is also used for continuum mechanics, which would match computational materials (when performed at the scale of the microstructure) or computational engineering (when performed at the process/component and system scales).

1.2.3 The ''Ternary Systems'': CME, ICM, IME, ICE

''CME'' Like Computational Materials Engineering It is worthy to note that ''engineering'' in the CME context is rather understood as engineering the properties of

a material than engineering the properties of a component, product, or system. A number of books by now have been published on CME such as [3] or [4].

"ICM" Like Integrative Computational Materials Modeling The classical scope of ICM approaches (e.g., [5]) is the description of materials *evolution* in two directions of integration. The horizontal integration along the processing chain aims at through process modeling and eventually shall describe materials starting from the homogeneous liquid up to the final failure. The vertical integration is well known as the multiscale approach and aims at the description of the properties of the materials starting from the *ab initio* level of the Schrödinger equation and ending at the scale of the material and/or component. This scale bridging is based on the same approaches as CM and CME. Modern ICM developments accept that in many cases a full integration over all scales is neither possible nor mandatory. A scale-hopping approach is thus introduced, focusing on only those effects being relevant for the final process and material property design.[1)]

"IME" Like Integrative Materials Engineering The abbreviation IME may be interpreted as either engineering of integrative materials or integrative engineering of materials. It does not contain a "C" and thus does not relate to "computational" approaches. Thus, either experimental or analytical methods (i) to engineer integrative materials such as composites or (ii) to engineer materials in an integrative approach may be understood here. Examples might be analytical approaches to calculate the properties of a composite by a mixture rule and empirical materials laws being derived from experimental information or experience-based tailoring of alloy compositions or process parameters. Respective models are extremely useful in the context of ICME in view of bridging gaps in the virtual chain, for speeding up individual simulation tools, for validation of simulation results, and many other aspects.

"ICE" Like Integrative Computational Engineering ICE might be understood as any combination of CE activities such as, for example, a virtual description of a production process comprising product design, machining of components, assembly and logistics, and even considering global markets providing the economic and ecologic boundary conditions for the respective component/product.

1.2.4 The "Quaternary" System: "ICME"

Summarizing the above interpretations, there is a discrepancy in the term *Engineering*, which is applied to a product/component on the one hand and to a specific material on the other hand. The adequate interpretation of "E" in ICME is focused on engineering of an entire component and its manufacture in the

1) Special Research Area "steel *ab initio*" at the RWTH Aachen University.

sense of ''ICE,'' with the engineering of the material eventually constituting the component in the sense of Materials Engineering (''ME'' or ''CME'') being only a very important part of the entire effort.

The focus of ICME is thus on engineering the properties of the component as a function of the *local properties of the material* inside the component [6]. These properties themselves have experienced an evolution and depend on the entire process history as well as on the shape of the component and the alloy composition. An instructive benchmark example for a successful ICME could be the prediction of the distortions of a transmission component, which are based on the eigenstrains within the component being influenced by almost each of the process steps during its manufacture and still reveal a dependence on the segregation pattern resulting from the continuous casting process at the very beginning of the component's life-cycle.

1.3
Historical Development of ICME

As computers and computation represent the key ingredient of ICME, the development of this discipline follows the development of computers and their use in society (Figure 1.3).Increasing computational capabilities increasingly allowed for mimicking of real processes in a virtual world. For this purpose models had to be developed, allowing describing physical processes on a computer at all. The most prominent method is the description of phenomena occurring in the continuum of the real world on a numerical grid using the finite difference methods (FDMs) and FEMs and their further derivatives. In the meantime, these methods have

Figure 1.3 Development of computers and computational power goes along with significant changes in their applications. In the 1960s, computers filled entire rooms, still had limited capabilities, and essentially were operated by experts only. Computers of the twenty-first century find a place on a table with their performance largely exceeding the one of a 1960s computer. Their ''operators'' changed into ''users'' and in general are normal people without special computational skills. Nowadays, research and development could not proceed as rapidly without computers.

reached a degree of maturity, making them even applicable to the qualification and certification of products.

FEMs, extended FEMs ''X-FEMs,'' computational fluid dynamics ''CFD,'' and computational damage mechanics ''CDM'' have been extremely successful and a number of relevant software packages are frequently used to describe and optimize individual processes in the frame of ''CE.'' Most progress in terms of ''ICE'' by now has been made in the area of structural materials and their mechanical properties. Computer simulations of macroscopic processes nowadays range from CAD-data to the finished product and in the past decade have been intensively used in many fields of application such as virtual crash tests.

Material data entering such simulations, however, by now in many cases have to be taken from experiments, from literature, or from other sources of information. Owing to a lack of more detailed information or high costs for their determination, such data are frequently assumed as constant, isotropic, homogeneous, and/or are based on other simplifications. Values for a dedicated material often are not available and are then approximated by drawing on similar materials. The variation in these values across the component, their dependence on temperature, and anisotropy are by now, in general, even entirely neglected.

The necessity for such approximations is due to the fact that computational models for materials, allowing for the prediction of materials properties, did not keep pace with the rapid developments of the macroscopic FEM models.

The historic development of CM aiming at the prediction of material properties has at least two different roots, one originating from the atomistic scale in a bottom-up approach and one starting from a thermodynamic, statistical perspective. The latter has proved the potential to tackle technical alloy systems. On the basis of the description of the Gibbs energy of the individual phases and the development of respective models, the CALPHAD method was established in the 1970s to assess a variety of data and combine them into suitable databases [1, 7]. Software and databases such as Thermo-Calc [8], JMatPro [9], FactSage [10], or Pandat [11] have meanwhile become key tools for modern alloy development.

The thermodynamic nature of these programs and databases, however, in general only allows the prediction of equilibrium conditions such as the fractions of individual phases being in equilibrium at a given temperature, the onset temperatures for the formation of specific phases, and many other most interesting thermodynamic data. Information can, however, be neither drawn on the evolution of these phase fractions in time (being mandatory to describe the kinetics of phase evolution) nor about their distribution in space (essentially corresponding to the microstructure, which eventually defines the properties of the material).

In the late 1990s, theoretical developments in the area of microstructure modeling such as the phase-field theory [12] and multiphase-field models [13, 14] have been combined with the above thermodynamic models [15–17]. Such combined models nowadays provide the key to describe and to control the microstructure evolution and eventually to tailor effective properties of technical materials and products [18]. The required data and parameter sets for such models can be obtained from even

more fundamental models such as the DFT, atomistic modeling, and molecular dynamic simulations e.g. by multi-scale modeling schemes [35].

Currently, all these approaches have reached a level allowing for valuable contributions to modern engineering tasks within the knowledge-driven production models. The capabilities of the software tools and the present availability of computational power make efforts toward the integration of all these approaches possible, meaningful, and timely. Such integration offers a relevant step forward in the direction of knowledge-based optimal design of tailored materials, components, and products with regard to their specific applications. Future ''ICME as an emerging discipline aiming to integrate CM science tools into a holistic system will accelerate materials development, transform the engineering design optimization process, and unify design and manufacturing'' [19].

1.4 Current Activities Toward ICME

Describing or even predicting the properties of a component is a key objective of ICME. These properties are essentially determined by the microstructure of the component. Tracking the local microstructure evolution – besides a number of other data – requires boundary conditions for all processes affecting the microstructure during the life cycle of the component. These boundary conditions can be provided by a variety of different FEM simulations on the component scale being daisy-chained to cover the entire production sequence and subsequent operational conditions.

Efforts to standardize and generalize data formats for the exchange of simulation results thus represent a major step toward successful future applications of ICME. Such a standard facilitates information exchange between the different software tools for numerous processes and also across the different length and time scales, affecting both the properties and the life-cycle of an engineering component. A suitable data standard easily links the successful FEM models used in mechanical engineering and CFD, amongst each other and especially with microstructure models such as the phase-field method, which actually seems to become the ''FEM for metallurgists''. This eventually will allow for tracking of the microstructure – and thus the properties of the component – starting from the sound initial condition of a homogeneous, isotropic, and stress-free melt and eventually ending in the prediction of failure under operational conditions. Furthermore, the effects of transformations in the microstructure on the properties of the component can be tackled by extracting local effective properties from the microstructure information and feeding them back into the simulation tools on the component level.

A structural framework for ICME, comprising a variety of academic and/or commercial simulation tools operating on different scales and being modular interconnected by a standardized data exchange, will allow integrating different disciplines along the production chain, which by now have only scarcely interacted.

This will substantially improve the understanding of individual processes by integrating the component history originating from the preceding steps as the initial condition for the actual process. Eventually, this will lead to optimized process and production scenarios and will allow effective tailoring of specific materials and component properties.

Recently, the high importance of an ''ICME'' [20] for the future economic development and competitiveness has been strongly emphasized in a study by the National Research Council of the United States [19]. A number of industrial companies and joint ventures already make use of an ICME' approach and obviously draw significant benefits from doing so (Tables 2.1–2.3 in [19]). The materials being addressed by now comprise Al-alloys, Mg-alloys, superalloys, titanium alloys, solders, and advanced high-strength steels. The benefits being specified by these companies are related to (i) the development, (ii) manufacture, and (iii) the application of products.

The *benefits for planning/development* are identified as

- reductions in materials development *time*,
- *improved materials properties* such as brittleness and strength,
- shorter material certification *times*,
- reductions in product development *time* (15–25% in some cases up to 50%),
- substantial reduction in experimental testing *efforts* in terms of *time* and *costs*,
- weight *savings* for specific components while maintaining the desired *functionality*,
- *improved capabilities* of the components,

The *benefits for manufacture/production*, among others, are exemplarily:

- reduction in manufacturing *costs*,
- *optimized* forging *processes*,
- *fast* and *cost-effective* optimized rolling *processes*,
- *optimized* microstructure *control* in investment castings,

For *operation/maintenance*, the following benefits are exemplarily stated:

- *savings* in operation and, especially, maintenance,
- *prediction of life cycles* of solder joints, (no alternative to ICME),

Looking at the expressions emphasized by *italics*, all these benefits are a result of pursuing the strategy of decreasing the dilemma between planning efforts taken and the eventual product value. During the materials/product design and development stage, ICME significantly reduces these planning efforts in terms of both the time and cost, while simultaneously increasing the product value by improved material properties and/or improved capabilities of the component.

In the United States, a number of universities and academic institutions started working on ICME [38], especially in large consortia, with industry, such as the ''Virtual Aluminum Castings'' [21]. Organizations such as the TMS, ASM, and

MRS aim at structuring all ICME activities in the United States and even in the world by a joint committee on ICME, by organizing a first world congress on ICME (TMS) or by composing the most valuable information about materials simulation in a recent handbook [22].

Although some companies already promote ICME on their web site, for example [23], details about the individual approaches to ICME being taken by industry and the results by now, however, are published only in a few cases such as ''Virtual Aluminum Castings'' [21], structural magnesium parts in automotive applications [24], and the development of superalloys for aerospace and power applications [25, 26]. These approaches, in general, draw back on proprietary developments of the individual companies for interfacing with available commercial tools and complementing them toward the desired ICME functionality.

In Europe, materials modeling on the basis of an integrative simulation approach has been investigated within the project ''Integrated Materials Simulation'' in the period 1993–2005 [5]. The conceptual approach of this project being characterized by modular, integrated multilevel models in the meantime has been adapted by the European industry within the framework of ''Through Process Modeling'' programs for commercial materials within the ''VIR.*''-projects [27, 28]. Several other European groups follow the objectives of integrated modeling such as the IMMPETUS group in Sheffield [29], the Hero-M activity at the KTH Stockholm [30], a through process modeling including in-service operations at the Imperial College [31] and the Interdisciplinary Centre for Advanced Materials Simulation in Germany [32]. Eventually, the AixViPMaP® platform for ICME [36] described in this book is also based on an academic, nonprofit activity. Some preliminary simulations of industrial steel components have been performed on the basis of this platform [33].

The efforts of commercial providers of simulation software aim at a steadily increasing integration of more and more functionalities into their own specific codes. This frequently leads to large general purpose tools instead of modular structures. Examples are the ESI Virtual Try-Out Space (VTOS) or the ANSYS Workbench Platform. These commercial software structures can be considered as strong in modeling a number of coupled processes (e.g., forging and heat treatments) at the component scale using FEM methods in the sense of an ICE. The underlying materials models most relevant for a successful ICME, however, are in most cases empirical and, in general, do not account for the preceding history of the material with respect to the component.

1.5
Toward a Modular Standardized Platform for ICME

In view of the common perception of the significant benefits being related to a successful implementation and application of ICME scenarios, the question arises about how to realize such scenarios successfully while at the same time taking care

of the interests of academia, the producing industry and the providers of simulation software.

Industrial approaches to ICME, as exemplarily detailed for Mg and Al castings above, by now often are stand-alone island solutions being designed to tackle dedicated problems. Such solutions in general draw back on commercial software codes being complemented by proprietary software to allow for an integrative description of specific, commercially relevant phenomena. Economic competition will prevent or at least substantially hinder the exchange of codes or interface routines and data.

Commercial providers of simulation software are highly interested and active in developing their own standards linking their proprietary codes toward their own ICME platforms, making their product portfolio more competitive. Although many of them already provide interfaces to their tools, their interest in creating and developing a generalized, open standard that also allows information exchange, for example, with software tools of their competitors or with tools originating from academia, is less pronounced. It does not seem probable that a general standard will be proposed or realized by one of the commercial simulation software providers in the near future.

To circumvent such limitations arising from competition issues, establishing a generalized, open standard in the frame of an academic setting seems meaningful. The expertise of an individual academic institute alone, however, is not sufficient to meet this ambitious objective. In contrast, the task requires the combined effort of a number of institutions contributing a broad range of expertise for various materials, for all processes along the value chain of a product, for the relevant phenomena and their modeling, for efficient computation and algorithms and much more.

Hierarchical structures with few experts aiming at coordinating such an activity thus will be less effective as compared to a self-organization of teams of experts with a broad spectrum of expertise heading for generalized solutions.

A German initiative aiming at fostering the excellence of German universities provided funding to a number of institutes at the RWTH Aachen University to investigate ''Integrative production technologies for high-wage countries'' in the frame of a cluster of excellence at the end of 2006 [34]. One of the larger projects in this cluster combined the profound expertise of nine university institutes renowned in materials and process development and simulation along the entire value chain. Already in the very early work-group meetings, the urgent need for a ''common language'' for the exchange of simulation results was identified. In the further course of this project, such a standard has been elaborated and implemented in a number of dedicated simulation tools. Simulation chains for dedicated test scenarios were then created and validated. In a second step, several of the simulation tools were implemented in a web-based grid infrastructure, allowing for setting up simulation chains and automatically running them remotely.

1.6 Scope of This Book

The scope of the book is to demonstrate a promising strategy toward a successful ICME being based on the standardization of information exchange. This pathway and its benefits are highlighted using the example of the AixViPMaP® platform and some test cases that have been used for its verification. The special scope of the AixViPMaP® platform is the definition and provision of an open, generalized standard allowing for information exchange between a variety of simulation tools. The major scope of this book is the communication of this standard and of the first experiences made in using it. Several further reasons extended the basis for writing this book:

- **First**: A major reason for publishing this book was to comprehensively summarize all work being performed during the period 2006–2011 within the project ''Virtual Process Chains for Processing of Materials'' of the Cluster of Excellence ''Integrative Production Technologies for High-Wage Countries.'' This work comprises the efforts of a consortium of nine institutes of the RWTH Aachen, all being renowned in the area of materials science and processing (casting, forming, annealing, joining, and coating) of metallic alloys (especially steels), polymers, and composites and two further institutes being well known in the areas of scientific computing and information management.
- **Second**: Only a publication in the form of a book allows to describe all structural ideas, underlying concepts, defined standards, results obtained for verification using the different test cases, and eventually even a description of how to use the platform as a user and how to join the platform as a provider. Many aspects being necessary for the successful operation of such a platform – especially the definition of standards – are hard to publish as stand-alone articles in journals.
- **Third**: The book might serve as a first handbook for future users of the simulation platform (especially small and midsize enterprises (SMEs) and academia) as well as for providers of simulation software, which would like to make their software/services available via such a platform.
- **Fourth**: The book will provide an integrative view on production processes and the resulting properties of materials and components for students of materials science and engineering, for students of mechanical engineering, and eventually also for people responsible for the design and layout of production processes.
- **Fifth**: A book on ICME seems timely in view of a particular community actually establishing itself with a First International World Congress on ICME, which took place in Pennsylvania in July 2011.

In fact, this book is not a book on ICME in general, as the area is huge and still not sufficiently mature for a sound review. The scope of the book is to summarize the general ideas of ICME, but especially to demonstrate a promising strategy toward a successful ICME being based on standardization of information exchange. This pathway and its benefits are then highlighted using the example of the AixViPMaP® platform and the test cases used for its verification. In

this context, the AixViPMaP® platform should not be identified as a dedicated software requiring an ''own manual'' and ''regular releases.'' The special scope (and content) of the AixViPMaP® platform is the definition and provision of an open standard allowing for information exchange between a variety of commercial and academic research tools. A second scope of the AixViPMaP® is the realization of simulation chains in an Internet-based environment – a GRID – drawing back on this particular standard.

To the best of our knowledge, such an open, modular standardization approach toward ICME involving both commercial and academic software tools has not been made till now. Communication of this first version of a standard for exchange of simulation results along a process chain and across different length scales (and of the benefits resulting from using it) thus is the major objective for writing this book. Such standards must be communicated in order to be spread, to find acceptance, and eventually to become a worldwide standard. As for standards in general, the authors are well aware that such a standard will surely further evolve in future.

This book is structured in two parts. In the first part (Chapters 2–7), the platform concept and its background are detailed. The second part (Chapters 8–12) describes several test cases being used to verify the platform functionality and to demonstrate the benefits of an ICME approach. Eventually, future perspectives for the further development of ICME using the approaches being detailed in this book are outlined in the final chapter.

References

1. Lukas, H.L., Fries, S.G., and Sundman, B. (2007) *Computational Thermodynamics – The Calphad Method*, Cambridge University Press, ISBN: 978-0-521-86811-2.
2. Raabe, D. (1998) *Computational Materials Science*, Wiley-VCH Verlag GmbH, Weinheim, ISBN: 3-527-29541-0.
3. Raabe, D., Roters, F., Barlat, F., and Chen, L.Q. (eds) (2004) *Continuum Scale Simulation of Engineering Materials: Fundamentals – Microstructures – Process Applications*, Wiley-VCH Verlag GmbH, Weinheim, ISBN-10: 3-527-30760-5.
4. Janssens, K.G.F., Raabe, D., and Kozeschnik, E. (2007) *Computational Materials Engineering: An Introduction to Microstructure Evolution*, Academic Press, ISBN-10: 9780123694683.
5. Gottstein, G. (ed.) (2007) *Integral Materials Modelling: Towards Physics Based Through-Process Models*, Wiley-VCH Verlag GmbH, Weinheim, ISBN: 978-3-527-31711-0.
6. Miller, F.P., Vandome, A.F., and McBrewster, J. (2010) *Integrated Computational Materials Engineering*, Alphascript Publishing, ISBN: 10:6130760477.
7. *http://www.calphad.org/* (accessed 20 January 2012).
8. *http://www.thermocalc.com* (accessed 20 January 2012).
9. *http://www.sentesoftware.co.uk/* (accessed 20 January 2012).
10. *http://www.factsage.com* (accessed 20 January 2012).
11. *http://www.computherm.com/pandat.html* (accessed 20 January 2012).
12. Kobayashi, R. (1993) Modeling and numerical simulations of dendritic crystal growth. *Phys. D*, **63** (3–4), 410–423.
13. Steinbach, I., Pezzolla, F., Nestler, B., Seeßelberg, M., Prieler, R., Schmitz, G.J., and Rezende, J.L.L. (1996) A phase

field concept for multiphase systems. *Phys. D*, **94**, 135–147.
14. Steinbach, I. (2009) Phase-field models in materials science – topical review modelling. *Simul. Mater. Sci. Eng.*, **17**, 073001.
15. Eiken, J., Böttger, B., and Steinbach, I. (2006) Multiphase-Field approach for multicomponent alloys with extrapolation scheme for numerical application. *Phys. Rev. E*, **73**, 066122.
16. Fries, S.G., Böttger, B., Eiken, J., and Steinbach, I. (2009) Upgrading CALPHAD to microstructure simulation: the phase-field method. *Int. J. Mater. Res.*, **100**, 2.
17. *http://www.micress.de* (accessed 20 January 2012).
18. Schmitz, G.J., Böttger, B., Eiken, J., Apel, M., Viardin, A., Carré, A., and Laschet, G. (2011) Phase-field based simulation of microstructure evolution in technical alloy grades. *Int. J. Adv. Eng. Sci. Appl. Math.*, doi: 10.1007/s12572-011-0026-y
19. National Research Council (2008) *Integrated Computational Materials Engineering: A Transformational Discipline for Improved Competitiveness and National Security*, National Academic Press, Washington, DC, ISBN: 0-309-12000-4.
20. Allison, J., Backman, D., and Christodoulou, L. (2006) Integrated computational materials engineering: a new paradigm for the global materials profession. *JOM*, **58** (11), 25.
21. Allison, J., Li, M., Wolverton, C., and Su, X.M. (2006) Virtual aluminum castings: an industrial application of ICME. *JOM*, **58** (11), 28.
22. Furrer, D. (ed.) (2010) *ASM Handbook*, Metals Process Simulation, Vol. **22B**, ASM International, ISBN-13: 9781615030057.
23. *http://www.rolls-royce.com/technology_innovation/material_tech/materials_process_modelling.jsp* (accessed 20 January 2012).
24. *http://www.production-research.de* (accessed 20 January 2012).
25. Backman, D.G., Wei, D.Y., Whitis, D.D., Buczek, M.B., Finnigan, P.M., and Gao, D.M. (2006) ICME at GE: accelerating the insertion of new materials and processes. *JOM*, **58** (11), 36.
26. Furrer, D.U. (2011) Application of phase-field modeling to industrial materials and manufacturing processes. *Curr. Opin. Solid State Mater. Sci.*, doi: 10.1016/j.cossms.2011.03.001
27. Hirsch, J. (ed.) (2006) *Virtual Fabrication of Aluminium Products*, Wiley-VCH Verlag GmbH, Weinheim, ISBN: 352731363X.
28. Hirsch, J. and Karhausen, K.F. (2011) in *Proceedings of the First World Congress in Integrated Computational Materials Engineering (ICME)* (eds J. Allison, P. Collins, and G. Spanos), John Wiley & Sons, Inc., and Wiley-VCH Verlag GmbH, Weinheim, pp. 203–210, ISBN: 352731363X.
29. Immpetus Sheffield A New Framework for Hybrid Through-Process Modelling, Process Simulation and Optimisation in the Metals Industry, *http://www.immpetus.group.shef.ac.uk/* (accesssed 20 January 2012).
30. Hierarchical Engineering of Industrial Materials (hero-m) Activity Started in 2007 at KTH Stockholm, *http://www.hero-m.mse.kth.se* (accessed 20 January 2012).
31. Li, P., Maijer, D.M., Lindley, T.C., and Lee, P.D. (2007) A through process model of the impact of in-service loading, residual stress, and microstructure on the final fatigue life of an A356 automotive wheel. *Mater. Sci. Eng. A*, **460–461**, 20–30.
32. *http://www.icams.de*.
33. Schmitz, G.J., Benke, S., Laschet, G., Apel, M., Prahl, U., Fayek, P., Konovalov, S., Rudnizki, J., Quade, H., Freyberger, S., Henke, T., Bambach, M., Rossiter, E.A., Jansen, U., and Eppelt, U. (2011) Towards integrative computational materials engineering of steel components. *Prod. Eng. Res. Dev.*, DOI: 10.1007/s11740-011-0322-1.
34. Allison, J.E., Liu, B.C., Boyle, K.P., Hector, L., and McCune, R. (2010) in *Proceedings of the Magnesium Technology Seattle, WA* (eds S.R. Agnew, N.R. Neelameggham, E.A. Nyberg, and W.H. Sillekens), Wiley, pp. 35–40.

35. Vaz Junior, M, de Souza Neto, EA., and Munoz-Rojas, PA. (eds) (2010) *Advanced Computational Materials Modeling – From Classical to Multi-Scale Techniques*, Wiley-VCH Verlag GmbH, Weinheim, ISBN-10: 3-527-32479-8.
36. Schmitz, G.J. and Prahl, U. (2009) Toward a virtual platform for materials processing. *JOM*, **61** (5), 26.
37. Roters, F., Eisenlohr, P., Bieler, T.R., and Raabe, D. (2010) *Crystal Plasticity Finite Element Methods in Materials Science and Engineering*, Wiley-VCH Verlag GmbH, Weinheim, ISBN-10: 3-527-32447-X.
38. Lados, D.A. (2009) Integrative materials design: achievements and opportunities. *JOM*, **61** (2), 67.

2
Basic Concept of the Platform

Georg J. Schmitz and Ulrich Prahl

2.1
Overview

Materials properties are the basis for the functionalities of almost any product. For many applications, the final materials properties result from a number of process steps. Each of these steps allows for adjusting the microstructure in order to ensure an eventually desired functionality, which may be important either for further processing or for the final application. Besides meeting this basic functionality (mechanical, medical, electronic/magnetic, thermal/thermomechanical, chemical, optical, or fluid dynamic, etc.), a broad spectrum of nonfunctional requirements has to be met by modern materials such as, for example, minimal costs for raw materials, robustness of their processing, or high quality of the resulting products (e.g., safety, reliability, or recycling capability). These nonfunctional requirements are subject to a dynamically evolving global market providing boundary conditions such as varying prices of raw materials or a limited availability of production plant capacity. A producer who can react best and fastest to these dynamic conditions and adjust his production rapidly will win in the market. In the long term, only a comprehensive simulation of materials, their production, and their properties will allow for a significant reduction and speedup of efforts for planning, designing, and redesigning of materials and production processes.

Materials science and engineering comprises different levels and functional fields, many of which – simultaneously or consecutively – are relevant to the final product properties and thus require an integrative description. In view of the complexity of even a single process influencing the complex microstructure of a technical alloy grade and, accordingly, the properties of the material, any kind of analytical approach becomes obsolete when aiming at generic predictive capabilities. Only an integrated computational materials engineering (ICME)-type approach thus will enable the exploitation of the limits of optimum materials performance, optimal processing conditions, or even an optimal product. It seems important to note that – in the case of a process chain – the global optimum for the chain not necessarily corresponds to a chain where each of the processes is optimized individually. An example might be a casting process being followed by a

Integrative Computational Materials Engineering: Concepts and Applications of a Modular Simulation Platform,
First Edition. Edited by Georg J. Schmitz and Ulrich Prahl.

homogenization heat treatment. A cast part remaining in a mold at a high temperature for an extended time will lead to reduced productivity of the casting process, but might lead to a substantial reduction in the efforts spent for the heat-treatment process. In addition to savings in process time, savings in energy might also be expected as reheating of the cast part to the heat-treatment temperature can be avoided.

The basic ingredients of a strategic approach toward an integrative computational materials engineering (ICME) and their *implications* are

- allowing for use of existing and verified models to a maximum extent: *extendable, modular;*
- closing existing gaps in the present manifold of models by mapping the materials and the process chain, aiming at the provision of a *comprehensive* concept;
- speeding up individual models by data reduction where applicable: *adaptable;*
- speeding up individual models by efficient programming: *efficient;*
- enabling and speeding up information exchange between different models: *standardized;*
- integrating different process scales (length, time): *comprehensive, adaptable;*
- being useful for different types of materials and processes: *generic and/or adaptable;*
- using only models relevant to describe/predict the process: *modular;*
- model refinement or model reduction where necessary and/or beneficial: *extendable, modular;*
- facilitating creation of simulation chains by drawing on prior knowledge: *self-learning, knowledge integrative;*
- allowing for networking and use by different communities: *open*.

The *maximum use of existing and verified models* implies the need for an *extendable, modular* concept. Starting from the pragmatic concept of using all available and/or relevant models, it requires the option of future extensions in order to account for the integration of future models or of models not accounted for when setting up the concept. Future models may provide more detailed descriptions – descriptions of novel phenomena not described before, more efficient models, models with different degree of accuracy, and much more. Process chains can thus be created combining efficient simulations with an adequate level of detail.

Existing gaps in the model chain have to be filled to provide a comprehensive description of the history of the material with respect to the component. In the long term, such gaps must be closed by suitable numerical models. In the initial stages of the platform development, an incomplete set of models may be supplemented by replacing individual simulation steps by experimental information or by intentionally designed data such as, for example, ''synthetic microstructures.'' A common standard for information exchange with experimental facilities would be highly desirable in this context. This exchange could refer to geometric data such as 3D component shapes determined by optical 3D scanners or by X-ray computer tomography. For 3D microstructures, data reconstructed from a series of automatically recorded metallographic sections or from combined

focused ion beam/scanning electron microscopy technologies would be perfectly suited to complement numerical models and data.

Speeding up individual models is mandatory for efficient simulation chains and can be realized by *efficient* programming of the individual modules, for example, using parallel codes, or by data reduction by *adaptation* to the specific problem wherever a reduced information depth is still sufficient to tackle the phenomenon to be modeled in adequate detail. Even simple assumptions may be sufficient in some cases.

Speeding up the information exchange between different models is necessary to effectively simulate process chains and requires a *standardization* of information exchange between different models and also across different scales.

An integrative description of the history and, accordingly, of the properties of a component requires a *comprehensive* set of models for all processing steps at all length scales. At least one model for each process at each scale thus must be available. If a model for a particular process is missing, respective data from experiments might be used instead. In case a number of models are available in future for a specific process at a specific scale, the most appropriate model in terms of computational effort versus desired accuracy can be selected.

Speeding up the creation of simulation scenarios. Even if all modules for the simulation of a particular process chain are available at all scales, perform highly efficiently individually, and communicate effectively among each other, there is still a lot of work to be done to set up a dedicated simulation scenario. Especially, the provision of materials and process data has to be organized effectively. Concepts of *knowledge* management and *self-learning systems* have to be addressed in future. Such concepts may, for example, provide existing simulation chains as templates, which can more easily be adapted to a new situation as compared to creating an entirely new simulation scenario. Especially, inclusion or removal of dedicated models for specific process steps is facilitated by the modular platform approach.

In summary, the strategic approach described in this book is to provide an open, comprehensive, standardized, modular, and extendable modeling platform efficiently adaptable to specific materials, to a variety of production processes, and eventually describing product properties.

Production of real goods such as cars has emerged from an individualized production of a first car via mass production of standardized cars toward platform concepts based on a number of modules being configurable toward individualized cars meeting the individual customer demands in spite of mass production (Figure 2.1). Platform concepts turned out to be the best practice approach to provide individualized, customized goods, while at the same time retaining the cost benefits of mass production. In the same spirit, a simulation platform thus can and will provide individual solutions for a variety of materials/processes in spite of a limited but modular and standardized model map. Such a simulation platform may in future eventually become part of a larger virtual system and provide the basis for a holistic theory of production.

The platform concept described in this book is limited to continuum modeling. The descriptors for processes, components, and microstructures are thus essentially

(a) (b) (c)

Figure 2.1 Platform concept in production of cars. (a) Manufacture of an individual car does not need any standardization (image by Daimler AG). (b) Standardized cars can be produced much quicker and cheaper (image by Ford Company). (c) Individual cars can be realized in mass production by drawing on a modular, configurable production platform concept (image by Volkswagen).

field variables of, for example, alloy concentration, temperature, distortions, strains, and others. The length scales covered by the continuum descriptions in this context comprise the submicrometer (nanometer) scale, the scale of the microstructure (micrometers to centimeters), the component scale (millimeters to meters), and the facility scale (millimeters to several meters). The time scales range from nucleation and recrystallization processes (nanoseconds to microseconds), solidification and crystallization processes (microseconds to hours), heat treatments (hours/days), and operational conditions (days/years). The processes being modeled in the long term shall comprise a full description of the entire product life cycle starting from the homogeneous, isotropic, and stress-free melt, continuing via all further processing steps including forming/shaping, heat treatment, joining, cutting/machining, and eventually ending in description of failure under operational loads.

Discrete models and data from the smaller atomistic scale are coupled to the platform as effective values, for example, as thermodynamic properties entering CALPHAD-type databases, data for thermal conductivities of pure phases, properties of interfaces such as interfacial energies, and others.

Again, at the larger length scale of the factory, discrete data such as cycle times, energy consumption, circulating materials, and so on are forwarded to the respective models. On the other hand, variations in boundary conditions such as increasing prices for specific raw materials might trigger a replanning, with the redesign of the production process then performed using the platform. In the long term, this platform may even be extended and applied to logistics and factory layout processes.

The initial platform development started in early 2007 and has been based on the following basic strategy and approaches:

1) networking of available simulation applications in materials science and process engineering in a modular and standardized manner;
2) extension of present microstructure simulation models to close gaps in the model chain;
3) extension of present simulation applications at the process scale toward consideration of spatially resolved, anisotropic materials properties;

4) data reduction by extraction of effective properties from simulated microstructures;
5) operation of the platform using distributed simulations on a computational grid;
6) verification of platform performance for test cases of economic and scientific interest.

Networking of a variety of heterogeneous simulation models has to start somehow and somewhere before it can continue to further evolve in a kind of self-assembly process. Just as the definition and formulation of the HTML language as the basis for the present World Wide Web of computers, has been initiated at CERN in Geneva in the 1980s by a number of particle physics groups, a similar nucleus seems necessary in case of a future platform for ICME. As known from the nucleation theory, the boundary conditions must be suitable for nucleation, the activation energy has to be overcome, and the nucleus must be hypercritical to be stable and eventually to grow into a macroscopic crystal.

At the RWTH Aachen University, in 2006 the project ''Virtual process chains in the manufacturing and processing of materials'' was activated by governmental funding in the frame of the Cluster of Excellence ''Integrative Production Technologies for High-Wage Countries''. This project teams up the expertise of a number of institutes at the university, which have a high reputation in experimentation and process development from the laboratory scale to the production scale. This combined experimental/economical expertise has provided a sound basis for the production-oriented development of individual numerical models and software packages in the area of materials processing covering the entire value chain from casting; forming; heat treatment; and joining and coating for metallic alloys, composites, and polymers. This team, its direct interaction with the universities' informatics institutes and infrastructure and its integration into an even larger project aiming at a holistic view on production have provided the suitable initial and boundary conditions for the nucleation of an ICME platform – the Aachen (**Aix**) – **Vi**rtual **P**latform for **Ma**terials **P**rocessing (AixViPMaP®), as described in this book. Successful networking furthermore requires low thresholds to be overcome for participation in the network, while at the same time providing benefits to the individual participants and confidentiality wherever needed.

To *close gaps in the model chain*, especially, a further extension of microstructure simulation models is necessary. Currently, the description of diffusion-controlled phase transformations such as solidification processes, solid-state transformations, and recrystallization processes is possible even for technical materials comprising a number of alloying elements. Elastic strains and their influence on the microstructure have already been taken into account. Viscoplastic models have been included recently and are currently in the status of verification. Topics to be addressed in the midterm comprise, for example, (i) grain structures during hot and cold forming, (ii) formation of phases with substructure such as pearlite or bainite, (iii) microsegregation during solidification of flowing melts, (iv) formation and evolution of precipitates, (v) evolution of polymer microstructures evoked by heat exposure

and related development of inner properties of polymers, and (vi) prediction of mechanical and technological properties, in particular, fatigue, based on chemical composition and microstructures for both metallic alloys and polymers.

Current *process and component simulation models* can be significantly improved by taking into account local materials properties in the frame of ICME in future. Materials characteristics of process simulations describing production processes at the component scale by now are mostly considered as macroscopically averaged, homogeneous, and isotropic on the basis of tabulated values. Their dependence on process parameters such as temperature or inhomogeneous chemical compositions – like segregation or precipitates in the material – is currently either neglected or only approximated. In future, respective values will be replaced by effective parameters, which have experienced an evolution according to the upstream process steps simulated in microstructure models and can describe peculiarities of the materials such as anisotropy or spatially resolved inhomogeneities. This will eventually allow describing the response of a macroscopic component such as shape, distortions, or overall hardness on changes in its microstructure evoked by, for example, load conditions during operation.

An *extraction of effective properties* is mandatory as the simulation results of micromodels provide a maximum information depth in the form of spatial-temporally resolved microstructures largely exceeding what is required at larger length scales. To obtain information relevant to simulations on a larger length scale, a reduction of these data is thus necessary. This data reduction/extraction may be realized by methods of mathematical homogenization or by virtual testing, models of which are presented and discussed in Chapter 5.

All the above objectives of ICME, in principle, can be met by performing simulations at individual places with individual software and by exchanging data in the standardized format by e-mail or file transfer. The next challenging step is to compose and run a sequence of different simulations automatically. As, in general, not all software tools necessary to cover an entire chain are available at a specific location, distributed simulations on a computer grid are meaningful for this purpose. Grid operations of simulation chains further will largely facilitate the collaborative work of different groups from different locations and respective; approaches are presented and discussed in Chapter 6. An integrative view of the results of an entire simulation chain also demands suitable visualization methods. Such methods are described in Chapter 7. In the long term, such a web-based platform approach may lead to calculations on demand in case a suitable accounting scheme is additionally provided for commercial software codes.

Eventually, the performance of the platform has to be validated and its benefits have to be exploited. For this purpose, a number of test cases of scientific and economic interest have been specified in cooperation with industrial partners. The details and results of these test case scenarios are outlined in Chapters 8–12.

The following sections briefly introduce the basic concepts of the platform such as modularity, standardization, and web-based operations, each of which is intensively detailed in the different chapters of this book. The basic philosophy of the AixViPMaP® is to provide an open, modular, standardized, extendable, and

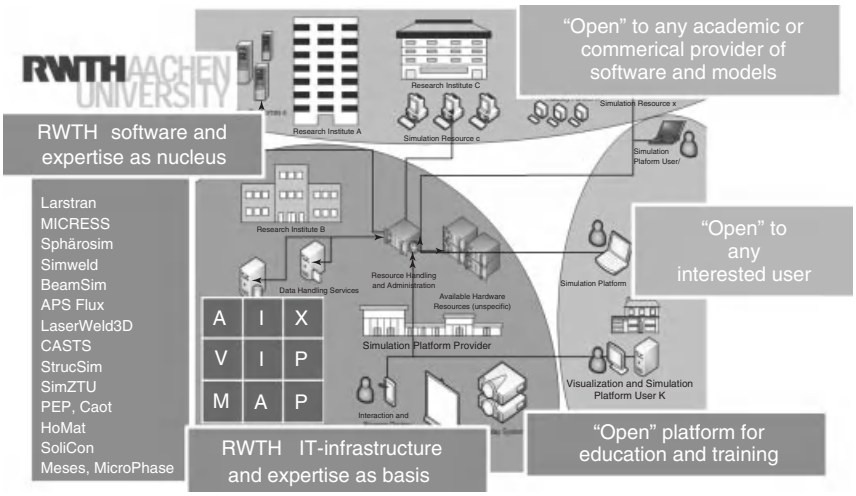

Figure 2.2 Vision of a simulation platform for ICME simultaneously matching the interests of academia, producing industry, and software providers. The RWTH Aachen University is sketched here as host for the platform concept, as detailed in this book, while the concept itself may in principle be installed and operated anywhere.

comprehensive platform for any type of simulation related to materials processing and production. AixViPMaP® thus will provide integration capabilities for both commercial and academic simulation tools. It is well understood that commercial providers will not release their code sources for this purpose. The concept thus draws on a standardization of information exchange between different software tools – commercial and/or academic – considered as ''black boxes'' and providing a standardized output or at least parser/sequencer routines, allowing for conversion of data into the platform standard. This platform will enable linking of available materials models and application-oriented simulation chains on the basis of a common standard in a bus-type architecture, allowing effectively simulating, developing, optimizing, and controlling process chains at different length scales and for a variety of materials. It shall be open to any commercial and academic software provider and to any interested academic or commercial user (Figure 2.2). Such a platform will both substantially decrease present planning efforts and allow for ''first time right'' approaches to new processes and products. Further, it will provide a number of new options for a holistic education, teaching, and training in the fields of materials and production engineering.

2.2 Open Architecture

Describing or even predicting the properties of a component is a key objective of ICME, which has been identified as a strategic approach for future

competitiveness as outlined in Chapter 1. These properties are essentially determined by the microstructure of the component. Tracking the local microstructure evolution – besides a number of other data – requires a variety of models and software tools for the description of different processes and phenomena to be combined.

A structural framework for ICME comprising a variety of academic and/or commercial simulation tools operating on different scales and being modular interconnected by a standardized data exchange thus will allow integrating different disciplines along the production chain, which by now have only scarcely interacted. This will substantially improve the understanding of individual processes by integrating the component history originating from preceding steps as an initial condition for the actual process. Eventually, this will lead to optimized process and production scenarios and will allow effective tailoring of specific materials and component properties. Such a concept will allow for monitoring the evolution of the microstructure – and thus the properties of the component – starting from the sound initial condition of a homogeneous, isotropic, and stress-free melt and eventually ending in the prediction of failure under operational conditions.

An *open architecture* will be a key ingredient of a strategic approach toward ICME. Anybody interested in profiting from ICME by performing simulations must be able to do so without major barriers. In the same spirit, anybody willing and capable to provide models or simulation tools should be able to easily include them into the ICME framework. Even if an open architecture is highly desirable, one has to account for the interests of commercial providers of simulation software as well. The easiest way and probably the fast lane to integrate academic and commercial model worlds thus seems to be the definition of a common language in the sense of an information exchange between different models based on a common, open standard. Future developments then may aim at web-based provisions of simulation tools and computer capacities in the frame of a ''calculation on demand.'' The term *open architecture* in this context thus should, however, not be confused with freeware solutions. It stands for a data standard enabling efficient communication between various tools and models. This standard is publicly documented and further developed on the basis of a public discussion, especially in the frame of the emerging ICME community.

2.3 Modularity

The *platform concept* is defined as modular and extendable, and thus nothing is known a priori about the models to be potentially incorporated into the concept in future. All models and software tools thus have to be considered as ''black-box''-type models interfacing with the rest of the world. The platform shall be capable of including present and future academic and/or commercial simulation tools. A priori source codes will not be available and the codes representing the modules of the platform have to be considered as individual modules, which have to interact via a defined information exchange. Modularity not only facilitates daisy chaining of

different modules when setting up a simulation chain but also especially allows for a fast and an easy redefinition and redesign of process chains allowing optimizing entire production scenarios.

2.3.1 Individual Modules

The basic prerequisite for each individual module is a defined input as an initial condition and a defined output as a result, with the module describing the spatiotemporal evolution between input conditions and output situation. Each module itself thus can be applied repeatedly in multiple iterations, taking the output of a simulation as the input for a subsequent simulation. In a similar manner, the output of a preceding module can be understood as an initial condition for a subsequent model, mimicking a different process. This leads to a directional topology for the information flow (Figure 2.3).

For the description of phenomena, which might be treated in a decoupled way at a dedicated scale, a specific process can be split into two or more simulations running either sequentially (although describing the same time period of the simulated process) or in parallel but acting on different parameters of the dataset. An example could be the simulation of the grain-size evolution during a hot rolling process being calculated independently of a heat-treatment simulation tackling diffusion and segregation at the same time in parallel (Figure 2.4).

The output of one module corresponds to the final conditions at the last time step and is provided for the subsequent module as the initial condition for the first time step. Data for all intermediate time steps of the individual processes are saved and stored centrally for further evaluation but not handed over between the different process simulations. Such a sequence of models eventually has to be established at any of the four continuum scales covered by the platform approach, that is, the submicrometer scale, the scale of the microstructure (micrometers to centimeters), the component scale (millimeters to meters), and eventually the facility scale (millimeters to several meters) (Figure 2.5). It is important that initial information not being modified by an actual simulation is channeled through this particular simulation in an unmodified manner in order to be available for other, subsequent models, in which this information might become important again.

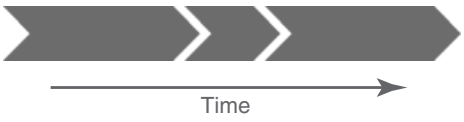

Figure 2.3 Principle of a simulation chain at a dedicated length scale. Earlier time steps representing the history of the component provide the input for its further evolution. The simulation times for the individual models may differ (as indicated by a ''shorter'' module in the middle).

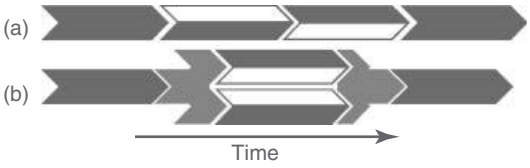

Figure 2.4 In case of decoupled processes or decoupled phenomena, simulation codes may be used (a) in a serial way or (b) in parallel. Both codes will then draw on the same initial conditions split by a small interface module but act on different parts of the dataset such as on grain sizes (code 1 exclusively) and concentration fields (code 2 exclusively). Both results will eventually be stitched together again by a small interface/service module to serve as input for the next process. Parallel operations may result in reduced simulation times. Stitching together individual simulation chains is particularly interesting when combining two components with own histories in a joining process such as welding eventually resulting in a single component again.

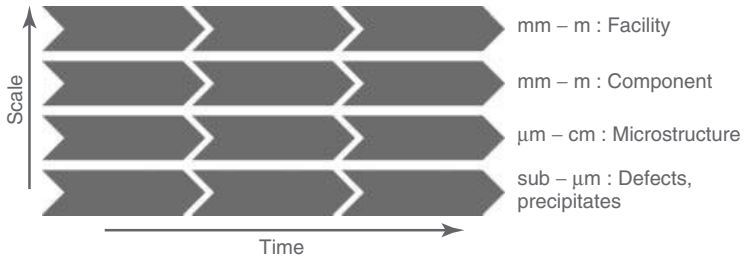

Figure 2.5 Simulation chains for phenomena occurring at the different length scales have to be established for each of the scales. In the next step, the interaction between the different scales has to be taken into account (Section 2.3.2).

2.3.2 Bridging the Scales

The scales being addressed by the platform by now are limited to continuum models in 2D and 3D. The methods being used at the component scale comprise, for example, CAx (e.g. computer aided design 'CAD' or computer aided manufacture 'CAM' or others), finite element methods (FEM), finite difference methods (FDM), and extended finite element methods (X-FEM). At the scales of the microstructure and in the submicrometer range – multiphase field models, cellular automata, CALPHAD type thermodynamics and kinetics, and CP-FEM (i.e., crystal plasticity–finite element method) are typical methods. The platform is further embedded between the smaller length scales of atomistic and *ab initio* simulations and the larger length scales of production machinery and factory layout/logistics, to which interfacing will be increasingly provided in the future.

Subsequent to the definition of a modular structure facilitating the information exchange at a given scale along the history of a component, an information exchange bridging between these different scales has to be realized by a suitable information flow.

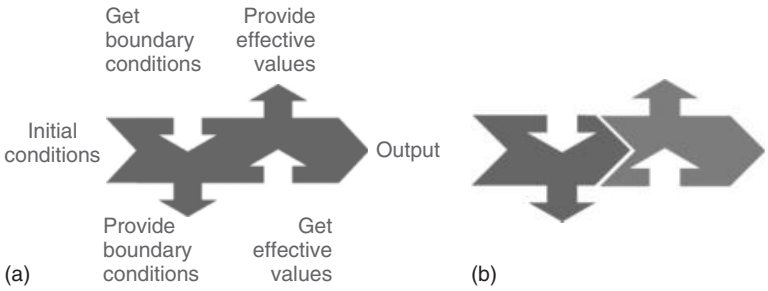

Figure 2.6 A basic module according to the AixViPMaP® platform concept (a) reveals a ''direction in time'' indicated by the arrowlike shape from left to right and ''directions in scales'' indicated by the upward and downward arrows. This basic module may be composed of submodules (b). An example could be a microstructure simulation only aiming at describing microstructure evolution being followed by a homogenization tool extracting effective properties from this calculated microstructure and providing the effective properties to simulation tools at the larger scale. The homogenization tool is colored as an interface module here (Section 2.3.3) as it does not alter the microstructure information.

The information flow from a larger scale to a smaller scale (''downscale'') comprises the *extraction of local information* from the large-scale model and providing it as boundary condition for a smaller scale model. Each module thus has to provide interfaces to ''provide local data'' and to receive ''boundary conditions.'' An example might be the temperature–time history of a specific volume element of the component during its casting process. This temperature–time history can be used as a boundary condition for the simulation of the solidification microstructure. Aspects of self-consistency for this kind of coupling are addressed in detail in Chapter 3.

The information flow from a smaller scale to a larger scale (''upscale'') comprises the *extraction of effective properties* from the small scale model and providing them as local properties for a larger scale model. Properties being determined at a small length scale are homogenized, respectively averaged by means of virtual testing and/or mathematical homogenization (Chapter 5), and fed back to the larger scale codes. The precision of simulations at the larger scale thus is significantly improved by consideration of locally varying, anisotropic properties evaluated from the smaller scale. Each module thus has to provide interfaces to ''provide effective data'' and ''receive effective data''. The structure of an individual module, which itself may be composed of submodules, is depicted in Figure 2.6. The overall arrangement of different modules in a scale-time-matrix is shown in Figure 2.7.

In a number of cases, the introduction of additional – scale bridging and process bridging – interface models has been identified as meaningful. These allow for a decoupling of the simulations on the different scales and further reveal a number of other benefits such as options for calculation of boundary conditions, effective values as detailed above. They also provide options for remeshing, data integration or data reduction, exploitation of metadata, and the management of the global frame of reference for the entire simulation scenario.

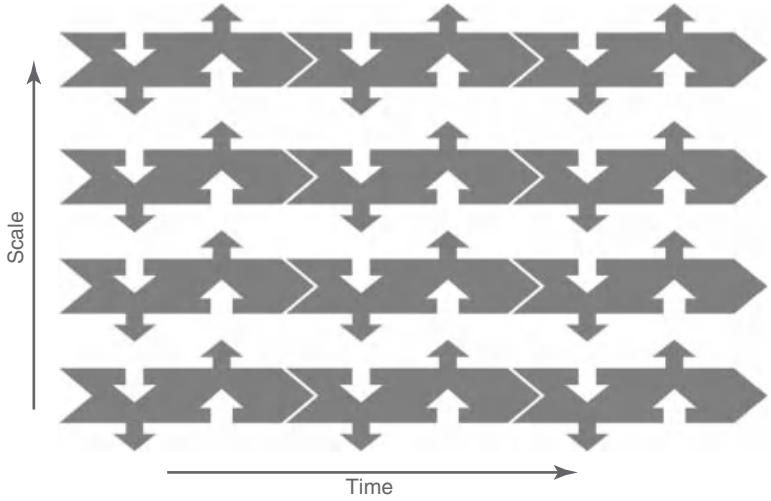

Figure 2.7 Modular structure of data exchange across different scales and along the evolution of a component.

2.3.3 Interface Modules/Services

The different process modules may be further complemented by interface modules or ''services'' (Chapter 6), (Figures 2.8 and 2.9). Such services may be used to evaluate and integrate information resulting from intermediate time steps of the process simulation (if not provided by the model itself) or to collect integrated data in the sense of data enrichment and data reduction strategies. These models may especially also monitor the overall history of the simulated process chain such as the absolute position/orientation of a component in a global frame of reference, the total (integrated) process time elapsed for the entire process chain, and the integrated energy consumption for the process chain or other data and save this information as metadata for further evaluation by the user. A further aspect of these services/interface modules are ''splitting'' or ''stitching'' functionalities, for example, for combining two independent simulation scenarios or two parts being joined by a welding process to form a single component (see also Figure 2.4).

Such services thus do not alter the existing data but enrich them with further information. They may further be used to distribute information on a number of parallel processes and to reintegrate results of parallel simulations into one comprehensive dataset. These models may moreover act as parser/sequencer routines for conversion of files into the platform standard.

Present microstructure models are computationally very demanding and the simulation of the microstructure of an entire component is still not within reach. A number of simulations of microstructures at different locations of the component may, however, be performed in parallel. This requires the selection of these specific locations and the provision of suitable boundary conditions by the large-scale code

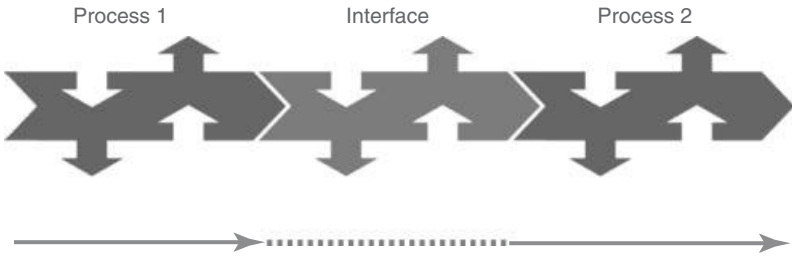

Figure 2.8 Interface modules or "services" allow for an enrichment of the data handed over from process to process, for example, by adding information evaluated from all individual time steps of the preceding process simulation. They do not alter the evolution state of the material or the component.

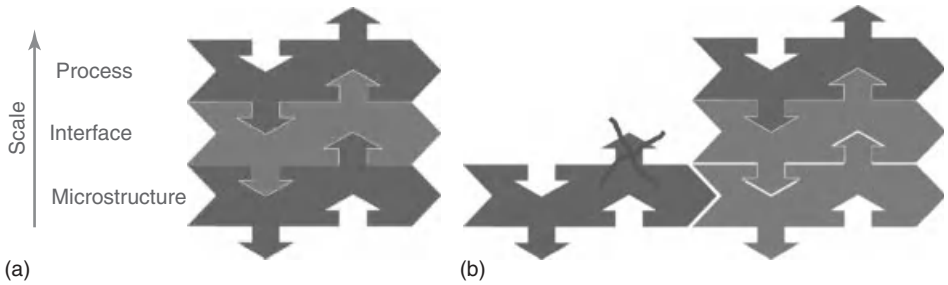

Figure 2.9 Interface model bridging the scales. In case a microstructure model itself cannot provide effective data (b), it might be complemented with a module taking the microstructure as input and calculating effective properties (e.g., by homogenization) for further transfer to the process scale.

for each of these positions. The actual choice of the positions of interest will depend on the interests of the user and has to be defined when setting up a simulation chain. Mapping algorithms then are needed to integrate the microstructure information (namely, the effective properties) of the different locations of the component, to interpolate these values, and to eventually map them onto the entire component (Figure 2.10).

2.3.4 Data Modules

The preceding chapters described the interactions of individual modules operating at different periods of the manufacture of a component and covering all the length scales of relevance. Besides drawing on initial and boundary conditions, all modules will need further data such as materials properties or process conditions for their operation. These data can be provided either as standardized databases

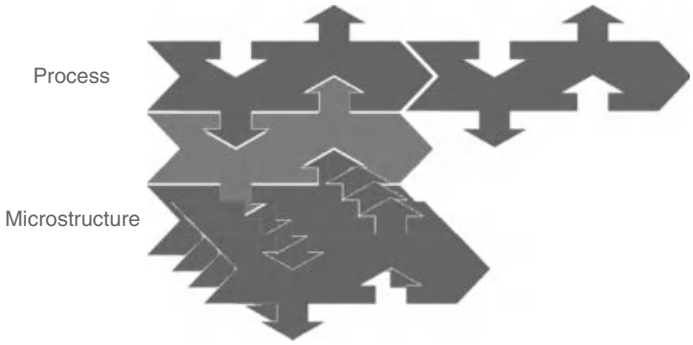

Figure 2.10 A number of different microstructure simulations at different locations of the component are often desirable. Boundary conditions for each of these points have to be provided. It is meaningful to include an interface module (gray) extracting these data for all time steps from different positions of the process simulation. Effective data then have to be extracted from all corresponding microstructure simulations. Furthermore, an interpolation scheme integrating the results of the local microstructure simulations and mapping them as effective data to the entire component can be applied via the interface module as well.

in case of nonprocess-dependent data or by well-defined calls to standardized functions for process-dependent data and materials laws. The entire platform thus is based on an integrative data and knowledge management system, allowing a structured and standardized storage and retrieval of information. In the first step, a standardized information exchange with the data modules has been realized, which is detailed in Chapter 4. In the long term, these data modules may develop into a virtual production intelligence (VPI) system, where not only data for the individual modules but also knowledge about comprehensive simulation scenarios can be accumulated and made available as templates for similar or even more complex tasks. This VPI system in future will also provide intimate links with real production processes and products.

Once a comprehensive platform has been created out of a map of different models and is able to provide even alternative solutions for a specific problem, a future task will be to select model scenarios with a level of detail appropriate to the desired/required degree of accuracy and a reasonable effort to perform the respective simulation. First approaches toward such a model map are addressed in the final chapter of this book.

2.4 Standardization

A comprehensive description of the characteristics of materials and components along the value chain – from casting of a homogeneous melt to final failure of a component during operation – requires the effective exchange of information

covering the entire materials and components history between a variety of modeling tools. Thus, the development of a uniform, standardized data format is mandatory.

Efforts to standardize and generalize data formats for the exchange of simulation results thus represent a major step toward successful future applications of ICME. A suitable data standard easily links, for example, the successful FEM models used in mechanical engineering and computational fluid dynamics among each other and especially with microstructure models such as the phase-field method, which actually seems to become the ''FEM for metallurgists.''

The nucleus for such a standard, as defined in the frame of the AixViPMaP® platform, is based on several software codes and models for materials processing available at the RWTH Aachen University, which have been adapted to a common standard based on the Visualization Toolkit (VTK) format by using semantic approaches and by drawing back on the university's IT infrastructure.

The standardization, in a first step, relates to a standardized exchange of data comprising information about the *geometry* of the simulated parts/processes, their boundaries, and field values within the simulation domain: scalar fields such as temperature and concentration of alloy elements; vector fields such as flow velocities or higher order tensors such as stresses/strains.

As a second step, an initial standard for the *exchange of materials models* between the different model levels of micromodeling and macromodeling, a user-programming interface based, for example, on Fortran subroutines must be provided. Similar to commercial finite element (FE) codes, material data depending on actual conditions or comprising a history are calculated on the basis of subroutines. A library for such subroutines will be made available in the near future, at least for elastic materials properties. Routines for nonlinear materials laws frequently are subject to proprietary rights.

These standards are already partially implemented in a number of simulation codes available at several institutes of the RWTH Aachen University and are described and discussed in detail in Chapter 4.

2.5 Web-Based Platform Operation

Standardization to that point is already most useful to exchange simulation results and to use simulation results of a preceding process as an initial condition for a simulation of the subsequent process step or to use macroscopic simulations to provide boundary conditions for microscopic simulations. Efforts for data conversion – by now representing a major part of work when performing coupled simulations – can thus be omitted or at least be strongly reduced.

In a next step, the number of different simulation tools may become part of a computational network. Presently, workflow sheets for process chains can already be easily edited, and simulations for some cases can be performed on a GRID.

All developed standards fulfill the requirements of GRID computing, especially in the sense of being independent of different operating systems. Definition and

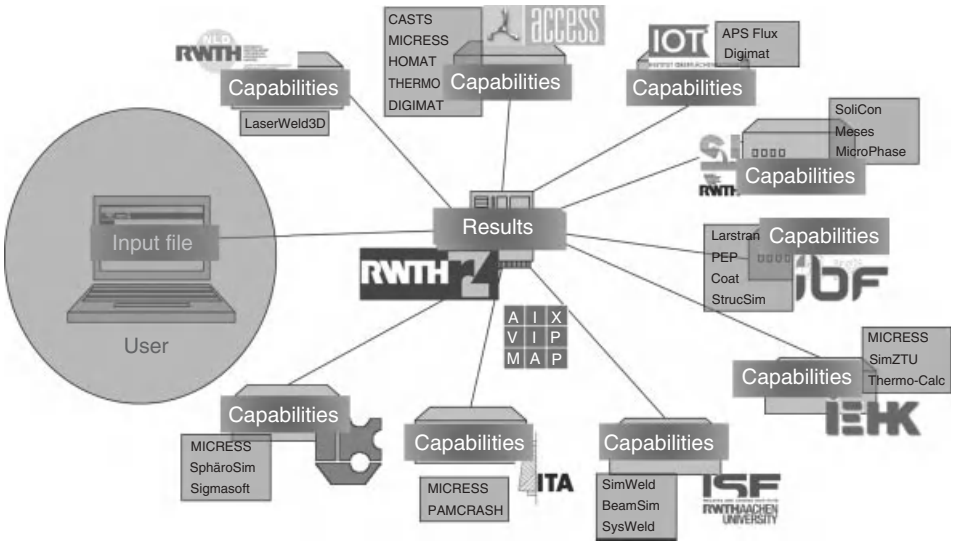

Figure 2.11 Scenario for distributed simulations running on a computer grid in an academic setting. Input files determining the workflow are submitted to a central computer, which allocates individual simulation tasks to computers, providing adequate capabilities. Results are then transferred to the central computer and can be evaluated by the user (see Chapter 6 for details).

control of the entire simulation chain and the exchange of simulation and material data are based on an ontological approach and are already realized on the web using a Condor system as middleware (Figure 2.11). The input file created with a Workflow Editor is submitted to the middleware, which checks for the software tools required and identifies computers capable of running these tools. The middleware further controls the timing between different simulations, provides conversion routines from/to the platform standard, and eventually collects the results and meta information. Details about the web-based platform operation are described in Chapter 6.

Eventually, the concept of integrative simulations will require and enable novel concepts of visualization and data evaluation. Already, the common data standard in this context can be considered to be very beneficial as users have to acquaint themselves essentially with only one postprocessing tool, allowing visualization of different processes and different length scales (Figure 2.12). More complex evaluation and visualization concepts are discussed in Chapter 7.

2.6 Benefits of the Platform Concept

An *open architecture* is a key ingredient of a strategic approach toward ICME. Such an open architecture obviously lowers the threshold for joining the platform

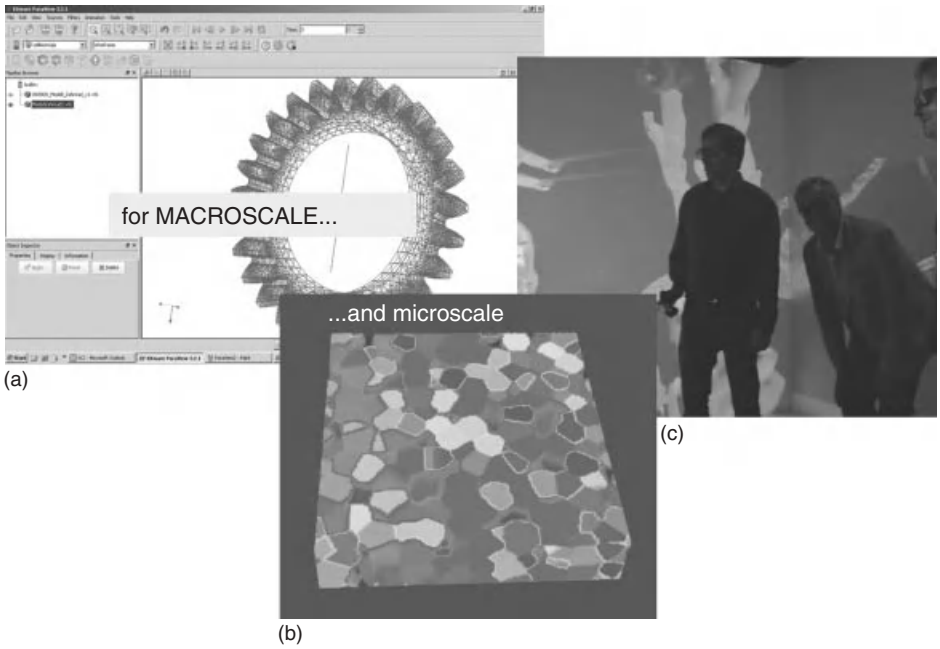

Figure 2.12 The standardized data format allows for visualization and evaluation of simulation data, drawing back on only one postprocessing tool for different process simulations and also for different length scales such as (a) the macroscopic component scale or (b) the scale of the microstructure. (c) This standard also allows for fully immersed visualization in 3D (Chapter 7).

for those interested in profiting from ICME either by performing simulations or by providing simulation codes. In case obvious benefits can be drawn from such a concept, the process of self-assembly of the ICME community will become self-amplifying. Joining or using the platform is considered as being beneficial for at least three different communities: providers of simulation software, industrial users of simulation codes/services, and academic institutions aiming to provide a holistic education and research.

2.6.1 Benefits for Software Providers

The platform benefits for providers of simulation expertise and codes – academic and/or commercial – are manifold. In the first place, an increased use of their codes is to be expected as the option of easily combining it with other tools will significantly expand the areas of application. The value of individual simulation results will increase. Besides a mere evaluation of the data as, in general, performed by now, these results can moreover be used as an initial condition for a subsequent simulation. This will increase the quality and precision of this second

simulation and thus present an added value. Integration of new and special features and functionalities being developed in academic codes, will thus be largely facilitated. Academic software solutions will thus find an easier and faster path into applications.

In the long term, new markets can be exploited in the area of ''calculation on demand'' or ''cloud computing,'' where users do not procure the software itself but only license it for a specific simulation task in a concept of ''software as a service'' (SaaS). This will open a market for customers especially from small and midsize enterprise (SME) companies not maintaining an own simulation expertise and/or infrastructure. Accounting and confidentiality schemes have to be implemented in the platform for this purpose. In the frame of ''SaaS,'' a few central software installations can be imagined. Such central software installations will largely facilitate software maintenance and software upgrades.

2.6.2 Benefits for Industrial Users

For industrial users, the platform will provide a number of academic and commercial simulation codes, allowing addressing the entire value chain from a homogeneous melt to failure under operational load. In general, such a comprehensive set of simulation tools being mutually coupled in an efficient way is not even available in a large-scale industry. The AixViPMaP® especially is interesting for SME companies, which do not maintain an own simulation expertise, for example, for costs reasons. On the basis of the sound experience available at the Materials Science Institutes at the RWTH Aachen University, the AixViPMaP® provides assistance for selecting appropriate simulation tools, setting up a simulation chain, and getting new users acquainted with the platform operation. Similar platforms may be run anywhere else by adequately skilled consortia while drawing on the same standards. Once a simulation chain is operational, it is up to the user to modify individual parameters and to exploit their effect on his products in the frame of parameter variations. A user, in general, is not expected to create own simulation scenarios from scratch. In detail, industrial users might benefit in one or more of the following aspects:

- improvement of their products and processes in terms of cost and time;
- providing a simulation history as an added value of their product to their customers;
- draw back on simulations originating from their suppliers to improve their own processes;
- minimizing risks for ''first time right'' products, where a classical trial-and-error approach bears unacceptable financial risks;
- reducing the design effort for new products/processes/materials in terms of costs and time;
- improving planning quality and, accordingly, the value of a product;
- increasing the predictability of process chains to decrease waste and recycling material;

- rapid adaptation to changes in a global market by prediction of effects of variations in production;
- knowledge capture and reuse;
- ... and many other potential benefits.

Preconfigured simulations of process chains can then be launched from any computer at the users' premises by submitting a job to the platform via the Internet, for example, to check effects of variations in parameters for individual process, for entire process chains, or of modifications of the chemical composition of the materials. Especially, the metadata being collected along the entire simulation chain such as cycle times for individual processes, overall energy consumption, and many others are most valuable for decision-making processes.

2.6.3
Benefits for Academia, Education, and Knowledge Management

Especially, the immersed visualization of simulation results makes the platform a unique tool for education. Phenomena at the scale of the microstructure can be directly ''observed'' and investigated in detail. The special benefit is a holistic understanding of mutual influences between different processes, which by now are considered as independent. Changes in initial conditions can easily be made and their effect on all downstream processes investigated. The processes by now, in general, are categorized into ''disciplines'', which only scarcely interact. The platform thus will provide new opportunities for interdisciplinary teaching and education. A further important aspect of the platform is to be seen in knowledge transfer and management. Successful simulation scenarios can be stored and retrieved in order to be adapted, adopted, and improved by future generations.

2.7
Verification Using Test Cases

For the verification of the developed platform concept and methodology and to demonstrate the benefits of such a simulation platform, practical test scenarios representing ''foundational engineering problems'' for an ICME approach have been defined in cooperation with industrial partners. These scenarios especially comprise process chains revealing strong links between the scales of the process and of the microstructure, where the evolution of the final microstructure and thus the resulting materials properties are influenced by all process steps. Although these test cases have been defined very specifically in terms of selected materials and process chains, they represent process chains for ''generic'' engineering components such as tubes, gear wheels, or bearings. The process scenarios being developed, for example, for a line pipe may thus later serve as templates for the manufacture of other components, such as superalloy tubes in power engineering. In total, the selected test cases map almost all of the most common processes from casting up to operational conditions.

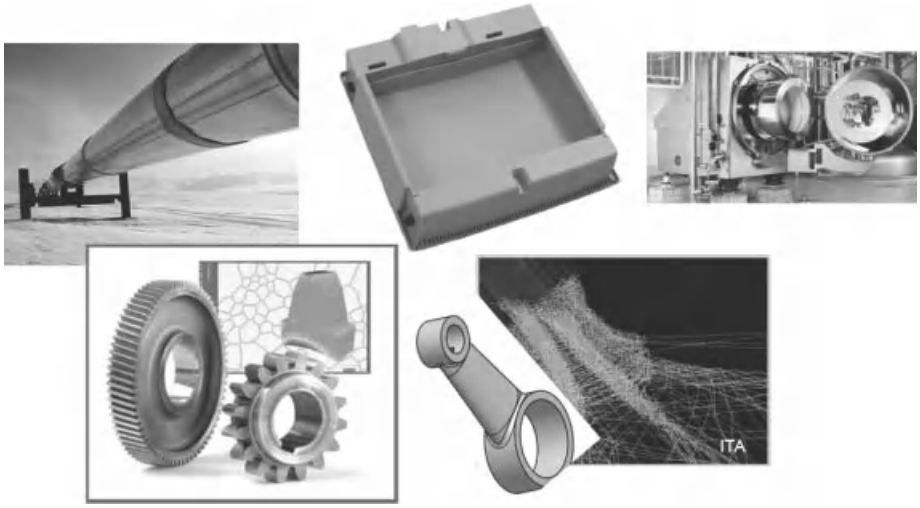

Figure 2.13 Five different test cases have been used to validate the performance of the platform and to demonstrate its benefits: a line pipe, a top box, a bearing, a gear wheel, and a piston rod (see text).

In detail, the following test cases, covering a number of different alloys, polymers, and composites, have been investigated (Figure 2.13).

- Pipeline: production of line pipe steels including hot rolling, U-O forming, welding, and heat treatments;
- Transmission component: control of grain-size stability in microalloyed steels during carburizing and subsequent laser welding;
- Mechanical properties of a plastic part for automotive applications as a function of inner properties;
- Investment casting of a textile-reinforced aluminum piston rod using ceramic textiles;
- Stainless steel bearing: distortions of cast precision bearing parts evoked by cyclic load conditions and related changes in microstructure.

The first integrative simulations for these dedicated test case scenarios and their experimental validation are detailed in Chapters 8–12. They reveal that specific properties or phenomena can only be understood in the frame of a holistic approach covering several process steps on both the process scale and the scale of the microstructure. Highlights of results comprise the prediction of flow curves for ferritic–pearlitic line pipe steels, the reduction of the experimental effort for the determination of flow curves, the optimization of the production of case-hardened components with respect to reduced carburization times while maintaining grain-size stability, determination of the influence of inner properties on mechanical properties of thermoplastic materials by simulation of spherolitic microstructures comprising anisotropy of the molecules, calculation of the local

effective, anisotropic modulus of textile-reinforced components, identification of a combination of segregations originating from solidification and mechanical stresses resulting from heat treatment and machining as origin of a martensitic transformation leading to failure of the component during service.

3
State-of-the-Art Models, Software, and Future Improvements

Markus Apel and Georg J. Schmitz

3.1
Introduction

In the previous chapter on ''basic introduction to the platform concept,'' all models and tools that might become part of a modular simulation platform were treated as black boxes. An integration of a variety of models (Section 3.2) into the platform concepts, however, also has major implications on the performance and the future development of these individual tools. These implications for the individual models comprise:

- Platform requests to individual models (Section 3.3):
  - capability of reading standardized data formats,
  - improved speed of individual models in view of overall platform performance,
  - improved model accuracy in view of error propagation,
  - robustness against a variety of initial conditions,
  - service-like channeling of information not relevant to the actual model but important to downstream models/information integrity.
- Platform benefits provided to the individual models comprise (Section 3.4):
  - improved quality of initial conditions,
  - consideration of local effective materials properties,
  - consideration of anisotropic materials properties.
- The timing of the information exchange between different models is also important (Section 3.5):
  - strong coupling of the models,
  - weak coupling of the models (handshake type of information exchange),
  - self-consistency of coupling.

Today, a vast number of different simulation models and software tools are available and ready to use within a platform concept. An overview of different simulation codes with the prospect of being used on an integrated computational materials engineering (ICME) platform is given in Section 3.2. These programs offer data interfaces for input and output in a variety of format specifications and standards. The hitherto development of different data formats can be regarded as

Integrative Computational Materials Engineering: Concepts and Applications of a Modular Simulation Platform,
First Edition. Edited by Georg J. Schmitz and Ulrich Prahl.

an evolutionary process, ruled by individual model requirements, the extension of software capabilities and the competition between the different programs with their proprietary data formats in different engineering and scientific applications, thus on the success in the market and by that on the strategies of the different software vendors. The activities presented in this book (Chapter 4) can be regarded as a contribution toward a standardized way of data exchange for a broad range of applications and therefore a more general and simpler way for the coupling of individual software codes across different scales and applications. Throughout this book, simulation examples of coupled simulations, mainly using established programs, are presented.

For an integrative process and materials modeling, model and software improvements will be an ongoing task within the next decades. Inherently, this action follows a moving target; with any new achievement, additional and more complex questions will arise and their solution will become within reach. The integrative approach is based on the need for a broad combination of methods as necessary elements for a successful process chain modeling. Even simple questions such as ''how does the surface hardness of a gear wheel change if the heat treatment time is reduced by 10%?'' can only be fully exploited by a combination of different simulation tools – software tools describing the implications for the handling and temperature history of the gear wheel and other tools that model the materials response on changing process conditions. The quality of the answers obtained by an integrative simulation strongly relies not only on the quality of the individual simulation tools that are combined in the simulation chain (some aspects are discussed in Section 3.3.2) but also on the implications due to the coupling between the individual processes. Considerations about accelerating the computing time are the topic of Section 3.3.3. The way of coupling different simulation models is determined by the underlying materials physics. The physical phenomena under consideration determine whether it is possible to separate different scales or whether such a separation will lead to an oversimplified description. Examples of both aspects are discussed in Section 3.5. We start with an overview of various software tools that are candidates or are already capable of operating in an ICME framework such as the AixViPMaP platform.

3.2 Overview of Existing Models and Software

A holistic ICME simulation chain is necessarily a multiscale and multidisciplinary task. Thus, different classes of models and software have to be combined. On a *macroscopic scale*, defined as the length and time scales suitable for the description of a process on a component level, continuum models are most frequently used. As an example, the temperature history during heat treatment of metallic components can be modeled by the continuum equations for energy (heat) transport, which is a mean field description for the evolution of the temperature with no consideration of the underlying atomistic processes such as phonon transport and scattering.

Usually, variations in thermophysical properties on the scale of the materials microstructure are also neglected. For macroscopic continuum simulations, materials properties are necessary input parameters, by definition they cannot predict materials properties. Materials properties can be taken into account in an indirect manner, for example, on the basis of criteria functions. Macroscopic continuum equations are typically solved by finite element, finite volume, or finite difference methods. Alternative numerical methods, for example, mesh-less methods, are available; however, by now they are not widely used. Concerning ICME and an open simulation platform, the specific numerical method is not primarily important. The decisive criterion is that all numerical methods provide their input and output data in format specifications readable by other programs and providing the necessary information for the underlying numerical methods.

Continuing with the example of a heat treatment process, a major objective of heat treatment is to control and modify the materials properties, for example, triggering a phase transformation. Phase transformations typically occur at the mesoscopic scale of the materials microstructure, for example, the formation of precipitates during hardening of Al alloys or martensite formation in rapidly cooled steels. The evolution of the microstructure can be also described by continuum equations, but now the variation in the properties (local composition, interfaces, mechanical properties, dislocation density, etc.) has to be handled locally on the scale of the microstructure. Here, phase field methods, level set, or cellular automation models are nowadays the most popular models. These methods, however, cannot predict the properties of the individual constituents of the microstructure, such as the heat capacity or the elastic properties of a ''pure'' phase. Instead, the scope of mesoscopic microstructure simulations is to predict the morphology of the microstructure and the kinetics of the microstructure evolution in a spatial and temporal resolved manner. (Average) engineering properties of interest, for example, yield strength, hardness, or corrosion properties, can then be derived from the microstructure. Among other methods, micromechanical modeling, virtual testing, or mathematical homogenization can be used to derive effective engineering properties from the knowledge of the microstructure topology and the properties of the pure phases (Chapter 5). Structure/property correlations and the respective modeling is a dynamic research area and considerable progress can be expected in the near future.

The state of the art for the calculation of materials properties of individual pure phases are nowadays atomistic *ab initio* methods that span a broad range from ''first principle'' quantum mechanics to ''semiempirical,'' starting from effective interaction potentials. At this stage, it is not necessary to fully integrate atomistic methods and simulation programs into an ICME simulation platform. Atomistic simulations require different skills and experiences from the users and the time period to derive serious answers is much longer than the required time for a successful engineering simulation on a finite element level. But most important, the ''data exchange'' between atomistic and mesoscopic can be reduced to the exchange of a single value or function – ''an effective property,'' for example, the value of the heat capacity as a function of temperature, which can be, for

example, incorporated into thermodynamic databases. Some widely used programs for ''atomistic'' simulations are listed below. They may play a crucial role in a holistic simulation approach for the calculation of unknown material data, not only for new materials for which the necessary properties are not yet comprehensively available but also for data of interfacial properties between different phases.

The following tables list – without any claim of being comprehensive – a number of different simulation programs together with their major field of application. Detailed information about the individual software packages can be easily found on the Internet. These programs represent only a minor fraction of available software packages that would fit into the AixViPMaP framework. A more comprehensive list of software for the simulation of metal processes can be found in [1] together with brief descriptions of underlying physical models. Further information can be found also in [10]. Currently, a high dynamics in the development of well-established or new software codes, both in the commercial and noncommercial fields, can be observed. The strength of the platform concept described in this book is that any model or tool – present or future – can be easily incorporated into the concept, on the basis of the standardized interfaces.

In contrast to the motivation for the necessity of the different scales given above in a top-down approach starting from the macroscopic scale of a component and going down to the atomistic scale, the following lists are sorted in a bottom-up-type scenario starting at the atomistic level and eventually ending at the continuum and engineering scale again, which represent the major focus of this book. The continuum models (Tables 3.3 and 3.4), already being implemented and/or used in the AixViPMaP context, are specially labeled.

The first category of programs is those for *atomistic calculations* of materials properties (Table 3.1). The density functional theory (DFT) and similar methods based on quantum mechanics have the power to compute unknown materials properties, which otherwise may be hardly determined. A rather new field of application is also the determination of collective properties of interfaces or the dynamics of dislocations on an atomistic scale. For this, molecular dynamics and related methods are often used. Data provided by atomistic techniques may in future be fed more frequently, for example, into CALPHAD-type thermodynamic databases or in databases for interfacial properties.

Table 3.1 Some selected software tools for quantum mechanics and *ab initio* simulations.

Name	Major application
VASP	Package for *ab initio* quantum-mechanical molecular dynamics (MD) using pseudopotentials and plane wave basis sets
SIESTA	DFT code for thousands of atoms, basis functions are atomic orbitals.
LAMMPS	Large-scale atomic/molecular massively parallel simulator

Table 3.2 Some selected software tools for computational thermodynamics and diffusion simulation.

Name	Major application	Type
Thermo-Calc	Thermodynamic calculations, phase diagrams, phase fractions	Commercial
DICTRA	Multicomponent diffusion, sharp interface model	Commercial
MatCalc	Thermodynamic and kinetic calculation, precipitation kinetics	Academic
Pandat	Thermodynamic calculations, phase diagrams, phase fractions	Commercial
FactSage	Thermodynamic calculations, phase diagrams, phase fractions	Commercial
TC-Prisma	Calculation of the evolution of precipitate distributions	Commercial

Table 3.2 lists software devoted to *computational thermodynamics*. These tools offer the possibility of computing phase fractions, phase composition, and driving forces for the reaction between different phases, in addition to the transformation temperature for different phases as a function of their composition. The thermodynamic variables do not include a length scale; thus, they already provide volume average values. In many technical processes, the transformation kinetic plays an important role. Instead of using microstructure simulation codes, often the prediction based on geometrical approximations (e.g., linear or spherical geometries) leads to valuable predictions. DICTRA includes multicomponent diffusion in a sharp interface framework to calculate phase transformation kinetics, while MatCalc uses a maximum Gibbs energy dissipation theorem to allow, for example, the simulation of precipitation kinetics. Computational thermodynamics needs the Gibbs free energy as a function of the thermodynamic variables as input data. Databases for many technical alloys and materials are nowadays available. The same holds for atomistic mobilities as the basis for the calculation of diffusion coefficients for the calculation of the phase transformation kinetics. New developments combine the use of thermodynamic data with models for nucleation and allow, for example, modeling the evolution of precipitate distributions (TC-Prisma).

Software packages listed in Table 3.3 have their major field of application in the *simulation of materials microstructures* and the evaluation of *materials properties*, which are often determined on a microstructural basis. The most popular method for the simulation of microstructure evolution nowadays is the phase field method [2]. The method allows simulations of the transformation kinetics and the microstructure evolution in 2D and 3D. The microstructure morphology is a result of the model and not an input. A few software packages are nowadays available for users who like to apply phase field simulation to microstructure-related problems instead of going into the methodology itself.

On the basis of a calculated or experimentally determined microstructures, tools such as DIGIMAT and HOMAT can be used to compute effective material data (Chapter 5). Such tools thus provide the link between the microscopic length scale and the macroscopic scale addressed by the programs operating at the process scale of the component.

Table 3.3 Some selected software tools for the simulation of materials microstructures and materials properties.

Name	Major application	Type	AixVipMap compatibility
MICRESS	Microstructure evolution, solidification, and solid state, 2D/3D multiphase field solver coupled to thermodynamic databases	Commercial	Yes
HOMAT	Mathematical homogenization of thermomechanical properties of multiphase materials	Proprietary	Yes
DIGIMAT	Nonlinear multiscale materials and structure modeling platform	Commercial	Partly
JMatPro	Phase equilibria, phase transformation, materials properties	Commercial	No
SphäroSim	Microstructure of polymers	Academic	Yes
PACE3D	Software package for phase field based microstructure simulation, fluid flow, and more	Academic	No
StrucSim	Microstructure modeling for metal forming	Proprietary	Yes
FiPy	Partial differential solver, also for phase field equations	Academic/ open source	No
OpenPhase	Open source phase field software	Academic/ open source	No
OOF2	Calculates properties from real or simulated microstructures	Academic/ free download	No

The programs listed in Table 3.4 comprise not only specialized simulation tools addressing a particular application, for example, SimWeld for the simulation of welding processes but also general finite element method (FEM) simulation programs, for example, ANSYS, allowing the simulation of a broad range of different processes. Those comprehensive FEM codes offer the possibility of investigating thermal, mechanical, or fluid flow problems and allow the coupling between different phenomena, often denoted as multiphysics capability.

3.3 Requirements for Models and Software in an ICME Framework

The requirements for existing simulation models and software can be divided into two different classes. On the one hand, it is the design and performance of the software especially for the operation on a simulation platform; on the other hand, the capabilities of the underlying simulation models determining the application range and the accuracy of the simulation results.

Table 3.4 Software packages for simulation on the macroscopic length scale.

Name	Major application	Type	AixVipMap compatibility
MAGMASOFT	Comprehensive simulation tool for metal casting, for example, mold filling, solidification, stresses, and distortion (FD based)	Commercial	Data format filter available
STAR-Cast	Investment casting, centrifugal casting, low-pressure die casting	Commercial	Yes
ProCAST	Comprehensive simulation tool for metal casting (FEM), different processes, and phenomena	Commercial	No
SIGMASOFT	Simulates casting of plastic materials	Commercial	Data format filter available
WinCast	Metal casting (FEM)	Commercial	No
SIMULIA/ Abaqus FEA	General FEM tool, mechanics, CFD, multiphysics, and electromagnetics	Commercial	Data format filter available
SYSWELD	Simulation of welding, distortion, and stresses	Commercial	Yes/partly
ANSYS	General FEM tool, mechanics, CFD, multiphysics, and electromagnetics	Commercial	No
SimWeld	Simulation of welding, weld pool geometry, and heat transfer	Proprietary	Yes
DEFORM	Metal forming, heat treatment, mechanical joining, and machining	Commercial	Yes/partly
Larstran/ Shape	Cold and hot metal forming	Commercial	Yes
FORGE 3D	Simulator for hot, warm, and cold forging	Commercial	No
LaserWeld 3D	Laser welding simulation	Proprietary	Yes
COMSOL	Multiphysics simulation package, thermal, electromagnetic, and structural mechanics	Commercial	No

[a] FD, finite difference; FEM, finite element method; CFD, computational fluid dynamics.

Concerning software design and performance within an ICME framework, important requirements are:

- appropriate data formats for input and output (Chapter 4),
- model quality and suitable interpolation schemes for incomplete data (Section 3.3.1),
- improved model accuracy in view of error propagation (Section 3.3.2),
- robustness against numerical parameter variations and a variety of initial conditions,

- improved speed of individual models in view of overall platform performance (Section 3.3.3),
- service-like channeling of information not relevant to the actual model but important for downstream models (Section 3.3.4).

3.3.1 Model Quality

A particular issue for the simulation of a complete process chain is the problem of incomplete information. Therefore, it must be possible to handle the problem of unknown material or process parameters by bridging this lack of knowledge, either by adequate interpolation or extrapolation schemes, or by any sort of intelligent guess for unknown data and conditions. Thus, it must be possible for the user to add this information manually, when requested. In such a case, it is useful to quantify the impact of these approximations or assumptions by a sensitivity analysis.

Often, ''predictive capabilities'' are requested for a simulation tool. This requirement is more devoted to the underlying simulation model than to the software itself. In general, the term ''*predictive*'' is difficult to define and often misleading. Any model has predictive power in the sense that on the basis of a given set of input parameters the model will create a set of output data, which actually is the model prediction. The question then is how good ''reality'' is approximated by the model and what would be the best model available. These questions can only be answered for a particular problem of interest. For example, for a well-characterized material, semiempirical materials models could be the method of choice and lead to superior results as compared to a fully physical-based model that may have limitations in covering all important aspects. On the other hand, extrapolations based on semiempirical criteria functions can lead to even qualitatively wrong results when new physical phenomena appearing outside the validated range. The same holds for the situation when a physical-based model provides only an insufficient representation of the underlying physics.

3.3.2 Improving Numerical and Model Accuracy

A basic requirement for a simulation model is that the numerical solution is a valid solution to the underlying model equations. In such a case, a model is predictive within the limits given by the model formulations. The requirement to ''compute right'' seems to be trivial at first glance; however, for many nonlinear phenomena, for example, fluid flow, dendritic growth, or materials plasticity, it is a highly nontrivial task to assure a mathematically correct and physically sound solution. This problem gains even more importance when different simulation codes are coupled together in a through process simulation along a simulation chain. Then, the input provided by the predecessor program may vary over a range where the succeeding simulation model may have a reduced level of confidence or numerical convergence criteria are violated. Such situations are not always

apparent, especially if the user has to treat a particular software as a black box and has only limited experience in the underlying physics or models. Owing to the wide range of processes and phenomena along the simulation chain, limited knowledge about critical parts will be rather the norm than an exception. One way to encounter this knowledge limitation is that a simulation chain is built up and operated by a team of users, each of them contributing deeper knowledge about the individual simulation tools. From the technical and numerical point of view, robust algorithms and error control are important elements.

Inevitable are benchmark problems for the test of the numerical accuracy of individual models. For the FEM method, numerous tests are documented for different fields of application, for example, by NAFEMS [3]. Individual and combined tests can be used in order to build up a reasonable test for an integrative simulation chain.

As an example, a basic test for phase field models is shown in Figure 3.1. A vital condition for a correct solution to a phase field model is that the interface curvature effect is reproduced precisely. If one neglects all other energetic and kinetic contributions, a spherical grain inside an isotropic matrix would shrink according to Eq. (3.1),

$$r\frac{\mathrm{d}r}{\mathrm{d}t} = -2\,\mu\sigma \tag{3.1}$$

driven by the reduction of surface energy σ, with r the radius, and μ the kinetic coefficient. Figure 3.1 shows the results of phase field simulations. In a diffuse interface model such as phase field, the number of grid cells across the interface is an additional numerical parameter and should be adjusted properly such that the diffuse interface results reproduce the sharp interface solution (denoted as the Gibbs–Thomson limit). The plot of the phase field solution for ($r\,\mathrm{d}r/\mathrm{d}t$) as

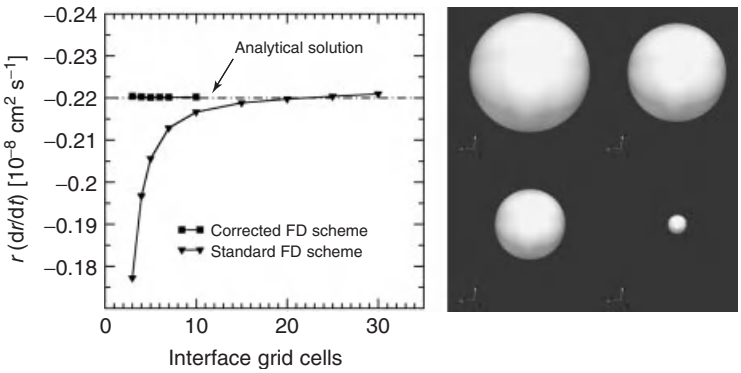

Figure 3.1 Numerical accuracy test for the phase field model [5]. Three-dimensional simulation of the curvature-driven shrinkage of a sphere. Improved discretization schemes lead to a higher accuracy and allow efficient computations for coarser grids.

a function of the number of interface grid cells shows that a new, corrected finite difference scheme introduced recently [4] leads to a much better convergence to the analytical result. This new scheme allows precise simulations on a coarser grid, which lead to decreasing computing times and memory consumption. The previous example relates to numerical discretization errors inherent in any numerical simulation.

3.3.3 Speeding Up Individual Models and Distributed Simulations

The computing time for a comprehensive process and materials modeling along an entire production chain is – and will remain in the near future – a serious limit to its applicability. If the computing time is too long, parameter variations are difficult to perform and/or oversimplifications are necessary in order to represent the entire process chain. Thus, simplifications can become necessary in view of an acceptable or available computer time rather than by the engineering requirements. The challenge of reasonable computing times will be an ongoing issue, because model refinements, in general, are inherently accompanied by an increasing demand of computer resources, for example, when switching from homogeneous materials properties to spatially varying properties. Typically, the model development is faster than the improvements in computer hardware or numerical algorithms. Thus, the computing time issue may be expected to become even more important in the future, despite the steadily ongoing progress in computer hardware known as *Moore's law*.

In general, it is not straightforward to define a certain upper limit for an acceptable computing time. In some sense, it depends on the patience of the user. To be a valuable tool for production planning or engineering applications, the requirement of performing a simulation ''overnight,'' in many cases, represents a reasonable target for an acceptable computing time.

Today's challenge is that the performance increase in computer hardware is not realized by an increasing speed of a single CPU, for example, by increasing the clock speed. Instead, it is now realized by an increasing number of available CPU cores on a computer, ranging from the simple multicore CPUs with four to eight cores on a modern desktop computer to massive parallel supercomputers, for example, the rank number one in the TOP500 list of November 2011, the computer Tianhe-1A with a total of 186 368 cores. Most users in academia and industry being seriously interested in ICME have access to computer hardware with around 1000 cores or even more. Thus, any software in an ICME context should take advantage of parallel computing environments.

Distributed Simulations The design of the AixViPMaP platform naturally makes use of distributed computing resources (Chapter 6). Individual simulation tasks can be run in parallel or sequentially on different computers, governed by the requirements of the handshaking data exchange schedule. In case of parameter variations, different simulation runs are independent tasks, which can straightforward be

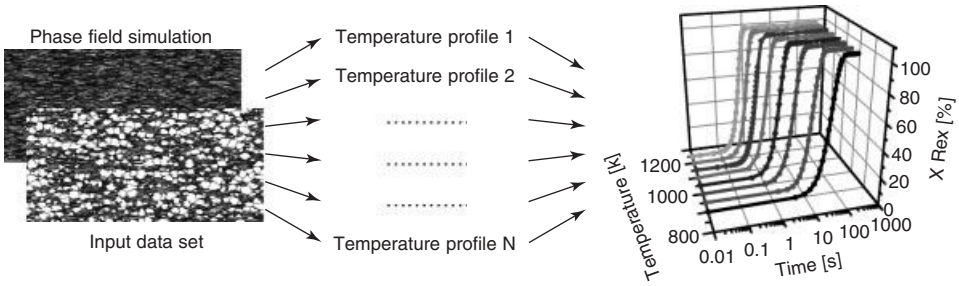

Figure 3.2 Scheme for the parallel processing of a parameter variation. The same initial structure and input simulation data set is subject to different temperature profiles, leading to different recrystallization curves.

computed in parallel. The role of the AixViPMaP platform scheduler is then to control and steer these individual tasks; the individual programs are not affected by this kind of ''parallelization'' except that necessary input data has to be available at program start and/or during run time. A scheme for a parallel parameter variation is shown in Figure 3.2. In this example, the recrystallization of a deformed material is simulated by a phase field model. The recrystallization kinetics depends on the annealing temperature due to the temperature dependence of the grain boundary mobility. In this set of simulations, all other temperature-dependent phenomena, for example, the nucleation rate have been neglected. In Figure 3.2, the computed recrystallization curves for different temperatures are shown in the graph on the right. Such microstructure simulations for different time–temperature curves are a common task in ICME because the local temperature profiles usually vary significantly over a larger component.

If a sufficient number of CPUs are available on the platform, such a parameter variation can be performed in the same wall clock time as one simulation for a single set of parameters. Of course, more time is necessary for the preparation and the evaluation of the results derived from parameter variations. Tools assisting the users in performing and analyzing such variations are thus useful elements of an ICME platform.

The possibility of running a larger set of parameter variations simultaneously is especially useful for the analysis of a longer process chain: on the one hand to determine the important parameters that have a decisive impact on the process, and, on the other hand, to verify the confidence level of the simulations by allowing sensitivity analysis not only for numerical but also for unknown physical parameters.

Parallel Coding The computing time for an entire simulation chain is often limited by only one computational demanding simulation step. The priority then is to speed up this bottleneck. Software developers of time-critical simulation models thus have to address parallel computing for further software development. However, the possible speedup for the whole simulation chain also follows Amdahl's law Eq. (3.2) [7],

which applies not only to a single simulation program but also to an entire simulation chain.

Equation (3.2) estimates the speedup S by parallel computing in comparison to serial computing.

$$S = \frac{1}{\left((1-P) + \left(\frac{P}{N}\right)\right)} \leq \frac{1}{(1-P)} \tag{3.2}$$

The term S denotes the speedup being defined as the calculation time for a serial calculation t_s divided by the time t_p for a parallel computation. $(1 - P)$ is the fraction of serial parts in the code, P is the fraction of the parallelized code, and N is the number of processors available for parallel computing. The major conclusion derived from this equation is how much the speedup S is limited by the serial parts of the program, for example, if the serial part (1 – P) requires about 10% of the total computational effort, the upper limit for the speedup is a factor of 10 even when the number of processors N goes to infinity. Bearing this in mind, it may be concluded that a reduction in the computing time for the whole simulation chain by one order of magnitude will be already a challenge. Thus, efficient and fast numerical algorithms are important for all individual simulation codes to reduce the overall serial part.

One inherent difficulty in parallel computing is the dependence on the hardware architecture. Numerical algorithms and the achievable performance, to a wide extent, depend on computer architecture. Essentially, two major programming paradigm are followed at present. Parallel computing on distributed computer systems is often realized by the message passing interface (MPI). MPI is a standard programming interface enabling data exchange between different programs or program sections running independently on different CPUs or computers in a network. Computer systems with a common (shared) memory allow a more direct way of parallel programming, realized in the OpenMP standard. OpenMP is an easy way to make use of parallel computing on a lower level, typically on the level of individual ''do loops'' in the program.

The best choice between these two programming concepts (or even a combination of both) to a large extent depends on the numerical algorithms used to solve the simulation model and the underlying data structures. Many approved and established algorithms have been developed or optimized on single CPU computers over many years. It is often an easier task to parallelize such algorithms using OpenMP. A potential disadvantage of OpenMP is that both memory size and number of CPUs are substantially limited for shared memory hardware. Standard shared memory computers presently have a size of 64 CPU cores; however, the number of CPU cores can be expected to increase in the future.

Examples of performance increase on the basis of OpenMP parallelization are given in Figure 3.3. The graph on the left shows the speedup obtained for two different microstructure simulations using the phase field program MICRESS [5]. Example 1 shows only a minor speedup of 1.8, almost independent of the number of cores. The simulation deals with a carburization process in steel. In this process, the microstructure evolution is determined by carbon diffusion, grain growth in

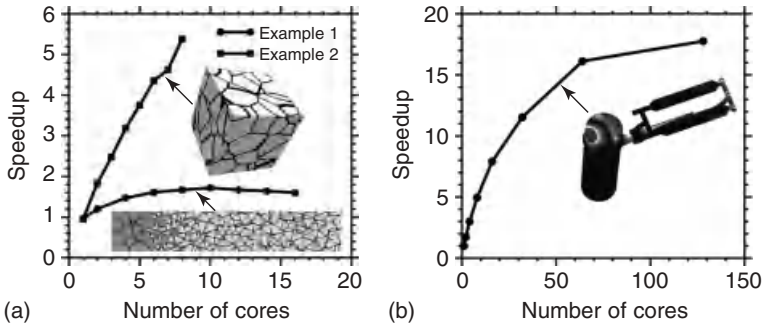

Figure 3.3 Speedup of the OpenMP parallel phase field code MICRESS [6] for two different microstructure simulation problems (a). Speedup for the macroscopic casting simulation code STAR-Cast obtained for the simulation of the melt filling into a ceramic mold (MPI parallelization, b).

austenite, and the nucleation and growth of ferrite. Because only the diffusion and some internal data handlings are computed in parallel, the serial part is still in the order of 50%. The gain in computing time is thus limited and saturates already for a few CPU cores. In the second example, the elastic deformation of a polycrystalline microstructure was computed in 3D. The most demanding part here is the solution of the stress and strain equations based on a standard matrix solver. This solver efficiently uses loop parallelization and because of the large size of the loops the serial part is much smaller as compared to the first example. This results in a larger speedup along with a better scaling behavior. It can be concluded that the performance gain of a particular simulation program is not only a unique feature of the number of CPUs or the program but to a wide extent also depends on the specific simulation task. The example in Figure 3.3b shows the speedup for a macroscopic casting simulation code STAR-Cast for up to 128 CPU cores based on MPI parallelization.

Precalculation Strategies Another possibility of circumventing long simulation runs in an ICME environment is to use precalculated data stored in a database. Interpolation and extrapolation schemes can be used to provide the information in the necessary parameter range without computing the required information every time. This is a canonic procedure not only for any handshake type of coupling but also for the scale bridging between the microscopic length scale of materials microstructures and the macroscopic scale of the component. For example, the parameter variation in the temperature-dependent recrystallization curves shown in Figure 3.2 can be performed independently and the results can be stored and used in later simulations. Such a decoupling will always work for consecutive processes. However, limits exist for the coupling across different length scales if the coupling between the scales or various phenomena must be considered as ''strong'' (Section 3.5).

3.3.4
Information Integrity

One major requirement to exploit the full potential of ICME is the integrity of the information being generated. It is important that any information not relevant to modeling an individual process step is still channeled through with appropriate modifications in order to be available as input information for further downstream models and software tools. An instructive example is a cold rolling simulation. Information about microsegregation and macrosegregation of different alloy elements and, for example, grain sizes and texture can be provided by a preceding simulation of a continuous casting of the component. While grain size and texture are severely altered by the cold rolling process due to dynamic and static recrystallization the distribution of the alloy elements – the segregation pattern – is essentially not influenced by this process. However, as the cold rolling process modifies the overall geometry of the component, the segregation pattern has to be mapped to this new geometry. A basic implementation of such mapping services seems not to be too complicated and just has to be done. It will not improve the performance of the individual model but provide a substantial benefit for platform operations aiming at, for example, life-cycle predictions.

The necessity for further service-type operations for individual models will increasingly emerge in the future, when more and more models have been combined and specific effects of upstream processes are identified as relevant for downstream processes and the properties of both material and component.

3.4
Benefits of Platform Operations for Individual Models

The platform benefits provided to the individual models comprise:

- improved quality of initial conditions (Section 3.4.1),
- improved quality of data (Section 3.4.2),
- consideration of local effective, anisotropic materials properties (Section 3.4.3).

These aspects will be further detailed in the following chapters.

3.4.1
Improved Quality of Initial Conditions

Any model has to draw on initial conditions, which are then further iterated during the actual simulations, allowing the monitoring of the evolution of the component and/or of its microstructure. The sound definition of initial conditions thus is an important task, as already minor changes in the initial conditions may evoke qualitatively different output. Presently, methods of defining initial conditions often comprise simple assumptions such as ''homogeneous,'' ''isotropic,'' and ''stress-free.'' Other methods to define initial conditions make use of experimental

data such as 2D-metallographical sections for the definition of microstructures. An even more complex 3D microstructure analysis of dendrite arrays has, for example, been used to provide boundary conditions for 3D flow simulations leading to the determination of anisotropic permeabilities of mushy zones [8]. In many other cases, synthetic microstructures are designed as initial conditions.

The major drawback of both experimental and synthetic microstructures is that they, in general, do not provide all the information necessary to describe relevant phenomena in sufficient detail. Experimental or synthetic microstructures, for example, provide the topological arrangement of the individual phases observed at different scales. In general, other important information such as crystallographic orientations or local segregation patterns are, however, omitted, as both their determination and implementation as an initial condition requires a substantial effort.

Individual models thus in future will profit from the platform concept by just reading all this additional and much more detailed information from the results file of a preceding simulation. The requirements for the individual models in this context comprise the capability of reading the standardized result files, a sufficient robustness with respect to a variety of initial conditions, and the provision of subroutines to model and evaluate effects related to the additional data.

Performing individual simulations on the basis of more detailed and sound initial conditions will drastically improve the quality of the model output. This output then serves as input for subsequent models. For these subsequent models, it again provides an improved and more comprehensive basis for the initial conditions.

3.4.2
Improved Quality of Materials Data

Another issue is the reliability of input data for the simulation. Often materials properties are taken from a database, implying a well-known materials state. In materials processing, the definition of the materials state is not self-evident as the materials properties not only depend on chemical composition and temperature but also on the materials history. Thus, it is not straightforward to select the correct materials law and adequate material data for a specific simulation. Simulation along the entire production chain, as described in this book, now offers the possibility of starting from a well-characterized initial situation and taking the entire production history into account. The selection of a proper materials description during or at the end of a process chain can be now made on the basis of the knowledge of the materials history. It can be expected that this will lead to a significantly higher accuracy for the results as compared to the present situation where material data are selected without prior knowledge about the process history.

3.4.3
Consideration of Local Effective Materials Properties

Another important development toward a more detailed approximation of the reality in macroscopic simulation tools is the step from uniform material data toward

spatial and temporal varying material data. This can be done by the coupling between the different scales, that is, between the mesoscopic and the macroscopic scales. On the mesoscopic scale, the materials microstructure and their responses on processing can be simulated, which leads to altered materials properties. This information can be transferred to the macroscopic scale, in the ideal case, for each compute node. However, this would be extremely computational expensive; therefore, interpolation schemes are necessary elements for this scale bridging. The platform concept is a promising way toward efficient, scale-bridging simulations. The local materials properties can even be exploited, including their full anisotropy in case the preceding simulations or the simulations at the smaller length scale provide additional information about texture and/or crystallographic orientation.

3.5
Strong and Weak Coupling of Platform Models

The AixViPMaP simulation platform relies to a large extent on a handshaking data exchange. This is an appropriate way if the simulated processes and phenomena can be decoupled in length and time scales. This is always the case for consecutive processes, for example, a heat treatment after a casting process. In this case, the end point of the casting simulation is the start point for the simulation of the heat treatment. This clear boundary holds on all different scales, on the macroscale, for example, for the temperature distribution, as well as on the microscale of the materials microstructure. Therefore, the coupling among the different simulations along the process chain can be considered as weak and no feedback loops are necessary.

The situation becomes entirely different when coupling different simulation models on different scales for the simulation of a single process step. Here, the coupling may be ''strong'' in the sense that phenomena on the microscale will have a direct impact on the processes on the macroscale and vice versa. Examples are the microstructure evolution during forging or rolling. Owing to the microstructural changes, mechanical properties such as the flow curve can change significantly, which in turn affects the macroscopic deformation itself or the necessary forming forces. Another example of a strongly coupled process is casting. For multicomponent alloys, the enthalpy is not a unique function of the temperature but depends on the microstructure, in particular, on the evolution of the individual phase fractions. The enthalpy enters the macroscopic heat balance equation, which determines the temperature distribution in the component and its cooling history. This cooling history in turn affects the local microstructure formation. Cooling histories being macroscopically calculated thus have to be consistent with the cooling history calculated on the basis of phase transformations on the microscale. One way to deal with these nonlinear coupling is the implementation of iterative schemes, allowing a self-consistent solution to the coupled multiscale simulations [9]. Much work is still to be done in this direction, for example, the development of fast converging iterative algorithms.

3.6 Conclusions

The integration of different models and simulation tools into an ICME platform places several requirements on the performance of these models. The model integration into a platform concept, however, opens a huge horizon for their further generalization and optimization. In contrast to individual models, a platform provides more comprehensive and more detailed information at the disposal of the individual models.

One of the first tasks to be met is the communication among different models and tools on the basis of a standardized information exchange. The standards are detailed in the following chapter.

References

1. Furrer, D.U. and Semiatin, S.L. (eds) (2010) *ASM Handbook*, Metals Process Simulation, Vol. 22B, ASM International p. 649.
2. Steinbach, I. (2009) Phase-field models in materials science – topical review. *Model. Simul. Mater. Sci. Eng.*, **17**, 073001.
3. NAFEMS, (2012) *http://www.nafems.org*.
4. Eiken, J. Oral Presentation at MRS Spring Meeting, San Francisco, 2011, to be published.
5. MICRESS, version 6.0 (2011), *www.micress.de*.
6. Altenfeld, R., Apel, M., an Mey, D., Böttger, B., Benke, S., and Bischof, C. (2011) Parallelizing Computational Microstructure Simulations for Metallic Materials with OpenMP, B.M. Chapman et al. (eds): IWOMP 2011, LNCS 6665, Springer Verlag, pp. 1–11.
7. Amdahl, G.M. (1967) Proceedings of the AFIPS Spring Joint Computer Conference, 1967, pp. 483–485.
8. Madison, J., Spowart, J.E., Rowenhorst, D.J., Aagesen, L.K., Thornton, K. and Pollock, T.M. (2012). Fluid flow and defect formation in the three-dimensional dendritic structure of Nickel-based single crystals,, *Met. and Mat. Trans. A*, Vol. 43A, pp. 369–380.
9. Böttger, B., Eiken, J., and Apel, M. (2009) Phase-field simulation of microstructure formation in technical castings – a self-consistent homoenthalpic approach to the micro – macro problem. *J. Comput. Phys.*, **228**, 6784–6795.
10. Furrer, D.U. and Semiatin, S.L. (eds) (2009) *ASM Handbook*, Fundamentals of Modeling for Metals Processing, Vol. 22A, ASM International.

4
Standardization

Stefan Benke and Georg J. Schmitz

4.1
Overview

Standardization in the context of the AixViPMaP platform currently covers two different aspects. In the first step, the simulation of manufacturing process chains requires the exchange of state variables describing the history of the material or component along the entire value chain from casting of the homogeneous melt to the application of the final product. The simulation of the individual process steps usually is performed by specialized simulation tools, which might be academic ''in-house,'' commercial software packages, proprietary industrial developments, or open source codes. In order to enable a seamless integration of the tools into the platform and the use of one common postprocessing tool for all simulation software packages, a standardization of the result data, geometry data, material data, and boundary conditions is required.

In the second step, which intervenes deeper into the different individual software tools, the standardization efforts extend to functional dependencies for modeling of the specific material behavior. In order to exchange the functional description of the material models between the simulation codes and to enable the realization of a strongly coupled, scale bridging simulation using different software codes on all involved length scales, an application programming interface (API) for user-defined material subroutines has to be standardized. These user subroutines may be used to model the thermal, mechanical, electrical, and metallurgical behavior of the material.

Common to all standardization activities on the AixViPMaP platform is the usage of very simple file formats and programming methods in order to keep the threshold for participation as low as possible. As most of the existing simulation tools in computational engineering of materials are – because of historical reasons – programmed in programming languages such as Fortran or C, the exchange of simulation data is easily realized by the use of plain ASCII or binary files rather than using databases or object-oriented programming methods. The additional advantage of this approach is that all basic file operations are supported by most of the various operation systems currently used.

Integrative Computational Materials Engineering: Concepts and Applications of a Modular Simulation Platform,
First Edition. Edited by Georg J. Schmitz and Ulrich Prahl.

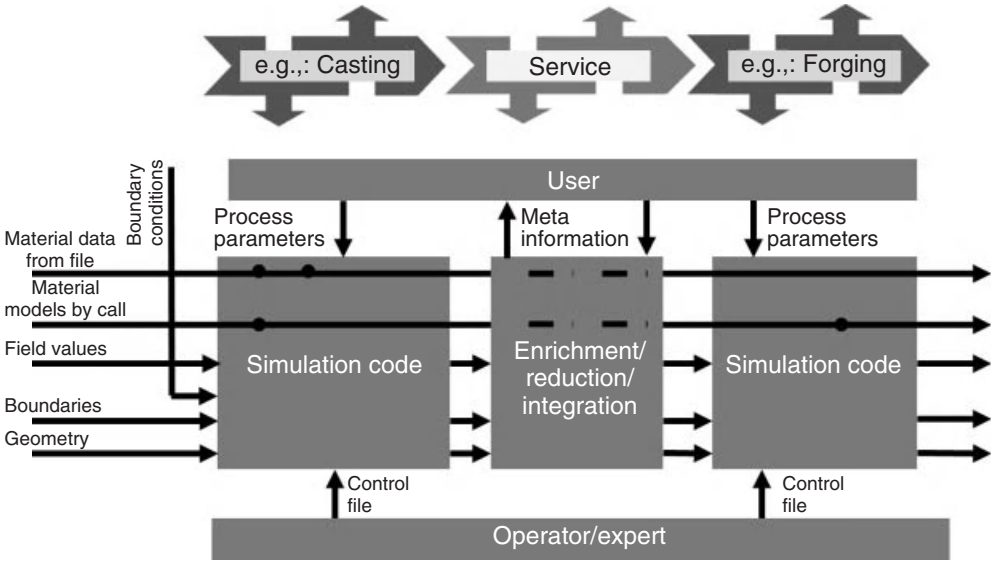

Figure 4.1 Scheme of the bus-type information flow between two different modules of the AixViPMaP® simulation platform. Individual simulation tools are daisy chained along the different processes steps of the entire production process. The information exchange is file based, using VTK files for geometry, boundaries, and field values, ASCII files for material data from file.

This chapter documents preliminary standards for the file-based data exchange and the API. In view of the ongoing exploration of the possibilities of the platform, the current state of the documentation serves as a very basic standard. An updated version may be found at the AixViPMaP site [1]. In the long term, further development should become a cooperative effort of an international community, for example, in the frame of the TMS committee on integrated computational materials engineering (ICME).

An overview of the standardization efforts to be taken is depicted in Figure 4.1. The following sections describe the present status with respect to standardization of geometry and APIs.

4.2 Standardization of Geometry and Result Data

The description of the discretized component geometry on the macroscale and the morphology of the microstructure on the microscale are both based on the file format of the Visualization Toolkit (VTK) [2]. VTK is an open source toolkit for the visualization of discretized data stemming from various sources such as numerical simulations, computed -tomography, or others. The toolkit is distributed by Kitware Inc. and is basically written in C++. It provides a number of predefined

data structures and methods for the handling of data files, the manipulation of mesh and result data, and their visualization. A number of software applications based on VTK are available as open source software, highlighting ParaView [3] as one of the most popular tools for data visualization, especially in 3D. This leads to the fact that the VTK-file format – besides netCDF and HDF – is one of the most popular open file formats for numerical result data.

Since the VTK-file format is a very basic and universal file format for discretized data, several extensions and standardizations are needed while keeping the compatibility to the basic format. The missing data in the file are especially the information on previous simulation steps, unit systems, coordinate systems, and timing data. These have now been included into an extended file header, as described in the next section. The standardization issues are mostly related to the nomenclature of the datasets containing group and result data. The rest of the file coincides with the ASCII or binary version of ''legacy file format,'' which is documented in detail elsewhere [4] and is briefly recalled here. In general, the file consists of five basic parts [4]:

1) The first part contains the file version and the identifier of the file format.
2) The second part is the header. It consists of a character string that may be 256 characters long. On the AixVipMap platform, this character string is used to transport information about process step and process time as well as about the unit system (Section 4.2.1).
3) The third part defines either the ASCII or binary file type format. Both types are used on the AixViPMaP platform.
4) The fourth part comprises information about the geometry and topology of the dataset. Currently, only discretized geometries are used on the platform. The discretization types currently being used are structured points, mainly for microstructure descriptions from phase-field simulations; structured grids; and unstructured grids, mainly for macroscopic finite element (FE) process simulations.
5) The last part of the file contains the dataset attributed or field variables, which may be scalar-, vector-, or tensor-type data. The keywords describing the attribute values are standardized in Section 4.2.3. The field variables are also used to define geometric group information, as defined in Section 4.2.2.

The naming of the result files follows a specific naming scheme in order to organize the result files in a meaningful manner. The name of the result files consists of the English name of the individual process step followed by a sequential number counting the number of simulations using this type of process step, a dot, followed by the sequential number of the time step writing this process step, and eventually the extension ''.vtk.'' For example, the name of the result file stemming from the second heating step within a process chain is given by: `heating02.10.vtk`. Here, the number 10 refers to the 10th time step of the process step.

4.2.1 Extended File Header

The header of the generic VTK-file is extended on the AixViPMaP platform in order to store the information on the simulation step, which may be used on a higher abstraction level and for postprocessing purposes. The header section at the beginning of the VTK-file looks as follows:

```
#vtk DataFile Version 2.0
process_step time=n genericSI|modifiedSI
```

Where the process_step is the English name of the simulation process step, time is the current simulation time in time units as given by the unit system. The *unit system* is defined either as generic SI unit system or a modified SI system using arbitrary units. For a modified SI unit system, the conversion factors to the SI unit system must be defined as follows:

```
process_step time=n modifiedSI l=1.0E-06 f=1.0
t=1.0 dt=273.15 p=1.0 to=0.0 c=wt
```

For non-SI unit systems, the factors for converting the field variables and measurements into SI units must be declared. They are defined as follows:

`l`	Scaling factor from length units to SI units (meter)
`f`	Scaling factor for forces to SI units
`t`	Scaling factor for temperature units
`p`	Scaling factor for time periods
`dt`	Temperature offset to 0 K in temperature units
`to`	Time offset in time units
`c =wt|at`	Defines either mass or atom percent for species concentration

If a factor is not given, it is implicitly assumed to be a unit factor or a zero offset.

4.2.2 Geometric Attributes

Geometric attributes are currently used to store information about the groups of geometric entities. Thus, they are used to define a subset of the discretized cells or points of the geometry under consideration. In FE analysis, the definition of point or cell groups is very common. They are mostly used to define geometric regions for the application of initial and boundary conditions. As the VTK-file format does not provide a special data structure for the storage of groups, they are defined as attribute field datasets on points or cells.

Material ID The attribute field `Material ID` is intended to decompose a part or context geometry into several geometric regions that consist of different materials. The attribute field is stored as a generic "`CELL DATA`" field as an integer number. The number corresponds with the identifier of the material. All material identifiers should – but need not – be sequentially numbered.

Groups of Points The point groups are stored as an attribute dataset on points. The naming convention for these groups is defined such that the name should start with the prefix "`POINT_GROUP_ ...`". Here, the dots are placeholders for the unique naming suffix. The *attribute values* are defined as integer values for all points of the model. If a point belongs to the group, its attribute value should not be zero. All other points not being members of the actual group should have a zero attribute value. It is advised that all point groups should be sequentially numbered and that this number should be used as the attribute value in order to allow set operations on the point groups.

Groups of Cells The cells are defined in the same way as the groups of points. The naming scheme for cell groups starts with the prefix "`CELL_GROUP`" followed by a unique naming suffix. Both parts of the name must be connected by an underscore. If a cell is a member of a group, its integer attribute value should not be zero. All other cells must have a zero attribute value. Here again, it is advised that all cell groups should be sequentially numbered and that this number should be used as the attribute value in order to allow set operations on the point groups.

4.2.3 Field Data

In the following, the names of the field datasets are defined and standardized in order to enable an automatic processing of the data by the different simulation tools and the enricher/parser software. Basically, the name of the field data is given by the English name of the field variable. The names are case insensitive but may not be separated by whitespace characters. Data items not being updated in the current simulation step, for example, because of a lack of material model, should be passed unchanged to the following simulation step (Table 4.1).

4.3 Material Data

Different types of material data – especially thermodynamic and thermophysical – are relevant to ICME. Thermodynamic and kinetic data are relevant, for example, to model microstructure evolution and also to account, for example,

Table 4.1 Standardized names for the field variables in attribute datasets.

Entity	Type	SI unit
backstress	Tensor	Pa
concentration_*Xx*[a]	Scalar	wt%|at%
dislocation_density	Scalar	$1\,m^{-2}$
displacement	Vector	M
enthalphy[b]	Scalar	$J\,m^{-3}$
equivalent_strain_rate	Scalar	$1\,s^{-1}$
equivalent_strain	Scalar	1
equivalent_plastic_strain	Scalar	1
equivalent_stress	Scalar	Pa
fraction_crystalline[c]	Scalar	1
heat_flux	Vector	$J\,mm^{-2}$
hydrostatic_strain	Scalar	1
hydrostatic_stress	Scalar	Pa
grain_size[d]	Scalar	M
grain_size_min	Scalar	M
grain_size_max	Scalar	M
nodal_force	Vector	N
material_orientation[c]	Tensor	1
phase_frac_*name*[e]	Scalar	1
plastic_strain	Tensor	1
spherulite_number[c]	Scalar	1
spherulite_diameter[c]	Scalar	M
stiffness_hooke	Tensor	Pa
strain	Tensor	1
strain_energy[f]	Scalar	J
strain_energy_density	Scalar	$J\,m^{-3}$
strain_rate	Tensor	$1\,s^{-1}$
temperature	Scalar	K
temperature_rate	Scalar	$K\,s^{-1}$
velocity	Vector	$m\,s^{-1}$
shear_rate[c]	Vector	$1\,s^{-1}$
liquidus_temperature	Scalar	K
solidus_temperature	Scalar	K
vaporisation_temperature	Scalar	K
heat_of_fusion	Scalar	$J\,m^{-3}$
heat_of_condensation	Scalar	J/m^3
density_at_rt	Scalar	$kg\,m^{-3}$
density_at_liquidus	Scalar	$kg\,m^{-3}$
density_at_solidus	Scalar	$kg\,m^{-3}$
density_at_vapor	Scalar	$kg\,m^{-3}$
rho_cp_at_rt	Scalar	$J\,m^{-3}\,K$
rho_cp_at_liquidus	Scalar	$J\,m^{-3}\,K$
rho_cp_at_solidus	Scalar	$J\,m^{-3}\,K$
rho_cp_at_vapor	Scalar	$J\,m^{-3}\,K$
specific_heat_mass_at_rt	Scalar	$J\,kg^{-1}\,K$

Table 4.1 (*continued*)

Entity	Type	SI unit
specific_heat_mass_at_liquidus	Scalar	J/kg K
specific_heat_mass_at_solidus	Scalar	J kg^{-1} K
specific_heat_mass_at_vapor	Scalar	J kg^{-1} K
thermal_conductivity_at_rt	Scalar	W m^{-2} K
thermal_conductivity_at_liquidus	Scalar	W m^{-2} K
thermal_conductivity_at_solidus	Scalar	W m^{-2} K
thermal_conductivity_at_vapor	Scalar	W m^{-2} K

[a] *Xx* is the abbreviation of the name of the chemical species.
[b] Stored enthalpy of the material at a given temperature.
[c] Only for plastics/polymers.
[d] Average grain size for a macroscale process simulation.
[e] Where `name` is the English denomination of the phase, for example, austenite, ferrite, bainite, srx (static recrystallized), drx (dynamically recrystallized), mrx (metadynamically recrystallized), and so on.
[f] Total strain.

for phase fractions, enthalpies, or other thermodynamic values being required as effective local values for simulations at the process scale. The standardization of such data has already largely taken place within the CALPHAD community in the form of the widespread thermodynamic database "*.tdb" file format. Many databases for technical alloy systems are commercially available and can be accessed by APIs provided by the respective software companies. Present activities aim at generating data also for interfacial properties. A standard for storage and retrieval of such data has to be developed in future. Several thermophysical data such as density and thermal expansion coefficient can be extracted as temperature- and composition-dependant values from these databases both for pure phases and phase mixtures.

For the exchange of thermophysical material data along the process chain – stemming from experiments or a weak coupling between the length scales – a simple file-based format is used on the simulation platform. The term *material*, however, is somehow not quite unique and scale dependent. For *ab initio* simulations, the material data may describe the properties and the interaction of single atoms; in microscale simulations, the term material may be identified with the properties of the pure phase, which may be a mixture of several chemical species, whereas in macroscale process simulations it corresponds to the effective properties of a representative volume element.

The material data is stored in plain ASCII files. They can be created by the use of a text editor, data logging programs, or scale bridging tools such as homogenization or virtual testing software codes (Chapter 5). The file consists of lines containing key words and data. The data describes basically the material properties as tables of

the temperature or other state variables. The following applies to all keyword and data lines of the material data file:

1) The first nonblank character of a keyword line must be a slash (/).
2) A line beginning with a hash (#) is a comment line and is ignored as well as any blank characters ( ).
3) A line may be maximum 256 characters long. There is no case sensitivity.
4) Parameters and options are separated by a comma (,). A keyword must also be followed by a comma, if any parameters are given.
5) If a parameter owns a value, the equal sign (=) is always used. The value may be a number or a character string.
6) A line ending with a comma (,) is continued in the next line.
7) Character strings as well as keywords may be 80 characters long.
8) All properties are defined in SI units.

The keywords for the naming of the data sets are usually the English standard names of the thermal, physical, mechanical, electrical, or optical property. The keywords already defined are given in Table 4.2. As mentioned before, an updated list of keywords can be found on the AixViPMaP site [1].

The data tables in the data section define, in general, piecewise linearized functions of the data values. The functions always depend on the temperature, and may also depend on other state variables. The type of interpolation scheme for the calculation of the values in between the supporting points is left to the software tool. The definition of the tables is as follows:

Table 4.2 Keywords for the naming of material data sets.

Keyword	Description
CONDUCTIVITY	Thermal conductivity
DENSITY	Density
DRIVING FORCE	Driving force of phase transformation
FRACTION SOLID	Volume fraction solid during solidification
FRACTION LIQUID	Volume fraction liquid during condensation
HEAT CAPACITY	Volume-specific heat capacity
HEAT OF FUSION	Volume-specific heat of fusion
HEAT OF MELTING	Volume-specific heat of meting
HEAT OF CONDENSATION	Volume-specific heat of condensation
HEAT OF EVAPORATION	Volume-specific heat of evaporation
ENTHALPY	Volume-specific total enthalpy
ELASTICITY	Hooke tensor
PINNING FORCE	Zener force
MOLAR VOLUME	Volume of a mole atoms
TEMPERATURE SOLIDUS	Solidus temperature
TEMPERATURE LIQUIDUS	Liquidus temperature
TEMPERATURE GASEOUS	Gaseous temperature
YIELD STRESS	Yield stress

- Each line defines the data values for one combination of the temperature and optional solution-dependent state variables.
- The first columns of values define the material properties. The number of properties depends on the grade of the material anisotropy.
- The last column always defines the temperature.
- The properties must be listed in ascending order of the state variables and the temperature.
- The columns are separated by a comma (,).

Thermophysical data are, in general, defined as volume-specific properties. The directional dependence of material properties is defined by the `TYPE` parameter that may have the values `ISOTROPY/ISO`, `ORTHOTROPY/ORTHO`, or general `ANISOTROPY/ANISO`. The sequence of the directional-dependent coefficients for second-order tensors is as follows:

- **Orthotropy**: 11, 22, and 33 direction,
- **General anisotropy**: 11, 12, 13, 21, 22, 23, 31, 32, 33.

For fourth-order tensors such as the Hooke tensor in elasticity, the sequence of the coefficients is given by:

- **Orthotropy**: 1111, 1122, 2222, 1133, 2233, 3333, 1212, 1313, 2323,
- **General anisotropy**: 1111, 1122, 2222, 1133, 2233, 3333, 1112, 2212, 3312, 1212, 1113, 2213, 3313, 1213, 1313, 1123, 2223, 3323, 1223, 1323, 2323.

The example dataset for the temperature-dependent density of generic low carbon steels is as follows:

```
/DENSITY
    7.849E-06,    0.0
    7.630E-06,  650.0
    7.650E-06,  700.0
    7.400E-06, 1300.0
    7.317E-06, 1434.0
    7.310E-06, 1440.0
    7.105E-06, 1500.0
    7.012E-06, 1510.0
    7.000E-06, 1525.0
```

The stress–strain curves of an aluminum alloy are defined as a function of the temperature and the equivalent plastic strain as follows:

```
/YIELD STRESS, TYPE=VON MISES
  179.58,   0.00,   0.00
  160.74,   0.00, 100.00
   99.50,   0.00, 200.00
  218.68,   0.02,   0.00
```

```
193.03,   0.02, 100.00
119.22,   0.02, 200.00
```

Here, the first column lists the yield stress for a given combination of the equivalent plastic strain and temperature. The second column defines the equivalent plastic strain, here 0.00 and 0.02, as the first solution-dependent state variable and the last column defines the temperature values 0.0, 100.0, and 200.0 as the second solution-dependent state variable. The values are ordered first by the plastic strain and then by the temperature. In this example, only a linear stress–strain curve is displayed. By repeating the block for each strain, the example could be extended to a more complicated situation.

4.4 Application Programming Interface

Besides the file-based exchange of discretized field variables and material data, the standardization of the programming interface is used to convey functional dependencies such as thermal or mechanical material models between the different software codes. These functions are coded as subroutines or functions using a high-level programming language and are called many times during a calculation run. On the basis of the modularized structure of the platform, as displayed in Figure 4.2, the subroutines may transport the functional dependencies along the *horizontal* and the *vertical* direction of the map. The horizontal axis links the different software codes keeping the same scale or the same level of detail. The material models coded in these functions thus may be reused by the different software codes. This enables, for example, the use of a consistent material model in all codes. On the vertical axis of Figure 4.2, the use of the programming interface

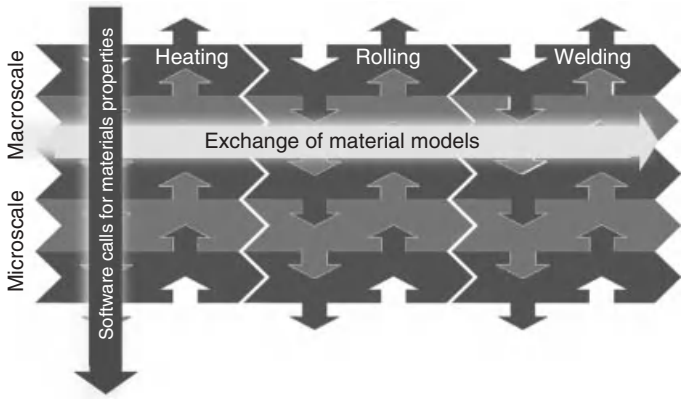

Figure 4.2 User programming interfaces for the exchange of material models between the software codes of the simulation chain, and the calculation of effective properties from smaller length scales.

may enable a direct link between the software codes at different length scales. Thus, it enables a strong coupling between the simulations on different length scales and the use of multiscale material models. This is especially helpful to realize multiscale material models using the multi level finite element analysis method or the numerical calculation of effective material properties based on discretized microstructures originating from transient phase-field models, virtual models such as DIGIMAT, or discretized metallurgical images. In principle, the call of any external software tool is possible as the subroutine itself may write the input to files and call any program by the use of a system call and read the results from file after the program run again.

The programming interfaces, which are currently already standardized, interact at different levels with the simulation software code and are very similar to programming interfaces already being implemented in several existing software codes such as ABAQUS, ANSYS, or FEAP. The standardized programming interfaces for the user subroutines are

- **USER_MATERIAL_TM**: user-defined mechanical constitutive material models,
- **USER_MATERIAL_HT**: user-defined thermal material laws,
- **USER_EXPANSION**: user-defined models for stress-free strains stemming from thermal dilatation or the volume change due to phase transformations,
- **USER_PHASE_TRANSFORMATION**: user-defined models for the description of phase transformations.

The definition of the programming interface comprises the definition of a fixed formal name of the subroutine and an argument list. The argument list defines the type, size, and content of the variables exchanged between the calling program and user subroutine. The variables are classified into three groups:

- Variables to be defined by the user. This is the required information for the calling program.
- Variables passed to the subroutine for information purpose. These variables should not be changed, and it is advised that the calling program passes a copy of the variable to the subroutine.
- Variables to be updated.

All subroutines are evaluated at each integration point of the discretized geometry. The subroutines may be called several times during an iterative solution procedure for the resolution of a geometric or material nonlinearity. The information on the iteration step and the calling sequence during the solution procedure is passed to the subroutine by several flags described in the following text.

The communication between the user subroutines is realized with the help of an integer and a real array. These arrays are used to store the user-defined state variables at each integration point. The calling program must ensure to pass the correct array of state variables to the call of the subroutine at each integration point. The size and the use of the state variables must be defined by the user. Subroutines for the initialization and the output of the variables for postprocessing are not standardized, and the features are left to the software provider.

4.4.1 USER_MATERIAL_TM Subroutine

The USER_MATERIAL_TM subroutine is used to implement a user-defined material model into an existing software code. The subroutine may be exchanged by the different software tools being used for the simulation of a process chain at a given length scale. For multiscale material models, the subroutine may consist of a complete calculation tool or a system call that, for example, passes the effective tangential material stiffness to the calling program at a larger length scale.

The formal programming interface in FORTAN notation of the subroutine is given by:

```
 SUBROUTINE USER_MATERIAL_TM (STRESS,DSTRSEPS,DSTRDTEMP,ENERGY,
1                             STRESS,STATEV,NSTATV,STRAIN,
2                             DSTRAIN,TIME,DTIME,TEMP,DTEMP,
3                             NAME,NTENS,PROPS,NPROPS,COORDS,
4                             ISTEP,IITER,IELEM,IGAUSS,ISTATUS)
CHARACTER   NAME(80)
REAL              STRESS(NTENS),STATEV(NSTATV),ENERGY(2,2),
1                 DSTRDEPS(NTENS,NTENS),DSTRDTEMP(NTENS),
2                 STRAIN(NTENS),DSTRAIN(NTENS),STRESS(NTENS),
3                 PROPS(NPROPS),COORDS(3),TIME,DTEIM,TEMP,DTEMP
INTEGER           NTENS,NSTATV,NPROPS,ISTEP,IITER,IELEM,IGAUSS,
1                 ISTATUS
user coding to define DSTRDEPS, STRESS, STATEV
and, if necessary, ENERGY, DEPSDTEMP
The solution dependent state variables may be updated

END
```

A number of routines for simple linear elasticity written in FORTRAN and C can be found on the AixViPMaP web site [1] for free download. In the following text, the variables are described in detail. The ordering of the directions of the stresses and strains is as follows: first, the direct components are ordered by the direction followed by the shear directions again ordered after their directions.

Variables Required by the Program

DSTRDEPS(NTENS,NTENS)	The algorithmic tangent matrix of the constitutive model with respect to the strains. The variable DSTRDEPS(I,J) defines the change of the Ith stress component caused by an infinitesimal change of the Jth component of the strain tensor. Remember, the calling program may accept only the symmetric part of the array.

DSTRDTEMP(NTENS)	The algorithmic tangent matrix of the constitutive material model with respect to the temperature. Here, DSTRDTEMP(I) defines the change of the Ith stress component caused by an infinitesimal temperature change.
STRESS(NTENS)	The array contains the Cauchy stress tensor at the beginning of the increment and must be updated in this routine to be the stress tensor to the end of the increment.
ENERGY(2,2)	The strain energy at the end of the increment and its derivation with respect to the strain. ENERGY(1,1) is the reversible part of the strain energy, ENERGY(2,1) is the irreversible part of the strain energy, and ENERGY(1,2)and ENERGY(1,2) contain the corresponding linearized deviations.

Variables to Be Updated

STATEV(NSTATV)	The array contains the solution-dependent state variables. They correspond to the values at the beginning of the increment, unless they are updated by other user-defined subroutines. The values passed correspond only to the current integration point for which the subroutine is passed and they may be used for data exchange between the user subroutines. The memory allocation is left to the calling program. In addition, there should be the possibility in the calling program to initialize and output the variables.

Variables Passed in for Information

STRAIN(NTENS)	The array contains the total strains at the beginning of the increment, for example, the equilibrium state of the previous step. The definition of the strain is left to the calling program. For compatibility reasons, the use of the Lagrangian strain in large deformation analysis should be preferred. For coupled thermomechanical problems, this is the stress-generating part of the strain only. Other stress-free strains such as thermal strains and dilatations due to phase transformations are calculated by the UEXPAN subroutine and have already been subtracted.
DSTRAIN(NTENS)	The array of strain increments within this load step. As before, these are the mechanical parts of the strain only.
TIME	The simulation time information at the beginning of the increment.
DTIME	The time period covered by the current increment.
TEMP	The temperature at the integration point at the beginning of the current increment.
DTEMP	The temperature change during the previous time increment.

NAME	The user-defined name of the material region, left justified.
NTENS	Number of the stress or strain components.
NSTATV	Number of solution-dependent state variables that are associated with this material model.
PROPS (NPROPS)	User-specified array of material constants associated with this user material as defined in the input file of the calling program.
NPROPS	User-defined number of material constants.
COORDS (3)	The current coordinates of this integration point.
ISTEP	Number of the current time step.
IITER	Current iteration number.
IELEM	Number of the element.
IGAUSS	Number of the integration point within the element.
ISTATUS	Flag indicating if the routine is called at the beginning of the increment (ISTATUS=1), at the end of the increment (ISTATUS=2), or elsewhere (ISTATUS=0).

4.4.2 USER_MATERIAL_HT Subroutine

The thermal counterpart of the previously described subroutine is the USER_MATERIAL_HT programming interface. It is used to implement a thermal material model with a complex thermal behavior including the release or consumption of the heat of fusion, heat of evaporation, heat of solidification, heat of melting, or the heat release during solid-state transformations. The programming interface is a subclass of the user–material programming interface. Thus, it should provide the same user-defined variables and should be called at the same integration points as all other subroutines. The header and input/output variables of the USER_MATERIAL_HT routine expected from the driver routine are as follows:

```
SUBROUTINE USER_MATERIAL_HT (ENTHALPY,DENTHALPYDT,CONDUCTIVITY,
1                                STATEV,NSTATV,TIME,DTIME,NAME,
2                                PROPS,NPROPS,COORDS,NDIM,ISTEP,
3                                IITER,IELEM,IGAUSS,ISTATUS)
CHARACTER     NAME(80)
REAL          ENTHALPY,DENTHALPYDT,CONDUCTIVITY(3,3),
1             CONDUCTIVITY(3,3),STATEV(NSTATV),PROPS(NPROPS),
2             COORDS(3)
INTEGER       NDIM,NSTATV,NPROPS,ISTEP,IITER,IELEM,IGAUSS,
1             ISTATUS
user coding to define ENTHALPY,DENTHALPYDT and CONDUCTIVITY

END
```

Variables Required by the Program

ENTHALPHY	The total volume specific enthalpy at the integration point.
DENTHALPHYDT	The linearized derivation with respect to the temperature at the integration point.
CONDUCTIVITY(3,3)	The current conductivity of the material at the integration point.
DCONDUCTIVITYDT(3,3)	The deviation of the current conductivity of the material at the integration point with respect to the temperature.

Variables to Be Updated

STATEV (NSTATV)	The array contains the solution-dependent state variables. They correspond to the values at the beginning of the increment, unless they are updated by other user-defined subroutines. The values passed correspond only to the current integration point for which the subroutine is passed, and they may be used for data exchange between the user subroutines. The memory allocation is left to the calling program. In addition, there should be the possibility in the calling program to initialize and output the variables.

Variables Passed in for Information

NDIM	The number of coordinates indicating a 2D or 3D analysis.

The description of the remaining variables passed for information is given in detail in the section titled Variables Passed in for Information.

4.4.3 USER_EXPANSION Subroutine

The programming interface of the user expansion subroutine must be considered as a subset of the programming interface for user material models. The subroutine can be used to implement stress-free eigenstrains stemming from thermal dilatations or from density changes caused by phase transformations. The implementation of the programming interface should enable the use of the solution-dependent state variables as used in the USER_MATERIAL_TM subroutine in order to allow the realization of complex models for phase transformations. The subroutine should be called at the same integration points, as the other user subroutines. The ordering of the calling sequence of the several subroutines is left to the calling program. The formal interface of the user subroutine is as follows:

```
SUBROUTINE USER_EXPANSION   (EXPANSION,DEXPANDTEMP,STATEV,
1                           NSTATV,TIME,DTIME,TEMP,DTEMP,
2                           PROPS,NPROPS,NAME,COORDS,NTENS,
3                           ISTEP,IITER,IELEM,IGAUSS,ISTATUS)
CHARACTER  NAME(80)
REAL            EXPAN(NTENS),DEXPANDT(3),PROPS(NPROPS),
1               STATEV(NSTATV),COORDS(3),TIME,DTIME,TEMP,
2               DTEMP
INTEGER         NTENS,NSTATV,NPROPS,ISTEP,IITER,IELEM,IGAUSS,

1               ISTATUS
user coding to define EXPAN, DEXPANDT and update STATEV if nec-
essary.

END
```

Variables Required by the Program

`EXPANSION (NTENS)`	The tensor of the total stress-free strains for the current configuration. The ordering of the components of the tensor in Voigt notation coincident with the stresses and strains, in general.
`DEXPANDTEMP (NTENS)`	The linearized derivation of the stress-free strains with respect to the temperature.

Variables to Be Updated

`STATEV (NSTATV)`	The array that contains the solution-dependent state variables as described before.

Variables Passed in for Information The description of the variables passed for information is given in detail in **Variables Passed in for Information**.

4.4.4 USER_PHASE_CHANGE Subroutine

This programming interface allows the definition of a user-defined material model for the solidification and solid-state transformations. It consists basically of two interfaces: the interface to the user material subroutine, which has to deliver the thermal and mechanical material model, and the interface to the user expansion subroutine, which is realized as a subclass of the user material interface. The user expansion subroutine takes care of the density changes and eigenstrains during the

solid-state transformation and includes them into the calculation of the mechanical submodel. The communication between all subroutines should be realized by the usage of the same fields of the user-defined state variables. All subroutines should have access to the same variable space and should be called at the same integration points. This subroutine is intended to be a generalized interface to manipulate the phase fractions of the several metallurgical phases in a multiphase analysis, to interact with the calling software code in a more detailed way, and to allow the user to change the chemical composition and others. Usually, the volume or mass fractions of the metallurgical phases are stored as user-defined state variables. Thus, the phase changes may be simply modeled internally in the USER_MATERIAL_HT subroutine or in more detail using the subroutine described here.

The header and input/output variables of the USOLID routine expected from the driver routine are as follows:

```
SUBROUTINE USER_PHASE_CHANGE      (ENTHALPY,DENTHALPYDT,
1                                   DMASS,DRIVINGFORCE,
2                                 SPECIES,DSPECIES,NSPECIES,
3                                   PFRAC,DPFRAC,NPFRAC,
4                                   STATEV,NSTATV,TIME,DTIME,
5                                   TEMP,DTEMP,PROPS,NPROPS,
6                                   NAME,COORDS,NDIM,ISTEP,
7                                   IITER,IELEM,IGAUSS,ISTATUS)

CHARACTER  NAME(80)
REAL             ENTHALPY,DENTHALPYDT,DMASS(NPHASES),
1                DRIVINGFORCE(NPFRAC,NPFRAC),
2                SPECIES(NPFRAC,NSPECIES),
3                DSPECIES(NPFRAC,NSPECIES),
4                PFRAC(NPFRAC),DPFRAC(NPFRAC),STATEV(NSTATV),
5                TIME,DTIME,TEMP,DTEMP,PROPS(NPROPS),COORDS(3)
INTEGER          NDIM,NSTATV,NPROPS,ISTEP,IITER,IELEM,IGAUSS,
1                NSPECIES,NPFRAC,ISTATUS

user coding to define ENTHALPY, DENTHALPYDT, DMASS, DRIVINGFORCE,
SPECIES, DSPECIES, PFRAC or DPFRAC. All variables are optional and
depend largely on the calling software code

END
```

Variables Required by the Program

ENTHALPHY	The total volume-specific enthalpy at the integration point.
DENTHALPHYDT	The linearized derivation with respect to the temperature at the integration point.

DMASS (NPFRAC)	The increment of exchanged mass between the phases during the last time step. To fulfill the balance of mass, the sum of the exchange quantities should vanish.
DRIVINGFORCE (NPFRAC,NPFRAC)	The forces driving the transformation between the several phases.
SPECIES (NPFRAC,NSPECIES)	Chemical composition of the phases.
DSPECIES (NPFRAC,NSPECIES)	Change of the chemical composition of the phases.
PFRAC (NPFRAC)	Volume fraction of the distinguished metallurgical phases.
DPFRAC (NPFRAC)	Change in the volume fraction of the distinguished metallurgical phases.

Variables to Be Updated

STATEV (NSTATV)	The array contains the solution-dependent state variables. They correspond to the values at the beginning of the increment, unless they are updated by other user-defined subroutines. The values passed correspond only to the current integration point for which the subroutine is passed, and they may be used for data exchange between the user subroutines. The memory allocation is left to the calling program. In addition, there should be the possibility in the calling program to initialize and output the variables.

Variables Passed in for Information

NDIM	The number of coordinates indicating a 2D or 3D analysis.
NSPECIES	Number of the chemical species for each metallurgical phase.
NPFRAC	Number of phases.

The description of the remaining variables passed for information is given in detail in **Variables Passed in for Information**.

4.5 Future Directions of Standardization

The above standardization scheme has been implemented in a number of software codes available at the RWTH Aachen University, and converters have been

programmed to transfer results of some commercial codes into this standard, which by now essentially covers thermodynamic and thermomechanical aspects. The combination of different simulation tools – both academic and commercial – has allowed for the successful simulation of some test scenarios (Chapters 8–12). It should be noted that the standardized data exchange between the different models drastically reduced the load of data conversion, a significant effort before introducing the standard. Further development of this standard has to be discussed within the emerging ICME community and to proceed between users of ICME concepts and software developers – academic and/or commercial – providing respective models and tools.

References

1. *http://www.aixvipmap.de.*
2. *http://www.vtk.org.*
3. *http://www.paraview.org.*
4. *http://www.vtk.org/pdf/file-formats.pdf.*

5
Prediction of Effective Properties

Gottfried Laschet, Tatyana Kashko, Stephan Benke, Mehmet Öte, and Kirsten Bobzin

5.1
Introduction

Materials properties characterize the functionalities of almost any product. For many industrial applications, the final materials properties result from a number of process steps. Each of them allows the tailoring of the microstructure in order to achieve a desired functionality. As introduced in Chapter 2 about the basic concepts, *bridging the scales* is an essential feature of the multiscale analysis of the material's production steps on an integrated computational materials engineering (ICME) platform. In the case of multiscale materials modeling and in *homogenization* in general, one proceeds from lower scales upward in order to obtain effective materials properties accurately. Alternatively, in process modeling, it is important to be able to step down to the scale of the real, heterogeneous material. The technique is known as *localization* or *recovering method*. This coupling between the scales corresponds to a *serial*, handshake-type exchange of data (e.g., stresses, strains, etc.) passing up and down the scales. A more predictive alternative is the *concurrent* coupling in which both scale models are strongly coupled as in the multilevel finite element (FE^2) method [1].

In this chapter, we review and apply homogenization methods to a variety of heterogeneous materials. Several methods have been proposed in the past century to predict the effective elastic properties (see, e.g., [2, 3] for a recent review). First, Voigt and Reuss formulated rigorous lower and upper bounds for the effective modules of composites. For microstructures composed of a matrix and spherical or ellipsoidal inclusions, the effective elastic constants can be easily obtained by *mean-field homogenization* methods. These include the Mori–Tanaka method [4] and the interpolative double inclusion method [5], which is implemented, for example, in the DIGIMAT-MF program [6].

If the material exhibits a complex but periodic microstructure, the effective properties can be evaluated by the *asymptotic homogenization method* (AHM) [7, 8]. For periodic microstructures with linear behavior, this method is really efficient. It can be extended to nonlinear behavior, but the method then requires an elastoplastic FE analysis of the unit cell in each integration point of the

Integrative Computational Materials Engineering: Concepts and Applications of a Modular Simulation Platform,
First Edition. Edited by Georg J. Schmitz and Ulrich Prahl.

macromodel. However, no specific constitutive law is needed at the macroscale: it is deduced from the homogenization calculation of the nonlinear behavior at the microscale. This method, similar to the FE^2 and other *nonlinear computational homogenization* methods [9], leads to very high computational costs even in the presence of massive parallel computing. Further techniques realize virtual tests of constructed microscale boundary value problems and apply averaging techniques to the microstresses and microstrains and the Hill–Mandel condition [10] to the internal work. Note that such first-order homogenization schemes have been extended by Kouznetsova *et al.* [11, 12] in order to model localization and size effects.

In order to reduce the computational effort in the presence of materials nonlinearity, Michel and Suquet [13] propose *the nonuniform transformation field method* in combination with fast Fourier transformation (FFT). Recently, Fritzen and Böhlke [14] combined this method with the FE one and applied it to random 3D polycrystals to determine their effective elastoplastic behavior. In the AHM framework, Fish and coworkers [15, 16] propose an alternative simplification method in which the inelastic strains are considered as materials eigenstrains and the equilibrium equations are expressed in terms of equilibrated microstresses. By this approach, the bottleneck of solving large nonlinear systems at the microscale is removed.

Since the pioneer work of Sanchez-Palencia [7], several publications [17, 18] have treated and applied the AHM to thermal and fluid flow problems. In these publications, the flow is assumed to be of Stokes type, which leads to the classic Darcy law for a porous medium. In order to analyze effusion cooling of porous materials in turbomachines, Laschet [19] derived a generalized Forchheimer law, where the permeability is a function of the geometry and also depends on the mean velocity of the unit cell.

In Section 5.2, the AHM is briefly outlined for a thermoelastic material with a periodic microstructure and eigenstrains. Then, the application to materials exhibiting a *random microstructure* is addressed (Section 5.3). Postprocessing the macroscale results by the localization step is described in Section 5.4. In Section 5.5, a dedicated, novel two-level homogenization scheme is presented for semicrystalline thermoplastics (see also Chapter 10). Virtual testing in the framework of nonlinear computational homogenization is described in Section 5.6. The numerical implementation of the methods to determine effective properties is outlined in Section 5.7. Eventually, the different methods for the determination of effective properties are compared and two applications are presented in Section 5.8.

5.2 Homogenization of Materials with Periodic Microstructure

5.2.1 Static Equilibrium of a Heterogeneous Material

The AHM assumes that the heterogeneous material is built at the microscale by the periodic repetition of a representative volume element (RVE) (Figure 5.1). At

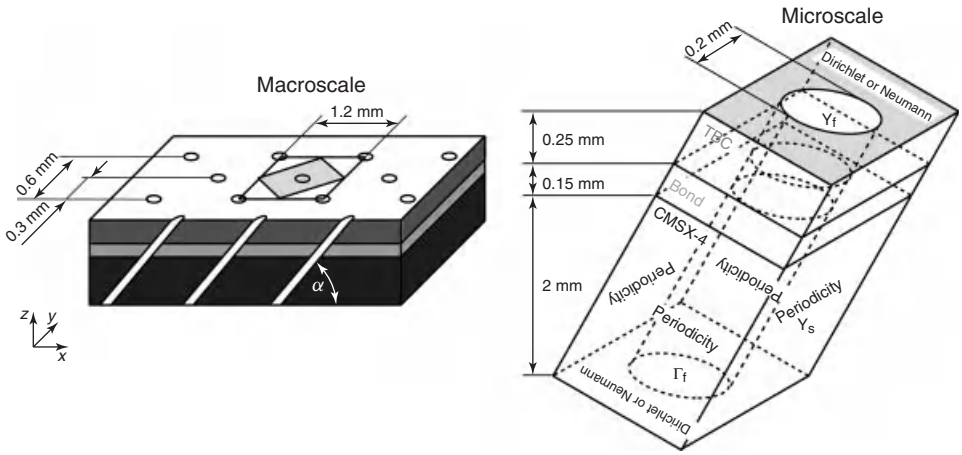

Figure 5.1 Definition of a periodic unit cell for the example of an effusion-cooled multilayer plate built of a CMSX-4 substrate, a MCrAlY bondcoat, and Y_2O_3-stabilized ZrO_2 thermal barrier thermal barrier coating (TBC) as used in gas turbines [20].

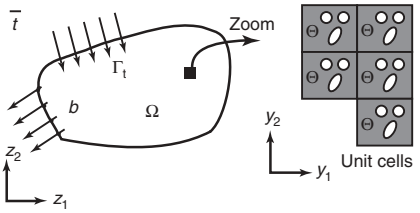

Figure 5.2 Static equilibrium of a heterogeneous material.

the macroscale, this heterogeneous material with volume Ω is in a *static equilibrium* with the body forces b_i, the prescribed surface tractions $\bar{t}_i$ on Γ_t, and displacements $\bar{u}_i$ on Γ_u (Figure 5.2). The sample is further subjected to a temperature variation $\Delta T = T^h - T_r$, where T_r is a reference temperature being set to 0 °C without loss of generality.

In the macroscopic reference, coordinate system $\mathbf{Z} = (z_1, z_2, z_3)$ (Figure 5.2), the static equilibrium of the heterogeneous material is given by

$$\frac{D}{DZ_j}\sigma_{ij}^h + b_{i=0} \tag{5.1}$$

As a pure elastic behavior of the heterogeneous material is assumed, the stress tensor σ_{ij}^h is related to the total strain $\varepsilon_{ij}^h(\mathbf{u}^h)$ by following the generalized Hooke law:

$$\sigma_{ij}^h = H_{ijkl}^h\left(T^h\right)\left[\varepsilon_{kl}^h\left(\mathbf{u}^h\right) - \alpha_{kl}^h\left(T^h\right)\Delta T - \kappa_{kl}^h\right] \tag{5.2}$$

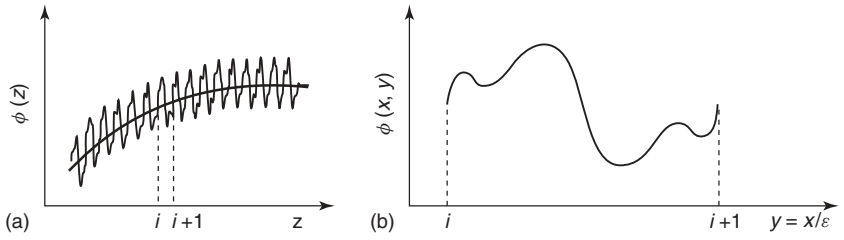

Figure 5.3 (a) A strong oscillating function on the macroscale and (b) one period of this function on the microscale.

Both the Hooke matrix H^h_{ijkl} and the thermal expansion coefficient α^h_{ij} are temperature-dependent quantities. The volumetric eigenstrains κ^h_{ij} depend only on the position $\mathbf{Z}$ and are generally present in polycrystalline materials. To complete the boundary value problem, the applied surface tractions $\bar{t}_i$ and displacements $\overline{u}_i$ must verify on Γ_t and Γ_u, respectively:

$$\sigma^h_{ij} \cdot n_j = \bar{t}_i; \quad u^h_i = \overline{u}_i \tag{5.3}$$

5.2.2 Periodicity and Two-Scale Description

A heterogeneous material has a regular periodicity if its field variables φ satisfy

$$\varphi(\mathbf{Z} + \mathbf{NY}) = \varphi(\mathbf{Z}) \tag{5.4}$$

with

- $\mathbf{N} = \begin{bmatrix} n_1 & 0 & 0 \\ 0 & n_2 & 0 \\ 0 & 0 & n_3 \end{bmatrix}$ where n_1, n_2, and n_3 are integer numbers;
- $\mathbf{Y} = [Y_1, Y_2, Y_3]^T$ constant vector, whose components describe the materials periodicity (Figure 5.4).

In the homogenization theory, the periodicity Y is small compared to the specimen's dimensions. As the function φ, such as the Hooke matrix, varies strongly in the neighborhood of an arbitrary point Z_0 (Figure 5.3), two scales are introduced in order to describe the dependency of each physical quantity:

- *a macroscopic, global variable* $\mathbf{x}$, which measures the variation of the mean value of function φ from unit cell to unit cell;
- *a microscopic, periodic variable* $\mathbf{y}$, which represents the strong variation of the function within each unit cell.

The scale ratio ε between the micro- and macroscale, defined by $\mathbf{y} = \mathbf{x}/\varepsilon$, is usually a small factor, which also specifies the size ratio between the RVE and the specimen. The material at the macroscale can thus be described as the combination of identical unit cells of extension (εY_1, εY_2, and εY_3) (Figure 5.4).

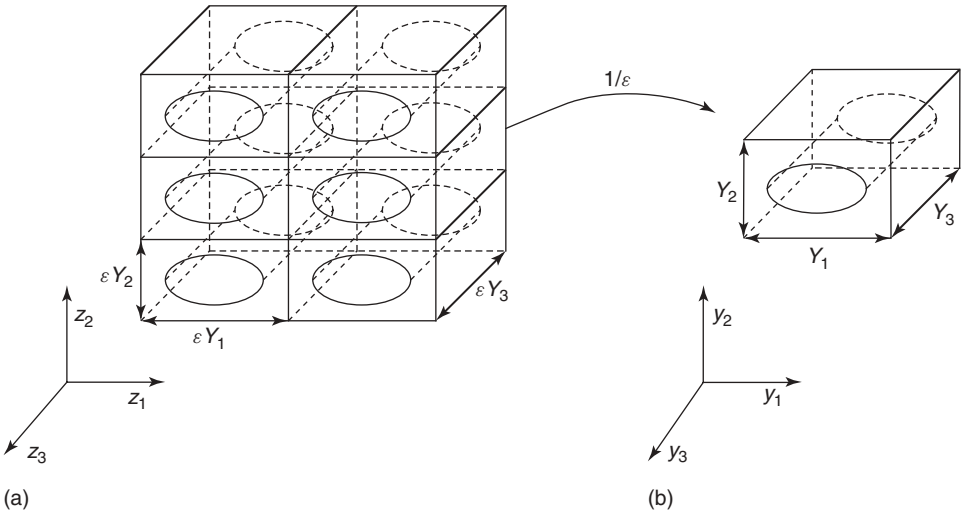

Figure 5.4 Periodic building of (a) the heterogeneous material and (b) the corresponding RVE.

5.2.3 The Asymptotic Homogenization Method

The starting point of this method is a formal asymptotic expansion of the periodic displacement and temperature fields, $\mathbf{u}^h$ and T^h on the heterogeneous material with the aspect ratio ε:

$$\begin{aligned}\mathbf{u}^h(\mathbf{Z}) &= \mathbf{u}(\mathbf{x},\mathbf{y}) = \mathbf{u}^0(\mathbf{x},\mathbf{y}) + \varepsilon\mathbf{u}^1(\mathbf{x},\mathbf{y}) + \mathrm{O}\left(\varepsilon^2\right)\\ T^h(\mathbf{Z}) &= T(\mathbf{x},\mathbf{y}) = T^0(\mathbf{x},\mathbf{y}) + \varepsilon T^1(\mathbf{x},\mathbf{y}) + \mathrm{O}\left(\varepsilon^2\right)\end{aligned} \tag{5.5}$$

As the displacement and the temperature field expansions are both limited to the first order here, the corresponding homogenization scheme is named *first-order homogenization method*. Expansions up to the second order have been introduced by Y.-P. Feng & J.-Z. Cui [21] in order to capture microstructural size effects. This formalism is complex and not discussed further here.

The Hooke matrix H^h_{ijkl}, the thermal expansion coefficients α^h_{ij}, and volumetric eigenstrains κ^h_{ij} are assumed to be a periodic function on the unit cell, and their first-order asymptotic expansions are given by

$$\begin{aligned}H^h_{ijkl}\left(\mathbf{y},T\right) &= H^0_{ijkl}\left(\mathbf{y},T^0\right) + \varepsilon T^1(\mathbf{y})\frac{\partial H_{ijkl}}{\partial T} + \mathrm{O}\left(\varepsilon^2\right)\\ \alpha^h_{ij}\left(\mathbf{y},T\right) &= \alpha^0_{ij}\left(\mathbf{y},T^0\right) + \varepsilon T^1(\mathbf{y})\frac{\partial \alpha_{ij}}{\partial T} + \mathrm{O}\left(\varepsilon^2\right)\\ \kappa^h_{ij}(\mathbf{x},\mathbf{y}) &= \kappa^0_{ij}(\mathbf{x},\mathbf{y}) + \varepsilon\kappa^1_{ij}(\mathbf{x},\mathbf{y}) + \mathrm{O}\left(\varepsilon^2\right)\end{aligned} \tag{5.6}$$

The serial developments (Eqs. (5.5) and (5.6)), the differential operator $D/DZ_i = (\partial/\partial x_i) + (1/\varepsilon)\left(\partial/\partial y_i\right)$, and the following stress definitions

$$\begin{aligned} S_{ij}^{r} &= H_{ijkl}\left(\mathbf{y}, T^0\right) E_{kl}\left(\mathbf{u}^r\right) \quad \text{macroscopic stress} \\ s_{ij}^{r} &= H_{ijkl}\left(\mathbf{y}, T^0\right) e_{kl}\left(\mathbf{u}^r\right) \quad \text{microscopic stress} \\ p_{ij}^{0}\left(\mathbf{x}, \mathbf{y}, \mathrm{T}\right) &= H_{ijkl}\left[\alpha_{kl}\left(\mathbf{y}, T\right)\Delta T^0 + \kappa_{kl}^{0}(\mathbf{y})\right] \quad \text{eigenstress} \end{aligned} \tag{5.7}$$

where $\mathbf{u}^{\mathrm{r}}$ specifies either $\mathbf{u}^0$ or $\mathbf{u}^1$ and E_{kl} and e_{kl} are the macroscopic and microscopic total strains expressed in terms of either $\mathbf{x}$ or $\mathbf{y}$, respectively [20], are introduced in the static equilibrium condition (Eq. (5.1)), leading to a system of differential equations, which can be sorted with respect to the scale ratio ε. The differential equations related to the different powers of ε are discussed in the following:

1. ε^{-2} term: $$\frac{\partial}{\partial y_j} s_{ij}^{0}(\mathbf{x}, \mathbf{y}) = 0 \tag{5.8}$$

These differential equations are homogeneous. As the Hooke matrix is positive definite, $e_{ij}(\mathbf{u}^0) = 0$ and $\mathbf{u}^0(\mathbf{x},\mathbf{y}) = \mathbf{u}(\mathbf{x})$. Thus, the first term of the serial expansion, $\mathbf{u}^0$, depends only on the macroscopic variable $\mathbf{x}$ and not on the microscopic one.

2. ε^{-1} term: $$\frac{\partial}{\partial y_j} S_{ij}^{0}(\mathbf{x}, \mathbf{y}) + \frac{\partial}{\partial y_j} S_{ij}^{1}(\mathbf{x}, \mathbf{y}) - \frac{\partial}{\partial y_j} p_{ij}^{0}\left(\mathbf{x}, \mathbf{y}, T^0\right) = 0 \tag{5.9}$$

This differential system is linear in $\mathbf{y}$. Its solution is composed of the global solution: $\mathbf{u}^1(\mathbf{x}, \mathbf{y}) = \overline{\mathbf{u}}^1(\mathbf{x})$ of the homogeneous system plus a special solution of type

$$u_i^1(\mathbf{x}, \mathbf{y}) = -\zeta_{\mathrm{i}}^{\mathrm{rs}}(\mathbf{y}) E_{\mathrm{rs}}^{0}(\mathbf{x}) + \psi_i(\mathbf{y}) \tag{5.10}$$

where $\zeta^{\mathrm{rs}} = \left[\zeta_{\mathrm{x}}^{\mathrm{rs}}, \zeta_{\mathrm{y}}^{\mathrm{rs}}, \zeta_{\mathrm{z}}^{\mathrm{rs}}\right]$ with $\mathrm{rs} = xx, yy, zz, xy, xz, yz$ are periodic microscopic displacement fields induced by the initial strains E_{rs}^{0} [20]. Furthermore, $\psi(\mathrm{y})$ are microscopic displacements generated by the eigenstress p_{ij}^{0} due to thermal expansion and/or volume changes of the material phases.

The special solution (Eq. (5.10)) is introduced into the system (Eq. (5.9)). Then, the initial uniform strains $E_{\mathrm{rs}}^{0}(\mathbf{x})$ are extracted from this system, leading to

$$\begin{aligned} E_{\mathrm{rs}}^{0}(\mathbf{x}) & \left[\frac{\partial H_{ijrs}\left(\mathbf{y}, T^0\right)}{\partial y_j} - \frac{\partial\left[H_{ijkl}\left(\mathbf{y}, T^0\right)\left(e_{kl}\left(\zeta^{\mathrm{rs}}\right) + e_{kl}(\psi)\right)\right]}{\partial y_j}\right] \\ & + \frac{\partial p_{ij}^{0}\left(\mathbf{x}, \mathbf{y}, T^0\right)}{\partial y_j} = 0 \end{aligned} \tag{5.11}$$

As the initial strains and generalized eigenstrains can be specified on the unit cell separately, the modified system (Eq. (5.11)) can be split into

$$\begin{aligned} \frac{\partial}{\partial y_j} H_{ijrs}\left(\mathbf{y}, T^0\right) &= \frac{\partial}{\partial y_j}\left[H_{ijkl}\left(\mathbf{y}, T^0\right) e_{kl}\left(\zeta^{\mathrm{rs}}\right)\right] \\ \frac{\partial}{\partial y_j} p_{ij}^{0}\left(\mathbf{x}, \mathbf{y}, T^0\right) &= \frac{\partial}{\partial y_j}\left[H_{ijkl}\left(\mathbf{y}, T^0\right) e_{kl}(\psi)\right] \end{aligned} \tag{5.12}$$

A variational formulation is applied to both systems (Eq. (5.12)) in order to determine the unknown displacement fields ζ^{rs} and ψ. This formulation is summarized in Ref. [20]. Then, the 3D RVE of the heterogeneous material is discretized by linear isoparametric volume elements, leading to following linearized systems in the nodal values $\mathbf{Z}^{\mathrm{rs}}$ and Ψ of the unknown displacement fields ζ^{rs} and ψ:

$$\begin{aligned}\mathbf{K}\left(T^0\right)\times\mathbf{Z}^{\mathrm{rs}} &= \mathbf{g}_{rs}^{\mathrm{im,H}}\left(T^0\right)+\mathbf{g}_{\mathrm{rs}}^{\Delta T,H}\left(T^0\right)\\ \mathbf{K}\left(T^0\right)\times\mathbf{\Psi} &= \mathbf{g}^{\mathrm{im,p}}\left(T^0\right)+\mathbf{g}^{\Delta T,\mathrm{p}}\end{aligned} \tag{5.13}$$

where

- $\mathbf{K}(T^0)$ is the classic elastic stiffness matrix;
- $\mathbf{g}^{\mathrm{im,H}}$ and $\mathbf{g}^{\mathrm{im,p}}$ are implicit surface tensions, which are induced by the jump of either the Hooke matrix or the eigenstress at the phase interfaces;
- $\mathbf{g}^{\Delta T,H}$ and $\mathbf{g}^{\Delta T,\mathrm{p}}$ are implicit body forces, which are induced by the temperature dependence of either the Hooke matrix or the eigenstress in each phase of the RVE.

3. ε^0 term: The solution of the ε^0 term leads to the definition of following effective thermoelastic properties of the heterogeneous material:

- Effective Hooke matrix:

$$H_{ijkl}^{\mathrm{hom}}\left(T^0\right)=\frac{1}{|Y|}\int_Y\left[H_{ijkl}\left(\mathbf{y},T^0\right)-H_{ijrs}\left(\mathbf{y},T^0\right)e_{\mathrm{rs}}(\zeta^{\mathrm{rs}})\right]\mathrm{d}\,y \tag{5.14}$$

- Effective eigenstress:

$$p_{ij}^{\mathrm{hom}}\left(T^0\right)=\frac{1}{|Y|}\int_Y\left[p_{ij}\left(\mathbf{y},T^0\right)-H_{ijrs}\left(\mathbf{y},T^0\right)e_{\mathrm{rs}}\left(\Psi\right)\right]\mathrm{d}\,y \tag{5.15}$$

where |Y| is the volume of the RVE.

The generalized effective eigenstrains $\kappa_{ij}^{*,\mathrm{hom}}$ are obtained easily by inverting the relation:

$$p_{ij}^{\mathrm{hom}}=H_{ijkl}^{\mathrm{hom}}\kappa_{ij}^{*,\mathrm{hom}}=H_{ijkl}^{\mathrm{hom}}\left[\alpha_{ij}^{\mathrm{hom}}+\kappa_{ij}^{\mathrm{hom}}\right] \tag{5.16}$$

Relation (Eq. (5.16)) is expressed for $\Delta T = 1$ K and cannot simultaneously provide the effective thermal expansion coefficients $\alpha_{ij}^{\mathrm{hom}}$ and the effective transformation strains $\kappa_{ij}^{\mathrm{hom}}$. Two homogenization runs with HOMAT ([18], see HOMAT in Section 5.7.1) are needed: one including the volumetric strain κ_{ij} and one without it.

Finally, in order to get the effective engineering properties, the predicted Hooke matrix is made symmetric and then inverted. From the effective flexibility matrix S_{ijkl}^{hom}, the orthotropic Young modulus (E_x, E_y, and E_z), shear modulus (G_{xy}, G_{xz}, and G_{yz}), and the Poisson coefficients (ν_{xy}, ν_{xz}, and ν_{yz}) can be derived. In the special case of a quasi-cubic global behavior, not only the effective Young modulus,

shear modulus, and the Poisson coefficient ν but also the quantity μ^*, which is a measure for the degree of cubic anisotropy, can be extracted [2]:

$$\mu^* = H_{11} - 2H_{44} - H_{12} \tag{5.17}$$

5.3 Homogenization of Materials with Random Microstructure

For heterogeneous materials with random microstructure (Figure 5.5), the definition of an RVE plays a central role in the derivation of their effective properties. Indeed, it is a delicate and not trivial task, compared to materials with a periodic microstructure, where the size of the RVE is defined by the periodicity of the microstructure. In contrast to periodic microstructures, at first, a sound description of *the morphology* of the random microstructure by statistical quantities is required, as outlined by Torquato [22]. For this purpose, the four Minkowski functionals can be used: the phase volume fraction f_i, its inner surface S_i, its mean curvature integral B_i, and the Euler–Poincarré characteristic χ_i, which measures the connectivity of the considered phase i. On the basis of these morphological descriptors, different estimates for the characteristic lengths of a geometrical unit cell, named *window*, are presented in the sections titled Two-Point Probability Functions and Spectral Analysis. Also, the location of the window affects the prediction of the effective properties of a material with random microstructure, as shown in Section 5.3.2. Several randomly extracted windows are then used in a statistical homogenization procedure, as detailed in Section 5.3.3, not only to evaluate the mean effective property and its variance but also to derive the RVE adequate to the considered physical property, for example, thermal conductivity (TC) or permeability.

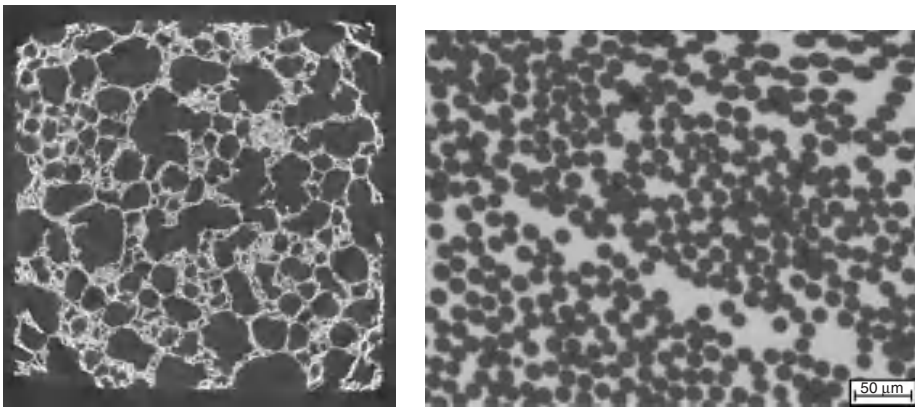

(a) (b)

Figure 5.5 2D sections of heterogeneous materials with random microstructures: (a) an open-cell metallic foam, made of iron powder, and (b) a roving of Al_2O_3 fibers being infiltrated by an aluminum alloy ($AlZn_6$).

5.3.1 Morphology Analysis and Definition of the RVE

In order to describe a random microstructure/morphology of a heterogeneous material, a characteristic function, named *phase indicator function* $\varphi_i(\mathbf{x})$ is introduced. $\mathbf{x}$ defines the position in the material with random microstructure. The volume fractions f_i of the different phases Φ_i expressed by

$$f_i = \frac{V(\Phi_i)}{V} = \frac{\int \varphi_i(\mathbf{x})\, \mathrm{d}\, V}{V} = \langle \varphi_i(\mathbf{x}) \rangle \tag{5.18}$$

correspond to the mean value of the phase indicator function. Note that the porosity P of a porous material is a special case of the volume fraction definition for a two-phase material. In order to describe the geometrical scattering within the microstructure, the covariance between two points, $\mathbf{x}$ and $\mathbf{x} + \mathbf{h}$, of the microstructure is evaluated. It expresses the probability that these two points belong to the same phase. On the basis of this covariance, it is possible to define a *geometrical correlation function* [23]:

$$R_P(u) = \frac{\langle [\varphi(\mathbf{x}) - P]\, [\varphi(\mathbf{x} + \mathbf{u}) - P] \rangle}{P - P^2} \tag{5.19}$$

where

- the denominator $P - P^2$ is the variance of $\varphi(\mathbf{x})$;
- u is the norm of the translation $\mathbf{u}$.

Note: Such a translation can be specified parallel to the x, y, and z directions, leading to the definition of R_{P_x}, R_{P_y}, and R_{P_z}, respectively.

Finally, the searched *characteristic length* of the microstructure, expressed in the x, y, and z directions, can be calculated by making the integral of the geometrical correlation functions R_{P_x}, R_{P_y}, and R_{P_z} over the whole domain:

$$C_x = \int_0^{L_x} R_{P_x}(x)\, \mathrm{d}\, x; \quad C_y = \int_0^{L_y} R_{P_y}(y)\, \mathrm{d}\, y; \quad C_z = \int_0^{L_z} R_{P_z}(z)\, \mathrm{d}\, z \tag{5.20}$$

where L_x, L_y, and L_z are the lengths of the material in the x, y, and z directions, respectively.

These characteristic lengths are a good measure of the random microstructure. Kanit *et al.* [23] and Borbely *et al.* [24] used these characteristic lengths to specify the smallest possible dimensions of their initial guess of the RVE size. The following two methods have been selected in order to evaluate these characteristic lengths:

- the two-point probability function [22, 24];
- the spectral analysis [25, 26].

Two-Point Probability Functions The two-point probability functions s_2^{mm}, s_2^{pp}, and s_2^{mp} are evaluated numerically by the random generation of a large number of points ($>10^6$) in x, y, and z directions, respectively. The indices m and p in

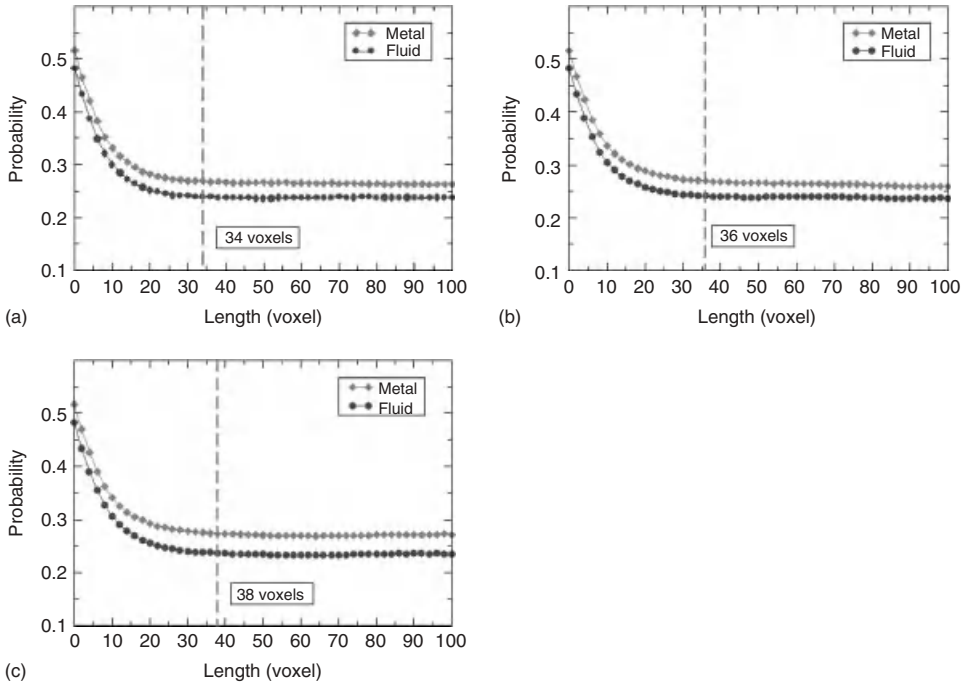

Figure 5.6 Two-point probability functions s_2^{pp} and s_2^{mm} in the *x*, *y*, and *z* directions of an Inconel 625 foam (P = 44.6%). These functions reach their limit after (a) 34, (b) 36, and (c) 38voxels, respectively (1 voxel = 22 µm).

general stand for two different phases such as *metal* (m) and *pore* (p) or *matrix* (m) and *precipitate* (p). Without the loss of generality, the following explanations are given for a porous metal. Thus, for a porous metal, s_2^{pp} specifies the probability that both points are void nodes and s_2^{mm} the probability that both points are in the metal, whereas s_2^{mp} expresses the probability that one point is in the metal and the other is in a void. The smallest point distance at which these probability functions reach their limit value defines the searched correlation length [24] (Figure 5.6).

Spectral Analysis For the determination of the characteristic length by spectral analysis, the random microstructure is first digitalized, for example, by identifying several cross sections from a 3D computed tomography (CT) scan of the foam being depicted in Figure 5.5 or from 2D metallographic sections. Subsequently, path lines are defined over the respective digitalized 2D sections (Figure 5.7a) [25].

A phase function $\varphi(s)$ is then defined along the considered path *s*, with $s = x$, *y*, or *z*. In the case of a two-phase material, this function has the value 1 in the black areas and 0 in the white ones. Note that usually more than five phase functions are

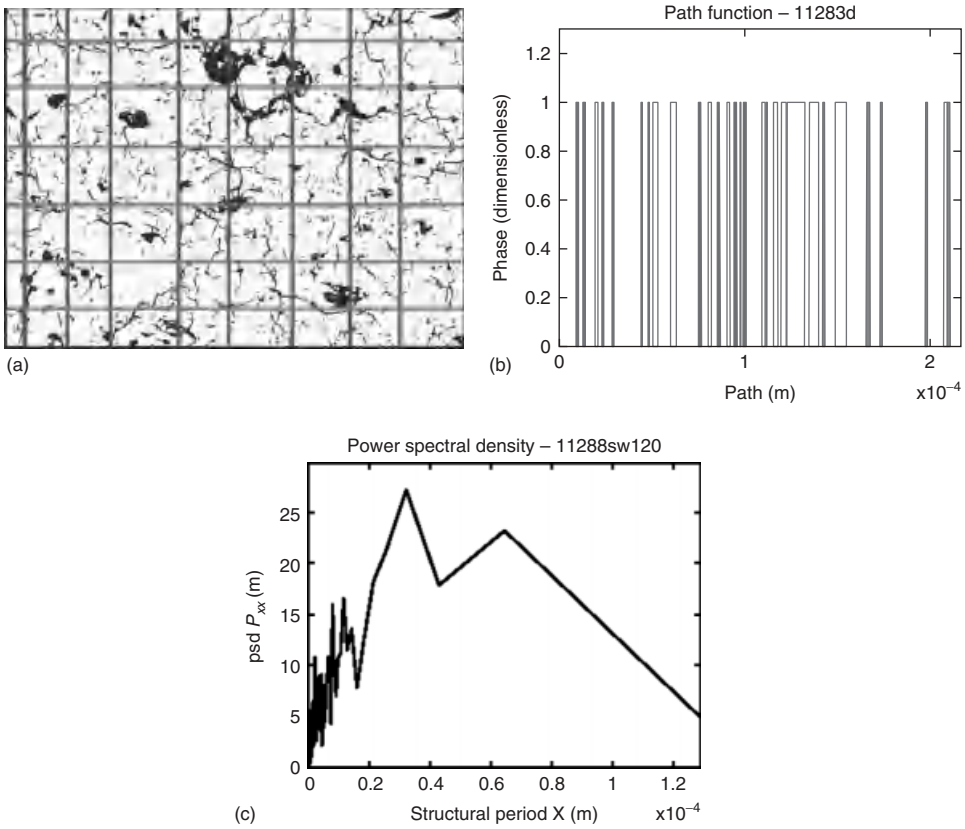

Figure 5.7 Digitalized image of (a) a thermally sprayed TBC with 1D path lines in *X* and *Y* directions, (b) the path function, and (c) the corresponding the power spectral density.

specified in each 2D cross section of a CT scan, parallel to the considered structural direction.

The spectral analysis was primarily carried out for materials with random microstructure by Bobzin *et al.* [25]. The autocorrelation function $R_{xx}(\sigma)$ of the phase function φ is then expressed by

$$R_{xx}(\sigma) = \lim_{s \to \infty} \frac{1}{S} \int_0^{L_s} \varphi(s)\varphi(s+\sigma)\,\mathrm{d}\,s \tag{5.21}$$

where s and σ are spatial coordinates and L_s is the 1D path length.

The power spectral density (psd) function then is eventually defined as the Fourier transform of the autocorrelation function (Eq. (5.21))

$$S_{xx}\left(f_s\right) = \int_{-\infty}^{\infty} R_{xx}(\sigma) e^{-i2\pi f \sigma}\,\mathrm{d}\,\sigma \tag{5.22}$$

where f_s is the structural frequency in (m^{-1}). This frequency is the reciprocal of the period C_x, C_y, or C_z.

The psd function $S_{xx}(f_s)$ is evaluated in order to detect its large peaks, which represent dominant periods in the structure. The path length s in Eqs. (5.21) and (5.22) is assumed to be infinite. The discretized psd function for a limited path length is estimated by Kammeyer and Koschel [27]:

$$S_{xx}(f_s) = \frac{1}{L_x} \left| \xi(f_s, L_x) \right|^2 \tag{5.23}$$

with $\xi(f_s, L_s)$, the discrete Fourier transform of the phase function $\varphi(s)$ given by

$$\xi(f_s, L_x) = \int_0^{L_x} \varphi(s) e^{i2\pi f_s L_S} \, \mathrm{d}\, s \tag{5.24}$$

The psd, corresponding to the path line of Figure 5.7b, is represented in Figure 5.7c. The large peak at 0.032 mm can be considered as the dominant contribution for this path line. However, the location of this psd peak varies for different paths within a digitalized image. Thus, an averaging over all specified path lines per 2D image is performed in order to get the desired period in each structural direction. This mean value itself is again averaged over the defined cross sections per structural direction to get the characteristic lengths for a geometrical unit cell of the random material. This method has been applied successfully to different open-cell metallic foams, with examples for the mean psd profiles in the directions x, y, and z shown in Figure 5.8.

5.3.2
Influence of the RVE Position on the Effective Elastic Properties

Subsequent to the elaboration of estimates for the *size* of the RVE, the *position* of the RVE may reveal further effects on the effective properties of materials with random microstructure. To evaluate these effects again a ceramic coating produced by air plasma spraying (APS) is used as an example. This material is characterized by a high porosity level and by microcracks (Figure 5.9). To

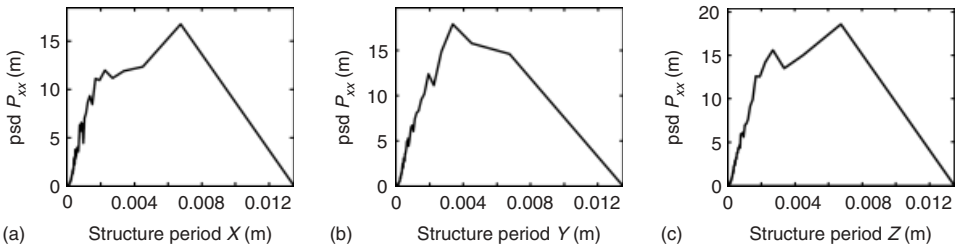

Figure 5.8 Mean power spectral density in the (a) x, (b) y, and (c) z direction for an Inconel foam [26, 28]. The deduced characteristic lengths for the RVE are $C_x = 6.68$ mm, $C_y = 3.4$ mm, and $C_z = 6.66$ mm.

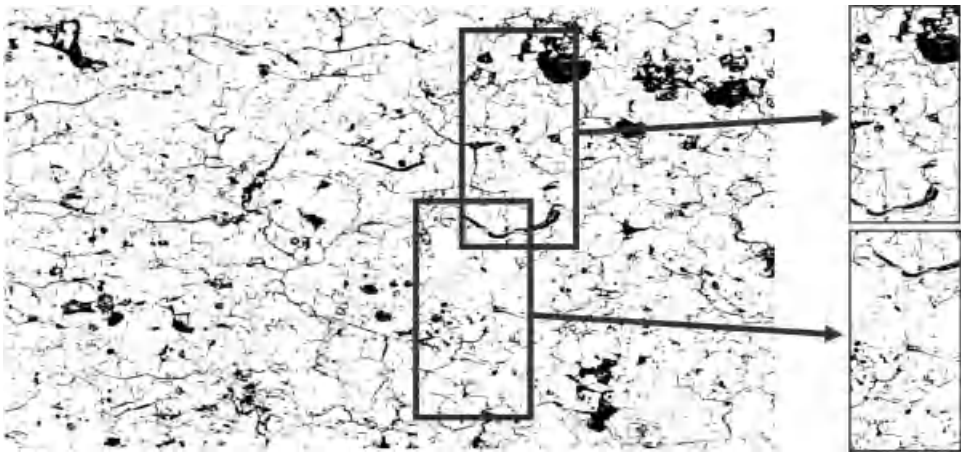

Figure 5.9 Segmented SEM image of the APS coating (porosity = 25.4%) and two extracted RVEs with maximal and minimal porosities.

determine its effective elastic properties, the scanning electron microscopic (SEM) photograph is, at first, binarized with an appropriate threshold. Hence, two distinguished phases, the ceramic phase and the pores, are identified. The 1D spectral analysis method, as outlined in the section Spectral Analysis, is then applied in both directions in order to specify the characteristic lengths of the RVE yielding, for example, $L_X = 32.03\ \mu m$ and $L_Y = 64.42\ \mu m$ for the specific example. Volumes with this size being extracted from the real microstructure are not periodic [29]. However, as outlined in Section 5.3.3, periodic boundary conditions (BCs) are the most suitable ones and are thus applied here in a weak sense: only nodes belonging to the same phase are linked together. Note that the AHM requires a fictive Young modulus for the void phase. A detailed study by Bobzin *et al.* [30] reveals that $E_{void} = 50\ MPa$ is an appropriate value and provides a large contrast to the modulus of the ceramic ($E_{cer} = 220\ GPa$).

To elaborate the dependency of the effective Young modulus on the RVE position, 50 RVEs of identical size corresponding to the characteristic lengths as specified by spectral analysis ($32.03 \times 64.42\ \mu m^2$) are extracted randomly from the digitalized image of the microstructure. The RVEs with minimal (21%) and maximal (25.5%) porosity provide $E^{eff} = 126$ and $111\ GPa$, respectively. The entire dependency of the effective Young modulus with the RVE position is shown in Figure 5.10a and the porosity distribution in Figure 5.10b. This distribution is characterized by the mean value of 121 GPa and a standard deviation of 3.8 GPa. Globally, one can say that both distributions are related: RVEs with larger porosity have lower effective Young's modulus and vice versa. But, not all RVEs with similar porosity present the same E^{eff}. Indeed, the shape of the voids affects the results noticeably. Note that a nonlinear dependency of E^{eff} on the porosity is observed, which differs strongly from the classical mixture rule.

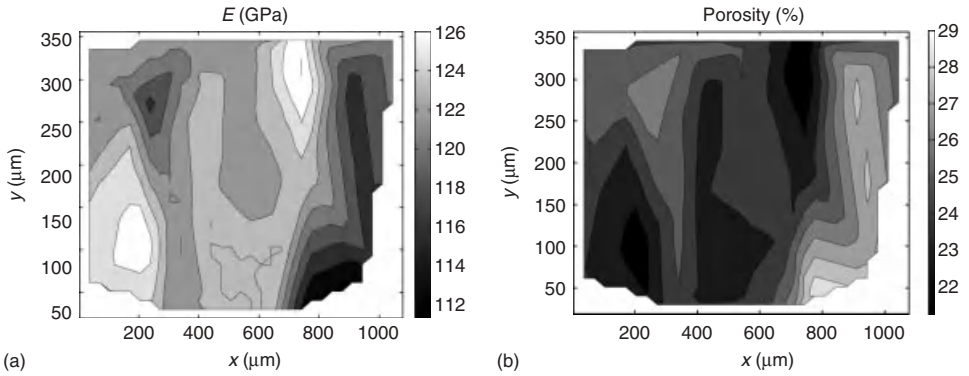

Figure 5.10 Distribution of (a) the effective Young modulus and (b) the porosity of 50 randomly extracted RVEs of the APS sample.

5.3.3 Stochastic Homogenization

On the basis of the extraction of multiple RVEs, a novel procedure for *stochastic homogenization* of materials with random microstructure has been developed recently [31]. This scheme involves the following steps:

1) The characteristic lengths, determined either by spectral analysis or via the two-point probability functions, specify the dimensions of the first guess of the RVE.
2) Then, M volumes with this geometrical extension are extracted from the heterogeneous material via a Monte Carlo ansatz. In order to realize an efficient stochastic homogenization scheme, the morphology of each extracted volume is analyzed by the evaluation of the four Minkowski functionals via the Michielsen formalism [32]. These mean statistical quantities are the phase volume fraction, the inner surface, a mean curvature integral, and the Euler–Poicarré norm. The last norm gives a measure of the connectivity of the phase such as the pore volume in a foam. These quantities allow the selection of N volumes from the M initial ones with a volume fraction, for example, close to the mean volume fraction.
3) To reduce the mesh dimension of each extracted volume, a dedicated mesh generation tool has been written. This program joins $l \times m \times n$ voxels to one linear hexahedron element [26].
4) The AHM is then applied to evaluate the effective mechanical and thermal properties or the permeability of each extracted volume. As the extracted volumes are nonperiodic, it is a delicate task to apply self-consistent BCs. Kanit *et al.* [23] have shown that compared to kinematic uniform BC and static uniform BC, periodic BC applied to a material with a random microstructure yields effective values varying less with the unit cell size (Figure 5.11). Therefore,

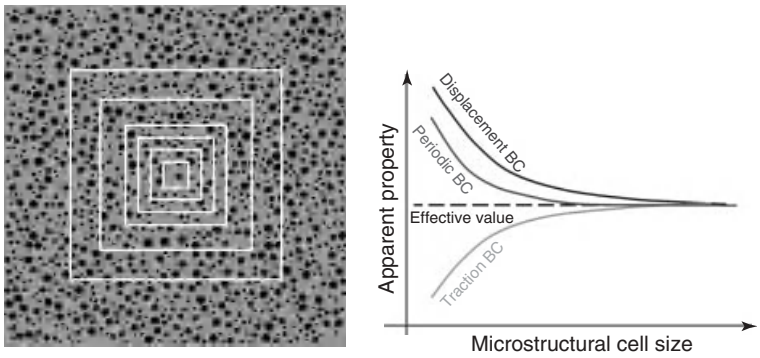

Figure 5.11 Influence of extracted window size and the applied boundary conditions on effective property of a material with random microstructure [34].

periodic BCs have been applied *in a weak form*: only nodes, whose projection belongs to the same phase, are linked periodically.

5) Using the effective properties G_N^{eff} of the N extracted volumes, their mean effective property $\overline{G}_N^{\text{eff}}$ and the variance σ_N^2 are evaluated. In order to be sure that the calculated mean effective property is accurate and to know how many volumes are needed to reach this accuracy, the confidence interval theory [33] is applied. For a given risk (e.g., $r = 5\%$) and a desired precision ε^*, the confidence interval CI_N is expressed as

$$\text{CI}_N = \overline{G}_N^{\text{eff}} \pm z_{1-r/2} \frac{s}{\sqrt{N}} \tag{5.25}$$

where

- $s^2 = \left(\sum_i^N \left(G_i^{\text{eff}} - \overline{G}_N^{\text{eff}} \right)^2 \right) \Big/ (N-1)$ is an approximation of the variance of the mean effective property $\overline{G}_N^{\text{eff}}$;
- $z_{1-r/2}$ is the value of the normal distribution whose probability density function F gives the confidence $1 - r/2$. For $r = 5\%$, we have $F(z_{1-r/2}) = 0.975$ with $z_{1-r/2} = 1.96$.

As $N \geq 30$, the effective properties G_N^{eff} follow a Gaussian normal distribution in accordance with the central limit theorem. From this, it follows that the half confidence interval CI_N exhibits the following relative error:

$$\varepsilon_{\text{rel}} = z_{1-r/2} \frac{s}{\overline{G}_N^{\text{eff}} \sqrt{N}} \tag{5.26}$$

As yet the precision ε^* is desired, we have

$$N \geq z_{1-r/2}^2 \frac{s^2}{\overline{G}_N^{\text{eff},2} \varepsilon^{*,2}} \tag{5.27}$$

Inequality (Eq. (5.27)) is essential. It specifies the minimum number, N, of samples (=extracted unit cells) required in order to evaluate, for a given precision ε^*, the mean effective property of the heterogeneous material within the desired confidence interval. If the required precision is reached, the actual dimensions of the extracted volume specify the searched *physical RVE*. Otherwise, either the number of sampling, N, or the size of the extracted volume must be increased. In the latter case, the statistical procedure restarts again at point 2) until the desired precision ε^* is reached. *The physical RVE size definition thus is a postprocessing result of the developed stochastic homogenization procedure.*

Moreover, as outlined by Trias *et al.* [35] and Kanit *et al.* [23], the RVE size depends on the considered physical property and on their mismatch on the microstructure. Indeed, a larger volume size is required for a composite with a strong property mismatch, such as carbon-fiber-reinforced plastics, than those with less mismatch and for the determination of an effective damage parameter than for the effective elasticity modulus. These results confirm Torquato's assumption [22] that classes of physical properties exist:

- **Class A**: thermal and electric conductivity, diffusion coefficient;
- **Class B**: elasticity modulus, viscosity parameter;
- **Class C**: permeability and sedimentation rate.

Each class requires an own RVE definition. For example, because of the strong influence of the connectivity of the pores and their tortuosity, the permeability prediction of a porous material requires a larger RVE than the prediction of its effective thermal conductivity.

5.4 Postprocessing of Macroscale Results: the Localization Step

Coupling to the macroscale simulation is realized by a localization step comprising the evaluation of the microstrains and microstresses on the RVE. The thermoelastic analysis using effective properties on the macroscale allows the evaluation of macrostrains and macrostresses in the sample and the tools. In regions with high stress concentrations, it is also important to know accurately the microstress and microstrain levels on the RVE. Indeed, they are needed to predict damage and/or failure initiation criteria on the RVE and to localize critical zones of the microstructure (Figure 5.12).

Therefore, at selected load increments, the macrostress and macrostrain states are extracted and transferred to the RVE, where they specify the BCs. In the framework of the AHM (Section 5.2.3), the asymptotic development of the displacement field (Eq. (5.5)) is introduced in the total strain expression:

$$\varepsilon_{ij}^{h}(\mathbf{z}) \approx \varepsilon_{ij}(\mathbf{x},\mathbf{y}) = \varepsilon^{-1} e_{ij}^{0}\left(\mathbf{u}^{0}\right) + \left[E_{ij}^{0}\left(\mathbf{u}^{0}\right) + e_{ij}^{1}\left(\mathbf{u}^{1}\right)\right] + 0(\varepsilon) \tag{5.28}$$

where $E_{ij}(\mathbf{x},\mathbf{y}) = 1/2\left[\left(\partial u_i/\partial x_j\right) + \left(\partial u_j/\partial x_i\right)\right]$ and $e_{ij}(\mathbf{x},\mathbf{y}) = 1/2\left[\left(\partial u_i/\partial y_j\right) + \left(\partial u_j/\partial y_i\right)\right]$ are the macro- and microstrains, respectively.

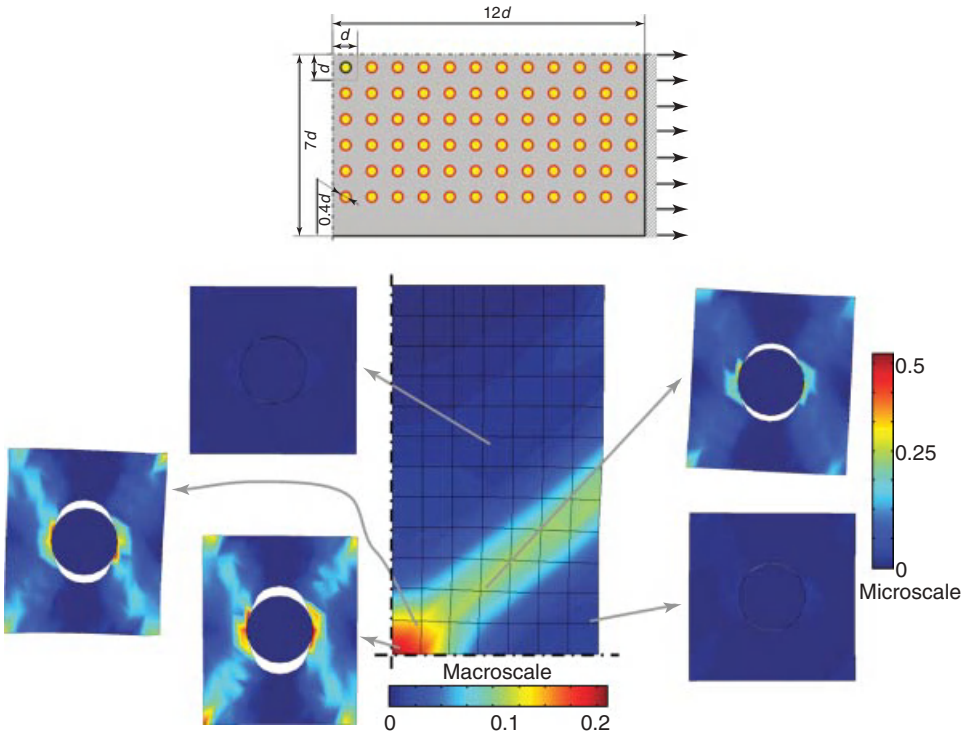

Figure 5.12 Composite plate under uniaxial tensile loading: strain localization due to damaging microstructure [12].

The special solution (Eq. (5.10)) for the displacement term $\mathbf{u}^1(\mathbf{x},\mathbf{y})$ allows to transform expression (Eq. (5.28)):

$$\varepsilon_{ij}(\mathbf{x},\mathbf{y}) = E^0_{ij}\left(\mathbf{u}^0\right) - e_{ij}\left(\zeta^{\mathrm{rs}}\right) E^0_{\mathrm{rs}}\left(\mathbf{u}^0\right) + e_{ij}(\psi) \tag{5.29}$$

This expression specifies the total microstrains in the RVE for the given macrostrains $E^0_{ij}(\mathbf{x})$. Similarly, by taking into account the definitions (Eq. (5.7)) of the macro- and microstresses, S_{ij} and s_{ij}, and the eigenstress $p^0_{ij}\left(\mathbf{x},\mathbf{y},T^0\right)$, the increment of microscopic stresses is given by

$$\Delta\sigma_{ij}(\mathbf{x},\mathbf{y}) = \Delta S^0_{ij} + \Delta s^1_{ij} - H_{ijkl}\left(\mathbf{y},T^0_* + \Delta T^0\right)\left[\Delta\varepsilon^{th}_{kl} + \Delta\kappa_{kl} + \Delta\varepsilon^H_{kl}\right] \tag{5.30}$$

where

$\Delta\varepsilon^H_{ij}(\mathbf{x},\mathbf{y}) = [H^{-1}_{ijkl}(\mathbf{y},T^0_* + \Delta T^0) - H^{-1}_{ijkl}(\mathbf{y},T^0_*)]\sigma^*_{kl}(\mathbf{x},\mathbf{y})$ specifies the strain increment induced by the variation of the Hooke matrix with the temperature;
T^0_* and σ^*_{ij} are the initial temperature and microstress state, respectively.

On the basis of these local stress/strain results on the RVE, material-dependent failure criteria can be applied in order to localize failure initiation in the heterogeneous material's microstructure at a specific load level.

5.5
Dedicated Homogenization Model: Two-Level Radial Homogenization of Semicrystalline Thermoplastics

Beyond the general homogenization schemes detailed above, a dedicated and newly developed two-level homogenization model for semicrystalline thermoplastics is presented briefly here in view of its relevance to one of the platform test cases (Chapter 10). Injection-molded semicrystalline thermoplastics are built at the microscale by an agglomeration of spherulites. Each spherulite grows from its monocrystal center radially and consists of lamellas of crystalline phase surrounded by amorphous molecules (Figure 5.13). Each crystalline lamella itself corresponds to a folded molecular chain. It is well known that the isotactic polypropylene (i-PP) has a helicoidal chain. The homogenization of an i-PP spherulite is delicate as the amorphous and crystalline phases are not separable. Moreover, it is not possible to produce bulk specimens of pure crystalline and pure amorphous phases. Therefore, an individual characterization of the properties of these individual phases at room temperature is impossible.

5.5.1
Mechanical Properties of the Amorphous and Crystalline Phases

In order to get the mechanical properties of the amorphous phase, Bédoui *et al.* [36] assume this phase to be *isotropic* and in a *rubbery state* at room temperature. The shear modulus at plateau G is related to the molecular mass between entanglements M_e by $G_{amorph} = \rho RT/M_e$, where ρ is the amorphous phase density, T the temperature, and R the ideal gas constant. The value M_e is set to 7 kg mol^{-1}. This leads to $G_{amorph} = 0.3$ MPa and consequently $E_{amorph} = 0.9$ MPa. Thus, the amorphous phase is quasi-incompressible with a Poisson coefficient of $\nu = 0.49993$.

The mechanical properties of the crystalline phase required for the homogenization scheme are deduced from *theoretical ab initio* calculations [37] and X-ray diffraction measurements [38]. The combination of these results leads, as outlined in to the specification of a highly anisotropic and monoclinic Hooke matrix for the crystalline phase. Indeed, this phase presents only a single symmetry plane

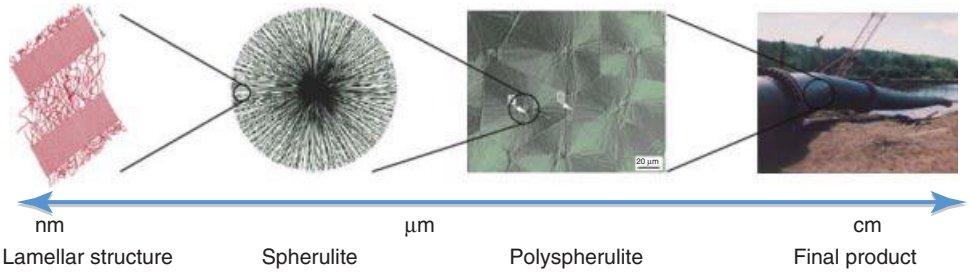

Figure 5.13 Structures of a semicrystalline thermoplastic at different length scales.

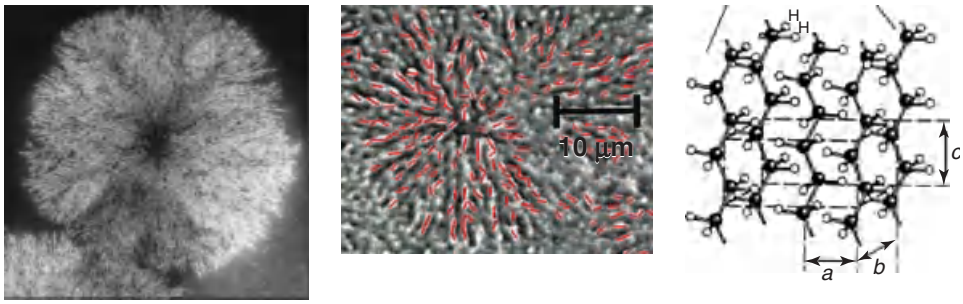

(a) (b) (c)

Figure 5.14 (a) 3D spherulite observed by atomic force microscopy (AFM); (b) lamellae in an isotactic PP spherulite [36]; and (c) the dimensions a, b, and c of the crystalline monobloc at the atom scale.

perpendicular to the molecular chain (direction c in Figure 5.14c) and the Young's modulus in the chain direction, E_c, is very high.

However, these are properties of the *mono-crystalline* i-PP. But, in spherulites and even in ultrahigh strength drawn PP films, there always exists an interface with tied amorphous molecules, as shown by Kamazewa *et al.* [39]. Thus, their Young's modulus differs from the monocrystal chain one and ultrahigh strength films are not purely crystalline. Therefore, based on the measurements of Sawatari and Matsuo [38], two variants of the chain Young modulus E_c have been introduced ($E_c = 21.24\,\text{GPa}$ (mean value) and $E_c = 17.57\,\text{GPa}$ (minimum value). Effects of the measurement uncertainties on the chain Young modulus are thus taken into account in the developed homogenization procedure.

Two-Level Homogenization Scheme A spherulite essentially is a radial distribution of crystalline lamellae and of amorphous molecules between them (Figure 5.14). This distribution is quasi radial around its monocrystal nucleus/center. Therefore, we introduce the following two-level homogenization scheme for semicrystalline thermoplastics such as i-PP:

- **Nanoscale**: homogenization of the individual bilamina formed by the crystalline phase and the amorphous layer;
- **Microscale**: homogenization of the spherulite by assuming a radial distribution of equivalent bilamina around its monocrystal center.

Homogenization of the Bilamina at the Nanoscale On the basis of the observations of Bédoui *et al.* [36], the geometry of the bilamina unit cell is specified (Figure 5.15). As the mean length is much smaller than the spherulite diameter, the lamellas are surrounded by tied amorphous molecules. To model this situation, Doyle [40] introduces an axisymmetric unit cell, characterized by the aspect ratio b/L (Figure 5.16). As the measurements of the degree of crystallinity via differential scanning calorimetry (DSC) provide a mean value

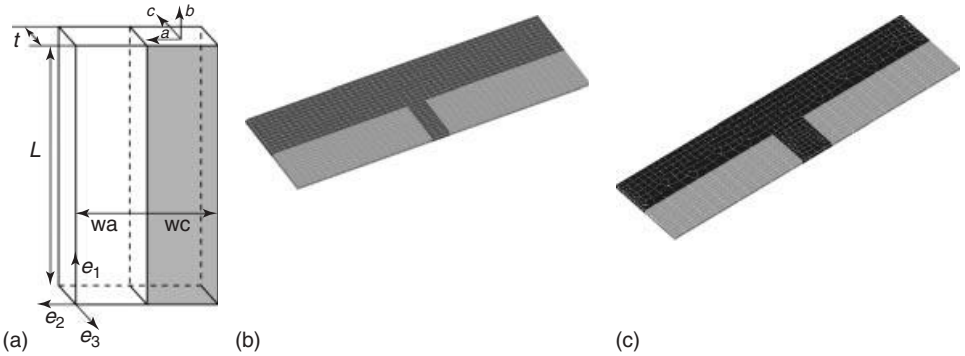

Figure 5.15 Bilamina of amorphous (dark area) and crystalline phase (light area), the definition of the local axis system and the crystallographic one (a). The definition of the local axis system and the crystallographic one; (b) first bilamina design variant, VAR1, with $b = 6\,\text{nm}$ and $L = 900\,\text{nm}$, leading to $b/L = 0.0667$; and (c) second variant VAR2 with $b = 10\,\text{nm}$, $L = 860\,\text{nm}$, and $b/L = 0.1163$.

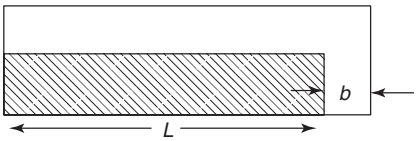

Figure 5.16 Axisymmetric bilamina unit cell defined by Doyle [40]. The dark crystalline phase is surrounded by tied amorphous molecules.

without any information about the bilamina design, two new designs are introduced at the crystalline degree $\kappa = 45\%$ (Figure 5.15). The homogenization results for the three bilamina designs and the mean Sawatari model are discussed in Chapter 10 (Section 10.7.3.2).

3D Radial Spherulite Model at the Microscale The effective bilamina is distributed radially around the spherulite center in practice as follows: in each Gauss point of the spherulite FE discretization, the normalized vector $\vec{G} - \vec{C}$ is expressed (Figure 5.17). It defines the growth direction of the crystalline lamella and corresponds to the $\vec{e}_1$ direction of the local bilamina axes (Figure 5.15a).

As currently no reliable information exists on how the crystalline lamella is oriented in the plane perpendicular to its growth direction, *a random distribution* is assumed there. Thus, the unitary basis vectors $\vec{e}_2$ and $\vec{e}_3$ are defined randomly in this plane. In each Gauss point, a rotation matrix between local and global axis system is expressed. This matrix then allows the rotation of the effective Hooke matrix of the bilamina in the structural axis system. As the bilamina orientation differs in each Gauss point, additional implicit volume forces are generated in each spherulite (Eq. (5.13)). These forces are added to the implicit forces generated by the

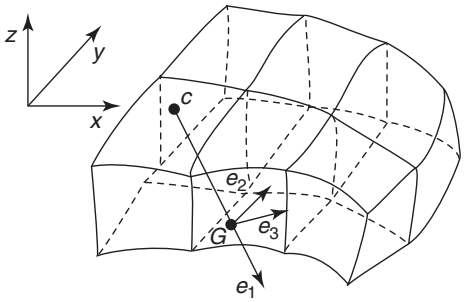

Figure 5.17 Definition of the local bilamina axis system $\vec{e}_1, \vec{e}_2$, and $\vec{e}_3$ in a spherulite Gauss point.

property discontinuity at the boundaries of the spherulite classes. Such spherulite classes with the same elastic properties are introduced in Section 10.4.3 in order to reduce the computational time. Results of this new 3D radial spherulite model are outlined in Section 10.7 where the multiscale modeling of an injection molded i-PP plate is presented.

5.6 Virtual Material Testing

Apart from the mathematical homogenization methods described in the previous sections, the use of virtual testing methods is widely used to determine the mechanical properties of heterogeneous microstructures. These methods imitate mechanical testing methods. The description of the geometry of the microstructure on the microscale may originate from metallurgical image analysis, from phase-field methods, from cellular automata simulations, or may be an artificially created synthetic microstructure. The most common application of virtual testing is the uniaxial tensile test on an RVE in order to determine the effective elastoplastic properties of a heterogeneous microstructure based on the known mechanical properties of the individual phases (Figure 5.18).

The application of the virtual testing methods is straightforward:

- The geometrical description of the microstructure is discretized numerically using FE or finite difference methods.
- The materials model and its properties are specified for each constituting phase of the RVE. For example, they can be elastic, viscoelastic, elastoplastic, or viscoelastoplastic.
- Proper periodic BCs are imposed on the outer boundary of the RVE.
- All information is passed to a standard FE or finite difference solver in order to evaluate the response of the discretized microstructure to the applied loading. Here, the use of a displacement- or force-controlled loading history is distinguished.

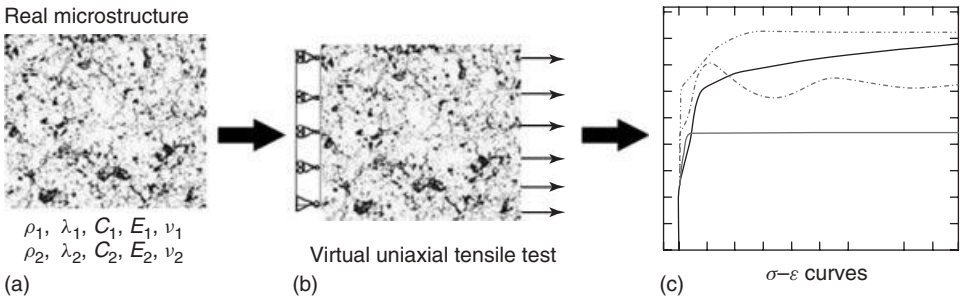

Figure 5.18 (a) RVE of a digitalized real microstructure containing two different phases (TBC and pores); (b) virtual uniaxial tensile test applied in the *x* direction on the RVE; and (c) the different inelastic stress–strain curves by tests in different directions.

The response of the RVE during the virtual test is used to determine the effective stress/strain curves or to identify other materials properties of the macroscopic materials model.

The above-described procedure can be coupled to optimization methods in order to identify an *optimal parameter* set of a complex macroscopic materials model [41].

5.7 Tools for the Determination of Effective Properties

The tools for determining effective properties of a heterogeneous material either by homogenization methods or by virtual testing are based on a defined description of the microstructure (i.e., the topology of the individual phases and their spatial distribution) and the properties of the individual phases. The strength of these methods is their possibility to consider orthotropic or anisotropic materials properties. The phase properties may be either given by *ab initio* calculations or provided by the models and/or databases. In this section, the implementation of the AHM (Section 5.7.1) and the program environment for virtual tests (Section 5.7.2) are outlined in the context of the ICME platform.

5.7.1 Homogenization Tool HOMAT and Its Preprocessor Mesh2Homat

The homogenization of a heterogeneous material starts with an accurate geometrical description of its complex microstructure. It can be either simulated directly by the multicomponent phase-field program MICRESS [42] or by the 3D cellular automata SphaeroSim for semicrystalline thermoplastics [43] or specified experimentally via 3D CT scans, SEM micrographs [30]. As mentioned in Section 5.2, the entire microstructure is not discretized at the microscale but only an RVE. For a material with periodic microstructure, its size is defined by the period, while for

materials with random microstructure, 1D spectral analysis or two-point probability functions are used to specify a first guess of the RVE size.

A unit cell with this extension is then extracted either randomly or in a deterministic way from the microstructure and enmeshed. To reduce the model size, several cells of MICRESS or SphaeroSim or voxels can be combined to one element. The homogenization method further requires the automatic generation of interface elements with zero thickness at the boundaries between grains, spherulite classes, or materials domains. These interface elements allow to calculate implicit forces induced by the discontinuity of the materials properties at these boundaries. To achieve this task, a dedicated program, named Mesh2Homat, is written.

Mesh2Homat The preprocessor Mesh2Homat in the first step reads the geometry of the unit cell. Three different input file formats are currently available: the standard platform exchange format VTK [44], the universal format of IDEAS, the Abaqus input format, and the MICRESS format, for which the possibility of reading the compressed grain information directly is retained.

This preprocessor automatically detects the interfaces between adjacent materials domains, grains, or spherulite classes and generates new nodes and the interface elements. It evaluates the outward normal to the free surfaces and defines the pair of periodic surfaces in function of the user specifications. Depending on the actual problem, 1D, 2D, or, per default, 3D periodic BCs can be specified on the unit cell. The microstructure solutions of MICRESS and SphaeroSim, available in the initial VTK format, are rewritten in a VTK file for the newly generated, unstructured grid of the unit cell. Eventually, Mesh2Homat exports the geometrical information for HOMAT into an ASCII file (*.hgeo) and generates a template of the HOMAT command file (*.hin). Note that the geometry file (*.hgeo) has an analogous structure as the input file of ABAQUS.

HOMAT The homogenization tool HOMAT [18], developed at ACCESS, uses asymptotic homogenization (Section 5.2.3) and allows the determination of the following effective properties:

- thermal conductivity, thermal capacity, and density;
- Darcy permeability;
- Hooke matrix, thermal expansion coefficients, Young and shear moduli, and Poisson coefficients.

This tool does not require any initial conditions except for an aerothermal homogenization. In this case, the stationary temperature and velocity fields on the unit cell are provided by the linked conjugate heat and fluid flow solver [18]. Only periodic BCs are specified. The tool evaluates microscopic periodic displacements on the unit cell, which are used to express the unknown effective properties (e.g., via Eq. (5.14)). Depending on the problem nature, up to 7 (thermomechanical) or 3 (thermal) boundary value problems, discretized by FEs, are solved on the

unit cell successively. For the mechanical homogenization, the rigid body modes are fixed automatically and the user can specify, if it is a 3D homogenization, a plane strain, or a plane stress one. The right-hand sides of these problems correspond to the materials discontinuities at the grain, spherulite, or materials boundaries plus the variation of the property inside each grain/domain (e.g., with the temperature or the orientation for spherulites). The evaluated effective properties of the unit cell are written in an ASCII file (*.hres) and in a *.mat file of ABAQUS type. Hence, the effective materials properties can be directly transferred to the macroscale simulation programs integrated into the ICME platform (ABAQUS, LARSTRAN, SYSWELD, etc). Moreover, for each right-hand side and component, the distributions of the implicit fluxes or forces and of the corresponding microscopic displacements on the unit cell are written in files of VTK type. These microscopic results can then be visualized with ParaView.

5.7.2 Program Environment for Virtual Testing

On the ICME platform, a programming environment for the automated evaluation of virtual tensile, shear, and compression tests has been realized [45]. The testing environment uses the discretized geometry of the microscale originating from phase-field simulations or metallurgical image analysis and creates a set of input files for the FE solvers ABAQUS or CASTS. These input files contain the description of the mesh, the definition of the phase morphology based on groups of FEs and the list of multipoint constraints for the definition of the periodic BCs. The description of the materials model and its parameters are read from a specific file for each phase. Thus, the choice of the materials model of the phase on the microscale is limited by the used solver and may be extended by the use of user materials subroutines, as described in Chapter 4. APython script automatically executes the virtual tests for each of the nine load cases (three tensile, three shear, and three compression), as shown in Figure 5.19 for either a force-controlled or a displacement-controlled setup. During the calculation, the script also evaluates the true stress versus true strain curves of the RVE by integrating the reaction forces on the RVE and the effective cross section of the deformed RVE configuration.

5.8 Examples

The following section gives some examples of the determination of effective material properties. First, the homogenization methods are compared based on a classical benchmark for composite materials with a periodic microstructure: a unidirectional (UD) glass fiber/epoxy composite. In Section 5.8.2, the variation of the effective thermoelastic and elastoplastic properties with the microstructure evolution during the austenite to ferrite phase transformation of low-carbon steel is presented. Eventually, the stochastic homogenization procedure is applied in

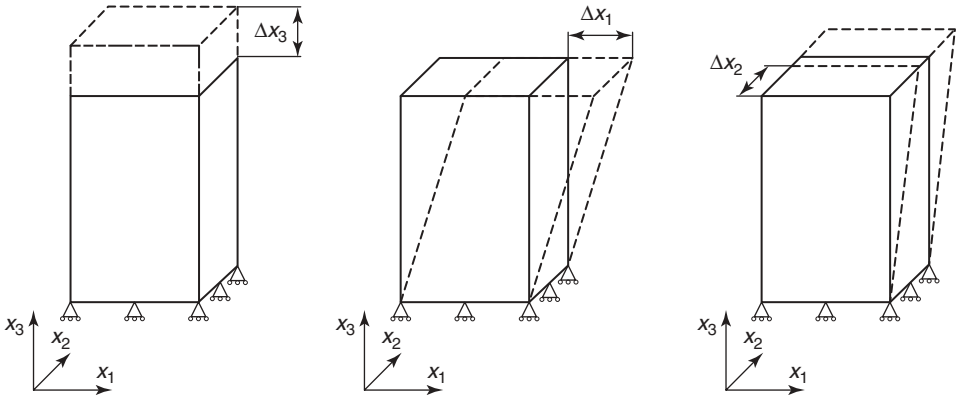

Figure 5.19 Schematic diagram of the loadings in a specific structural direction. The loads are sequentially applied in tension, compression, or shear in the three structural directions.

Section 5.8.3 to a metallic foam with random microstructure and compared to deterministic predictions.

5.8.1
Methods Comparison Based on a Benchmark

A UD glass fiber/epoxy composite material was first defined as a benchmark for homogenization methods by Bégis *et al.* [46]. The constituents have the following elastic properties – glass fiber: $E = 84\,\text{GPa}$; $\nu = 0.22$ and the epoxy matrix: 4 GPa; $\nu = 0.34$. The fiber volume content is 50.57%, and the fiber has a diameter of 118.6 μm. A square unit cell with a side of 150 μm is defined perpendicular to the fibers. Begis *et al.* achieved a pure plane strain homogenization of the square unit cell, assuming endless fibers. As HOMAT considers 3D unit cells, the fiber length must be specified. First homogenization tests show that a fiber length of at least $L_{\text{fiber}} \geq 50 \times L_{\text{edge}}$ must be selected in order to model endless fibers and $L_{\text{fiber}} = 50 \times L_{\text{edge}}$ is adopted here. In order to analyze the impact of finite fiber length, plane strain, and 3D homogenizations are performed with the asymptotic method in HOMAT. With the same 3D FE mesh, virtual tests have also been realized with ABAQUS. Moreover, results obtained by DIGIMAT-MF [6] with the mean-field Eshelby-based homogenization technique [5] are also included in Table 5.1. In the mean-field method, the UD fiber is treated as an inclusion and its aspect ratio A has to be specified for DIGIMAT. Preliminary test runs show that $A \geq 50$.

All schemes predict accurately the effective longitudinal Young modulus E_{L}. In the composite materials literature [47], it is well known that the transverse Young and shear moduli, E_{T} and $G_{\text{TT}'}$, are more sensitive. The 2D plane strain homogenization results of HOMAT continue to be in an excellent agreement with Begis *et al.* However, virtual testing and the mean-field approach reveal relative

Table 5.1 Effective mechanical properties (GPa) of a UD glass–epoxy composite benchmark sample.

Model	E_L	E_T	$G_{TT'}$	G_{LT}
Begis	43.565	12.80	3.13	–
HOMAT 2D	43.453	12.80	3.06	–
HOMAT 3D	43.394	12.69	3.08	4.03
DIGIMAT-MF	43.136	10.42	3.64	4.08
Virtual test	43.570	11.90	2.96	3.87

deviations of −7 and −18%, respectively, for the transverse Young modulus E_T. This numerical result illustrates that in virtual testing, the simultaneous application of periodic BCs, the fixations, and the desired uniaxial deformation mode is a delicate task mainly for transverse solicitations. These specifications are realized automatically in HOMAT and require no specific user effort. Note that the small discrepancy between 2D and 3D homogenization results illustrates that the adopted fiber length represents well an endless fiber.

5.8.2 Austenite–Ferrite Phase Transformation of a Fe–C–Mn Steel

The austenite to ferrite transformation is one of the most important solid-state reactions in steels. Owing to the fact that depending on chemical composition, both phases may have a significant different molar volume, eigenstrains, and eigenstresses play a role, and influence the phase transformation.

At first, the thermoelastic multi-phase-field model [48, 49], implemented in the software MICRESS [42], was used to simulate the evolution of the dual-phase steel microstructure during a cooling process. The corresponding microstructures specify the input for the homogenization procedure. As an example, a Fe 0.018wt%C 0.2wt%Mn steel is considered. The thermoelastic properties of ferrite and austenite together with their molar volumes are given in Table 5.2. The grain boundary energy ($\sigma_{\gamma-\alpha} = 10^{-4}$ J cm^{-2}) and mobility ($\mu_{\gamma-\alpha} = 2 \times 10^{-5}$ cm^4 J^{-1} s^{-1}) of their interface were assumed to be isotropic. In this simulation, ferrite grains nucleate at the intersections of the triple lines when a critical undercooling of 25 °C occurs. The initial RVE microstructure of 30 austenitic grains with random orientations is generated by a Voronoi tessellation (Figure 5.20). This RVE has an extension of $50 \times 50 \times 50\,\mu m^3$. Thus, the mean radius of an austenite grain is nearly 10 μm. In Figure 5.20, the evolution of the microstructure during the austenite to ferrite phase transformation, starting from 842 °C down to 697 °C, is shown.

The applied cooling rate is 4.8 °C s^{-1}. Owing to the low carbon content, the austenitic phase can completely transform into ferrite at the end of the cooling process at 697 °C.

Table 5.2 Materials properties of the austenite and ferrite phases: H_{11}, H_{12}, and H_{44} are the elastic coefficients of the cubic lattice; V_{mol} the molar volume; and α the thermal expansion coefficient

Phase	H_{11} (GPa)	H_{22} (GPa)	H_{44} (GPa)	V_{mol} (cm^3)	α (10^{-5} °C^{-1})
Austenite	154	122	77	7.1824	2.46
Ferrite	195	126	102	7.2757	1.75

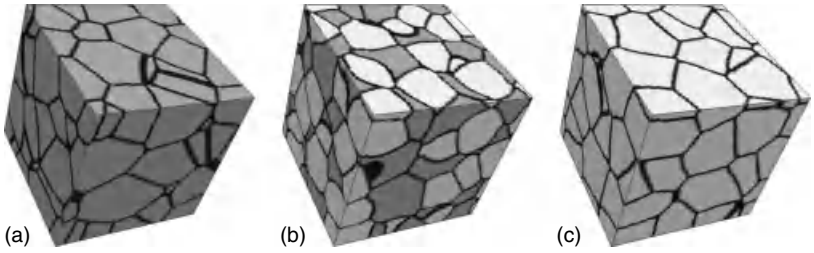

Figure 5.20 Evolution of a microstructure during the austenite to ferrite phase transformation. Austenitic grains are gray, ferritic ones are represented by a lighter area, and the grain boundaries are black (RVE size: 50 × 50 × 50 μm^3). The mean radius of an initial austenite grain is approximately 10 μm. (a) $t = 0$ s, $T = 842\,^{\circ}C$; (b) $t = 11.6$ s, $T = 798\,^{\circ}C$, $f_{fer} = 0.5$; and (c) $t = 36$ s, $T = 697\,^{\circ}C$.

Effective Thermoelastic Properties of the Fe–C–Mn Steel The detailed analysis in [49] of the effective Hooke matrix of the microstructure with a ferrite volume content of $f_{fer} = 0.5$ (Figure 5.20b) shows that the anisotropy of the effective Hooke matrix is marginal, and this microstructure thus reveals *a quasi-cubic global behavior* with $E = 154.87$ GPa; $G = 58.90$ GPa; $\nu = 0.315$; and a cubic anisotropic modulus $\mu^* = 4.81$ GPa (Eq. (5.17)). In Figure 5.21, the effective Young and shear moduli are plotted as a function of the ferrite volume content, obtained by (i) Eq. (5.14) for the homogenization, (ii) the classical volume averaging, given by Eq. (5.14) limited to the first term, and (iii) virtual testing. In fact, virtual mechanical tests have been performed by applying a uniform tensile load in each structural direction and measuring the corresponding total strain. In order to preserve the cubic shape of the RVE, only deformations normal to the load direction were allowed. The effective Young and shear moduli both reveal a quasi-linear variation with the ferrite fraction f_{fer}, except the virtual test result, which increases more slowly at higher f_{fer}. This behavior is most likely induced by overconstrained, not exclusively periodic BCs applied in these virtual tests. At the end of the phase transformation ($f_{fer} = 1$), a difference of 1.72% for E^{eff}, compared to the asymptotic homogenization result, is observed.

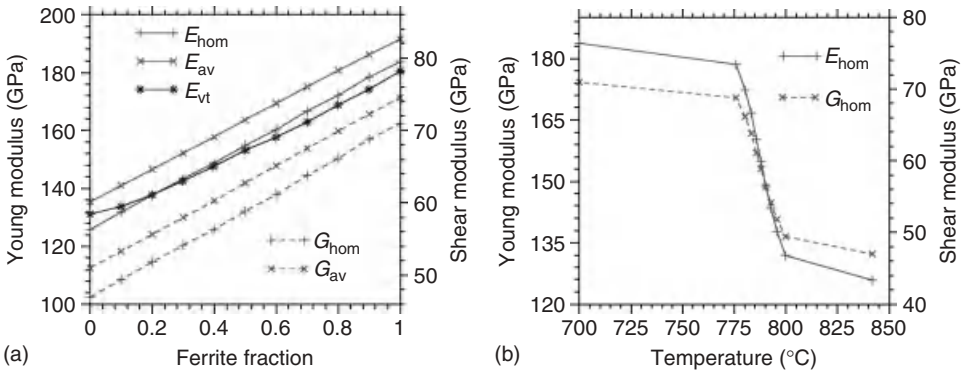

Figure 5.21 Effective Young and shear moduli of the polycrystal as function of (a) the ferrite volume content and (b) the temperature. Note that E_{hom} and G_{hom} are evaluated by asymptotic homogenization; E_{av} and G_{av} are volume averaging results; and E_{vt} is provided by a virtual test.

The periodic microscopic displacements ζ^{rs} are induced by the implicit forces generated at the grain boundaries because of elasticity and/or orientation discontinuities in the microstructure. Their variation over the unit cell improves E_{av} by 5.4%. This small correction is typical for a cubic polycrystal whose effective behavior is quasi isotropic and differs from the large corrections noted in UD composite or effusion cooled materials [18, 20]. In Figure 5.21b, the variation of the effective, homogenized Young and shear moduli with the temperature are outlined. These curves are important for the practice. They constitute, together with the temperature variation of ν^{hom}, α^{hom}, and $\mu^{*,hom}$, the needed thermoelastic materials properties of the considered steel.

Note that $\mu^{*,hom}$ varies from 7.56 GPa (austenite phase) to 1.55 GPa (ferrite phase) by passing 4.81 GPa at $f_{fer} = 0.5$. This last result indicates that after phase transformation, the ferrite polycrystal is less anisotropic and presents a more isotropic equivalent behavior, although the initial grain orientation distribution was set randomly and no texture was considered. Moreover, the quasi-linear variation of the effective thermal expansion coefficient and effective volumetric eigenstrain κ_{ii}^{eff} with the ferrite content is given in Ref. [49].

Effective Elastoplastic Flow Curves Next, the effective elastoplastic properties of the partially transformed steel during the austenite to ferrite transformation are evaluated by virtual tests. For three stages of the transformation, at 73.3%, 48.9%, and 24.5% volume fraction of austenite, the effective stress–strain curves of the RVE have been evaluated. Owing to the lack of detailed experimental data, a simple isotropic von Mises plasticity model has been used for the ferrite and the austenite phases. The hardening of the material is assumed to follow the Ramberg–Osgood model. The material properties are taken from the work of Alberg and Berglund [50]. During the calculation of the

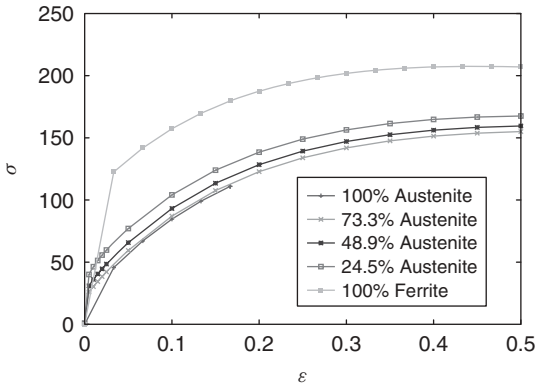

Figure 5.22 True stress versus true strain curves of the RVE during the austenite to ferrite transformation.

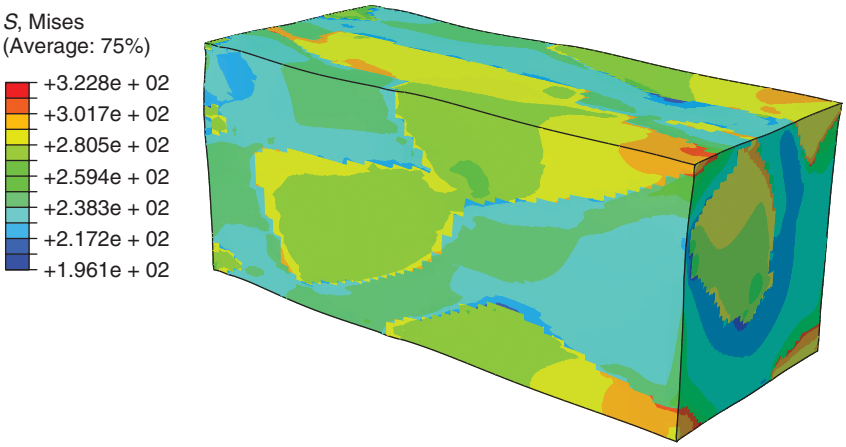

Figure 5.23 Local distribution of the von Mises equivalent stress on the surface of the RVE containing 24.5% austenite during its virtual tensile test in the z direction.

effective mechanical properties, the initial stresses caused by the eigenstrains of the austenite to ferrite transformation are neglected. As the basic materials models of the pure phases are isotropic, the effective response of the RVE is also isotropic. The effective stress–strain curves are displayed in Figure 5.22. Even for a low content of austenite, the effective yielding behavior decreases significantly and more than predicted by a simple mixture rule.

The distribution of the local von Mises stresses for the tensile test in z direction of an RVE with 24.5% austenite content is plotted in Figure 5.23.

The current prediction is limited because of the simplified materials laws of the pure phases. In general, the materials models may be extended in order to include anisotropy, dislocation density, or even damage evolution. The constraint for the

utilization of these extended models is the current lack of experimental data in the considered temperature range.

5.8.3 Application of the Stochastic Homogenization: Effective Thermal Conductivity of an Open-Cell Metallic Foam

The stochastic homogenization procedure, outlined in Section 5.3.3, is applied to improve the deterministic predictions of the effective TC of an open-cell metallic foam, outlined in Ref. [28]. Such metallic foams present two classes of pores, primary pores due to hydrogen bubbles entrapment and secondary pores located in the cell walls (Figure 5.24), and constitute a severe challenge for the homogenization procedure.

In order to derive a realistic 3D micromodel of the considered Inconel 625 foam sample, a CT scan with 435^3 voxels has been realized for a foam sample of 10^3 mm^3. First, the CT data set is cleaned by applying an appropriate filter. Then, the delicate step of segmentation is performed. The application of the 1D spectral analysis leads to a very large first guess for the foam RVE of $6.68 \times 3.4 \times 6.66\,mm^3$. From the foam center, such a unit cell is extracted and enmeshed.

As this large unit cell determined by spectral analysis is not suitable for the stochastic approach, two-point probability functions are expressed in order to get a more suitable first guess for the RVE size. Before this step is realized, Giraldi *et al.* [31] have improved the segmentation of the CT images by a local threshold corrected by a level set function. The discretized foam now presents a larger porosity: $P = 44.6\%$ against 35.8% (global threshold). In Figure 5.6, the s_2^{pp} functions are shown. They specify the following characteristic lengths: $0.782 \times 0.828 \times 0.874\,mm^3$. Its volume is 160 times smaller than that determined by 1D spectral analysis!

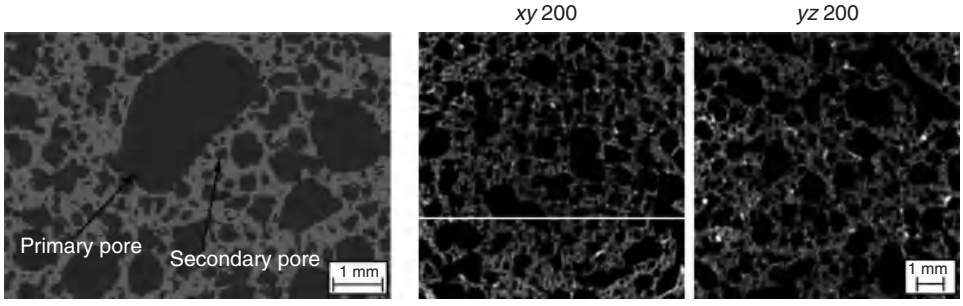

Figure 5.24 (a) Micrography of a slip reaction (SR) foam with primary and secondary pores and (b) 2D cuts of the Inconel 625 sample at a distance of 200 voxels from the origin in the *xy* and *yz* planes. Moreover, a 1D path line is drawn in the cross section of *xy* 200.

Table 5.3 Mean effective TC of the Inconel 625 foam, its confidence interval, and deviation from the experimental value ($k_{exp} = 0.395\,\mathrm{W\,(mK)^{-1}}$).

Cases	Number of samples	RVE size (voxels^3)	$\bar{k}$ (W (mK)$^{-1}$)	CI (%)	Δk_{exp} (%)
1	100	$34 \times 36 \times 38$	0.466	± 5.36	17.9
2	200	$34 \times 36 \times 38$	0.457	± 4.16	15.7
3	100	$68 \times 72 \times 76$	0.427	± 3.51	8.10
4	31	$102 \times 108 \times 114$	0.433	± 1.20	9.60

Following Borbely *et al*. [24], these dimensions specify the smallest possible RVE size. But, the corresponding RVEs are smaller than the largest foam pore, which clearly shows the necessity to improve the first guess for the foam RVE.

Nevertheless, the s_2^{pp} RVE guess is used initially in the stochastic homogenization procedure. To avoid additional discretization errors, a fine mesh is generated in which each voxel corresponds to a linear hexahedron element. Then, 100 unit cells are extracted randomly. Each of these cells has been homogenized thermally with HOMAT. Table 5.3 gives the effective mean TC at 100 °C, its confidence interval, and the relative deviation from the experimental value.

The confidence for the original s_2^{pp} unit cell (case 1) is not satisfactory: the allowed risk of 5% is overshoot. Therefore, the number of extracted unit cells is either increased ($N = 200$) (case 2) or the unit cell size is multiplied by a factor 2 (case 3) or 3 (case 4). Owing to the expensive homogenization runs with a tripled unit cell, only 31 homogenizations have been performed. Doubling and tripling the dimensions of the first unit cell guess lead to a significant increase in confidence and the deviation from the experimental TC becomes less than 10%. This result outperforms the amelioration obtained by doubling the number, N, of samples. Therefore, *it is more predictive to enlarge the dimensions of the initial* s_2^{pp} *unit cell than to increase the number of extractions in the stochastic homogenization procedure*.

In Figure 5.25, the mean effective TC is plotted as a function of the temperature for both variants of the extended unit cell as well as for the large spectral analysis one. The comparison of the results on Figure 5.25 is meaningful: the fine tuning of the threshold provides up to 300 °C effective TC values, which are in excellent agreement with the experimental ones. They substantially improve the results obtained by the initial model [28]. This result points out that the definition of the threshold is the most sensible parameter. Moreover, the effective mean values of the stochastic homogenization do not deviate significantly from the value predicted with the large spectral unit cell. Thus, *the searched physical RVE corresponds to the doubled* s_2^{pp} *unit cell*. Note that above 400 °C the experimental TC increases more than linearly. This stronger increase is due to radiation heat transfer inside the pores, which is neglected in the homogenization scheme.

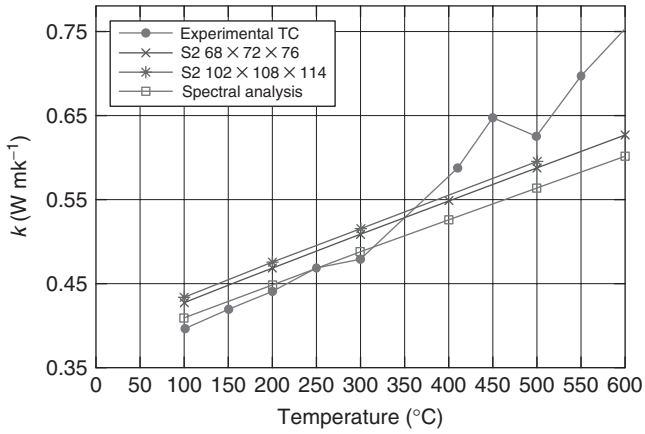

Figure 5.25 The mean effective TC predicted by stochastic homogenization and the experimental one (line with dots). Note that deviations above 400° are attributed to radiation effects.

5.9 Conclusions

The key role of the determination of effective properties for a heterogeneous material with a complex microstructure in the context of multiscale analysis of the manufacturing process steps of products has been outlined. The versatility of the presented AHM to predict mechanical and thermal effective properties of different kind of materials has been demonstrated. Owing to the direct prediction of all materials properties in one simulation and to the automatic definition of the periodic BCs, the homogenization tool HOMAT outperforms slightly in thermoelasticity the virtual testing approach. These virtual tests are widely used in nonlinear mechanics in combination with the Hill–Mandel principle [10]. On the other side, AHM in the ICME framework has to be extended in the near future to also take the nonlinear materials behavior into account. For the evaluation of the effective Darcy permeability and/or TCs, no method more accurate than AHM exists.

The variety of the presented applications is rather broad, going from simple UD fiber-reinforced composites to open-cell metallic foams. The coupling to the direct microstructure evolution simulation with the multiphase and multicomponent phase-field model opens new application opportunities as illustrated by the austenite to ferrite phase transformation of low-carbon steel. Moreover, the application to semicrystalline thermoplastics has demonstrated the necessity to develop a dedicated homogenization procedure.

The stochastic homogenization of open-cell foams has shown that further research is needed to specify a more predictive guess of the RVE size than provided by two-point probability functions and 1D spectral analysis. Thus, for a given materials property, the definition of the RVE size is still an open issue.

Further research will focus on finding alternatives to the time-consuming FE^2 method [1]. Indeed, the application to each process step of the manufacture of a line-pipe or a gear component is currently still unrealistic. The combination of the homogenization method with modern model reduction techniques [16] is a cost efficient way to realize multiscale materials analysis in an ICME framework in the near future. Another research direction will consist in the derivation of *novel constitutive materials laws with microstructure parameters* from several direct microstructure evolution calculations and by applying the homogenization method. For example, during solidification, the permeability of the mushy region might be then expressed not only as function of the fraction solid but also as function of the dendrite arm spacing and the orientation of the dendrite network.

References

1. Feyel, F. and Chaboche, J.-L. (2000) FE^2 multi-scale approach for modelling the elastoviscoplastic behaviour of long fibre Sic/Ti composite materials. *Comput. Methods Appl. Mech. Eng.*, **183**, 309–330.
2. Nemat-Nasser, S. and Hori, M. (1999) *Micromechanics: Overall Properties of Hererogeneous Materials*, 2nd edn, Elsevier Science, Amsterdam.
3. Kanouté, P., Boso, D.P., Chaboche, J.-L., and Schrefler, B. (2009) Multi-scale methods for composites: a review. *Arch. Comput. Methods Eng.*, **16**, 31–75.
4. Mori, T. and Tanaka, K. (1973) Average stress in a matrix and average elastic energy of materials with misfitting inclusions. *Acta Metall. Mater.*, **23**, 571–574.
5. Pierard, O., Friebel, C., and Doghri, I. (2004) Mean-field homogenization of multi-phase thermo-elastic composites: a general framework and its validation. *Compos. Sci. Technol.*, **64**, 1587–1603.
6. (2009) DIGIMAT MF, User Manual, Version 4.0.1, e-Xstream Engineering, December 2009, *www.e-xstream.com/digimat/digimat-fe.html*.
7. Sanchez-Palencia, E. (1980) *Non Homogeneous Media and Vibration Theory*, Lecture Notes in Physics, Vol. **127**, Springer, Berlin.
8. Guedes, J.M. and Kichchi, N. (1990) Preprocessing and post-processing for materials based on the homogenization method with adaptive FE methods. *Comput. Methods Appl. Mech. Eng.*, **83**, 143–198.
9. Ghosh, S., Lee, K., and Moorthy, S. (1995) Multiple scale analysis of heterogeneous elastic structures using homogenization theory and Voronoi cell FE method. *Int. J. Struct. Solids*, **62**, 27–62.
10. Hill, R. (1963) Elastic properties of reinforced solids: some theoretical principles. *J. Mech. Phys. Solids*, **11**, 357–372.
11. Kouznetsova, V., Geers, M., and Brekelmans, W. (2002) Multi-scale constitutive modelling of heterogeneous materials with gradient enhanced computational homogenization scheme. *Int. J. Numer. Methods Eng.*, **54**, 1235–1260.
12. Massart, Th., Kouznetsova, V., Peerlings, R., and Geers, M. (2010) in *Advanced Computational Materials Modeling: From Classical to Multi-Scale Techniques* (eds M. Var, E.A. de Souzade Neto, and P.A. Munoz-Rojas), Wiley-VCH Verlag GmbH, pp. 111–164.
13. Michel, J.-C. and Suquet, P. (2004) Computational analysis of nonlinear composite structures using the non-uniform transformation field analysis. *Comput. Methods Appl. Mech. Eng.*, **193**, 5477–5502.
14. Fritzen, F. and Böhlke, T. (2010) 3-D FE implementation of the non-uniform transformation field analysis. *Int. J. Numer. Methods Eng.*, **84**, 803–829.

15. Fish, J., Shek, K., Pandheeradi, M., and Shephard, M. (1997) Computational plasticity for composite structures based on the homogenization method: theory and practice. *Comput. Methods Appl. Mech. Eng.*, **148**, 53–73.
16. Yuan, Z. and Fish, J. (2009) Multiple scale eigendeformation-based reduced order homogenization. *Comput. Methods Appl. Mech. Eng.*, **198**, 2016–2038.
17. Hornung, U. (1997) *Homogenization and Porous Media*, Springer-Verlag, Berlin.
18. Laschet, G. (2002) Homogenization of the thermal properties of transpiration cooled multi-layer plates. *Comput. Methods Appl. Mech. Eng.*, **191** (41–42), 4535–4545.
19. Laschet, G. (2008) Forchheimer law derived by homogenization of gas flow in turbomachines. *J. Comput. Math.*, **215**, 467–476.
20. Laschet, G. and Rex, S. (2008). Effective thermoelastic properties of flat and curved transpiration cooled multilayer plates via homogenization. ASME Proceedings of Turbo Expo, GT2008-50590.
21. Yong-Ping Feng and Jun-Zhi Cui (2004) Multi-scale analysis and FE computation for the structure of composite materials with small periodic configuration under condition of coupled thermoelasticity, *Int. Jnl. for Num. Meth. in Engng.*, **60**, 1879–1910.
22. Torquato, S. (2006) *Random Heterogeneous Materials: Microstructure and Macroscopic Properties*, Springer-Verlag Inc., New York, November 2006.
23. Kanit, T., Forest, S., Galliet, I., Mounoury, V., and Jeulin, D. (2003) Determination of the size of the representative volume element for random composites: statistical and numerical approach. *Int. J. Solids Struct.*, **40**, 3647–3679.
24. Borbely, A., Kenesi, P., and Biermann, H. (2006) Estimation of effective properties of particle-reinforced metal-matrix composites from micro-tomographic reconstructions. *Acta Mater.*, **54**, 2735–2744.
25. Bobzin, K., Lugscheider, E., Nickel, R., and Kashko, T. (2006) Advanced homogenisation strategies in material modelling of thermally strayed TBC's. *Adv. Eng. Mater.*, **8** (7), 663–669.
26. Laschet, G., Kashko, T., Angel, S., Scheele, J., Nickel, R., Bleck, W., and Bobzin, K. (2008) Microstructure based model for permeability predictions of open-cell metallic foams via homogenization. *Mater. Sci. Eng. A*, **472**, 214–226.
27. Kammeyer, K. and Koschel, K. (1998) *Digitale Signalverarbeitung*, B.G. Teubner, Stuttgart.
28. Laschet, G., Reutter, O., Sauerhering, J., Fend, Th., and Scheele, J. (2009) Effective permeability and thermal conductivity of open-cell metallic foams via homogenization on a microstructure model. *Comput. Mater. Sci.*, **45**, 597–603.
29. Bobzin, K., Nickel, R., Parkot, D., and Kashko, T. (2007) Microstructure dependency of the material properties: simulation approaches and calculation methods. *Steel Res.*, **78** (10–11), 790–797.
30. Bobzin, K., Bagcivan, N., Parkot, D., Kashko, T., Laschet, G., and Scheele, J. (2009) Influence of the definition of the representative volume element on effective thermo-elastic properties of thermal barrier coatings with random microstructure. *J. Therm. Spray Technol.*, **18** (5–6), 988–995.
31. Giraldi, L., Laschet, G., and Mathes, M. (2010) Influence of the segmentation technique on the effective thermal conductivity of open-cell metallic foam. Proceedings of ECCM-10, Paris, May 2010.
32. Michielsen, K. and De Raedt, H. (2001) Integral-geometry morphological image analysis. *Phys. Rep.*, **347** (6), 461–538.
33. Ohser, J. and Mücklich, F. (2000) *Statistical Analysis of Microstructures in Materials Science*, 1st edn, John Wiley & Sons, Ltd.
34. Kouznetzova, V. (2002) Computational homogenization for multi-scale analysis of multi-phase materials. PhD thesis, Eindhoven University of Technology, Netherlands.
35. Trias, D., Costa, J., Turon, A., and Hurtado, J. (2006) Determination of the

critical size of a statistical representative volume element (SRVE) for carbon reinforced polymers. *Acta Mater.*, **54**, 3471–3884.

36. Bédoui, F., Diani, J., Regnier, G., and Seiler, W. (2006) Micromechanical modelling of isotropic elastic behaviour of semi-crystalline polymers. *Acta. Materialia*, **54**, 1513–1513.

37. Tashiro, K., Kobayashi, M., and Tadokoro, H. (1992) Vibrational spectra and theoretical 3-D elastic constants of i-PP crystal: an important role of anharmonic vibrations. *Polym. J.*, **24** (9), 899–919.

38. Sawatari, C. and Matsuo, M. (1986) Elastic modulus of i-PP in the crystal chain direction as measured by X-ray diffraction. *Macromolecules*, **19**, 2653–2656.

39. Kamazawa, M., Yamada, K., and Takayanagi, M. (1979) Preparation of ultrahigh modulus i-PP by means of zone drawing. *J. Polym. Sci.*, **24**, 1227–1236.

40. Doyle, M.J. (2000) On the effect of crystallinity on the elastic properties of semi-crystalline polyethylene. *Polym. Eng. Sci.*, **40** (2), 330–335.

41. Rieger, A. (2005) Zur Parameteridentifikation komplexer Materialmodelle auf der Basis realer und virtueller Testdaten. Dissertation, Universität Stuttgart, Bericht I-14.

42. (2009) MICRESS, Version 5.5, June 2009, *www.micress.de*.

43. Michaeli, W. and Baranowski, T. (2010) Simulation of microstructure formation in injection molded semi-crystalline thzermoplastic parts. *J. Polym. Eng.*, **30** (1), 29–43.

44. Schroeder, W., Martin, K., Avila, L. and Lorenzen, B. (2010) *The VTK User's Guide*, 11th edn, Kitware Inc., ISBN: 978-1-930934-23-8.

45. Scheele, J. (2010) Entwicklung einer Programmumgebung zur Durchführung Virtueller Tests an virtuellen Gefügestrukturen, Diplomarbeit RWTH Aachen, April 2010.

46. Bégis, D., Duvaut, G., and Hassim, A. (1982) Homogénéisation par Éléments Finis des Modules Élastiques de Matériaux Composites. Report no. 101, INRIA.

47. Berthelot, J.-M. (1999) *Composite Materials: Mechanical Behavior and Structural Analysis*, Springer-Verlag, New York.

48. Steinbach, I. and Apel, M. (2006) Multi-phase field for solid state transformation with elastic strain. *Physica D*, **217**, 153–160.

49. Laschet, G. and Apel, M. (2010) Thermo-elastic homogenization of 3-D steel microstructure simulated by the phase-field method. *Steel Res. Int.*, **81**, 637–643.

50. Alberg, H. and Berglund, D. (2003) Comparison of plastic, viscoplastic, and creep models when modeling welding and stress relief heat treatment. *Comput. Methods Appl. Mech. Eng.*, **192**, 5189–5208.

6
Distributed Simulations

Thomas Beer, Tobias Meisen, and Rudolf Reinhard

6.1
Motivation

Within the acronym ICME, ''I'' as ''integrated'' already implies a notion of multiple entities being used as building blocks for a higher level objective. As already discussed in the previous chapters, the use of multiple different simulation models, each covering a different aspect of the material's behavior or targeting different scales or different kinds of the material's treatment, is a substantial quality behind the idea of integrated computational materials engineering (ICME). Different approaches trying to make different models accessible for practical application are available. A common example is the development of dedicated systems implementing different models and/or analysis tools that are used in a single discipline. Haupt [1] has proposed a solution embedding different materials models and analysis utilities implemented as MATLAB routines. This allows for access via a web interface, which can be used by a human user to browse a repository of models and associated media, such as images of microstructures, or even programmatically by means of a service-oriented architecture. The implemented analysis tools can be controlled from a web front end, triggering MATLAB calculations – transparently to the user – on a back end that has access to a pool of MATLAB computing resources. This approach is well suited for tools using MATLAB scripts, as several widespread tools, for example, Abaqus, are able to handle MATLAB routines. In different domains of application, for example, spaceflight [2], similar approaches have been deployed. All of these approaches reveal the common characteristic of not being appropriate for the situation presented in this book: each simulation tool has to be realized considering the requirements of the platform. Hence, such an approach relies on tools allowing for source-code access and a software architecture that either allows for the appropriate modifications or provides tools being developed from scratch. Even if source-code access is granted, it might fail because of the time and cost required for its realization. Another approach is the use of a commonly accepted standard, being applied to describe data [3, 4]. This approach, however, will also fail if heterogeneous applications using different formats and semantics to describe data of a domain have to be interconnected. In this case, the

Integrative Computational Materials Engineering: Concepts and Applications of a Modular Simulation Platform,
First Edition. Edited by Georg J. Schmitz and Ulrich Prahl.

implementation of routines enabling the import and export of the standardized data format are required. This, in reverse, requires source-code access. A solution tackling this problem is the implementation of the so-called adapters, which realize a bridge between a common standard and the individual data format used by the application. The number of required adapters varies with the number of different applications and, accordingly, with the respective number of data formats. In a scenario, in which the required interconnections are identified on run time, adapters for each possible pair of interconnections between the applications are required. The maintenance effort of these adapters depends on the revision interval of the standard and on the data format of each of the applications. With regard to the standards, another problem is their dependency on the maintaining manufacturer or on the community defining the standard. If an extension of the standard becomes necessary or such an extension results in an incompatibility with existing adapters or applications, it will take a long time to run the required changes in the standard – if they are realized at all [5]. Hence, a common domain-specific standard will be feasible only if the complexity of data examined in the discipline is low and if the domain is well known. Furthermore, the manufacturers of the domain-specific applications need to commit to the standard.

For a small number of tools, these approaches may even work well. Commercial examples include products from the ESI Virtual Try-Out Space®[1] series, which consist of a unified user interface wrapped around pre-/postprocessing modules and a decent simulation kernel suited for a special simulation task. This is an example of a fixed simulation pipeline and conceptually does not scale to flexible connections of heterogeneous simulations. More approaches to simulation coupling have been reviewed in brief in [6].

As stated by Rajan [7, 8], the question of interconnection between simulation tools and/or the underlying models, describing different aspects of the material's behavior, is evidently getting more important and is crucial to the development of the ICME domain. The aforementioned examples work well for a special kind of simulation tasks, but they lack the necessary flexibility for dynamic connection of the different simulation tools needed for the kind of simulation platform proposed in this book.

The following section covers the infrastructural platform architecture realizing the interconnection on the technical level. Section 6.3 highlights the transformation of data, which is the most crucial part, to assure the interconnection on the data level. The last section details how user access to the platform is realized by means of a web interface.

6.2 The AixViPMaP® Simulation Platform Architecture

The approach proposed in this book makes use of simulation tools that implement the different models with all their heterogeneity in terms of data formats, operating

1) Virtual Try-Out Space® is a registered trademark of the ESI Group.

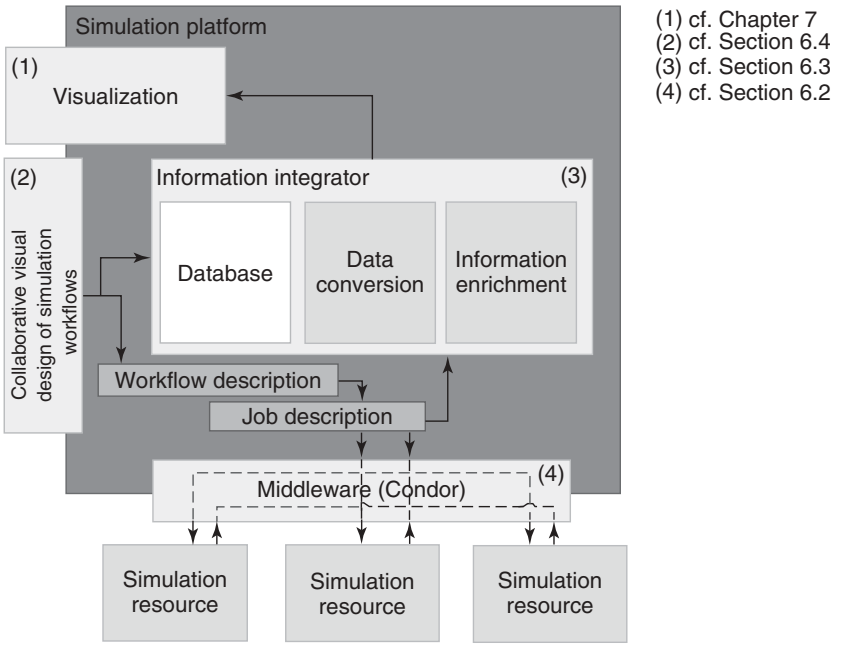

Figure 6.1 The infrastructural architecture of the AixViPMaP®.

systems, and other requirements solving the ''connectivity issue'' at a nonintrusive level. The infrastructural architecture is depicted in Figure 6.1.

Multiple computing resources, that is, the hardware and software needed for each particular simulation tool, have to be connected on different levels. The lowest level is the technical level: while an existing hardware infrastructure offering network connections to all of the involved hardware resources is mandatory, a software layer is also required, making all resources aware of the overall system. Since the late 1990s, the field of ''grid computing'' researches technologies dealing with the dynamic connection of distributed computing resources [9]. Every distributed system inherently suffers from a large number of potential security risks. Those technologies involve a high degree of security- and reliability-related modules and – as a consequence – a high amount of administrative workload. For many settings, especially in an academic surrounding, this extra workload can hardly be provided, and, thus, the high degree of security available in commercial grid and cloud services cannot be reached without skilled administrative staff. The presented platform architecture thus makes use of the Condor High Throughput Computing toolset [10]. Condor provides a low-level resource management and scheduling functionality, as it is used for grid engines as well. Although Condor explicitly claims it is not a grid middleware, it has several features in common with these. It also provides interfaces to the prominent grid middleware Globus [11] as well as to UNICORE [12], which in turn offer options to use Condor

as a scheduling component. Thus, on request, it is even possible to embed the presented architecture into a bigger, more powerful, and perhaps even more securely distributed computing system.

The overall architecture of the platform proposed in this book is constructed in a star topology. Each resource connects to the Condor central manager and advertises its capabilities to it. For this purpose, the Condor tools have to be installed in each machine that hosts a simulation tool. In view of security concerns, only connections to the central manager have to be allowed. It is not necessary to expose a system to all machines of the platform. The execution of a program on the distributed system can be realized by using two different concepts. The first concept assumes that software resources are being installed on special hardware resources, the term "*resource*" thus mapping the combination of software and hardware parts that, in their combination, are able to perform a specific task. The second and more powerful concept is the distribution of software on-the-fly to any resource meeting certain criteria needed to execute it. Resources can thus be dynamically selected without the need for preconfigured and maintained software on every single resource of the system. In most cases, these criteria include a suitable operating system and hardware architecture that a certain binary was built for. The use of platform-independent executable formats, such as an interpreted byte code, adapts even more to this concept as it depends only on the appropriate interpreter that needs to be installed on the executing machine, regardless of both the hardware architecture and the operating system. In practice, however, an *ad hoc* distribution of simulation tools is often not possible for either technical reasons or because of licensing issues.

To actually execute a distributed task, involving multiple resources, the system is reliant on the knowledge about those resources and especially of their mutual dependencies, allowing the data flow and the order of execution to be controlled in an appropriate way. Condor includes the directed acyclic graph manager (DAGMan) [13] to evaluate dependencies between the single simulations and to detect independent subgraphs that can be executed in parallel if adequate and sufficient resources are available. As in any grid system, Condor requires proper configuration files that need to be composed for the execution of each single simulation task. In the present case, this involves configuration files for each single simulation including infrastructural details such as network addresses, paths to the executables, paths to the input and output data, and environment settings of the operating system. Figure 6.2 sketches an abstract workflow (left), appropriate configuration files for DAGMan (upper right), and one of the referenced jobs (lower right). Setting up these files manually is very error prone and, regarding the idea of a flexible simulation platform, would not perform any better than manually driving every single simulation. The proposed solution to overcome this problem of inefficiency is the eb interface, presented in Section 6.4. Besides the technical interconnections between the simulation tools that will be provided via the presented gridlike distributed architecture, the interconnection on the data level has to be accomplished by a meaningful connection of individual simulations. This connection on the data level is presented in the next section.

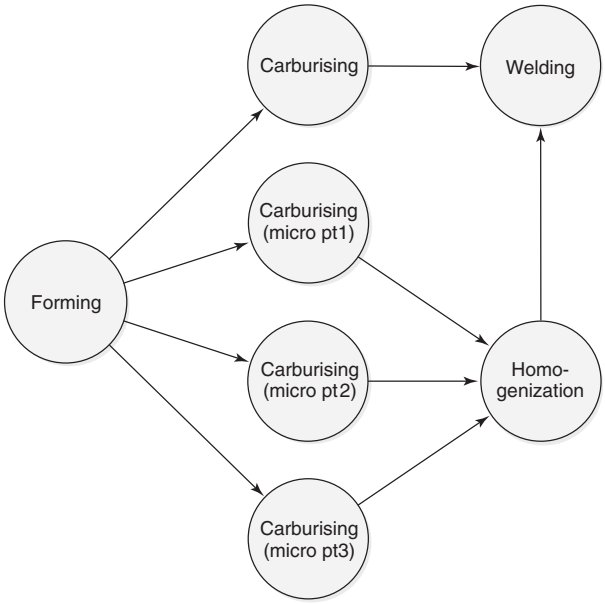

Example DAGMan dependency description:

```
# syntax: JOB JobName SubmitDescriptionFileName directory
JOB Forming forming.job results/Forming
JOB Carburising_macro carburising_macro.job results/Carburising_macro
JOB Carburising_micro_pt1 carburising_micro_pt1.job results/Carburising_micro_pt1
JOB Carburising_micro_pt2 carburising_micro_pt2.job results/Carburising_micro_pt2
JOB Carburising_micro_pt3 carburising_micro_pt3.job results/Carburising_micro_pt3
JOB Homogenization homogenization.job results/Homogenization
JOB Welding welding.job results/Welding

# syntax: SCRIPT [PRE | POST] JobName ScriptFile Arguments
SCRIPT PRE 6_Homogenization gatherMicroResults.sh Carburising_micro_pt?

# syntax: PARENT JobName CHILD JobName
PARENT Forming CHILD Carburising_macro Carburising_micro_pt1
Carburising_micro_pt2 Carburising_micro_pt3
PARENT Carburising_macro Homogenization CHILD Welding
PARENT Carburising_micro_pt1 Carburising_micro_pt2 Carburising_micro_pt3
CHILD Homogenization
```

Example Condor job description:

```
Executable = Forming.sh
Universe = Vanilla
Log = Forming.log
Output = Forming.out
Error = Forming.error
should_transfer_file = YES
when_to_transfer_output = ON_EXIT
InitialDir = Projects/id00000/Forming
Requirements = ((Machine==forming PC03.inst.org.net) || FORMING_CAPABLE) &&
(OpSys=="Linux")
transfer_input_files = Input/InitialData
```

Figure 6.2 A schematic simulation workflow graph (a) and appropriate examples for configuration files (b). Shown example: partial graph from test case gearing component (Chapter 9).

6.3 Data Integration

Several approaches to realize the interoperability between simulations of a single domain have been provided in the past (Section 6.1). In the field of materials science, a number of different applications exist using different file formats containing problem-specific data such as meshes, boundary conditions, and material properties [14]. Some formats are widely accepted such as the Abaqus input format or I-DEAS' universal file format, where both are supported by many commercial CAD/CAE tools. Others are only used by specific applications such as the Larstran PEP file format. Realizing an interconnection between such different simulation applications in the area of materials science thus requires a solution that can support heterogeneous file formats and understand the underlying semantics.

Generally, computer science examines such a problem in the research field of information integration. Overcoming heterogeneity and realizing interoperability between applications is considered as application integration. Section 6.2 discussed how the technical heterogeneity, addressing the problem of different operating systems and hardware requirements, can be overcome. In this chapter, the data integrator is presented as a solution to overcome other kinds of heterogeneity, namely, the syntactical, the data model, and the structural and the semantic heterogeneity [5, 15]. Syntactic heterogeneity arises as a result of the representation of data (e.g., number formats, character encoding), whereas the data model heterogeneity is given if the data is represented by different data models (e.g., relational database management systems (RDBMSs), hierarchical data formats (HDF5, XML), or structured formats such as comma-separated values (CSVs)). The most complex kinds of heterogeneity are the structural and the semantic heterogeneity. Structural heterogeneity addresses the problem of representing data in one data model in different ways. One example is the representation of structured meshes in Abaqus using keywords such as NCOPY, NGEN, and NFILL or simply defining it by specific nodes. Semantic heterogeneity comprises differences in meaning, interpretation, and type of usage of schema elements or data. A simple example is the representation of the nodal temperature. In the PEP format, it is denoted by number 18, whereas in Abaqus it is represented by the character string TEMP. Besides this, a data integrator also enables the consolidation of data being generated during a simulation process. This allows for extracting the data of an entire simulation process within a single format. Consequently, all data can be visualized within one viewer; see details in Chapter 7.

The architecture of the data integrator is based on a service-oriented approach. Thereby, a service bus realizes the communication between the different *services*. The data integrator contains several services that enable it to overcome the different kinds of heterogeneity. Syntactical and data model heterogeneity are overcome by using *adapter services*. These correspond to the interface modules mentioned in Chapter 2. In contrast to a common adapter-based approach, the adapter services of the data integrator do not need any domain-specific knowledge to fulfill their task. Their main purpose is to transfer the data stored in a file or database into a

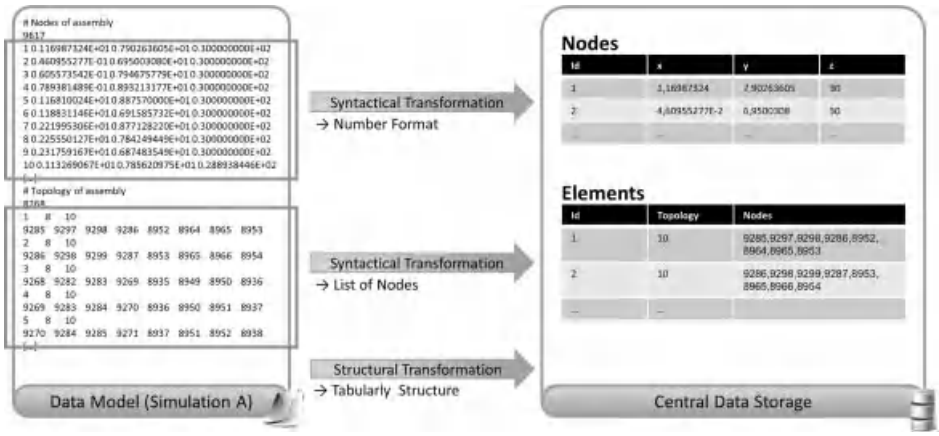

Figure 6.3 Integration of data into the central data storage (CDS).

relational database without considering the structure or the semantics of the data (Figure 6.3).

A relational database is used as a central data storage (CDS) because of the huge data volumes being generated and exploited in materials science simulation. This approach enables good scaling and the use of index algorithms such as the R-Tree [16, 17] for three-dimensional data or the X-Tree [17] for multidimensional data. The data integrator distinguishes two kinds of adapter services. *Integration services* are used to transfer data to the CDS, whereas *extraction services* are employed to transfer data from the CDS to a file or a database.

After the data has been integrated into the CDS, it is processed with the help of *analysis*, *planning*, and *transformation services*. An analysis service identifies the features that are fulfilled by the integrated process data (as-is state). Furthermore, this service analyzes which features have to be fulfilled so that the data can be extracted into a defined data format (target state). This information is used by a planning service to determine a process transforming the given set of features into the needed one (the ''plan''). Finally, transformation services process the data according to the determined plan. The features, as well as the existing transformations and their preconditions and effects, are described in a knowledge base. This knowledge base is expressed in the Web Ontology Language (OWL) and considers domain-specific knowledge. Figure 6.4 shows an example of the determination of a transformation process by using analysis and planning services.

The analysis service first determines the as-is state of the data stored in the CDS. In this example, the represented mesh consists of voxel elements and has a node property named temperature, being measured in Celsius. In addition, the indexing of the nodes and elements is closed, starting from zero. For extracting the data into the desired target format, the mesh has to fulfill a set of features defined in the target state. First, the mesh has to consist of hexahedrons and the temperature has to be presented by a property numbered 18. The indexing of nodes and elements has to be closed and start from one.

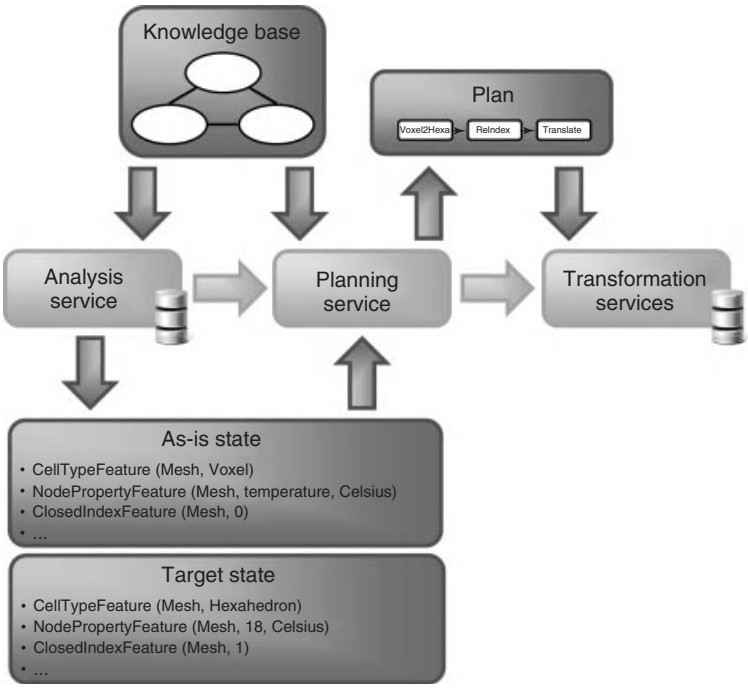

Figure 6.4 Determination of a transformation process using services.

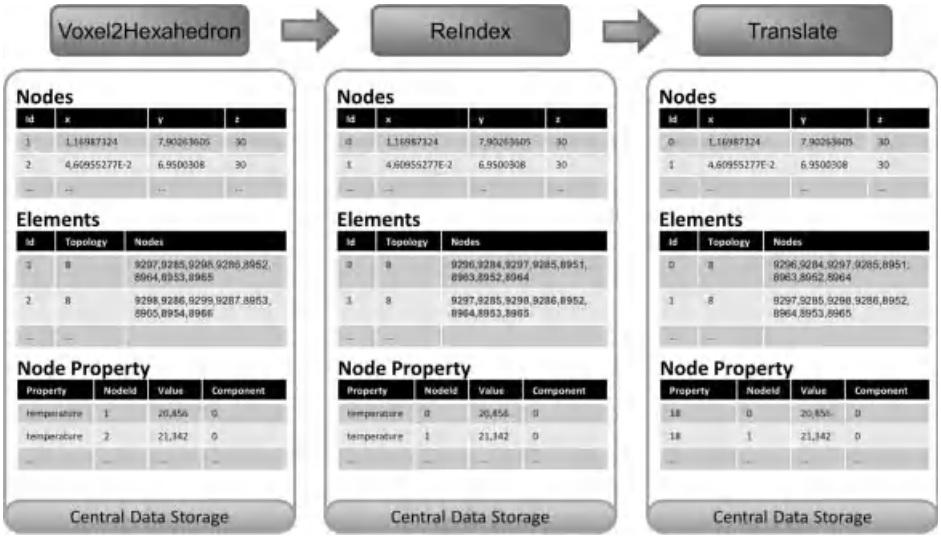

Figure 6.5 Transformation process.

As a result, the planning service determines a transformation process transforming the data into the desired target state. Following the example, the transformation process contains three steps: Voxel2Hexahedron, ReIndex, and Translate. Each of these transformations is realized as a separate service (Figure 6.5).

Implemented transformation services include *merging and splitting services* that can be used to modify the geometry of meshes, for example, by merging multiple meshes into one or by splitting a single mesh into distinct parts.

The data integrator is robust against changes in the requirements of data formats according to the structure and the semantics. Besides that, new data formats can be easily integrated into the data integrator by defining the integration and extraction service as well as the structural and semantic requirements. New transformation services are automatically used by the data integrator after they have been published in the knowledge base. In addition, the data integrator is scalable and can easily be extended because of the service-oriented approach.

6.4 Web-Based User Interface for the Simulation Platform

The simulation platform can be accessed by a web interface, based on the underlying system's architecture presented earlier and on a grid-computing approach. From a platform user's perspective, the complexity of both the IT infrastructure and the system details for individual simulation tools being offered via the AixViPMaP have to be abstracted and reduced to a usable level. Users do not want to write cryptic configuration files either for the configuration of each individual simulation tool or for the definition of dependencies and relations between them. The underlying systems (i.e., the Condor scheduler and DAGMan), however, require several configuration files to evaluate the involved computing resources and an appropriate order of execution. Thus, the generation of such configuration files has been automated, and now it is wrapped in a user-friendly graphical web interface. To access this interface, no proprietary software needs to be installed on the user's machine beyond a JavaScript-capable web browser. In the following, different areas of the present web interface is described according to the typical workflow of a simulation task.

The main feature of the user interface is provided with the Workflow Editor. In the field of grid computing, the term *workflow* is used as a description of how different grid resources (hardware and software components) will be connected and what their dependencies are in order to accomplish a higher level simulation task.

All simulation tools actually being integrated into the platform are listed in a drop-down menu. Each simulation step is represented by a graphical object that comprises the configuration details of the respective simulation tool (Figure 6.6). These objects form the nodes of a simulation graph. Dependencies between the steps are modeled by graph edges defining data input and output (Figure 6.7). Data integration steps are placed between the simulation tools. Thus, the data integration

Figure 6.6 Different simulation objects with various parameters being made available by the Workflow Editor.

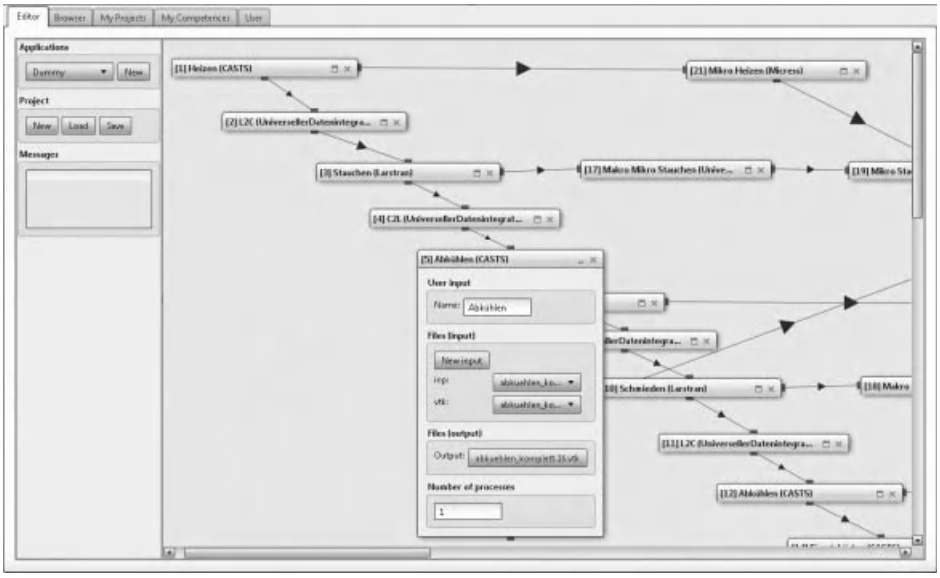

Figure 6.7 Example of a complex workflow graph. Shown example: test case gearing component (Chapter 9).

module can track the origin of data and further provide the *data translation and enrichment services*, as discussed in the previous section.

A detailed configuration of the single simulation steps is typically performed by means of native configuration files for each application. Selected options may be added to the Workflow Editor interface as well, allowing to change them without modifying the configuration files – in case the application provides such options. For each simulation tool, only the appropriate input data files are displayed. Uploads and downloads of these files are performed by the user and handled by an online file manager offering the same interaction metaphors as common file managers of current operating systems (Figure 6.9).

Workflows can be saved to the system for later execution or for further editing. Each user can provide access to selected projects to other users of the system, so that a cooperative development of complex simulation graphs and tasks is supported.

When a workflow is ready for execution – that is, when all simulation inputs are connected properly, either by selecting a file or by redirecting the output from another simulation node to it – the ''ready'' flag is displayed on the project browser (Figure 6.8). Subsequently, any user having access to the project can instantiate and execute it. The system will then automatically generate configuration files for each single simulation step within the workflow and eventually generate a directed acyclic graph description representing the dependencies between the individual simulations. In a further step, these files are used by the DAGMan and the Condor scheduler, which selects and claims the corresponding resources, sends the appropriate data to the appropriate resources, and collects the simulation results, retaining the overall dependencies between the individual simulations. The underlying Condor scheduler also detects independent subgraphs from the overall workflow description and files them to be processed in parallel on the distributed resources.

The results can then be downloaded via the file management system for a further analysis and postprocessing by simple visualization tools such as ParaView or by more complex intern visualization systems as, for example, described in Chapter 7 (Figure 6.9).

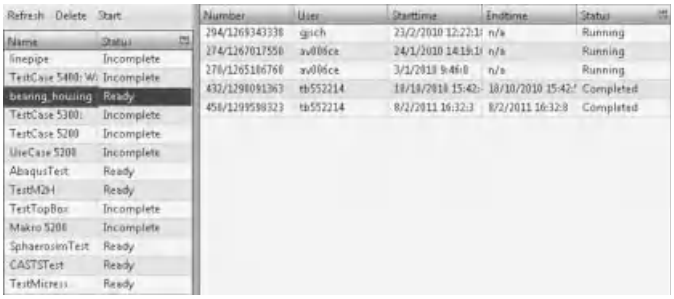

Figure 6.8 The project browser provides an overview of finished and running instances of simulation workflows.

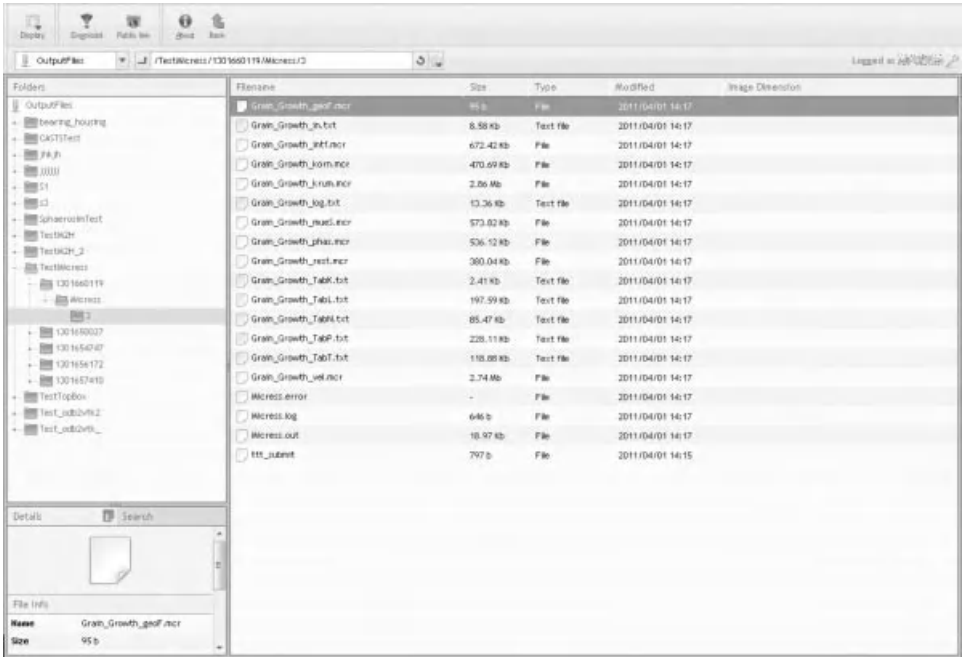

Figure 6.9 Data access through the online file manager module. Example shows the examination of microstructure results.

References

1. Haupt, T. (2010) Cyber infrastructure for integrated computational material engineering. Proceedings of the Magnesium Technology, 2010.
2. Kalden, O., Fritzen, P., and Kranz, S. (2007) SimVis a concurrent engineering tool for rapid simulation development. International Conference on Recent Advances in Space Technologies, RAST'07, pp. 417–422.
3. Anderl, R. and Trippener, D. (2000) STEP: standard for the exchange of product model data, *Eine Einführung in die Entwicklung, Implementierung und industrielle Nutzung der Normenreihe ISO 10303 (STEP)*, Teubner, Stuttgart, Leipzig.
4. Eversheim, W. and Schuh, G. (2004) *Integrierte Produkt- und Prozessgestaltung*, Springer.
5. Abdul-Ghafour, S., Ghodous, P., Shariat, B., and Perna, E. (2007) A common design-features ontology for product data semantics interoperability. IEEE/WIC/ACM International Conference on Web Intelligence, pp. 443–446.
6. Cerfontaine, P., Beer, T., Kuhlen, T. *et al.* (2008) *ICCSA 2008*, LNCS, Vol. **5072**, Springer, pp. 867–882.
7. Rajan, K. (2008) Materials informatics part I: a diversity of issues. *JOM*, **60** (3),50.
8. Rajan, K. (2009) Informatics and integrated computational materials engineering: part II. *JOM*, **61** (1),47.
9. Foster, I. and Kesselman, C. (2004) *The Grid: Blueprint for a New Computing Infrastructure*, Elsevier, ISBN: 1-55860-933-4.

10. Thain, D., Tannenbaum, T., and Livny, M. (2005) Distributed computing in practice: the condor experience. *Concurrency Comput.: Pract. Exp.*, **17** (2–4),323–356.
11. Foster, I. (2006) *IFIP 2006*, LNCS, Vol. **3779**, Springer, pp. 2–13.
12. Streit, A. (2009) *eStrategies*, vol. **9**, British Publishers Ltd, pp. 8–9.
13. Couvares, P., Kosar, T., Roy, A., Weber, J., and Wenger, K. (2007) Worflow Management in Condor, in *Workflows for e-Science* (eds I. Taylor, E. Deelman, D. Gannon, and M. Shields), Springer Press, ISBN: 1-84628-519-4. pp. 357–375.
14. Beer, T., Meisen, T., Reinhard, R. *et al.* (2011) *The Virtual Production Simulation Platform: From Collaborative Distributed Simulation to Integrated Visual Analysis, Production Engineering*, vol. **5**, Springer, Berlin, Heidelberg, pp. 383–391.
15. Leser, U. (2007) *Informationsintegration: Architekturen und Methoden zur Integration Verteilter und Heterogener Datenquellen*, 1st edn, Dpunkt-Verlag, Heidelberg.
16. Guttman, A. (1984) R-trees: a dynamic index structure for spatial searching. SIGMOD International Conference on Management of Data, ACM, pp. 47–57.
17. Berchtold, S., Keim, D.A. *et al.* (1996) *VLDB'96, International Conference on Very Large Data Bases*, Morgan Kaufmann, pp. 28–39.

7
Visualization

Thomas Beer and Tobias Meisen

7.1
Motivation

The ultimate goal of performing simulations in general and linked simulations in particular is a deeper understanding of the underlying processes and effects. Efficient means of data analysis thus are a mandatory component in the overall workflow of an integrated computational materials engineering (ICME) platform. The simulated phenomena can rarely be exploited/detected by generic computational methods. Even in cases in which such detection is possible, a visual representation of the detected results is highly desirable. Mere and raw numerical output of any kind, in general, is only graspable for a very small group of domain experts. Regarding the nature of ICME, several disciplines are involved, which are linked as a composite to describe the material's behavior. Interdisciplinary communication across domain boundaries is a crucial ingredient in any kind of successful integrative work. Besides its main purpose, the transformation of pure numbers into visual perceivable information, visualizations also serve as a decent means to support human communication and interdisciplinary discussions, as they provide a common basis to which all participants can refer. Common understanding can be achieved much easier, as compared to written or oral communication. While the latter often draws on terms being defined differently in different disciplines, visualization allows avoiding such misinterpretations at a very early stage.

Apart from the fact that visualizations are needed to get a glimpse of phenomena that cannot be analyzed by automatic algorithms, visualizations that point out those phenomena in a fully automated way cannot be generated. All simulation results originating from an integrated simulation workflow, as explained in Chapter 6, form a contiguous comprehensive representation of the material's state during each time step of the modeled process. Visualization data have to be extracted for each of these different steps and, subsequent to the extraction, merged into a common visualization context. This context not only involves multiple scales but also different temporal and spatial resolutions as well as different kinds of data fields (e.g., continuous temperatures at the macro level, discrete grain identifiers at the micro level). This data ''merging'' raises a couple of questions that have

Integrative Computational Materials Engineering: Concepts and Applications of a Modular Simulation Platform,
First Edition. Edited by Georg J. Schmitz and Ulrich Prahl.

not been addressed by common visualization applications till now. The following sections describe a number of steps necessary to transform the simulation result data into visualization data. Handling of visualization data with respect to their spatial and temporal relations and technical issues to be overcome to generate interactive visualizations of data are detailed. The last section gives an outlook for visualization and analysis techniques that will emerge from the integrative visualization approach.

7.2 Standardized Postprocessing

The Data Integrator allows all simulation data to be translated into a format suitable for visualization. The common format is the PolyData-format of the widely used Visualization Toolkit (VTK) software library [1]. This allows the use of free postprocessing tools such as ParaView [2]. After configuration of the initial simulation chain, the specialist's knowledge is required when preparing data for an integrative visual analysis. Within the postprocessing tools, for example, ParaView, standard visualization objects, such as object surfaces, cutplanes, or isosurfaces, can be extracted from each dataset interactively. Up to this point, the flow of work allows for a standardized postprocessing and visualization may proceed as known for each individual simulation result data.

For an integrated analysis of *all* datasets resulting from *all* distributed simulations of the workflow, a further step is required to prepare these datasets for visualization in a common context. From the datasets prepared within ParaView (Figure 7.1), only surface meshes are exported till now for performance reasons. Driving the complete visualization pipeline in real time during the integrated analysis process is not yet feasible. Besides performance issues, it is also a memory problem to keep full, unstructured volumetric data for all simulations in-core at once on regular workstation-class machines. As a wide range of display systems is targeted (next section), different amounts of visualization data can be handled interactively – a fact that has to be taken into account for the integrative visualization solution. Although the decimation of meshes is still a big topic in various domains (see [3] as an introduction), it is not presented in detail here. To point out the immense influence of a decimation approach on visualization results, a comparison of two different approaches is briefly outlined in the following text. The first one can be traced back to geometric error metrics, as proposed by Schroeder *et al.* [4]. On the basis of the local error that a decimation step produces with respect to the local curvature of the mesh, triangles are iteratively removed from the mesh. From a geometrical point of view, this approach delivers good results (Figure 7.2). But as soon as data values assigned to the mesh are affected, the results from a decimated mesh are insufficient, for example, as the temperature distribution for a given example is only rudimentarily reproduced by the decimated results. Generalizations of such decimation approaches to higher dimensionality can be used to include data values in the error metrics, which thus are not restricted only to geometrical errors. The

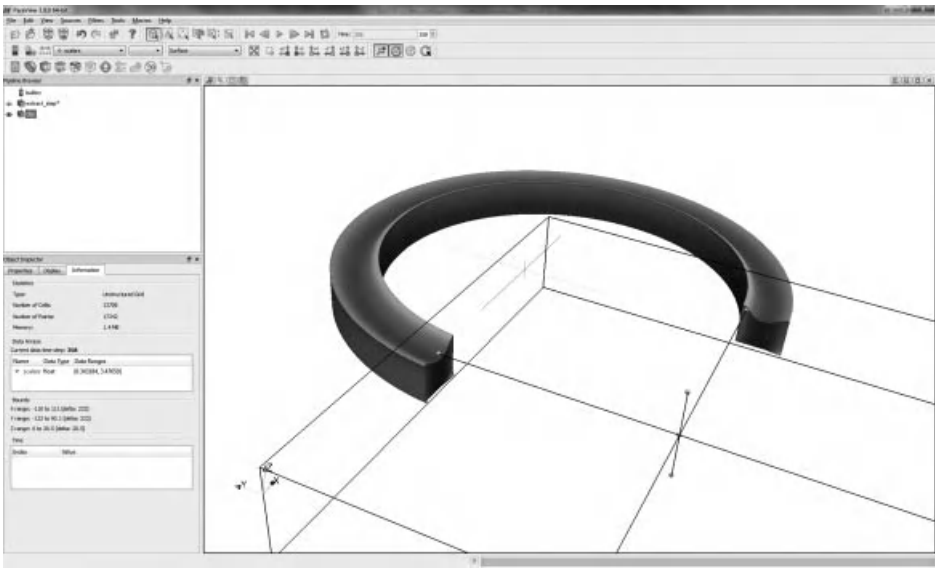

Figure 7.1 Analyzing and preparing a single dataset within ParaView. Shown example: gearing component (Chapter 9).

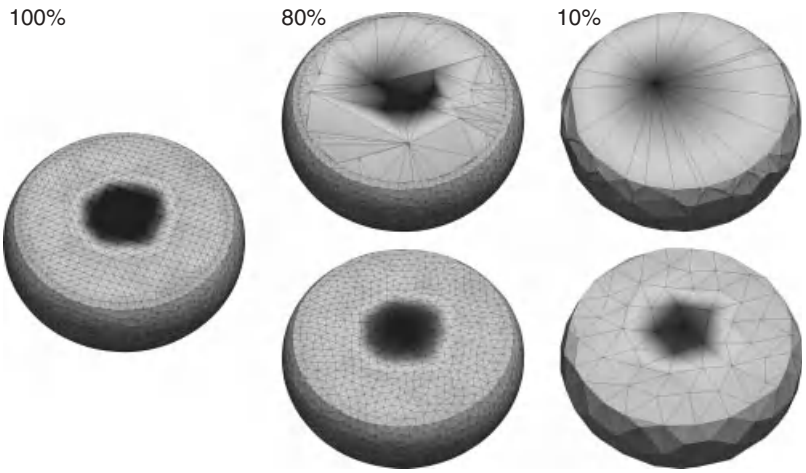

Figure 7.2 Comparing a remeshing (lower row) to a coarsening (upper row) decimation approach. Shown example: gearing component (Chapter 9).

quadrics approach of Hoppe [5] can be regarded as a prominent one. However, for practical application of these methods, the additional nongeometric metrics must be defined and their weights have to be chosen, that is, how ''bad'' a deviation of a specific data field (e.g., temperature), introduced by a decimation step, is compared to other fields or to the geometric errors. This involves a decent amount of domain

knowledge with respect to the special semantics that are implied to the data fields by the different simulation models. Thus, a straightforward quadrics approach is not easily transferable to heterogeneous simulation data.

Representing the principal approach of remeshing, at this point, the work by Valette and Chassery [6] is exemplarily outlined. It uses approximated Voronoi cells to create a uniform mesh resolution with either more or less triangles than the original mesh. Such meshes have been used with interpolated data values from the original mesh with sufficient result accuracy. Figure 7.2 illustrates that this approach can preserve information, for example, temperature distribution on the surface, which would have been removed by purely geometric-based decimation approaches. Although a remeshing takes considerably more time and memory resources (approximately five times in the presented case) as compared to the other methods, it still is a more practical approach than defining special metrics and weights for each different kind of dataset.

The decimated datasets can eventually be used for the integrated visualization of process chains resulting from the defined workflows.

7.3 Integrated Visualization

Integrative and interactive visual analysis of *all* result datasets of a simulation scenario is an important part of the integrated simulation approach. Current visualization solutions such as ParaView do not handle all aspects required for an integrated analysis yet. Thus, a visualization solution has been developed allowing analysis of different datasets in a common context/environment (Figure 7.3). To cope with the different kinds of visualization data in a common context, an abstraction layer has been introduced containing meta-information about the visualization data, focusing on their spatiotemporal properties according to the simulated process. The different datasets are referenced along with these properties and stored in a simple xml tree. Supported dataset formats in this context include the ''ParaView Dataset'' format, which basically consists of a collection of VTK data files. An appropriate runtime data model provides this information consistently to the different modules of the visualization application and enables them to attach module-specific information for their internal use. This approach allows for a shared data structure, but at the same time, by using an approach following the basic idea of role objects [7], no interdependencies between the otherwise independent modules arise, as it would be the case with a naïve shared data structure implementation. Figure 7.4 outlines the module structure of the visualization application developed for this purpose.

For an interactive exploration of the simulation results and their temporal relations in the simulated process, a hierarchical organization of the datasets' time frames is used. It is made accessible through a hybrid 2D/3D user interface. All datasets are placed on one or more global timelines. By the interactive manipulation of a dataset's position on a timeline, the visualization session can be dynamically

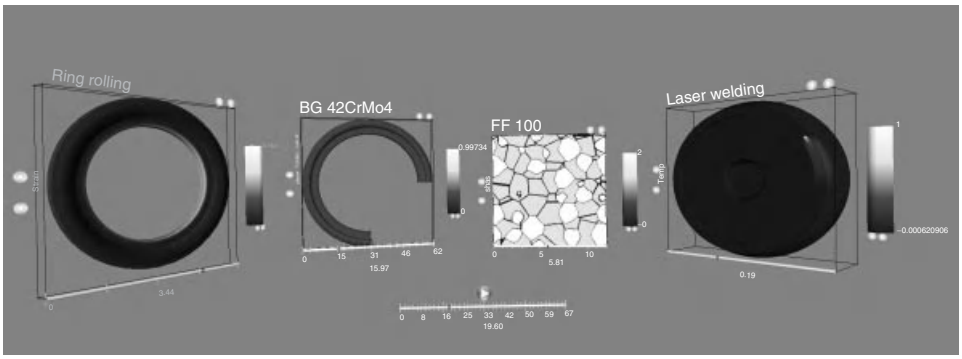

Figure 7.3 Integrated visualization of multiple simulation results. Shown example: gearing component (Chapter 9).

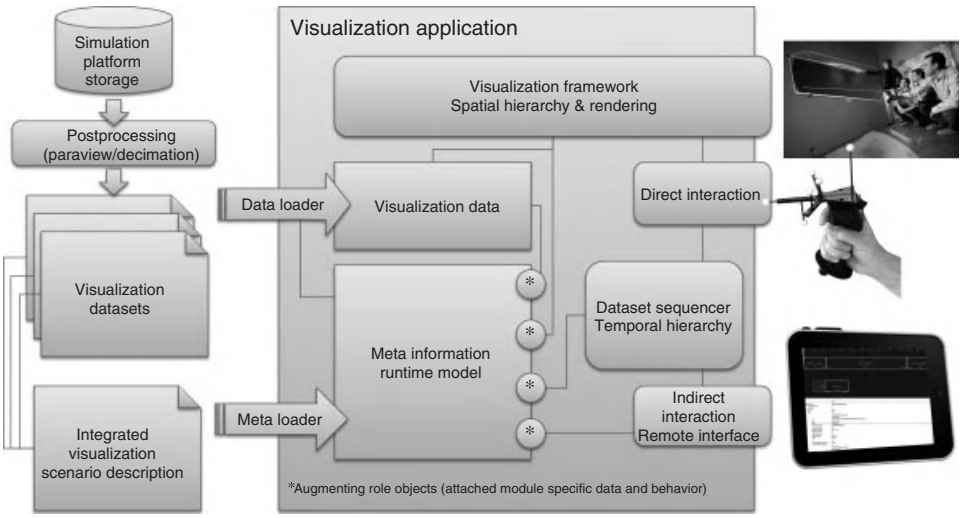

Figure 7.4 Architecture of an integrated visualization application.

reconfigured as needed on the fly. This allows, for example, starting a visualization session with all datasets aligned on the timeline according to the sequence given by the simulated process. During the analysis process, some subprocesses may become interesting and make a side by side comparison (in the sense of time) of these datasets more suitable, for example, to analyze differences in the microstructural behavior during subprocesses (e.g., similar heating steps). The traditional approach to this was to set up a new visualization scenario that includes just these datasets so that they can be analyzed side by side and at the same time. Referring back to the original process then would again require reloading the former visualization scenario and vice versa. These approaches tend to get annoying and confusing for the user and are not helpful when concentrating on the analysis process.

To give the analyst more freedom in the analysis process, the present solution is capable of dynamically changing these temporal relations between the datasets, that is, each dataset's position on the timeline, on the fly, and, interactively, through a special user interface. This *Dataset Sequencer* tries to follow interaction metaphors found in digital audio/video workstations and adapts them to the field of interactive data visualization.

In the *Dataset Sequencer*, each subprocess is represented by a rectangular object spanning its current lifetime on the global timeline (Figure 7.5). By interactively moving or resizing the object, the corresponding subprocess will be visualized during a different interval of the global time. To provide the user with information about the original temporal relations of the different subprocesses, their original time is displayed in the background. In addition, multiple tracks allow for the management of overlapping subprocesses, such as simulations on different scales that represent the same time interval of the simulated process. Thus, the temporal aspects of the visualization context can be manipulated interactively in an intuitive manner. The overall visualization solution is designed to be operated on systems

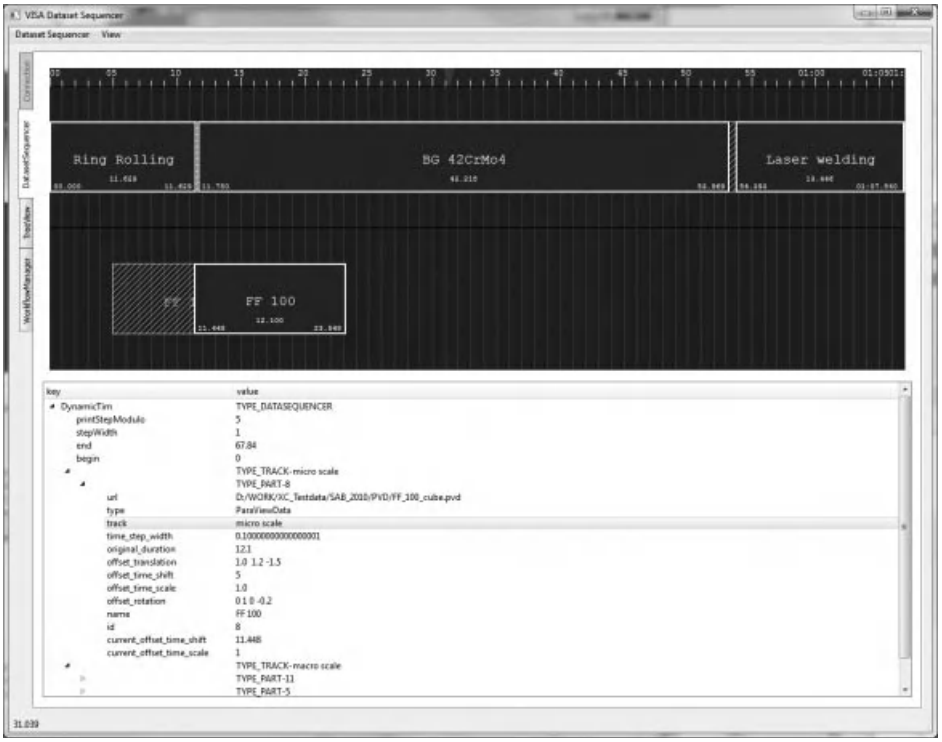

Figure 7.5 The employed interaction metaphor on top of the *Dataset Sequencer*: intuitive user interface for manipulation of the chronological configuration of a visualization scenario.

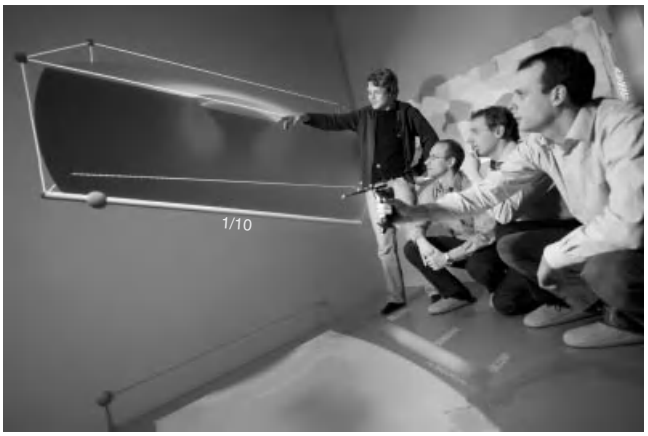

Figure 7.6 Collaborative visualization session inside an immersive virtual reality system, showing results from the gearing component testcase (Chapter 9).

ranging from notebooks to high-end distributed immersive Virtual Reality hardware architectures (Figure 7.6). According to the heterogeneity of the considered visualization hardware, the user interface can be used either remotely, drawing on, for example, a separate portable device when standing inside or in front of a large Virtual Reality system or as a local application on a desktop system along with the actual visualization. For more details about internals of the *Dataset Sequencer*, the interested reader is referred to [8].

As the aggregated visualization data from a simulated process chain easily leads to overload of the hardware of any visualization system, decimation processes and level-of-detail techniques have been incorporated into the visualization solution. These allow for adaptation to the capabilities of the desired visualization system.

The traditional motivation of introducing level-of-detail selection methods is to cope with resource constraints [3]. A more generic methodology for a visualization application would be the selection of ''adequate'' visualization data from a pool of different temporal and geometrical resolutions of the datasets to be visualized. In this case, one aspect of adequacy could consist in the optimal workload according to the technical constraints of the current display system. This would basically resemble the traditional resource-driven selection approach. Another aspect could be the adaption of the visualization to the displayed data, that is, to focus on ''important'' parts. Consequently, combining different metrics of adequacy could result in a balanced selection of data, providing adequacy in terms of both, technical resource usage and a high degree of ''important'' information. However, evaluating the ''importance'' of a single part of visualization data is highly specific to each discipline/domain. Different examples of domain-specific data analysis, for example, [9], and more generic approaches based on information theory, such as [10], are known from the field of scientific visualization. Balancing multiple objectives for optimal solutions is a very broad theoretical field and is applicable to

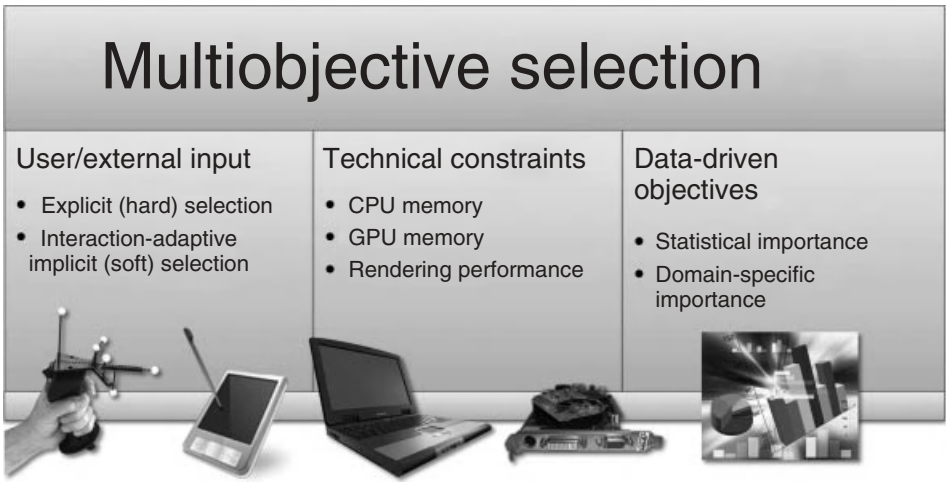

Figure 7.7 Multiple competing selection objectives.

many heterogeneous domains. Furthermore, it has been a field of active research for decades. A review of generic optimization methods for engineering application has been published by Marler and Arora [11]. In Figure 7.7, the competing classes of selection criteria are sketched.

Besides the multiobjective optimization problem, a further issue consists in the definition and implementation of domain-specific metrics. An example of such a metric could be based on differently evolving temperatures inside an object. In this case, microstructural evolution will most probably be influenced and thus those parts of the simulation data where temperature is not evolving homogeneously could be considered to be ''important'' by this metric. Regarding the computational and the memory load, as already discussed, it is not feasible to evaluate such a metric for the entire simulated process chain online during the analysis process. However, in practice, many of these phenomena are closely related to the object's geometry, making it possible to manually define a small number of representative points-of-interest for an object, at which these parameters shall be monitored. The next section describes how such points can be tracked offline throughout the data of a simulated process chain, as a preprocessing step to the visual analysis. From these traces, data values at the selected points can be analyzed efficiently and thus can be considered in the runtime selection algorithm of the visual analysis application.

The main purpose of visualization is to provide its user with information. Thus, besides technical and data-driven metrics, the user plays an important role in the visualization process. Implementations of such user assistance mechanisms always should consider the user as being the central part of the visual analysis process. Accordingly, the user must be able to override or manipulate the assistance process in a way that makes it possible to intuitively navigate the visualization into a user-defined state.

7.4
Data History Tracking

The tracking of data along the entire simulation process is one major advantage becoming possible in the wake of a homogeneous representation of the data. Besides the application, integration, and presentation layer, the platform also has an analysis layer containing methods to realize a data history tracking. *Data history tracking* is defined as the possibility of tracking data of an arbitrary time and space within the simulation process. In a very simple simulation process, a remeshing of the mesh, representing the simulated assembly, is not required. Hence, the data history tracking is realized by tracking the unique identifiers of each node and element of the mesh. In contrast to simple simulation processes, complex ones including the simulation of forming often result in the necessity for remeshing during the simulation process. In such a case, a mere tracking of the identifiers is not sufficient. In fact, it is necessary to identify a mapping between nodes and elements before the remeshing as well as afterwards. Detecting such a mapping requires additional information that has to be provided by the remeshing tool. Presently, the implemented data history tracking method can handle two kinds of such additional information (Figure 7.8).

In case of alternative A being processed, it can be translated to a problem presented as alternative B. The translation requires a generation of the displacement table by calculating the vector difference of each node coordinate in the source and the intermediate meshes. By doing so, each node of the source mesh can be localized as an absolute position in the remeshed mesh. Generally, this position is not represented by a node. Therefore, data, such as the temperature, are calculated by interpolating data from neighboring nodes. These neighbors are determined by

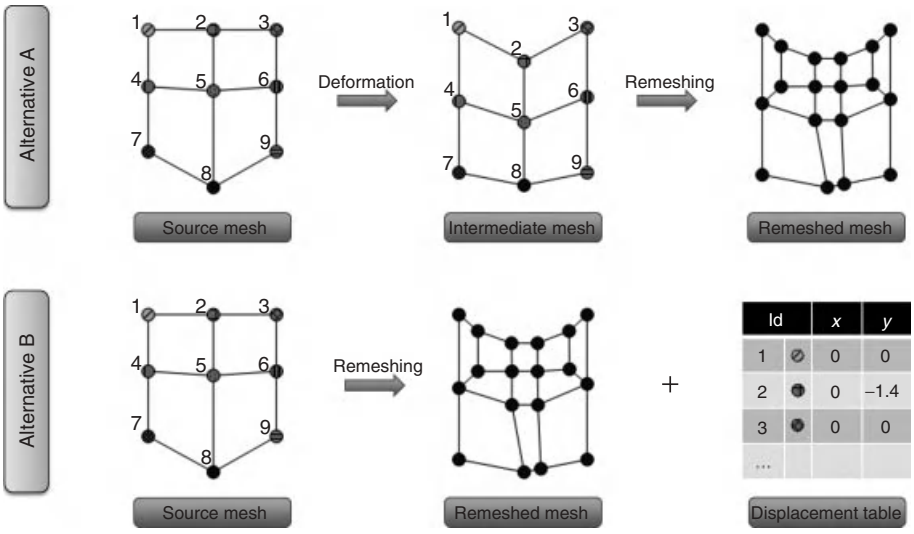

Figure 7.8 Supported alternatives of information about remeshing.

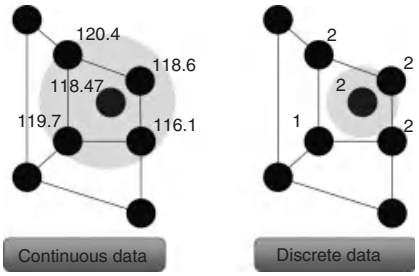

Figure 7.9 Strategies for continuous and discrete data.

using the R*-tree index structure [12]. This data-driven index structure is optimized for spatial access methods such as range or the nearest-neighbor queries (NN queries). The index is generated using minimum bounding rectangles.

By interpolating data for a position, the data history tracking algorithm considers different types of data. For example, temperature information can be interpolated by calculating the average temperature from neighboring nodes. On the contrary, information about the material has to be one element out of a fixed set of existing materials. Hence, different strategies for the determination of an interpolated value are implemented. The algorithm determines the strategy for each type of data using information stored in the knowledge base of the information system. The strategies for continuous and discrete data are depicted in Figure 7.9.

As mentioned earlier, the strategy for continuous data considers a configurable number of the NNs and determines the specific value by weighting the values of the NN. The weighting takes the distance between the position and the NN into account and is defined by the reciprocal of the ratio between this distance and the total distance. The total distance is the sum of all distances. In case of discrete data, the value is set to be equal to the value of the NN.

Displaying such point traces provides the user the possibility of analyzing how the material has moved throughout the simulated object during the simulated process. This can be used, for example, to analyze which temperature–time profiles an area of material has been exposed to. For the expert, this information can serve as an indicator of critical parts of the process such as the probability of phase changes that need to be investigated in more detail, for example, on the microstructural level. Furthermore, if those kinds of metrics can be described programmatically, the visualization solution could use them to determine the important parts that then should less likely be dropped but shown in the highest resolution technically possible during the visual analysis process. Extending this approach to the integration module (Chapter 6) will help extract even more optimized and contiguous visualization datasets in the future.

References

1. Kitware Inc. (2010) *The VTK User's Guide*, 11th edn, Kitware Inc., ISBN: 978-1-930934-23-8.
2. Kitware Inc. (2008) *The ParaView Guide*, Kitware Inc., ISBN: 1-930934-21-4.

3. Heok, T.K. and Daman, D. (2004) A review on level of detail. IEEE Computer Graphics, Imaging and Visualization'04, pp. 70–75, doi: 10.1109/CGIV.2004.1323963
4. Schroeder, W.J., Zarge, J.A., and Lorensen, W.E. (1992) Decimation of triangle meshes. SIGGRAPH'92, pp. 65–70, doi: 10.1145/133994.134010
5. Hoppe, H. (1999) New quadric metric for simplifying meshes with appearance attributes. IEEE Visualization'99, pp. 59–66, doi: 10.1.1.2.9544
6. Valette, S. and Chassery, J.M. (2004) Approximated centroidal voronoi diagrams for uniform polygonal mesh coarsening. *Comput. Graph. Forum*, doi: 10.1111/j.1467-8659.2004.00769.x
7. Fowler, M. (1997) Dealing with roles. The 4th Pattern Languages of Programming Conference, *http://martinfowler.com/apsupp/roles.pdf* (accessed March 28 2011).
8. Beer, T., Garbereder, G., Meisen, T., Reinhard, R., and Kuhlen, T. (2011) A multi level time model for interactive multiple dataset visualization: the dataset sequencer. *Advances in Visual Computing*, LNCS, Vol. **6939**, Springer, Heidelberg.
9. Reinders, F., Post, F.H., and Spoelder, H.J.W. (2001) Visualization of time-dependent data with feature tracking and event detection. *Vis. Comput.*, **17** (1), 55–71.
10. Wang, C., Yu, H., and Ma, K.-L. (2008) Importance-driven time-varying data visualization. *IEEE Trans. Vis. Comput. Graph.*, **14** (6), 1547–1554.
11. Marler, R.T. and Arora, J.S. (2004) Survey of multi-objective optimization methods for engineering. *Struct. Multidisc. Optim.*, **26**, 369–395.
12. Beckmann, N., Kriegel, H.-P., Schneider, R., and Seeger, B. (1990) The R*-tree: an efficient and robust access method for points and rectangles. Proceedings of the SIGMOD International Conference on Management of Data, pp. 322–331.

Part II
Applications

Integrative Computational Materials Engineering: Concepts and Applications of a Modular Simulation Platform,
First Edition. Edited by Georg J. Schmitz and Ulrich Prahl.

8
Test Case Line Pipe

Patrick Fayek, Hendrik Quade, Thomas Henke, Gottfried Laschet, Markus Apel, Eduardo Sambrano Rossiter, Markus Bambach, and Ulrich Prahl

8.1
Introduction

The worldwide demand for crude oil and gas has increased severely over the past years. This demand is connected with the need for fuel transport, commonly over large distances. With increasing prices for these resources, more and more solitary areas, exhibiting extreme environmental conditions, become profitable for exploitation, making it necessary to develop pipeline steels that are technologically and economically applicable. The large distances over which the fuels have to be transported usually make pipeline projects extremely cost intensive. Hence, either cost reduction or increased pipeline efficiency is aspired for.

Different approaches are commonly aimed at. On the one hand, a reduction in wall thickness is possible when applying steels with higher strength values, making it possible to reduce costs concerning materials consumption, transportation, as well as welding. On the other hand, the efficiency of a pipeline can be enhanced by increasing the operating pressure, which in turn requires the application of steels with higher strength and toughness values [1, 2]. According to Hillenbrand *et al.* [3], pipeline steels of grade X80 have been mostly applied because of their advantageous combination of strength and toughness, but steel grades up to X120 are currently under investigation. The mechanical properties of steels are mainly influenced by the steel's chemistry and the microstructure, which in turn is determined by the conditions present in the production process. Here, annealing, hot rolling, and controlled cooling of the plate are the main microstructure-determining process steps.

The aim of this chapter is to deliver a test scenario for the developed integrated computational materials engineering (ICME) simulation platform that eventually offers a cost-effective approach for the development of new steels and the adjustment of associated process parameters and conditions in order to create an optimized product with desired properties at minimal process and raw materials costs. The intention is to establish an integrative multiscale simulation model for the production of a pipeline tube, making it possible to consider all relevant phenomena at the macro- and microscale throughout the production process that influence the

Integrative Computational Materials Engineering: Concepts and Applications of a Modular Simulation Platform,
First Edition. Edited by Georg J. Schmitz and Ulrich Prahl.

Table 8.1 Chemical composition for a pipeline steel corresponding to X65 according to standard [4].

Steel	C	Si	Mn	P	S	V	Nb	Ti	CEV_{max}
L450MB	0.16	0.45	1.60	0.025	0.020	0.10	0.05	0.06	0.43

CEV_{max}, carbon equivalent value.
All values are given in mass percentage and maximal contents.

later performance characteristics of the product. The benefit of such an approach is obvious, for example, when the alloying concept is changed and process parameters have to be adjusted in order to create the most favorable product properties.

The manufacturing of an industrial pipeline tube involves the following process steps: the reheating of a steel slab produced by continuous casting, multiple hot rolling steps transforming the slab into a thick sheet, the subsequent cooling process, the U- and O-forming processes of the steel sheet, and its longitudinal welding. Note that the expansion and subsequent coating processes are not included in the present investigation. An integrated simulation approach constitutes a serious advantage compared to investigations that only describe the material's behavior during specific production steps (e.g., hot rolling, forming, or welding). In the present study, the material's behavior within a production process is influenced by the preceding process and determines the initial conditions for the subsequent one.

8.2 Materials

The material investigated in this test case is a typical pipeline steel of X65 grade. The chemical composition given in Table 8.1 is standardized for corresponding steel typically designated for piping applications in agreement with the German standard [4]. The carbon equivalent value (CEV_{max}) is also given in the table in order to estimate the weldability. The steel that is the subject of this study belongs to the standard listed in Table 8.1.

Metallographic analysis was performed in order to characterize the as-delivered state. The initial material is a hot rolled strip with a thickness of approximately 20 mm. Metallographic analysis at different magnifications (Figure 8.1) reveals a ferritic–pearlitic microstructure with distinct pearlite bands present in the microstructure that are elongated in the rolling direction. A mean pearlite content of 14% has been evaluated by image analysis of the metallographic sections.

In the following sections, characterization methods are introduced in order to establish or enrich models for the purpose of an adequate materials description in the specific simulations. Miscellaneous materials properties have to be considered. In fact, not all of them are derived experimentally but are extracted from databases.

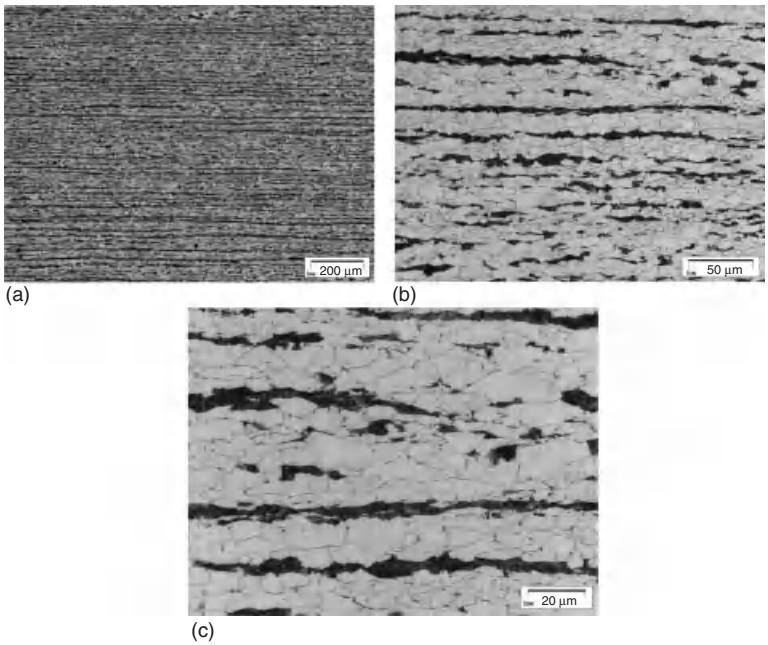

Figure 8.1 Metallographic sections at ×100 (a), ×500 (b), and ×1000 (c) magnification of the as-delivered steel microstructure. Pearlite is represented by darker areas, while ferrite is displayed in light gray.

Properties such as thermal expansion, molar volume, density, thermal conductivity, and so on, are calculated according to the chemical composition as a function of temperature using the software JMatPro [5] and are applied to the macroscopic heat treatment simulations.

8.3 Process

8.3.1 Overview of Process Chain

In the present study, the following steps of an industrial pipeline production process are considered: reheating process, hot rolling processes, the subsequent cooling process, pipe forming processes, and welding process. All processes are intended to be simulated on the microscopic as well as macroscopic scale. The following paragraphs give a general description of each process step and summarize the relevant process parameters and their influence on the material's characteristics. Moreover, the parameters that are treated in the simulations and have an impact on the material's properties are also described. The microstructural features being

taken into account are phase transformations, grain growth, work hardening, and dynamic and static recrystallizations.

8.3.2 Reheating

In the industrial pipe manufacturing process a cast slab is reheated in order to achieve appropriate production conditions for the subsequent hot rolling process in which the cast microstructure is destroyed. Industrial reheating temperatures for slab rolling vary between 1150 and 1250 °C. Since pipeline steels are required to exhibit both high strength and high toughness and the grain size importantly contributes to these properties, the effects of exposure to high temperatures on grain coarsening have to be known in order to control the grain size at the end of the reheating process and to provide appropriate initial conditions for the next process, the first hot rolling process step.

8.3.3 Hot Rolling

In plate rolling, the reheated cast steel slabs are hot rolled to a desired plate thickness commonly using one or two reversing roll stands. Typically, these hot rolling cycles involve about 10–20 passes. For controlling both the process and the final product quality, the knowledge of microstructure evolution and the material's strength during this rolling process is essential.

The flow stress of the processed material is the most important factor influencing the main process parameters, for example, rolling force and torque, during hot rolling [6]. Hot rolling of steel involves a wide range of microstructural reactions affecting the flow stress of the processed material, which basically can be divided into static and dynamic effects.

8.3.4 Cooling and Phase Transformation

The last rolling passes usually take place below the recrystallization stop temperature, leading to a dislocation-enriched austenite at the runout table. This highly deformed austenitic microstructure results in a faster transformation during cooling and a refined microstructure providing advanced strength and toughness properties. The improvement of additional properties can be achieved only when ferritic–bainitic microstructures are adjusted in contrast to ferritic–pearlitic ones [3, 7]. This transformation is commonly achieved by accelerated cooling optionally combined or adjusted with isothermal holding schemes. Figure 8.2 shows typical cooling strategies.

Microalloying complements the aforementioned measures. Niobium carbonitrides precipitating strain induced during rolling lead to finer austenite grains

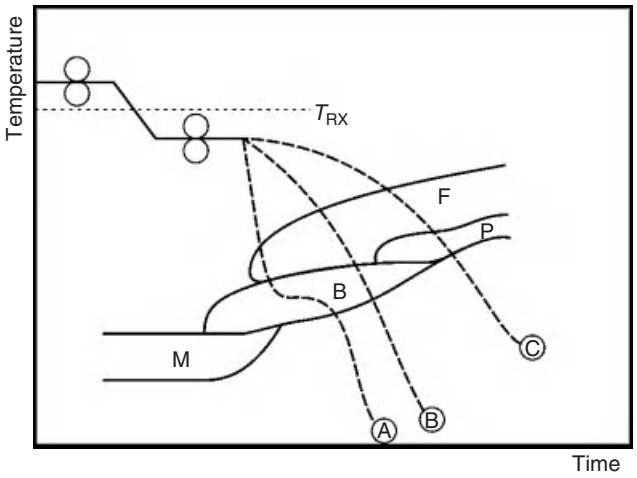

Figure 8.2 Schematic cooling strategies leading to ferritic–bainitic and ferritic–pearlitic microstructures. A, B, C are different cooling strategies. M, martensite; B, bainite; P, pearlite; F, ferrite; T_{RX}, recrystallization temperature.

during recrystallization. The recrystallization is retarded, leading to a higher deformed austenite before recrystallization and a finer microstructure subsequent to this transformation. Besides, niobium leads to precipitation hardening in both austenite and ferrite [3].

The application of high-strength steels is usually accompanied by thinner rolling products. Within the accelerated cooling process, thinner plates are more sensitive to distortion. Owing to this, a subsequent dressing process may become necessary [3].

8.3.5
U- and O-Forming

Plate forming into an open-seam pipe is performed in two main steps. These are shaping into a U-canning, followed by the second step in which the ''U'' is formed into an ''O''. The U-O-ing process is usually applied in the production of longitudinally welded pipes for a diameter range from approx. 400 to 1620 mm and length up to 18 m. The plate thickness range from 6 to 40 mm [44].

The main advantage of U-canning is its uniform and crease-free bent. From a ''U'' the shape of the open-seam pipe can best be produced. Using thin and high strength plates spring back becomes a relevant issue after bending. Therefore the U-ing has to be divided into two steps. At first, the plate is vertically bent with a plunger through two bending rolls and then is horizontally compressed by these bending rolls to compensate spring back. Then plates previously shaped into U-cannings are pressed along their entire length to form open-seam pipes in a single operation [44].

8.3.6
Welding

Usually, two different welding processes are applied for welding of pipelines, namely, submerged arc welding (SAW) for the longitudinal seam welding during the production process and gas metal arc welding (GMAW) for the circumferential seam welding in field during pipe laying. Arc welding processes provide a high energy input during a relative short time, bringing the material to melt and solidify fast, and are cost effective in terms of a high production rate. This process leads to the formation of three different zones, namely, weld bead, coarse grain zone, and fine grain zone, causing stress/strain concentrations near the weld bead and a distortion of the welded structure.

8.4
Experiments

8.4.1
Dilatometer Experiments

In order to analyze the transformation behavior, dilatometer experiments have been carried out on a *BÄHR DIL-805A/D* with machined samples of 9 mm × 4 mm × 1 mm size. Time–temperature transformation (TTT) diagrams are recorded for continuous heating and continuous cooling. Reheating experiments allow monitoring of the pearlite dissolution, and, eventually, annealing experiments serve to analyze the grain growth behavior (Figure 8.3).

For continuous heating, heating rates between 0.1 and 600 K s^{-1} were applied. For continuous cooling, each sample was austenitized at 1000 °C for 5 min and subsequently cooled at 14 different cooling rates down to room temperature. The change in the sample length was recorded as the function of temperature and the transformation start and end temperatures were determined. The cooled samples were prepared for metallographic analysis and etched with nitric acid to determine the phases present in the respective samples and the microhardness.

The pearlite dissolution during reheating was examined as follows. Samples were heated at 1 K s^{-1} to temperatures between 700 and 1200 °C. When the specified temperatures were reached, the samples were subsequently quenched to room temperature. This procedure allows monitoring the pearlite dissolution since after quenching the austenitized areas form martensite or remain as retained austenite, depending on the carbon concentration. The samples were prepared for metallographic analysis and etched with nitric acid, making it possible to reveal the former austenite grains and retrace the pearlite dissolution.

Annealing experiments were carried out at different temperatures in the austenite region to investigate the grain growth behavior. The samples were heated at a rate of 10 K s^{-1} to 950, 1050, 1100, and 1150 °C and quenched directly after reaching the specified temperatures as well as after dwell times of 10, 120, 600, 1000, and 2500 s, respectively. The quenched samples were prepared for metallographic analysis and

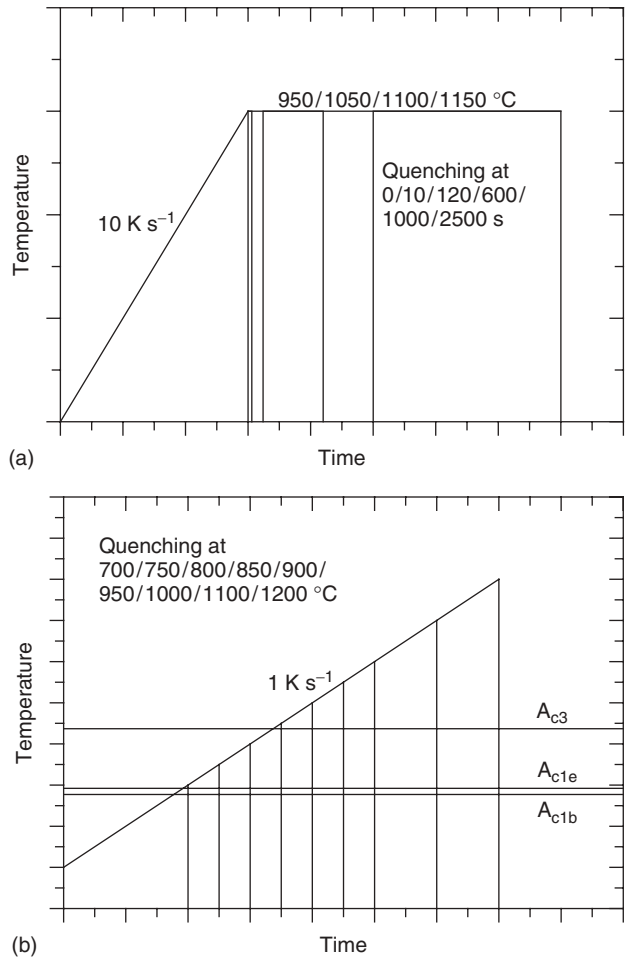

Figure 8.3 Schematic experimental thermal profiles for the grain growth (a) and the pearlite dissolution experiments (b). Displayed are the respective heating rates, holding temperature, and quenching temperature as well as holding and quenching times.

etched in picric acid to reveal the prior austenite grain boundaries. The austenite grain size was determined based on the metallographic analysis using the linear intercept method in agreement with the standard [8].

8.4.2
Compression Tests to Determine Flow Curves and DRX Kinetics

To characterize the material's dynamic recrystallization (DRX) behavior, a series of compression tests were conducted in which cylindrical specimens of 10 mm in

diameter and 15 mm in height were compressed. A more detailed description of the testing series, the materials model, and its parameter determination are given in the test case gearing component in Chapter 9.

8.4.3 Tensile Tests

Tensile tests are the most common experiments used to characterize the mechanical behavior of materials. Quasi-static tensile tests were performed for the underlying steel at room temperature in order to derive its elastoplastic constitutive law. The experiments were carried out on a *ZWICK 100* testing machine with an optical strain measurement device. Four samples were tested at room temperature in rolling and transverse directions. The sample geometry was chosen according to the standard [9], with a sample length of 40 mm and a diameter of 8 mm.

8.4.4 Welding Experiments

Welding experiments were carried out in order to calibrate the welding simulations. Within the experiments, the weld seam geometry and rated RMS (root mean square) current and voltage are measured to determine the energy input. Temperature measurements were used to simulate the microstructure evolution in the HAZ (heat-affected zone) and to verify the simulated heat and temperature distributions. During solidification of the weld pool, a columnar grain substructure develops in the weld seam. In the HAZ, grain growth, recrystallization, phase transformations, precipitation formation, and dissolution take place, which are all reflected in the inhomogeneous microstructure of the weld zone, for example, of a weld seam after GMAW of a steel plate (Figure 8.4). Qualitatively different microstructures can be identified as a function of distance to the weld pool. In the HAZ below

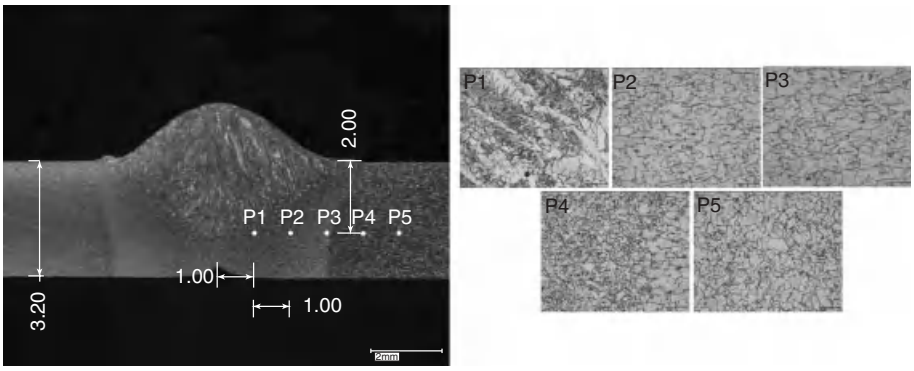

Figure 8.4 Micrograph (cross section) of a GMA weld in a DC01 steel plate. Microstructure simulations are performed for different points.

the weld pool can be roughly separated into a coarse and a fine grain zone. The achievable mechanical properties of the welded structures are essentially affected by the inhomogeneous microstructure in the weld seam.

Geometric measurements of the experimentally welded pipes were carried out using an optical 3D scanner before and after the welding process. With a two-camera system, the scanner captures the displacement of the pipe in comparison with a stripe pattern; this is cast by a projector onto the surface of the object to be measured. A juxtaposition of individual measurements is possible by bonded reference points. The recorded digital data points are the basis for subsequent cross-linking and further analysis.

8.5
Experimental Process Chain

To validate any simulation result, it is indispensable to directly compare simulations with real processes. For this purpose, an entire process chain was designed on a laboratory scale. This process chain consists of all necessary production steps to manufacture a longitudinal weld pipe. Figure 8.5 gives an overview of the conducted multipass hot rolling schedule including reheating steps. During this process rolling, forces and temperatures were measured.

Figure 8.6 illustrates the temperature evolution and the maximal rolling forces gained during the process. The temperatures were measured using pyrometers in front of and behind the rolling gap. Intermediate dwell times, in which the temperature could not be measured, are interpolated.

Further process parameters are summarized in Table 8.2. After the last rolling pass, the strip was rested and cooled down to room temperature.

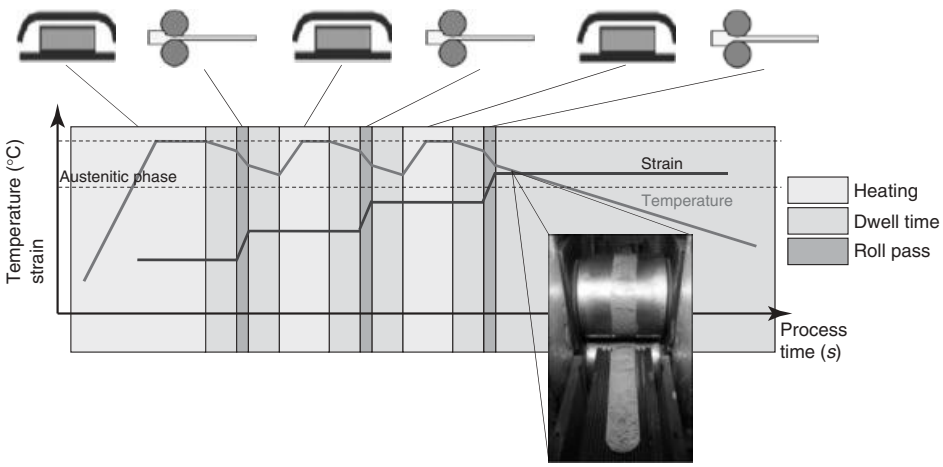

Figure 8.5 Schematic presentation of the experimental multipass hot rolling process chain.

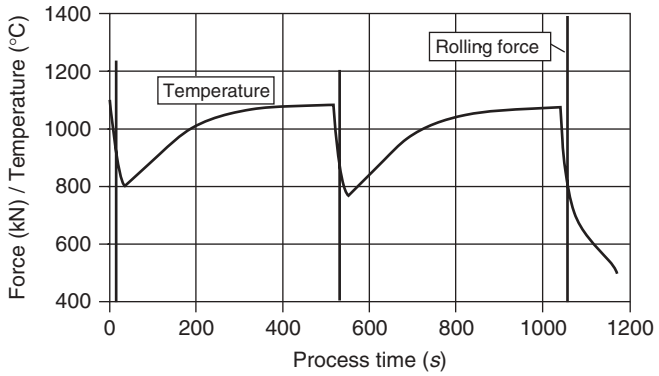

Figure 8.6 Measured rolling forces and temperature evolution during multistep hot rolling.

Table 8.2 Process parameters of the experimental process chain.

Initial strip height	19.9 mm	–	–
Height reduction	2.9 mm (pass 1)	7.6 mm (pass 2)	5.5 mm (pass 3)
Final height	4 mm	–	–
Diameter of rolls	200 mm	–	–
Rotation velocity	0.16 min^{-1}	–	–
Intermediate annealing	$T = 1150\,^{\circ}C$	$t = 480$ s	–
Measured values	Rolling forces	Strip temperature before roll gap	Strip temperature behind roll gap

After reaching room temperature, the strip was cut and formed in a U-O-ing process to become an open-seamed pipe (Figure 8.7). Here, the forces and spring back were measured.

As a last step of the experimental process chain, the longitudinally seamed pipe was gas metal arc welded. Temperature measurements were carried out, as well as voltage and current measurements, in order to calibrate the energy consumption. Subsequently, metallographic analyses were carried out.

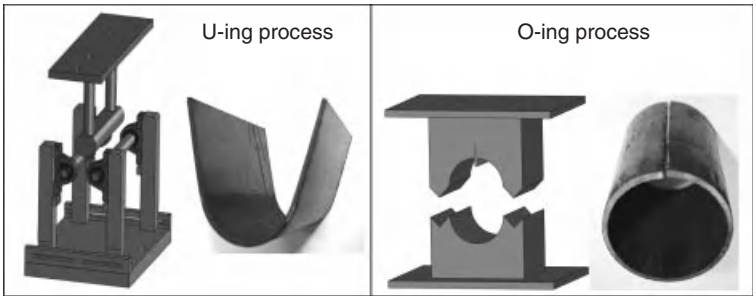

Figure 8.7 U-ing and O-ing process on a laboratory scale.

8.6
Simulation Models and Results

8.6.1
Reheating

8.6.1.1 Phase-Field Simulations of Austenite Formation during Reheating

The phase transformation from ferrite–pearlite to austenite has been studied on the microscale by means of MICRESS simulations, making it possible to locally consider pearlite dissolution as well as carbon distribution in the austenite formed. Boundary conditions for these simulations are provided from simulations on the macroscale in the form of space-resolved time–temperature profiles. An experimental micrograph is digitalized and used as an initial condition for the simulations (Figure 8.8).

The use of digitalized images ensures that the simulated microstructures exhibit a sufficiently realistic grain size distribution. The phase fraction of pearlite in the utilized steel was measured by means of image analysis and found to be approximately 14.0%.

The MICRESS simulations are performed using linearized phase diagrams as described in [10, 11] and assuming paraequilibrium conditions (Figure 8.9). Hence, carbon is the only element that is supposed to redistribute at the phase interfaces. As input parameters, the respective slopes of the linearized phase lines are entered, as well as the carbon concentrations at certain reference temperatures. Besides linearized phase diagrams, Thermo-Calc coupling is used in order to provide reasonable diffusion parameters.

The rate of a phase transformation is, in addition to the nucleation conditions, also determined by the interfacial energies σ_{ij} and mobilities μ_{ij} between the phases present. These are calculated according to Eq. (8.1b and b) and parameters from

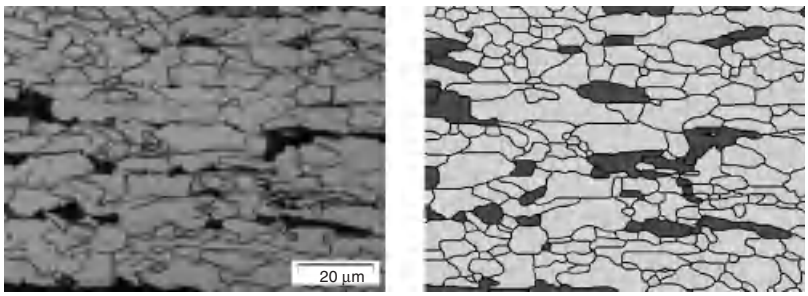

Figure 8.8 Real metallographic picture of the steel grade (a) and the corresponding digitalized microstructure for use in MICRESS simulations (b). Ferrite corresponds to the light-colored areas, while pearlite is identified by dark-colored regions.

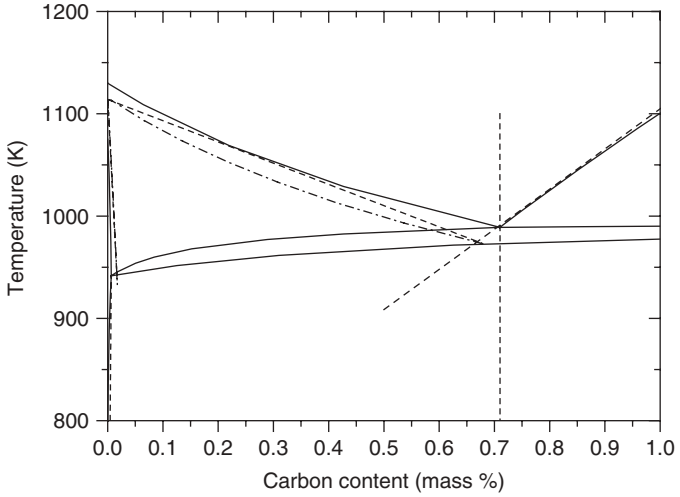

Figure 8.9 Linearized phase diagram describing the respective phase stability regions as input for MICRESS under paraequilibrium conditions. The displayed phase diagram was calculated using Thermo-Calc [12].

Ref. [13] that are summarized in Table 8.3.

$$\mu_{ij}^{0} = \frac{d_{ij} \cdot \nu_D}{k_B \cdot T} \tag{8.1a}$$

$$\mu_{ij} = \mu_{ij}^{0} \cdot \exp\left(-\frac{Q_{ij}}{R \cdot T}\right) \tag{8.1b}$$

8.6.1.2 **Results of the Phase-Field Simulations during Reheating**

The multicomponent and multi-phase-field model of MICRESS was used to simulate the transformation of the ferritic–pearlitic microstructure into austenite during the reheating process at different heating rates. Therefore, a real micrographic image was digitalized and transferred into MICRESS and the present phases were assigned. Moreover, the presence and shape of various additional microstructure

Table 8.3 Parameters for microstructure simulations taken from [13] for the respective interface combinations present.

Parameter	f:f	f:a	a:a	p:p	f:p	a:p
d_{ij} (Å)	2.4	2.5	2.6	3.9	3.2	3.3
Q (kJ mol^{-1})	160	160	185	200	200	162.5
σ (J m^{-2})	0.5	0.4	0.7	1	0.9	0.9

f, ferrite; a, austenite; p, pearlite.

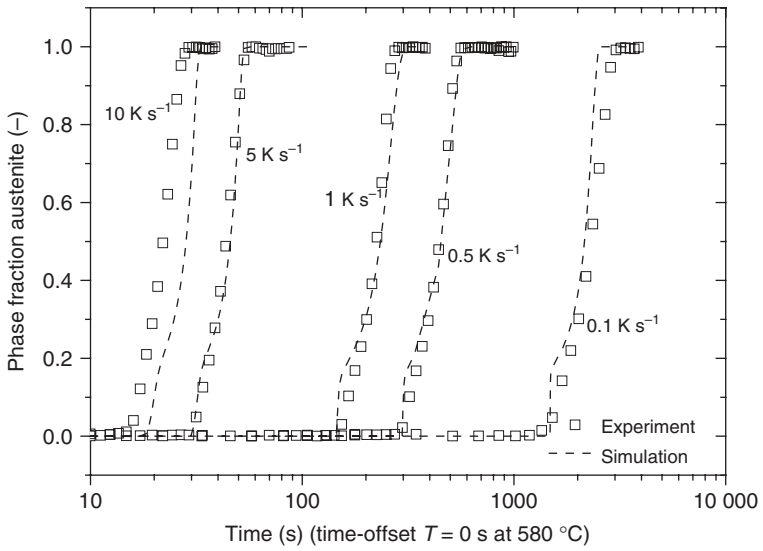

Figure 8.10 Phase fraction curves at different heating rates as function of the logarithmic representation of the time. The time was offset to 0 at 580 °C.

features, such as precipitates, can be also predicted. The temperature-dependent mobility data additionally allows consideration of the austenite grain growth and coarsening phenomena during and after the transformation in case an initial representative microstructure with a sufficient number of grains is available.

Figure 8.10 shows phase fraction curves of austenite from experimental data and MICRESS simulations at different heating rates. Especially in the range of medium heating rates, the simulated curves match the experimental curves quite well. For higher and lower heating rates, the deviation increases moderately. For a high heating rate of 10 K s^{-1} the transformation onset and downset temperatures are slightly overestimated, while for a low heating rate of 0.1 K s^{-1} these transformation temperatures are slightly underestimated. Nevertheless, the applied model exhibits a sufficient accuracy in the relevant range of cooling the respective heating rates and thus is applicable for most technical heating processes.

Experiments, as described in Section 8.4, were carried out in order to monitor the dissolution of the ferritic–pearlitic microstructure and the transformation into austenite. The metallographic images at several quenching temperatures are compared to simulated microstructures in Figure 8.11. MICRESS simulations were carried out on the basis of the same conditions as applied in the experiments. Results are shown at the same temperatures. The general phenomena of the transformation such as the transformation from the pearlitic phase fractions into carbon-rich austenite or the subsequent or partly even simultaneous nucleation of austenite at the grain boundaries of the surrounding ferrite matrix can be described well using the phase-field model.

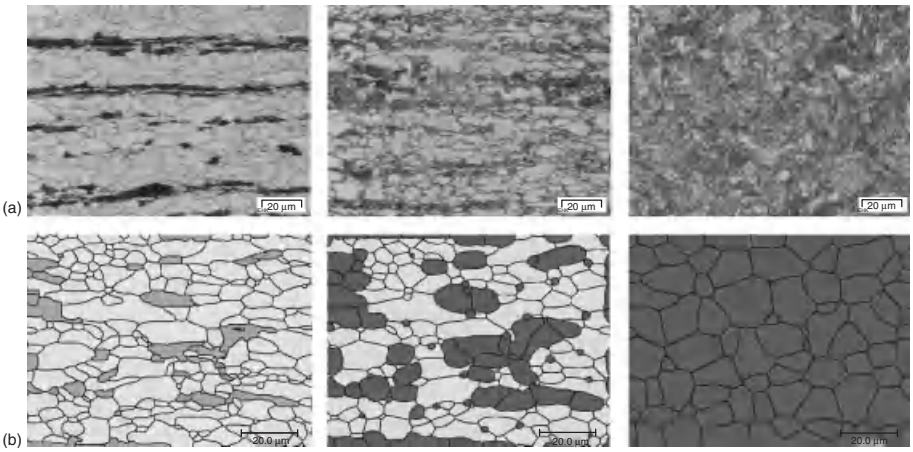

Figure 8.11 Metallographic images from dilatometer experiments showing different states of austenite formation and ferrite–pearlite dissolution (a) and microstructures simulated with MICRESS (b) at 700, 800, and 950 °C (from left to right). Heating rate was 1 K s^{-1}.

Subsequently, the present ferrite phase is consumed by growth of the already formed austenite grains and by nucleation of further austenite grains. Eventually, between 900 and 950 °C, the smaller austenite grains disappear and the larger ones grow by ripening, leading to a coarser final microstructure. Even without an exact adjustment of parameters concerning, for example, the nucleation and the interfacial mobility, the presented model already provides reasonable and valuable results.

8.6.1.3 Reheating Simulations with CASTS

CASTS simulations are used to simulate the macroscopic reheating process. The heat impact on a slab on the laboratory scale as well as the phase transformation and effect of grain growth during reheating are modeled.

The grain growth can be entered following the Leblond model [14] by a numerical fit of the experimentally determined data at different annealing temperatures. The diffusion-controlled phase transformations are simulated based on a nonisothermal Avrami model. The foundations of this model are given in the following equations according to [15, 16].

$$\varphi_k = \varphi_k^{\max}\left(\varphi_j^{i-1} - \varphi_k^{i-1}\right)\left(1 - \exp\left(b_k\,(T)\,\tau_i^{\,n_k(T)}\right)\right) \tag{8.2a}$$

$$\tau_i = \Delta t_i + \left(\frac{-\ln\left(1-\varphi_k^{(i-1)}\right)}{b_k\,(T)}\right) \tag{8.2b}$$

$$n_k(T) = \frac{\ln\left[\dfrac{\ln(1-\varphi_s)}{\ln(1-\varphi_f)}\right]}{\ln\left(\dfrac{t_s}{t_f}\right)} \tag{8.2c}$$

$$b_k(T) = \frac{-\ln(1-\varphi_k)}{t_k^{n_k(T)}} \tag{8.2d}$$

Herein, φ is the volume fraction of the corresponding phase (lower index) and time step (upper index). τ is the theoretical time needed to form the volume fraction of the respective phase in the previous time step. The parameters b and n may be extracted from isothermal transformation experiment. The indices s and f indicate the start and finish time and volume fraction of the considered phase [16]. The continuous heating and cooling procedures are calculated in defined temperature increments. For each increment, a set of temperature-dependent Avrami exponents and factors are used to calculate the transformed fraction. Figure 8.12 shows the results obtained from experiments and simulations performed with different heating rates.

8.6.1.4 **Results of the CASTS Reheating Simulations**

A time–transformation diagram for the heating process was modeled on a geometric model of the slab. The results from dilatometer experiments and simulations performed with CASTS are compared in Figure 8.13. The Avrami coefficients assumed for the simulations allowed for a quite accurate reproduction of the experimental observations.

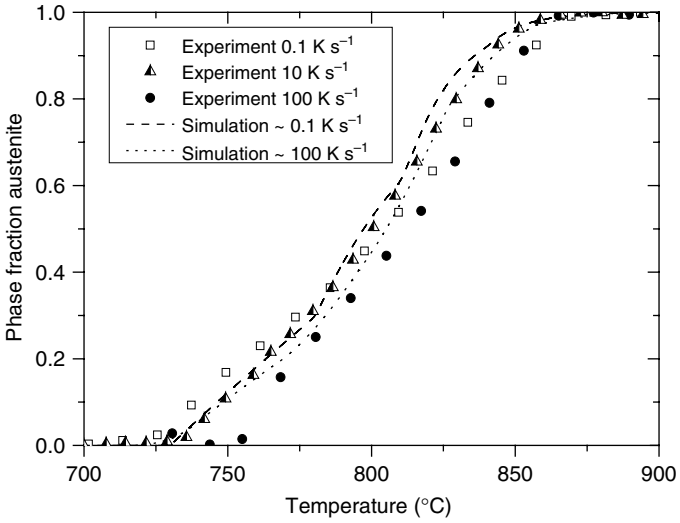

Figure 8.12 Simulated temperature-dependent austenite phase fractions at different heating rates.

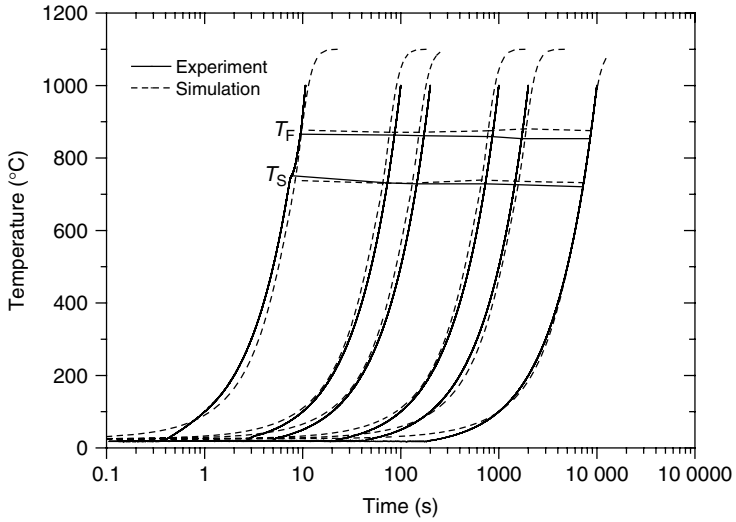

Figure 8.13 Time–temperature transformation diagram for heating as measured in a dilatometer (solid lines) and as calculated with the calibrated model in CASTS (dashed lines).

This provides a model capable of describing the phase transformation on the macrolevel on the basis of point-resolved temperature profiles. This model enables to monitor the time–temperature profile of an experimental assembly and, simultaneously, to observe the related locally occurring phase transformations (Figure 8.14).

The evolution of grain size is included into the process simulation using the Leblond model [14] fit to experimental data. Respective heating simulation results prove that the presented approach is able to model the material's reaction to heat exposure. The phase transformations were modeled on the microscopic and macroscopic scale, and both simulation tools, MICRESS and CASTS, offer the possibility of monitoring the grain size evolution at the micro- or macroscale,

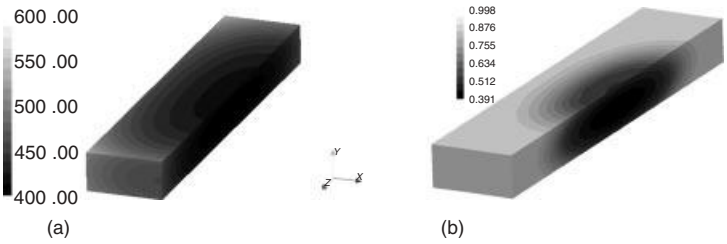

Figure 8.14 Profiles of the temperature (a) and the austenite phase fraction (b) within the steel slab during the heating process.

respectively. Time–temperature profiles from macroscopic simulations can be used as boundary conditions for MICRESS simulations, rendering it possible to track the microstructure evolution on every integration point of the pipeline tube. The information obtained from these simulations such as grain size, grain size distribution, temperature, and phase distribution in the slab can be forwarded to subsequent simulations.

8.6.2 Hot Rolling

To capture microstructure evolution, including dynamic recrystallization, for a high number of rolling passes, models that represent the average state of the microstructure and its effect on the mechanical response are used. The modeling of these processes generally involves events occurring on the microscale such as change in grain size and recrystallized fraction. Many models also include measures of the dislocation density [17].

The three-pass hot rolling process at the laboratory scale was simulated using the commercial finite element (FE) code DEFORM-2d^{TM}. Therefore, not only the process values, for example, rolling forces, but also the microstructure evolution in the work pieces were taken into consideration. Hence, a microstructure-based flow stress model capable of considering the static and dynamic recrystallization kinetics and grain growth and its effect on the flow stress was used. Table 8.4 illustrates the specific equations used to describe the DRX behavior with a link to the material's flow stress being determined from a series of compression tests.

An initial grain size of about 80 μm was determined metallographically. The specimens were compressed to the strain of 0.75 at constant true strain rates varying from 0.01 to 100 s^{-1} and temperatures varying from 750 to 1200 °C. The parameters determined from this testing series are summarized in Table 8.5. Figure 8.15 illustrates the experimental flow curves from 800 to 1200 °C at various strain rates (black) in comparison with the model predictions in terms of flow stresses and DRX kinetics.

The static recrystallization (SRX) model used to predict the material's softening during reheating was investigated by Minami and Sicilliano. The equations used, including their parameters, are illustrated in Table 8.6.

8.6.2.1 Results of the Hot Rolling Simulations

FE simulations of the multipass rolling schedule (Figure 8.16), including the intermediate annealing steps, were simulated using the commercial FE tool Deform 2d with the included AVRAMI-based microstructure model. The model was deduced from the microstructure-based flow stress model, as described above.

FE simulations of the multipass rolling schedule, including the intermediate annealing steps, were simulated using the commercial FE tool Deform 2d along with the AVRAMI-based heat treatment model described in Section 8.6.1.

Table 8.4 Equations used to describe the DRX behavior.

Phenomenon	Equation	
Zener–Hollomon parameter	$Z = \dot{\varepsilon} \exp\left(\frac{Q_w}{RT}\right)$	(8.3)
Peak strain	$\varepsilon_p = a_1 d_0^{a2} Z^{a3}$	(8.4)
Critical strain	$\varepsilon_c = a_4 \varepsilon_p$	(8.5)
Steady-state strain	$\varepsilon_{ss} = e_1 \varepsilon_p + e_2 d_0^{e3} Z^{a4}$	(8.6)
Work hardening	$\frac{\sigma}{\sigma_p} = \left[\frac{\varepsilon}{\varepsilon_p} \exp\left(1 - \frac{\varepsilon}{\varepsilon_p}\right)\right]^c$	(8.7)
Hardening coefficient	$C = C_1(1 - \exp(C_2 \cdot \ln Z^{C_3}))$	(8.8)
Maximum flow stress	$\sigma_p = \frac{f_1 \cdot Z^{f2}}{\sin h\,(f_3)}$	(8.9)
Fraction of dynamic recrystallization	$X_{DRX} = 1 - \exp\left[d_1 \left(\frac{\varepsilon - \varepsilon_c}{\varepsilon_{ss} - \varepsilon_c}\right)^{d2}\right]$	(8.10)
Dynamic recrystallized grain size	$d_{DRX} = b_1 \cdot Z^{b2}$	(8.11)

Table 8.5 DRX parameters – X65.

Parameters			
$Q_w = 385611\,\mathrm{kJ\ mol^{-1}}$	–	–	–
$a_1 = 1.404E3$	$a_2 = 0$	$a_3 = 0.166$	$a_4 = 0.8$
$b_1 = 5230$	$b_2 = -0.15$	–	–
$d_1 = -0.35$	$d_2 = 2.5$	–	–
$e_1 = 1.5$	$e_2 = 8.731E{-}6$	$e_3 = 0$	$e_4 = 0.2783$
$f_1 = 2.011E{-}3$	$f_2 = 0.187$	$f_3 = 0.0102$	–
$C_1 = 0.5$	$C_2 = -25608E6$	$C_3 = -6.616$	–

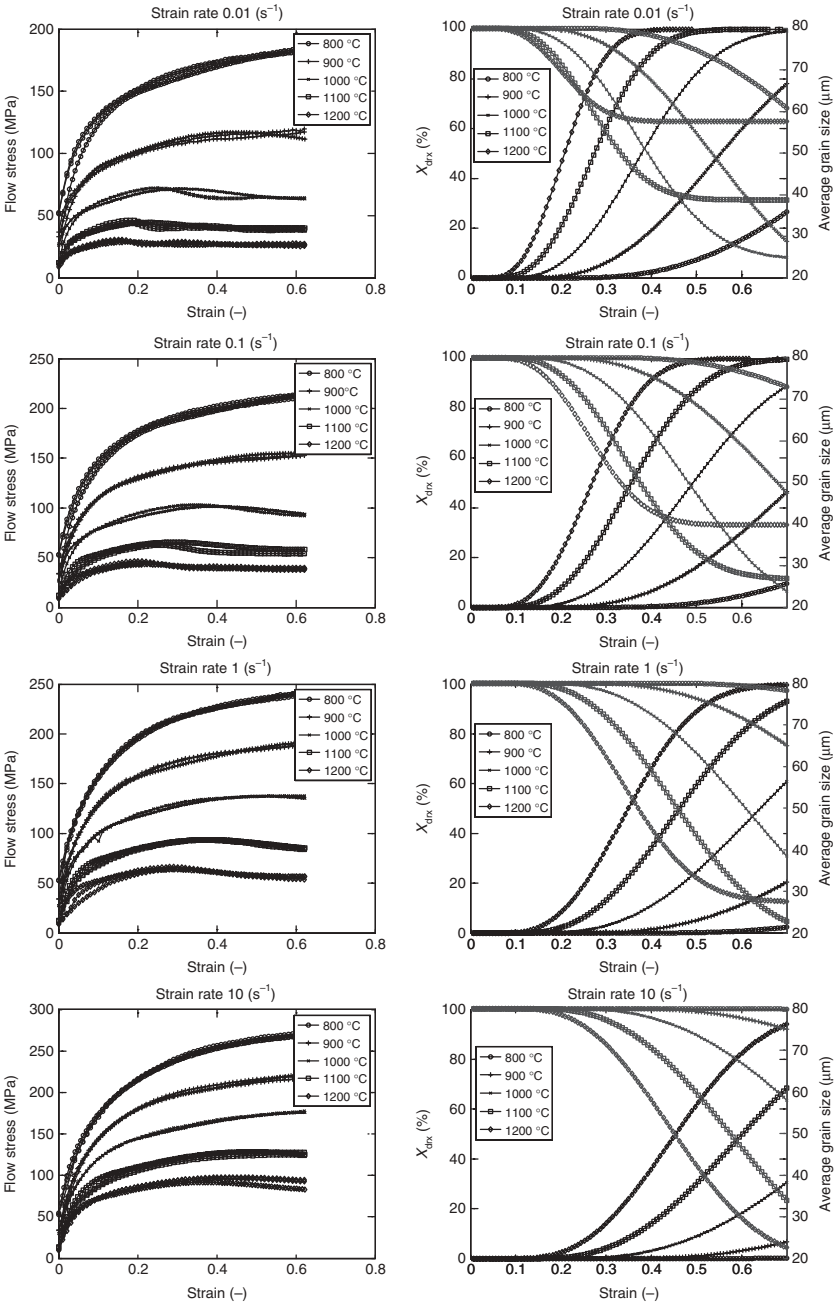

Figure 8.15 Experimental flow curves (denoted by symbols) of X65 and results calculated by the microstructure model (lines). An almost perfect match can be observed.

Table 8.6 SRX model investigated by Minami and Sicilliano [18].

Phenomenon	Equation
Fraction of static recrystallization	$X_{SRX} = 1 - \exp\left[-\ln 2\left(\frac{t}{t_{0.5}}\right)^{1}\right]$ (8.12)
Time to gain 50% volume fraction	$t_{0.5} = (-5.24 + 550 \times 0.041)10^{-18} \cdot \varepsilon^{(-4+77\times0.041)}$ $\cdot d_0^2 \cdot \exp\left(\frac{330000}{RT}\right)$ (8.13)
Recrystallized grain size	$d_{SRX} = 1.9 \cdot \varepsilon^{-0.67} \cdot d_0^{0.67}$ (8.14)

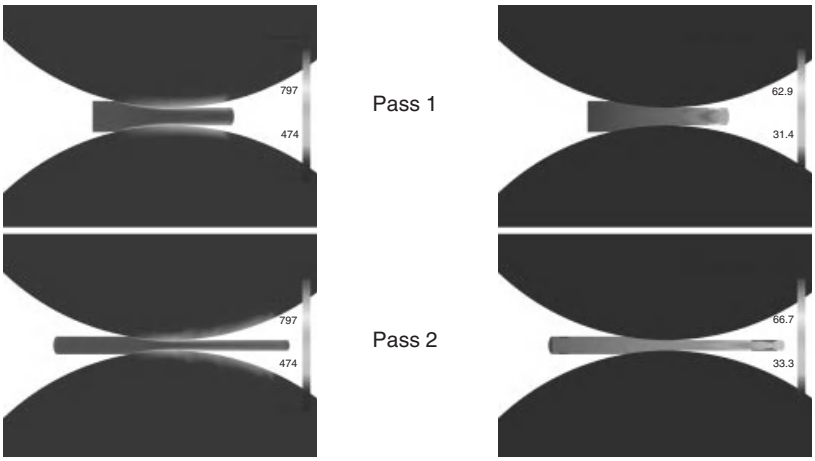

Figure 8.16 Forming simulation results showing temperature distribution (a) and grain size distribution (b) during hot rolling passes 1 and 2.

8.6.3 Cooling and Phase Transformation

8.6.3.1 Phase-Field Simulations of Austenite to Ferrite–Pearlite Transformation

Phase-field simulations for the austenite to ferrite–pearlite transformation were performed using the phase-field code MICRESS. It provides information about the processed microstructure for subsequent microscopic materials flow description and for expressing effective stress–strain curves via virtual testing of representative

volume elements (RVEs). Boundary conditions according to the linearized phase diagram and the mobilities were analogous to those used within the heating simulations. Diffusion parameters were provided by Thermo-Calc coupling. The simulations are performed from initially homogeneous austenite microstructures. During cooling, ferrite is formed, leading to an enrichment of the remaining austenite. Subsequently, the enriched austenite forms pearlite and is considered as an ''effective'' phase in the simulations.

8.6.3.2 Results of the Phase-Field Simulations for Ferrite–Pearlite Formation

Phase-field simulations of the ferrite and pearlite formation from austenite during cooling were performed again using the multi-phase-field model of MICRESS. An undeformed homogeneous austenitic microstructure is studied, taking into account the impact of the hot rolling passes only in terms of austenite grain size (fully recrystallized austenite) (Figure 8.17). The ferrite formation leads to a carbon enrichment of the austenite phase and to a subsequent transformation of the enriched austenite into pearlite.

Figure 8.18 shows the carbon profile for a magnification of the simulation domain shown in Figure 8.17. Along the displayed lines within the pictures, virtual line scans were evaluated for different time steps (Figure 8.19). With increasing movement of the grain boundary, the carbon content increases in the remaining austenite regions. Furthermore, the carbon content in the austenite regions is higher at the grain boundaries, while it is lower in the grain center. The carbon content of the growing pearlite is in agreement with Thermo-Calc calculations, predicting the eutectoid point for this steel to be at 0.7% carbon.

Metallographic analyses reveal a pearlite content of approximately 14% for the investigated steel exhibits. The microsimulations predict a slightly lower pearlite content of approximately 12%.

The multiphase model is able to qualitatively predict the ferrite and, subsequently, the pearlite formation from a homogeneous austenite. The carbon content in both ferrite and pearlite is reasonably described as well as the fraction of pearlite, when comparing to metallographic images.

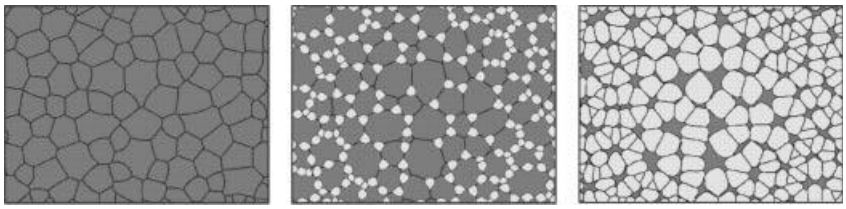

Figure 8.17 Formation of ferrite and pearlite grains from a homogeneous austenitic microstructure. The figures show (a) an initial austenite microstructure (dark gray), (b) the nucleation of ferrite (light gray) preferably at triple junctions and in interface regions, and (c) the growth of ferrite grains and the diminishing of austenite. The carbon-enriched austenite eventually transforms into pearlite.

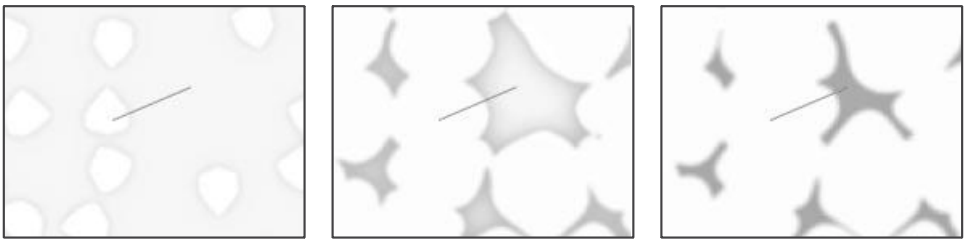

Figure 8.18 Line scans along a ferrite–austenite grain boundary during cooling, showing the carbon enrichment in the yet present austenite grain. Light areas correspond to regions with low carbon concentrations, whereas dark areas represent regions with higher carbon concentrations.

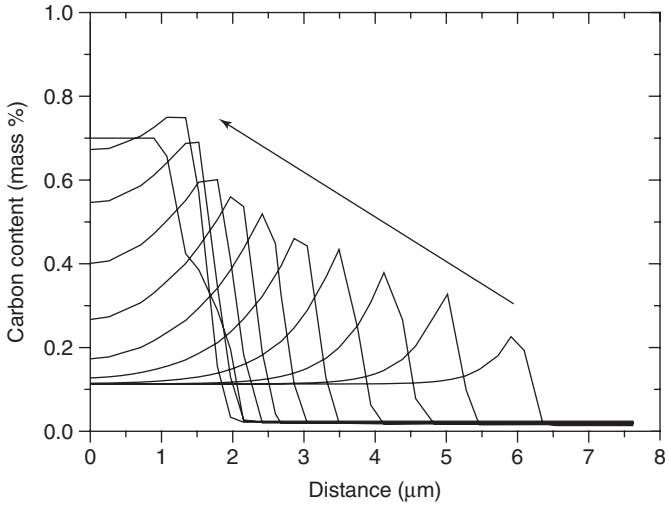

Figure 8.19 Carbon concentration in the ferrite–austenite interface region along a virtual line scan (Figure 8.18) during the growth of a ferrite grain into a shrinking austenite grain. The arrow indicates the direction of the interface movement.

8.6.3.3 **Cooling Simulations Using CASTS**

The software CASTS was used to simulate the phase transformations occurring during cooling. Diffusion-controlled phase transformations, following the principles presented before, are described. Moreover, the software is able to consider thermal or mixed mode phase transformations according to, for example, models from Koistinen and Marburger [19].

Figure 8.20 shows a comparison of experimentally determined phase fractions as a function of temperature and simulated ones at denoted cooling rates. Simulated is the austenite to ferrite and pearlite transformation.

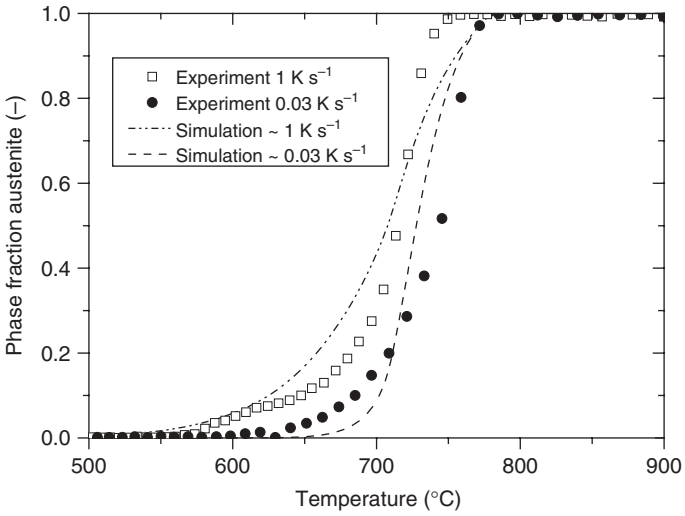

Figure 8.20 Experimental and simulated austenite phase fractions at different cooling rates.

8.6.3.4 Results of the Cooling Simulations with CASTS

Cooling simulations at the macroscopic process scale were carried out with CASTS. The model was calibrated for the diffusion-controlled phase transformation from austenite into ferrite and pearlite.

An experimentally determined TTT diagram for the austenite to ferrite–pearlite transformation has been compared to the calculations (Figure 8.21). The transformation start temperature (T_s) is quite accurately determined, while the transformation finish temperature (T_f) is overestimated for slow cooling rates and underestimated for high cooling rates. Nevertheless, the implemented model is sufficiently accurate for technical applications.

8.6.4 U- and O-Forming

8.6.4.1 Multiscale Simulation for Flow Curve Evaluation

The multiscale simulation is based on the ambition to describe the macroscopic equivalent stress–strain curves of arbitrary steels just by the knowledge of their chemical composition and microstructure. In the present investigation, it is assumed that a ferritic–pearlitic microstructure, as shown in Figure 8.1, is obtained after the cooling process. To describe its elastoplastic nonlinear behavior, material models have to be developed or specified in order to describe the mechanical response of each single phase.

Therefore, the concept of RVEs is introduced, as outlined in Chapter 5. On the RVE, a precise description of the phase distribution and their morphology is achieved. The single-phase models need to take into account the microstructural features such as grain size, interlamellar spacing, and chemical composition.

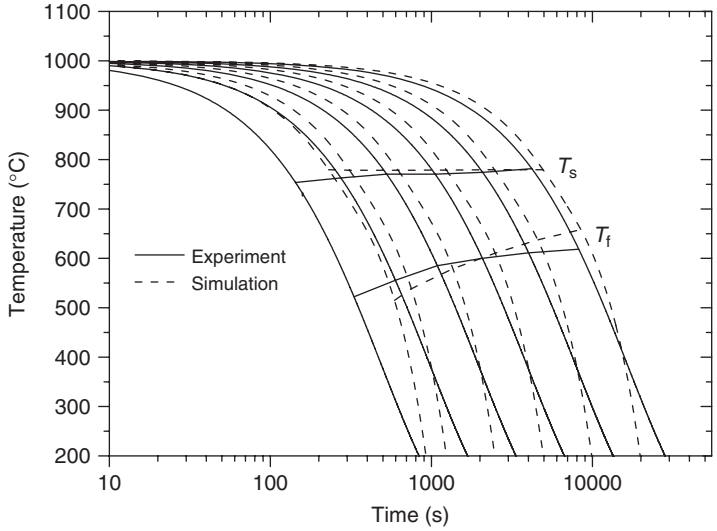

Figure 8.21 Experimental and simulated time–temperature curves from dilatometer experiments and CASTS simulations, including transformation start and finish temperatures.

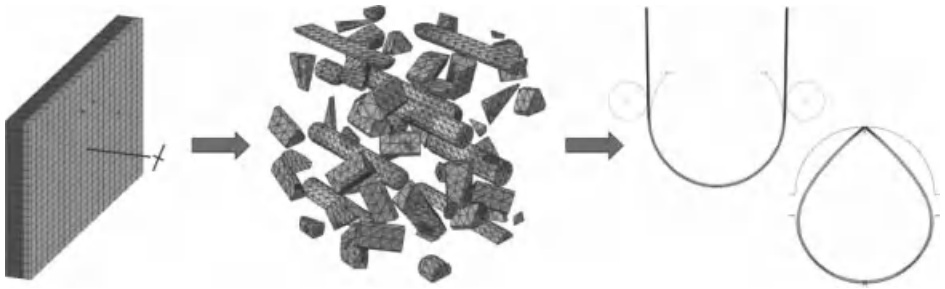

Figure 8.22 Schematic representation of the multiscale approach built of three scales: a ferrite–cementite bilamella on nanoscale, an RVE on the microscale, and the macroscopic forming simulations.

In addition, as pearlite is a eutectoid phase and composed of alternate ferrite and cementite lamella, a new two-level homogenization procedure is introduced.

First, at the nanoscale, the bilamina ferrite/cementite is homogenized (Figure 8.22). Here, the derivation of the mechanical properties of the cementite phase is delicate. Indeed, since cementite is metastable at all temperatures with respect to graphite and its saturated solution in iron, it is not possible to produce a single-phase cementite test specimen. To circumvent this difficulty, the Hooke matrix of a single orthorhombic cementite crystal predicted by molecular dynamics calculations [20, 21] is adopted here. The effective anisotropic elastic properties of

the ferrite/pearlite bilamina are evaluated with HOMAT [22], whereas the effective elastoplastic stress–strain curves are determined by virtual tests with ABAQUS [23].

Then, at the microscale, the pearlite is treated as an equivalent anisotropic phase in an elastoplastic ferrite matrix. The phase fractions and morphologies of the ferrite and pearlite phases are evaluated from metallographic images and are introduced in the RVE generation, achieved with the commercial DIGIMAT FE software [24]. The microstructures generated in this way are random. Next, virtual tensile and shearing tests are performed with ABAQUS to derive the effective flow curves in each material's direction.

This two-level homogenization scheme thus allows the derivation of an equivalent homogeneous material description for the simulations formed on the macroscale. Figure 8.22 shows a schematic description of the three-level multiscale approach.

Elastic Properties of Ferrite and Pearlite The effective elastic properties of the pearlite phase are a result of the homogenization scheme applied on the ferrite and cementite bilamina at the nanoscale. The elastic behavior of ferrite is assumed to be isotropic, and the respective properties are 208 GPa for Young's modulus and 0.287 for Poisson's ratio. The elastic properties of the cementite, as extracted from *ab initio* calculations [20] and [21], are orthotropic. In addition, between ferrite and cementite, an orientation relationship exists. Following Zhang and Kelly [25], who observe only the Isaichev relationship ($[301]_{cem}//[1\bar{1}2]_{fer}$; $[010]_{cem}//[111]_{fer}$; $[\bar{1}03]_{cem}//[110]_{fer}$) for hypoeutectoid steels such as the underlying pipeline steel, we adopt this relationship between the ferrite and cementite phases. Then, a bilamina with 4 µm height and depth and a width of 0.23 µm was created and meshed with 3600 hexahedral elements according to scanning electron microscopic (SEM) analyses and subsequently subjected to tests covering all shear and stress directions. Owing to the cementite orthotropy and the existing orientation relationship, the predicted effective Hooke matrix of the bilamina is fully anisotropic with coupling terms between extension and shear. The in-plane shear stiffness is significantly lower than that of the transverse ones.

Plastic Properties of Ferrite and Pearlite In a further step, elastoplastic constitutive laws are formulated for both phases present. The ferrite flow curve is calculated according to Rodriguez' empirical model [26], defined by Eq. (8.15a–e), wherein the flow stress is described as a function of an intrinsic term σ_0 that is connected to the chemical composition and by the term $\Delta\sigma$ that describes the hardening behavior dependent on the dislocation density evolution. Moreover, a geometrical factor α, the Taylor factor M, the mean dislocation free path L, a factor k_2 referring to the recovery of dislocations, the shear modulus µ, and the Burgers parameter b are to be specified. The dislocation density evolution can be described as a function of the strain, making it possible to establish a correlation to plastic deformation. The mean free path is approximated by the mean grain size. In addition, this model allows the consideration of an initial dislocation density, which is useful because ferrite in pearlite is expected to exhibit higher dislocation densities than the ferritic matrix. It has to be mentioned that the Rodriguez model neglects the yield point

elongation due to Lüders band formation [27].

$$\sigma_f = \sigma_0 + \Delta\sigma = \sigma_0 + \alpha M \mu b \sqrt{\rho} \tag{8.15a}$$

$$\frac{\mathrm{d}\rho}{\mathrm{d}\gamma} = \left.\frac{\mathrm{d}\rho}{\mathrm{d}\gamma}\right|_{\text{stored}} - \left.\frac{\mathrm{d}\rho}{\mathrm{d}\gamma}\right|_{\text{recovery}} = \frac{1}{bL} - k_2\rho \tag{8.15b}$$

$$\Delta\sigma = \alpha M \mu b \left[\frac{k}{k_2}\left[1 - \exp\left(-k_2 M\varepsilon\right)\right] + \rho_0 \exp\left(-k_2 M\varepsilon\right)\right]^{0.5} \tag{8.15c}$$

$$k = \frac{1}{bL} \tag{8.15d}$$

$$\begin{aligned}\sigma_0 = {} & 77 + 80\%\mathrm{Mn} + 750\%\mathrm{P} + 60\%\mathrm{Si} + 80\%\mathrm{Cu} \\ & + 45\%\mathrm{Ni} + 60\%\mathrm{Cr} + 11\%\mathrm{Mo} + 5000\mathrm{N_{ss}} + 5000\mathrm{C_{ss}}\end{aligned} \tag{8.15e}$$

Similar to the flow curves for ferrite, the description of the pearlitic phase is given by the following expression:

$$\sigma_f = \sigma_0 + 3\mu b \lambda^{-1} + \alpha' \mu b \sqrt{\rho} \tag{8.16}$$

Hereby, the geometry factor is slightly different, and the pearlite lamellar spacing is considered. Note that in a similar approach from Suh *et al.* [28], the chemical composition is not considered but the interlamellar spacing S_0 and the cementite volume fraction F_Θ is accounted for in their empirical model formulated as a Swift equation. These empirical models provide reference curves for the novel multiscale approach presented here.

Within this scheme, pearlite was initially modeled as an elastic phase [29] and later more accurately as an elastoplastic phase. For the elastoplastic case, a further approximation is made: the orthorhombic cementite phase is assumed to be always elastic in contrast to an elastoplastic ferrite phase within the pearlite. Virtual tensile and shearing tests have been performed to derive the effective flow curve of the pearlite phase. These curves overestimate the empirical curves calculated according to Rodriguez and Gutierrez [26] and Suh *et al.* [28]. Therefore, it became necessary to also consider cementite as an elastoplastic phase [30]. Since cementite is metastable, its yield curve is deduced from nanoindentation tests. Adopting an orthotropic Hill's yield behavior for the cementite phase, the simulated flow curves of the pearlite phase are, for a given lamella spacing, between the two empirical predictions, as shown in Figure 8.23.

RVE Generation The RVE generation is based on the analysis of metallographic images. The volume contents of the two phases are evaluated using image analysis software. The microstructure shows a banded arrangement of pearlite in the undeformed state. Depending on the size and shape of the pearlite inclusions, they are classified into elongated and prismatic ones. Besides, the mean grain size is determined by the linear intercept method from the metallographic images in order to determine this parameter for the flow curve description of ferrite. The mean grain size was determined to be nearly 5 μm. Since the dislocation mean free path also determines the yield level of the material, the grain size was measured in

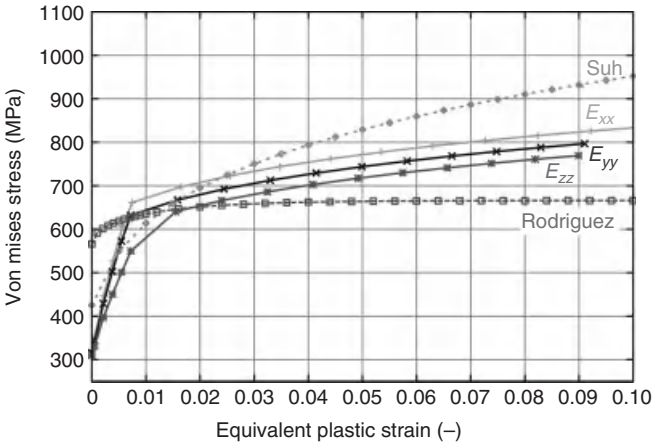

Figure 8.23 Effective predicted elastoplastic stress–strain curves of the pearlite phase for a lamella spacing of 0.23 µm compared to the models of Rodriguez and Gutierrez [26] and Suh *et al*. [28]. These curves are calculated with an orthotropic elastoplastic behavior of the cementite phase.

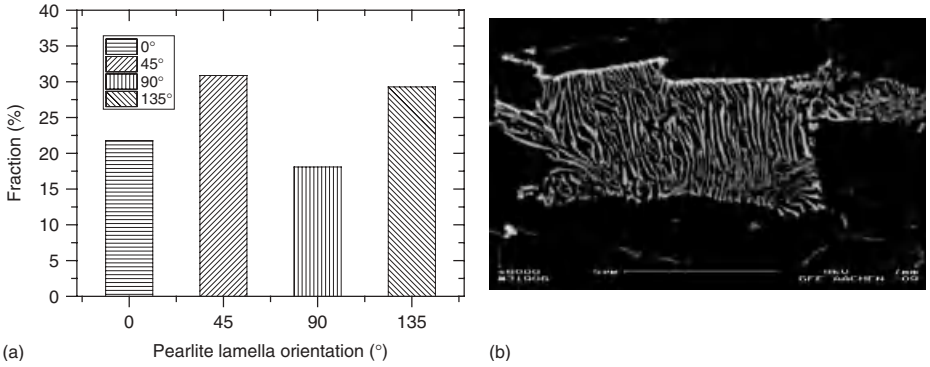

Figure 8.24 Distribution of the pearlite lamella orientation in the microstructure of Figure 8.1 (a) and SEM image showing the ferritic–pearlitic structure and the orientation variation in a pearlite inclusion (b).

the rolling direction as well as in the transverse direction and used in the flow curve descriptions for the respective loading directions. Electron microscopy analyses are carried out on the underlying steel in order to determine the mean interlamellar spacing (0.23 µm) within the pearlite phase. The respective width of cementite and ferrite in pearlite are derived either optically or from the thermodynamic relation of the eutectoid. The SEM images (Figure 8.24) were additionally used to characterize the pearlite phase in more detail. Therefore, the lamellar orientations in reference to the rolling direction X were evaluated and partitioned into four

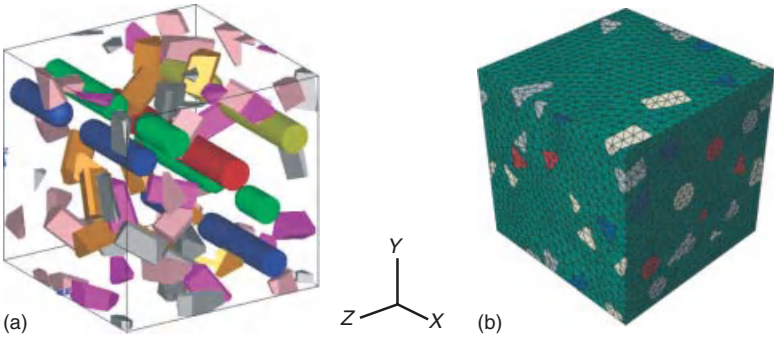

Figure 8.25 RVE of a microstructure generated using DIGIMAT FE, showing the morphology of pearlite. The different colors distinguish spherocylindrical, elongated pearlite from prismatic pearlite, and also the different lamella orientations of the pearlite (a); enmeshed RVE used for virtual test simulations with ABAQUS (b).

groups, namely, 0, 45, 90, and 135°. The RVEs have an edge length of 400 μm and are generated randomly by using DIGIMAT FE [24] (Figure 8.25). The resulting RVE has a pearlite content of 14.1 vol% and 6 elongated and 36 prismatic inclusions have been generated randomly within the volume. Both the inclusion types are then further divided into four groups based on the relative amount of the four distinguished pearlite lamella orientations.

Virtual Testing Virtual uniaxial tensile tests were performed using ABAQUS [23], with the aim of deriving the effective macroscopic flow curves of the pipeline steel on the basis of its microstructure description and the mechanical properties of each phase. The mesh, shown in Figure 8.25, is built of quadratic tetrahedral elements. Periodic boundary conditions are applied on the free surfaces of the RVE. Ferrite, in every simulation, was assumed to be fully elastoplastic, while pearlite was assumed to be either elastic or elastoplastic.

8.6.4.2 Results of the Multiscale Simulation for Flow Curve Evaluation

In order to conduct forming simulations taking into account different pearlite contents of the microstructures in the sheet center and border, the effective stress–strain curves of the underlying steel have to be determined. The new three-level multiscale approach outlined in Section 8.6.4.1 allows the performance of this essential upscaling step.

In order to investigate the influence of the distribution of the pearlitic phase, 10 randomly generated RVEs were subjected to virtual uniaxial tensile tests. The maximum difference between the calculated flow stresses is at the peak 25 MPa, qualifying the underlying approach and giving evidence of reproducibility of the obtained results.

Subsequently, for a given RVE microstructure, uniaxial tensile tests were performed with the effective anisotropic elastoplastic constitutive law of the

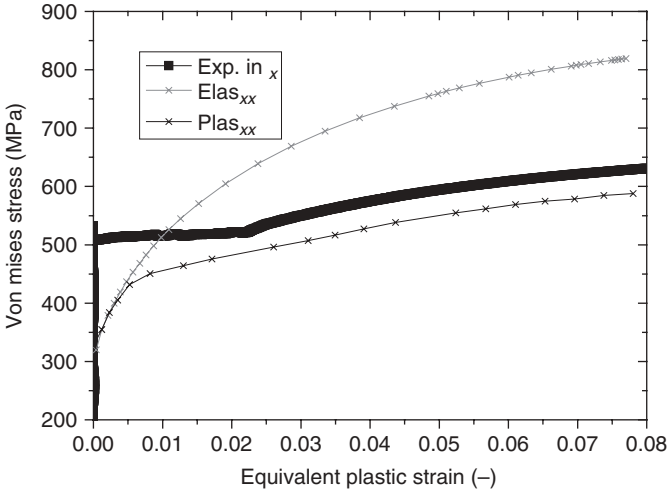

Figure 8.26 Influence of the elastic (Elas$_{xx}$) and elastoplastic (Plas$_{xx}$) constitutive laws on the effective yield behavior of the underlying dual-phase steel and comparison with the experimental curve (Exp).

pearlitic phase obtained by homogenization at the nanoscale of a full elastoplastic cementite–ferrite lamella (Figure 8.23). In Figure 8.26, the relation between the von Mises stress versus the equivalent plastic strain is shown for the elastic and elastoplastic pearlite behavior. Both the results are compared with the experimental tensile curve, obviously revealing that the elastic model predicts a highly stiff behavior. In contrast, the flow curve obtained on the basis of an elastoplastic modeled pearlite shows a slightly lower stress level and exhibits a similar hardening behavior (20 MPa) as compared to the experimental flow curve. Thus, the effective full elastoplastic materials law had to be adopted for the eutectoid pearlite phase. Note that in the results displayed in Figure 8.26, the Lüders band formation was neglected. In a further approach, a model was introduced based on [31] in order to take this phenomenon into account.

Uniaxial virtual tensile tests in transverse and longitudinal directions were also performed using the full elastoplastic materials model (Figure 8.27). In the transverse direction, a larger yield stress than in the rolling direction was obtained. However, at larger strains, a similar hardening behavior is obtained on different stress levels, being slightly higher than that in the transverse direction. The numerical results show a similar yield and hardening behavior as determined experimentally. In spite of that, independent of the tested direction, the predicted curves are slightly below the experimental curves. This deviation may originate from neglecting inhomogeneities in the ferrite matrix in the virtual tests. Recently, Kadkhodapour *et al.* [32] observed that the ferrite matrix in dual-phase steels reveals higher dislocation densities and hardening close to inclusions as compared to regions far from them.

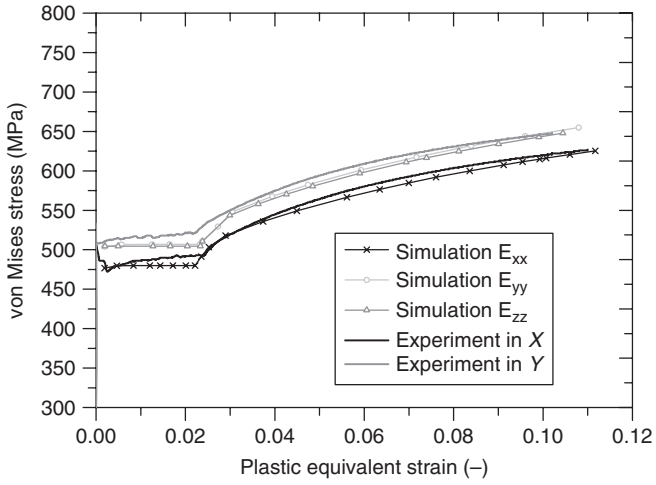

Figure 8.27 Experimental and predicted stress–strain curves of the ferrite/pearlite steel in rolling direction *X* and in the transverse direction *Y*. The results for the simulated ones in *Z* direction are also displayed.

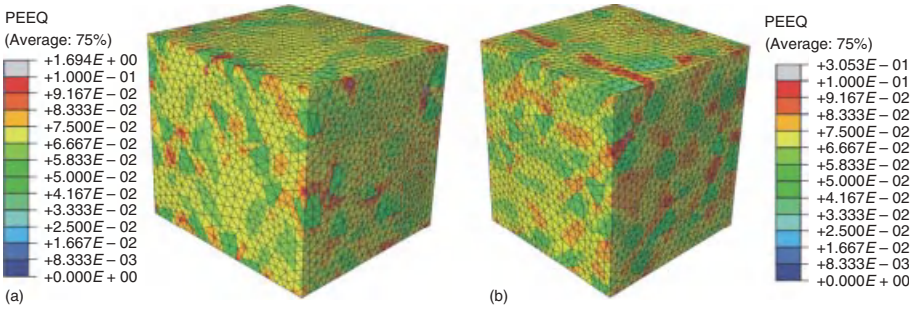

Figure 8.28 Equivalent plastic strain distribution on the ferrite/pearlite microstructure RVE-1 under macroscopic strain $E_{XX} = 0.07$ (a) and $E_{YY} = 0.07$ (b).

The different effective yield behavior in the *X* and *Y* directions can, on the one hand, be explained by the different mean free dislocation paths considered in the flow curve description. For transverse directions, smaller grain sizes were determined as for the rolling direction, resulting in a higher strain level according to the Hall–Petch relation. On the other hand, this difference can be explained by the analysis of the deformation of the steel microstructure. In Figure 8.28, the distribution of the equivalent plastic strain on the RVE microstructure is shown for an imposed total strain of 7% in both the rolling *X* and transverse *Y* directions.

The ferrite matrix deforms differently but, in both cases, essentially close to the pearlitic phase. Moreover, the transverse loading leads to the formation of shear bands with high strain localization near the elongated cylindrical pearlite inclusions

oriented to the rolling direction (Figure 8.28b). This locally larger plastic flow induces a higher effective von Mises stress and accordingly a higher elastoplastic yield curve in the transverse than in the rolling direction. The orthotropy of the hot rolled and subsequently cooled steel sheet is so significant that it cannot be neglected in the macroscopic U- and O-forming simulations.

8.6.5 Welding

8.6.5.1 Fundamentals of the Welding Simulations

The essential elements of a welding simulation [33] are the calculation of heat entry, the evolution of the temperature field and the weld geometry (process simulation), the simulation of the microstructure and technological properties (materials simulation), and the simulation of the mechanical properties, including residual stresses and possible distortions (structure simulations) (Figure 8.29).

For an integrative welding simulation interfacing of the numerical models for these three elements is necessary. The mechanical behavior significantly depends on the heat transfer, the microstructure evolution, and thermal stresses [34]. To model heat transfer, the software SimWeld [35] was used. SimWeld enables the determination of energy input, the energy distribution, the weld pool geometry, the HAZ geometry, and the weld bead geometry. The response of the materials microstructure on the welding is simulated with MICRESS. Owing to

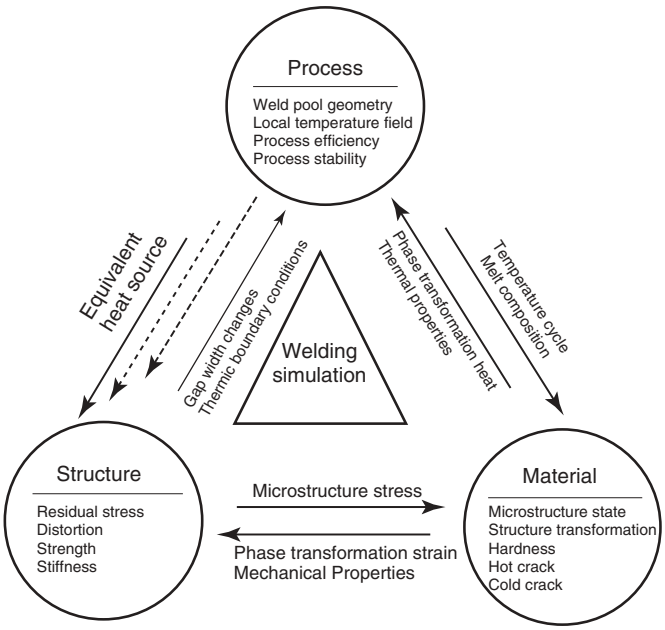

Figure 8.29 Integrated welding simulation composed of the three main components and their interaction.

computational restrictions, only representative areas can be mapped in a single calculation.

In the present stage, the main features of the microstructure evolution, namely, a dendritic solidification structure in the weld pool, as well as phase transformations and grain growth in the HAZ are obtained qualitatively. However, there are still limitations in the treatment of the solid-state reactions, especially at higher cooling rates. Several physical parameters are not known precisely and have to be calibrated with the help of reference experiments. The commercial software SYSWELD [36] is used for thermal stress analysis. In the spirit of the ICME platform, the virtual welding process is coupled with the previous metal forming processes and incorporates the stress–strain state right after the U-/O-forming process into the thermal stress analysis.

Process Simulation The welding process simulation was carried out with the software package SimWeld. The modeling of the welding process consists of three submodels: heat source, heat transfer in the work piece, and deformation of the melting pool's free surface.

The submodel for the heat source considers thermoelectric processes in the free-wire length, drop formation, and drop detachment, as well as control algorithms for power sources [37]. This submodel regards the process as transient and calculates the energy parameters for a short time (about 0.5 s). The submodel heat source provides the energy input, the effective average voltage, the effective average current, the pulse frequency (just for the pulse process), and so on.

Electrical power is calculated separately for the anode area (on the surface of a drop of an electrode) and the cathode area (a surface of a welding pool) [38, 39]. For the calculations of the heat flux in both anode and cathode areas, volt equivalents from the arc are used. The temperature, power, and mass of the drops melting off from the electrode are calculated in additional submodels.

Typically, a circular heat flux distribution caused by the welding arc on a surface is used in welding process models according to Rykalin and Rosenthal [40].

$$q(r) = \frac{3Q}{\pi r^2} e^{\left(3/r_e^2\right) r^2} \tag{8.17}$$

This distribution, based on the Gauss distribution, was developed as an analytical solution and allow the construction of an analytical process model of the welding, such that sufficiently accurate results could be obtained. Cylindrical distributions also have been applied and offer satisfactory results. In the model used in this test case, an intermediate distribution between a circular and a cylindrical distribution is applied:

$$q(r) = \frac{\sqrt{3Q}}{0.886\pi r^2} e^{\left(3/r_e^4\right) r^4} \tag{8.18}$$

The model for calculating the weld seam geometry is constructed as a further development of the model from Oshi-Sudnik [43].

The heat transfer submodel is based on the numerical solution of nonlinear heat diffusion equations with advective transport due to the heat source movement. In

the heat transfer model, a quasi-stationary temperature field is moving together with a heat source consistent with the welding speed. The submodel for the welding pool calculates the spatial position of the free boundaries of the welding pool. Boundary conditions of the heat transfer submodel depend on the spatial position of the welding pool; therefore, the calculation of the welding pool is based on an iterative solution of these two submodels [34].

The input parameters for the welding process simulation with SimWeld are the basic technological process parameters such as wire geometry, wire material and wire speed, protective gas composition, contact pipe distance, voltage, current, frequency, cable geometry, current source regulation, and so on. The output parameters are the electric and thermal characteristics of the process, the arc length and pressure, temperature field, and weld seam geometry.

In a nonstationary time scale simulation of distortion and residual stresses, it is possible to assume that the welding pool dimensions do not change. Therefore, in most cases, they may be calculated using a stationary approach, and the welding pool is thus simulated as quasi-stationary. The numerical algorithms in SimWeld are optimized to reduce calculation times of the temperature field and the geometrical form of the weld pool. Furthermore, an automatic generation of a grid is possible for the principal welding joint types and multiwire processes may also be simulated using SimWeld.

Generation of an Equivalent Heat Source The equivalent heat source is generated according to Goldak *et al.* [41] (Figure 8.30). It is described by two half-ellipsoids, a front ellipsoid (index *f*) and a rear ellipsoid (index *r*). Both are characterized by a maximal power intensity *q*, a half-length *a*, a half-width *b*, and depth *c*. Using the constraint of heat flux continuity at the boundary of the two ellipsoids, the number of independent parameters in the model reduces to five. The geometrical parameters are calibrated using experimental measurements of the weld pool size in addition to temperature near the weld pool. Furthermore, the temperature measurements can be used to calibrate the process efficiency.

Figure 8.31 illustrates the simulated temperature field and both weld seam and heat source geometry, which is obtained from the weld pool dimensions. The calculated heat input can be further distinguished as the heat input attributed to

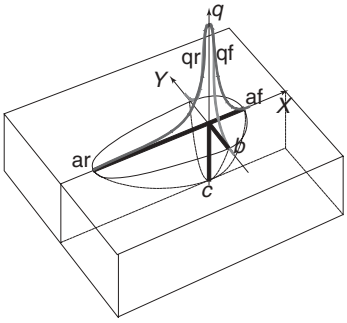

Figure 8.30 Double ellipsoid heat source used in SimWeld, according to Goldak *et al.* [41].

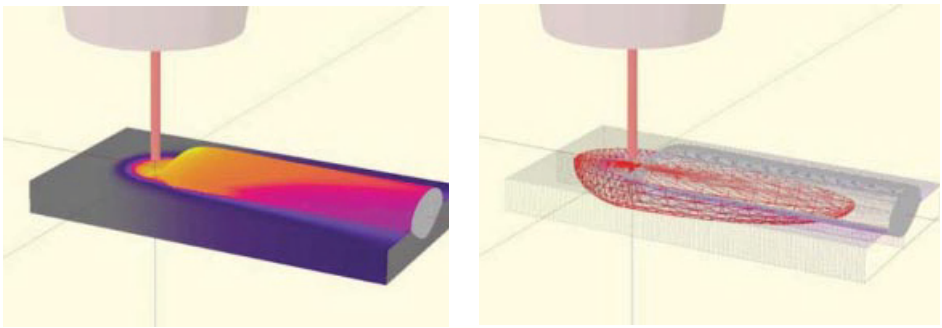

Figure 8.31 (a) Visualization of the heat source calculation in SimWeld with the welding process simulation results and (b) the heat source geometry.

the arc (Gauss distribution on the weld pool surface) and the heat input attributed to the droplets from the welding filler material (homogeneously distributed over the entire volume of the effective heat source (EHS)).

Structure Simulations In order to assess the effect of welding, including the heat transfer and the phase transformation on a complete structure, the entire assembly was simulated using the commercial finite element method (FEM) software SYSWELD (Figure 8.32). This code takes into account the thermophysical effects as well as the mechanical assessment of the structure. For the transfer of the EHS model from SimWeld to SYSWELD, an interface between SimWeld and SYSWELD has been implemented. The mesh elements are distinguished in groups that are attributed to materials or process properties. For instance, the weld line is defined by describing the path of the welding heat source.

From a numerical point of view, the material of the wire is of special interest. As the wire is fed continuously during the welding process, the corresponding elements have to appear numerically during the computation. The geometry of the

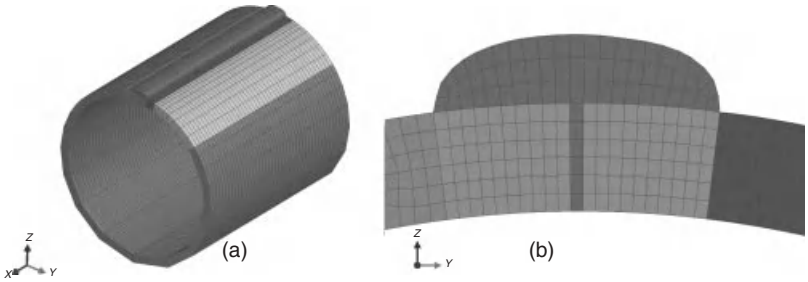

Figure 8.32 (a) SYSWELD mesh of the weld assembly including the weld seam and (b) wire definition, according to the chewing gum method.

weld seam is predicted by the SimWeld simulation, which affects the definition of the mesh in the area of the weld seam. The modeling of the filler material requires no specific user interaction beside the definition of the filler zone in the mesh. The addition of the material is managed through a defined metallurgical law, which transfers material with properties close to chewing gum and molten material, above a user-defined temperature.

The so-called chewing gum method considers the initial filler material revealing a low Young's modulus (1,000 MPa) and yield strength (245 MPa). Hence, the material of the wire does not affect the mechanical computation initially. After passing a threshold temperature, the properties are switched to those of the austenite phase. During the subsequent cooling to room temperature, the wire elements take part in the phase transformation in the same way as ordinary austenite elements. Hence, these elements become relevant for the mechanical computation. The phase transformations are described based on the Leblond model [42] implemented in SYSWELD. The software is linked to a materials database containing the thermophysical and mechanical properties.

8.6.5.2 Results of the Microstructure Evolution during Welding

The microstructure evolution of the welding process on a microscale is carried out using the phase-field code MICRESS [11]. Characteristic integration points in the weld pool and HAZ are considered, and their temperature–time histories are extracted from macroscale simulations and transferred into the simulations on the microscale.

Figure 8.33 shows schematically the relevant stages of the performed microstructure simulations including the solidification in the weld pool and the subsequent solid-state transformations into the final microstructure. Phenomena considered within the simulations are the dendritic solidification of the weld pool,

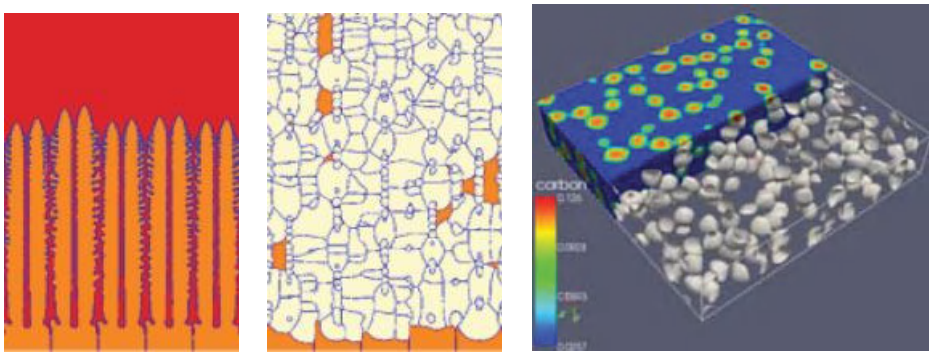

Figure 8.33 Dendritic solidification of δ-ferrite in the joint (a), subsequent formation of austenite (b) as well as phase transformations, recrystallization, and grain growth in the heat-affected zone (c, depicted are carbon and α-phase distributions during the $\gamma-\alpha$ transition).

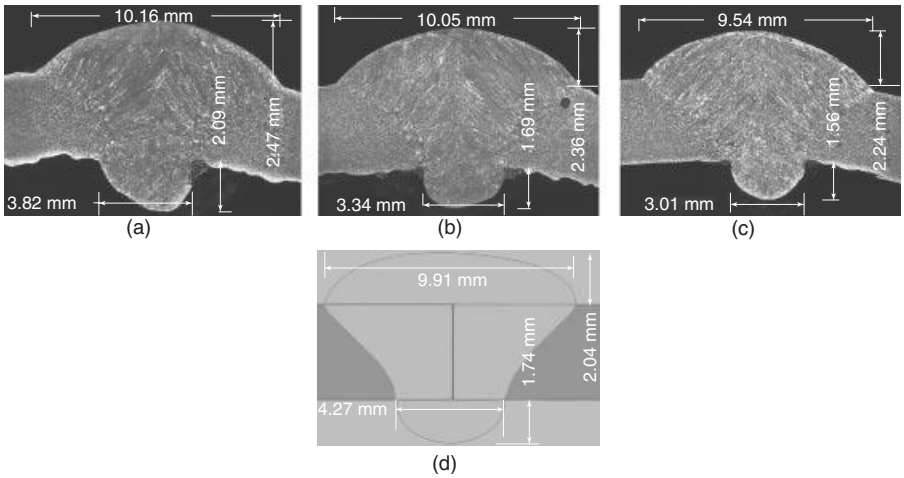

Figure 8.34 Geometry of the weld cross section by GMAW in experiment (a–c) and calculated (d).

the peritectic reaction, diffusion and grain growth, and the subsequent solid-state phase transformations.

8.6.5.3 Results of the Macrosimulations of the Welding Process

Several weld experiments were carried out to validate the accuracy of the calculation of weld seam geometry and temperature field of a GMAW process. The temperature was measured at the surface of the steel plate at a distance of 7.5 mm from the joining center. The results of a numerical simulation are compared to experimental findings in Figure 8.34. The calculated shape of the cross section is in good agreement with the experimental cross section. A slightly larger cross-sectional area is calculated for the weld seam as compared to the experimental situation. This is probably due to an overestimated value of the calculated heat capacity of the process, leading also to a slower predicted cooling process as measured (Figure 8.35). However, calculated and experimental results are in sufficient agreement.

The accuracy of the simulation models, to a large extent, depends on the model calibration. Calibration is especially required for the determination of parameters for the heat input and arc pressure depending on the arc length, current, joint type, and material. This procedure can be performed by comparison of simulated weld seam dimensions with the results of corresponding experiments. Determination of an effective thermal voltage drop at the anode U_{anode} also requires a justification, which is performed by the comparison of simulated voltage oscillations and wire melting rate with experiments.

Experiments were carried out to verify the integration of both simulation tools (SimWeld and SYSWELD) and to analyze the additional value gained by their coupling. Figure 8.36 shows the comparison of the experimental cross section with the calculated situation. In addition, the results of the structural simulation are

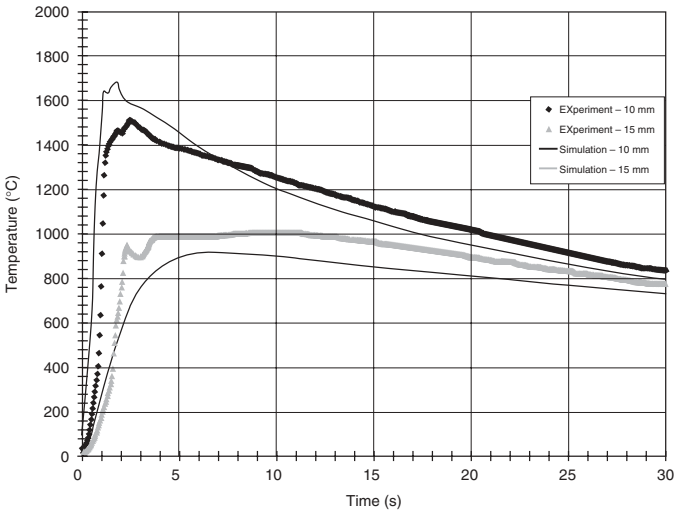

Figure 8.35 Temperature cycles for welding of a steel S355: solid curves, calculated data; dashed line, experimental data.

shown after the implementation of the calculated cross section in the 3D mesh of SYSWELD.

The pipes were welded at 45 cm min^{-1} welding speed, 10.5 m min^{-1} wire speed, and 20 mm contact tube distance. The material was API 5L X65. A comparison of the weld width at the top and bottom shows a good correlation of the calculated top width with the experimental measurements. Although the width at the bottom shows good agreement with the experimental measurements, the bottom weld width is overestimated. A possible reason may be associated with the influence of the convective heat transfer on the weld formation in case of a full penetration weld. The fusion line has a concave shape, as shown in the metallographic image in Figure 8.36. Such influences on shape formation cannot be considered in the frame of a mere conductive heat transfer model. By the calculation of distortion and residual stress using the EHS calculated with SimWeld, a melting zone was

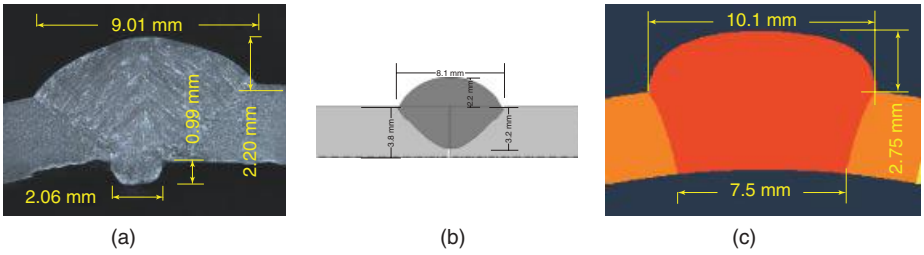

Figure 8.36 Comparison between weld seam geometry from experiment (a) obtained with SimWeld (b) and simulated with SYSWELD (c).

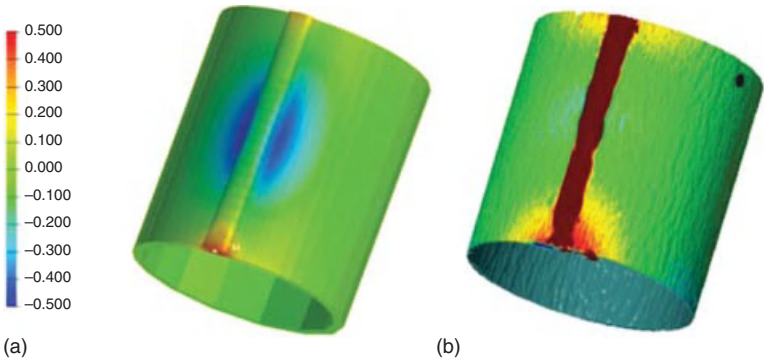

Figure 8.37 Comparison of calculated (a) and experimentally determined (b) pipe distortion.

measured and the dimensions on the top correlate very well with the experiment (Figure 8.36). At the bottom, the calculated weld seam shows a discrepancy in the measured dimensions. This discrepancy may indicate that the heat conduction in the radial direction is overestimated and/or the heat conduction in the tangential direction is underestimated. A mesh refinement may also help to decrease this effect.

The numerical results show that the calculation of the heat source and weld seam geometry with SimWeld linked to FE structural simulations provides a good alternative to the welding simulation, decreasing the demand for experiments. Thereby, an evaluation of the mechanical weld seam properties is possible from easy laboratory experiments a priori to cost-intensive welding experiments in the pipeline production process.

Using the software platform, SimWeld is able to perform a physically based SAW process simulation. An EHS is generated describing the geometric extent and the energy distribution caused by the welding process. The integrated approach was introduced here combining the EHS computation in SimWeld with the mechanical FE simulation of the global assembly in the SYSWELD code.

FEM simulations using SYSWELD were carried out in order to calculate distortion and residual stress due to the welding impact. The mesh, generated according to the pipe dimensions, includes the weld seam geometry that was calculated with SimWeld. Moreover, the simulations were carried out with the equivalent heat source calculated in SimWeld analog to the model of Goldak *et al.* [41].

The comparison between simulated and experimentally obtained results is presented in Figure 8.37, showing a fair agreement. At the beginning and at the end of the weld seam, a good quantitative agreement can be identified and demonstrated. In the middle of the weld seam, a zone of negative displacement can be identified, which does not correlate with the measurements and can be explained by the discrepancy between the theoretical and mechanical properties used in the simulations and the real properties modified during the milling and bending process. Further improvements of the entire process chain simulation will reduce these discrepancies in future.

8.7 Conclusion and Benefits

This chapter has summarized the present status of the test case line pipe in the framework of the virtual platform for the multiscale simulation of materials processing. The applied simulation tools and established models were described, and obtained results for the applied steel were presented. The complex process of pipe manufacturing makes clear that an approach that is able to describe the whole process with all of its influencing parameters, the impact of the processing on the material, and the resulting product properties is necessary. For example, it is not sufficient to simply know the grain growth kinetics during heating for calibrating the rolling parameters. The microstructure development in the following process steps also depends on, for example, the number of rolling passes, the pass reduction, and the recrystallization kinetics. A high reheating and rolling temperature does not, therefore, necessarily result in a coarse grain structure. Moreover, the resulting microstructure obtained after hot rolling cannot be used to evaluate the product properties for the application without considering the microstructural changes caused by the welding process. The effort of process design is significantly reduced when all influencing factors are treated simultaneously.

Within the thermomechanical treatment, it could be shown that monitoring and a description of the phase transformation, the grain size evolution, the temperature distribution and recrystallization phenomena could be successfully modeled. The subsequent microstructure evolution was modeled including the formation of ferrite, the carbon enrichment of austenite, and a subsequent formation into pearlite.

For the microstructure after the hot rolling process, it was shown that effective properties could be modeled starting from the homogenization of a ferrite–cementite bilamella in a multiscale approach. RVEs were then applied in order to deduce the effective flow behavior of the steel and applied in forming simulations.

The welding simulation shows that the used model was able, for example, to accurately predict the weld seam geometry and to tackle possible distortion due to residual stresses. With the outlook of considering residual stresses evoked by the previous cooling of the steel sheet, further model improvements are to be motivated. The qualitative description of the microstructure evolution is intended to be developed in order to eventually gain information and to evaluate the properties of the resulting product.

The results of this test case show that all presented models are capable and able to simulate the occurring process and material-related phenomena with a sufficient accuracy. A complete coupling of the described processes enables to calculate, for example, the microstructure evolution over the complete process chain linked to characteristic points in the macroscopic assembly and a subsequent evaluation of the materials properties. Although the presented matter is still to be seen in the frame of an on-going process, the advantages offered by this holistic approach are already evident.

References

1. Bhadeshia, H.K. (1998) Alternatives to the ferrite-pearlite microstructures. *Mater. Sci. Forum*, **284–286**, 39–50.
2. Shanmugam, S., Ramisetti, N.K., Misra, R.D., Hartmann, J., and Jansto, S.G. (2008) Microstructure and high strength-toughness combination of a new 700 MPaNb-microalloyed pipeline steel. *Mater. Sci. Eng. A*, **478**, 26–37.
3. Hillenbrand, H.G., Gräf, M., and Kalwa, C. (2001) Development and Production of high strength pipeline steels. Niobium Science and Technology: Proceedings of the International Symposium Niobium, Orlando, FL, 2001 (Europipe).
4. DIN (2009) German Version EN 10208-2:2009. *Steel Pipes for Pipelines for Combustible Fluids – Technical Delivery Conditions – Part 2: Pipes or Requirement Class B*.
5. Sente Software Ltd. (2005) JMatPro User's Guide, Sente Software Ltd., Guildford.
6. Kirihata, A., Siciliano, F., Maccagno, T.M., and Jonas, J.J. (1998) Mathematical modeling of mean flow stress during hot strip rolling of multiply-alloyed medium carbon steels. *ISIJ Int.*, **38** (2), 187–195.
7. Shanmugam, S., Ramisetti, N.K., Misra, R.D.K., Mannering, T., Panda, D., and Jansto, S. (2007) Effect of cooling rate on the microstructure and mechanical properties of Nb-microalloyed steels. *Mater. Sci. Eng. A*, **460–461** (15), 335–343.
8. DIN (2003) German Version EN ISO 643:2003. *Steels – Micrographic Determination of the Apparent Grain Size*.
9. DIN (2009) German standard: 50125:2009. *Testing of Metallic Materials – Tensile Test Pieces*.
10. Savran, V.I. (2009) Austenite formation in C-Mn steel. PhD thesis. University of Technology, The Netherlands.
11. Microstructure Evolution Simulation Software (MICRESS) (2009) User's manual, Release 5.3, October 2009.
12. Thermo-Calc Software AB (2010) Database TCFE6.
13. Thiessen, R.G. (2006) Physically-based modelling of material response to welding. PhD Thesis. Delft University of Technology, The Netherlands.
14. Leblond, J.-B. and Devaux, J. (1984) A new kinetic model for anisothermal metallurgical transformation in steels including effects of austenite grain size. *Acta Metallurgica.*, **32**, 137–146.
15. Geijselaers, H. (2003) Numerical simulation of the stresses due to solid state transformations. PhD thesis. University of Twente, Netherlands.
16. Simsir, C. and Gür, C.H. (2008) 3D FEM simulation of steel quenching and investigation of the effect of asymmetric geometry on residual stress distribution. *J. Mater. Process. Technol.*, **207**, 211–221.
17. Hodgson, P., Jonas, J., and Davies, C.H.J. (2009) *Modeling of Hot and Warm Working of Steels, Handbook of Thermal Process Modeling of Steels*, Taylor & Francis Group.
18. Minami, K. and Sicilliano, F. (1996) Mathematical modeling of mean flow stressduring hot strip rolling of Nb steels. *ISIJ Int.*, **36** (12), 1507–1515.
19. Koistinen, D.P. and Marburger, R.E. (1959) A general equation prescribing the extent of the austenite-martensitetransformation in pure iron-carbon and plain carbon steels. *Acta Metal.*, **7** (1), 59–60.
20. Jiang, C., Srinivasan, S.G., Caro, A., and Maloy, S.A. (2008) Structural, elastic, and electronic properties of Fe_3C from first principles. *J. Appl. Phys.*, **103** (4), 043502–043502-8.
21. Nikolussi, M., Shang, S.L. *et al.* (2008) Extreme elastic anisotropy of cementite, Fe_3C: first-principles calculations and experimental evidence. *Scr. Mater.*, **59** (8), 814–817.
22. Laschet, G. (2002) Homogenization of the thermal properties of transpiration cooled multi-layer plates. *Comput. Meth. Appl. Mech. Eng.*, **191** (41–42), 4535–4554.
23. Hibbit, Karlsson, Sorensen, Inc. (2009) Abaqus V6.9-2 User's Manual, Pawtucket.

24. Digimat Software, (2009) version 3.2, Louvain-la-Neuve, Belgium.
25. Zhang, M.-X. and Kelly, P.M. (1997) Accurate orientation relationships between ferrite and cementite in pearlite. *Scr. Mater.*, **37** (12), 2009–2015.
26. Rodriguez, R. and Gutierrez, I. (2003) Unified formulation to predict the tensile curves of steels with different microstructures. *Mater. Sci. Forums*, **426–432**, 4525–4530.
27. Gutierrez, I. and Altuna, M.A. (2008) Work-hardening of ferrite and microstructure-based modelling of its mechanical behaviour under tension. *Acta Material.*, **56**, 4682–4690.
28. Suh, D.-W., Bae, J.-H., Cho, J.-Y., Oh, K.-H., and Lee, H.-C. (2001) FEM modelling of flow curves for ferrite/pearlite two-phase steels. *ISIJ Int.*, **41** (7), 782–787.
29. Laschet, G., Quade, H., Henke, T., Dickert, H.-H., and Bambach, M. (2010) Comparison of elasto-plastic multi-scale analyses of the U-forming process of a steel line-pipe tube. Proceedings of the ECCM-10 Conference, Paris, France.
30. Laschet, G., Fayek, P., Quade, H., Henke, T., and Schmitz, G.J. (2011) Derivation of anisotropic flow curves of a ferrite/pearlite two-phase steel and their use in the forming simulation of a pipeline tube. Accepted on Complas-11, Barcelona, Spain.
31. Young, M.L. and Almer, J.D. (2007) Load partitioning between ferrite and cementite during elasto-plastic deformation of an ultrahigh carbon steel. *Acta Mater.*, **55**, 1999–2011.
32. Kadkhodapour, J., Schmauder, S., Raabe, D., Ziaei-Rad, S., Weber, U., and Calcagnatto, M. (2011) Experimental and numerical study on geometrically necessary dislocations and non-homogeneous mechanical properties of the ferrite phase in dual phase steels. *Acta Material.*, **59** (11), 4387–4394.
33. Radaj, D. (1999) Schweißprozesssimulaiton: Grundlagen und Anwendungen, DVS-Verlag GmbH, Düsseldorf.
34. Goldak, J., Zhou, J. *et al.* (2006) *Predicting Distortion and Residual Stress in Complex Welded Structures by Designers, Trends in welding research, proceeding of the 7th International Conference on Trends in Welding Research 2005*, pp. 531–539.
35. Bleck, W., Reisgen, U., *et al.* (2010) Methodology for Thermomechanical Simulation and Validation of Mechanical Weld-Seam Properties, Advanced Engineering Materials, **12**, (3), pp. 147–152.
36. Rieger, T. *et al.* (2010) Simulation of welding and distortion in ship building. *Adv. Eng. Mater.*, **12** (3), 153–157.
37. Dilthey, U. and Pavlyk, V. (2001) Recent advances in computer modelling of microstructure, IIW-Doc. XII-1660-01. Proceedings of the Intermediate Commission XII, Aachen.
38. Mokrov, O. *et al.* (2006) Heat-Source Modelling in GMA-Welding and its Integration in Stress-Strain-Analysis, Proceedings: 8th International Seminar "Numerical Analysis of Weldability". 25–27. September 2006, Schloss Seggau, Graz/Leibnitz, Österreich.
39. Pavlyk, V., Mokrov, O., and Dilthey, U. (2007) Heat source modelling in GMA welding and its integration in stress-strain analysis. *Math. Model. Weld. Phenom.*, **8**, 801–818.
40. Rykalin, R. (1974) Energy sources for welding. *Weld. World*, **12** (9–10), 227–248.
41. Goldak, J. *et al.* (1984) A finite element model for welding heat sources, *Met. Trans. B*, **15B**, 229–305.
42. Leblond, J.-B. *et al* (1986) A theoretical and numerical approach to the plastic behavior of steels during phase-transformation. *Journal of the mechanics and physics of solids*, **34**, (4), pp. 395–409.
43. Pavlyk, V. and Dilthey, U. (1998) Einsatz eines finite-elemente-programms zur berechnung von temperaturfeld und schmelzbadgeometrie beim WIG-Schweißen. *DVS-Ber.*, **194**, 43–46.
44. Brensing, K.-H., Sommer, B. Steel tube and pipe manufacturing processes, http://www.smrw.de/downloads/Steel_tube_and_pipe.pdf.

9
Test Case Gearing Component

Sergey Konovalov, Thomas Henke, Ulrich Jansen, Ario Hardjosuwito, Wolfram Lohse, Markus Bambach, and Ulrich Prahl

9.1
Introduction

Gearing components are an example of widely used machining parts in engine construction. Nowadays, development and optimization of materials and process chains are considered for improving production efficiency, aiming at reduction of production costs. Efficiency in gear manufacturing can be optimized by increasing carburizing temperature during case hardening, which reduces process duration significantly. However, any temperature increase is limited by tolerable grain coarsening, maintaining fine grain stability [1].

It is well known that grain size control at high-temperature annealing can be achieved by applying microalloying concepts. Using these concepts, stable precipitates may cause pinning of austenite grain boundaries by decreasing their mobility. Microalloying elements form stable, nanosized precipitates during continuous casting. Subsequent heat treatment and hot forming processes during gear manufacture lead to an evolution of precipitation size, composition, and density, being the result of particle nucleation, dissolution, coarsening, and growth. As precipitate size and density considerably affect the fine grain stability, the evolution of precipitate size and density have to be controlled and optimized along the entire process chain in order to achieve an optimal particle state for best grain size control [2].

The idea of the present test case is to investigate a process chain in which the precipitation evolution on the nanoscale is controlled by the macroscopic process parameters and interacts with the microscale grain growth, determining the final quality of the component gear. The investigation of the gear manufacturing process thus represents a process chain with various process steps and a multiscale interaction serving as an instructive example of the evaluation of the AixViPMaP platform and its universal data exchange and coupling approach. The optimization of the process chain and parameters will be performed to decrease process duration and/or increase energy efficiency. Simultaneously, the experimental effort for the description of phenomena and the determination of simulation parameters shall

Integrative Computational Materials Engineering: Concepts and Applications of a Modular Simulation Platform,
First Edition. Edited by Georg J. Schmitz and Ulrich Prahl.

be reduced. The capabilities of a process chain simulation approach toward optimization of process parameters and process chain design as well as an investigation of the robustness of a process chain in terms of fine grain stability during high-temperature carburizing will thus be highlighted.

9.2 Materials

A microalloyed case hardening steel with the composition given in Table 9.1 was investigated in the present work. It is a modified version of a typical steel grade designed for high-temperature case hardening, with additions of Nb and Ti in a defined relation to Al and N aimed at increasing fine grain stability. The material was produced industrially by continuous casting, hot rolling to a round rod with a diameter Ø 75 mm, and subsequent heat treatment to obtain a ferrite pearlite structure (FP annealing). In the as-delivered state, it reveals a ferrite–pearlite microstructure (Figure 9.1). For defined process chains, the stability of the grain size at different carburizing temperatures has been investigated in Ref. [3].

Table 9.1 Composition of the investigated steel grade 25CrMo4(Nb/Ti), wt%.

C	Si	Mn	P	S	Cr	Mo	Ni	Al	N	Nb	Ti
0.235	0.22	0.89	0.0104	0.0218	0.92	0.43	0.18	0.023	0.016	0.034	0.009

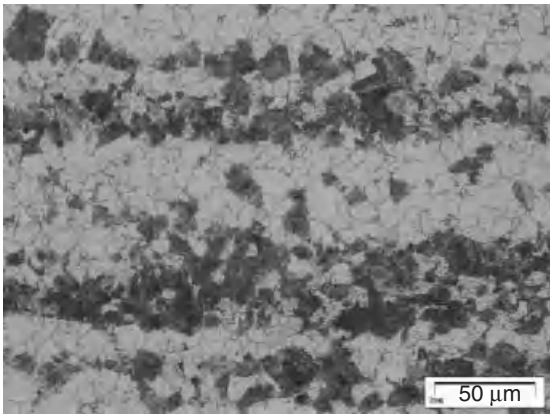

Figure 9.1 Initial ferrite–pearlite microstructure of a round rod after FP annealing.

9.3
The Process Chain

9.3.1
Overview

On the industrial scale, the manufacturing chain for a gearing preform typically consists of various process steps such as continuous casting, hot rod rolling, multistep forging to a gear preform, and annealing to adjust a suitable microstructure for machining of the final gear component's shape. After machining the preform, the final gear component is case hardened in order to achieve a hard case of tooth with a tough core.

For the investigation on the laboratory scale, continuous cast and hot rolled material is used and a starting cylindrical billet is prepared. Two hot forging steps are performed with subsequent FP annealing and later case hardening. For the sake of simplicity, the machining process has been skipped in this example process chain, as its effect on the precipitation state evolution can be neglected. The process chain has been investigated experimentally using a simplified geometry of a cylinder comprising a cavity. The final test component consists of a case hardened component joined to a ring by laser welding (Figure 9.2).

The initial sample geometry was a cylindrical specimen Ø $20 \times 30\,mm^3$ taken from the industrially manufactured round rod. These specimens then followed a multistep heating and forming path from the initial state to the final case hardened part (Figure 9.3). After each individual step, some specimens were taken apart for a detailed metallographic investigation. In addition, cylindrical dilatometer samples Ø $4 \times 10\,mm^3$ were prepared from some specimens to investigate the

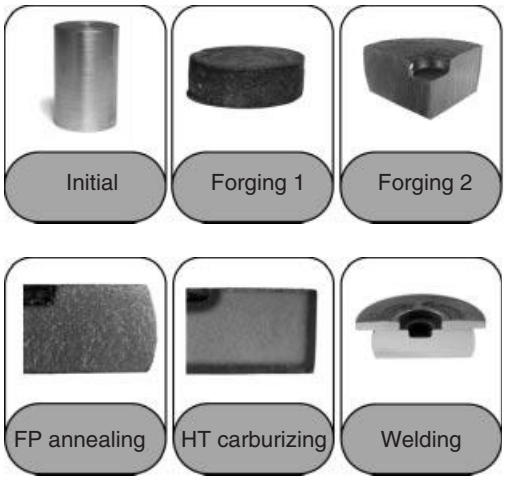

Figure 9.2 Experimental process chain for simplified gear preform geometry with different heat treatment steps.

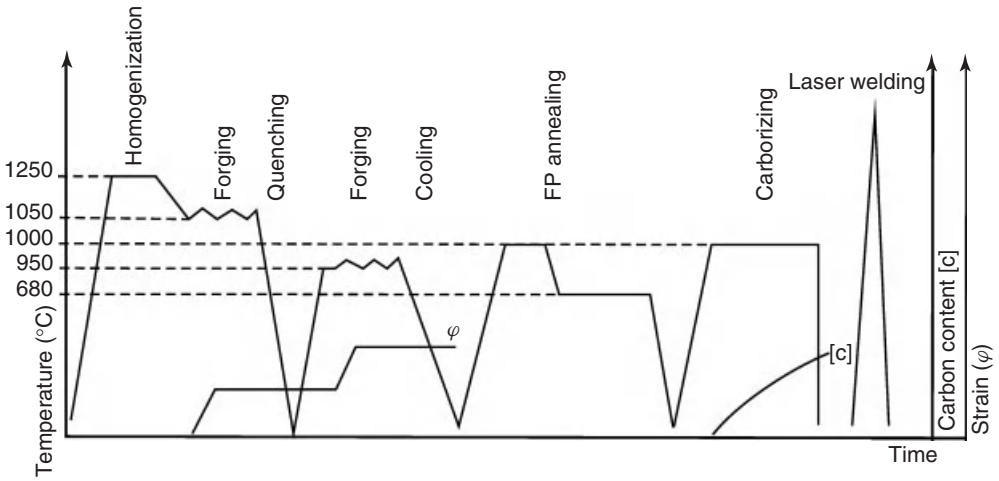

Figure 9.3 Time–temperature flow along the investigated process chain.

phase transformation or particle evolution using controlled heating or experimental process simulation by means of a Bahr dilatometer.

9.3.2
Hot Rolling and Forging

For gear manufacturing at the industry scale, rod-shaped hot rolled material is widely used. Typically, these billets are cut from the rod by shear cutting and then induction heated up to 1250 °C, homogenized for 10 min, and eventually cooled to a forming temperature of 1050 °C.

In the present laboratory study, the considered process chain starts with a cylindrical billet with a typical homogeneous microstructure after rolling. The hot rolling process was reduced to a simple hot compression by 18.5 mm to the height of 11.5 mm by applying a constant die velocity of 60 mm s^{-1} (forging 1). After compression, the specimens were quenched to room temperature.

For the following hot forging step (forging 2), the billets were heated to 950 °C and forged to a final geometry by compression plus forming of cavity. This second forging step was conducted with a constant die velocity of 20 mm s^{-1}. The hot forged specimens were subsequently slowly cooled down to room temperature.

9.3.3
FP Annealing

After forging, the deformed specimens were annealed to improve machinability. In detail, they were heated up to 1000 °C in a preheated muffle-type furnace with

a heating rate of about 5 °C s^{-1}. After holding for about 1 h, they were transferred directly into a further muffle furnace that was preheated up to 680 °C. At this temperature, the samples were held for 3 h to obtain the desired perlite–ferrite structure. Eventually, the billets were cooled down to room temperature by furnace cooling.

9.3.4 Machining

As the machining does not significantly affect the precipitation state in the material, this step has been omitted from the simulation chain without losing relevant information with respect to fine grain stability. Thus, the simulation of machining was not validated using experiments, and the samples were not machined by defined conditions.

However, the surface of the samples was polished manually with the smallest possible removal of metal. The scope of this treatment was to obtain the required quality of the surface for carburizing while simultaneously avoiding changes in the shape of the samples and their microstructure because of high abrasion and friction heat.

9.3.5 Carburizing

After preparation and cleaning of the simplified gearing component, case hardening was carried out in an industrial two-chamber vacuum furnace (type ALD-DualTherm) at a temperature of 1000 °C with subsequent high-pressure gas quenching using nitrogen. The pulse time regime (boost time and acetylene flow) was calculated with the furnace control software (Table 9.2). The carburizing program was designed for a surface carbon concentration of 0.7 % and a case hardening depth of 1 mm.

Table 9.2 Carburizing program.

Time (h:min)	Boost (s)	Flow (l h^{-1})
0:20	200	200
0:20	140	170
0:30	130	150
0:35	130	150
0:40	120	150
0:50	120	150
1:00	120	150
2:00	–	–

9.3.6
Laser Welding

The core of the gearing component was joined with a rolled ring of the same base material (ring thickness 3 mm) by deep penetration laser welding. For the principle part, a Nd:YAG laser system with a fixed optic is used. Both parts are fixed in a special clamping device, allowing for an axial weld. To demonstrate principle feasibility, a simple lap joint was selected. The thickness of the ring was 3 mm; the nominal weld depth was about 6 mm. The laser system used for welding was a Trumpf DruDisk 1003 disk laser with an optical wavelength of 1064 nm. The laser light is guided by an optical fiber of length 50 m and diameter 30 μm. The collimator lens has a focal length of 200 mm, and the focusing lens has a focal length of 400 mm. The beam is focused on the surface of the part; the diameter of the focal spot is 600 μm. The resulting Rayleigh length has a value of 50 mm. The laser power is adjusted at 3760 W, feed velocity equals 1.13 m min^{-1}, and argon is used as inert gas with a flow rate of 30 l min^{-1}.

9.4
Experimental Procedures and Results

9.4.1
Overview of Phenomena

Along the process chain, various phenomena are expected, especially during the hot forming and heat treatment processes involved. During the first forging operation, the samples are heated, deformed, and cooled to room temperature. During the heating and holding phases, the initial structure transforms into austenite. At elevated temperatures, grain growth will occur if time and driving force for growth are sufficient. Simultaneously, microalloyed particles may grow, dissolve, or nucleate depending on their initial state, their stability, and the imposed boundary conditions. Deformation of the material can lead to shape change, dynamic and static recrystallization, as well as particle nucleation or phase transformation induced by deformation. Eventually, during controlled cooling or quenching of the samples, the particle evolution and phase transformation from austenite to ferrite–pearlite, bainite, or martensite will proceed. Owing to microalloyed particles, some phenomena such as recrystallization can be inhibited or accelerated, for example, phase transformations. A similar complex interaction of phenomena is to be expected during forging.

The FP annealing and case hardening steps are accompanied by phase transformation and mutually interacting grain growth and particle evolution. All these phenomena depend on temperature evolution in the gearing component in time. For high-temperature carburizing, the grain growth regime is the most critical issue for high end properties. It depends on both the initial grain size and the

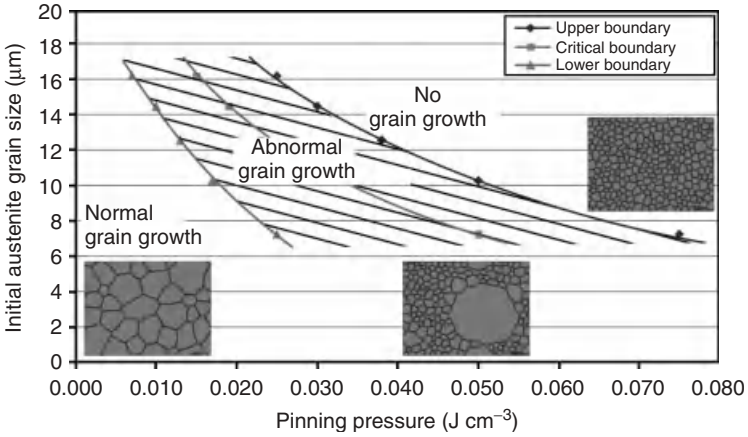

Figure 9.4 The grain growth regime depends on pinning pressure and initial austenite grain size [4].

pinning force (Figure 9.4). The stabilization of carbides can be reached by enrichment of carbon at the sample surface. In addition to the carbon distribution after carburizing, phase transformations from austenite to martensite, bainite, or ferrite–pearlite during the quenching may lead to distortions of the component.

The evolution and interaction of all activated metallurgical phenomena yield a high complexity in the process analysis as the properties of the material during process as well as finally in the gear component will be controlled by the precipitation state along the entire process chain.

9.4.2
Characterization of Dynamic Recrystallization and Grain Growth

In the experimental investigations, cylindrical specimens were heated in a radiation furnace and annealed for 10 min at a temperature of 1250 °C to homogenize the microstructure. The experimental setup for the forging steps is placed in a radiation furnace, allowing the experiments to be assumed isothermal. After the first forging step, the specimens were immediately quenched in water to analyze the microstructure and to change the dies for the next forging step. After changing the dies and preheating the setup, the specimens were placed directly into the compression furnace. Elastic prestress was applied in order to heat the specimens as fast as possible. After reaching the nominal temperature and performing the second forging step, the specimens were again immediately quenched in water. Grain size and recrystallized volume fraction were determined by means of light optical metallographic analyses. For all trials, the force displacement curves were also measured.

The temperature–time curve is illustrated in Figure 9.5. The starting austenitic microstructure was characterized by an average austenitic grain size of approximately 34 µm.

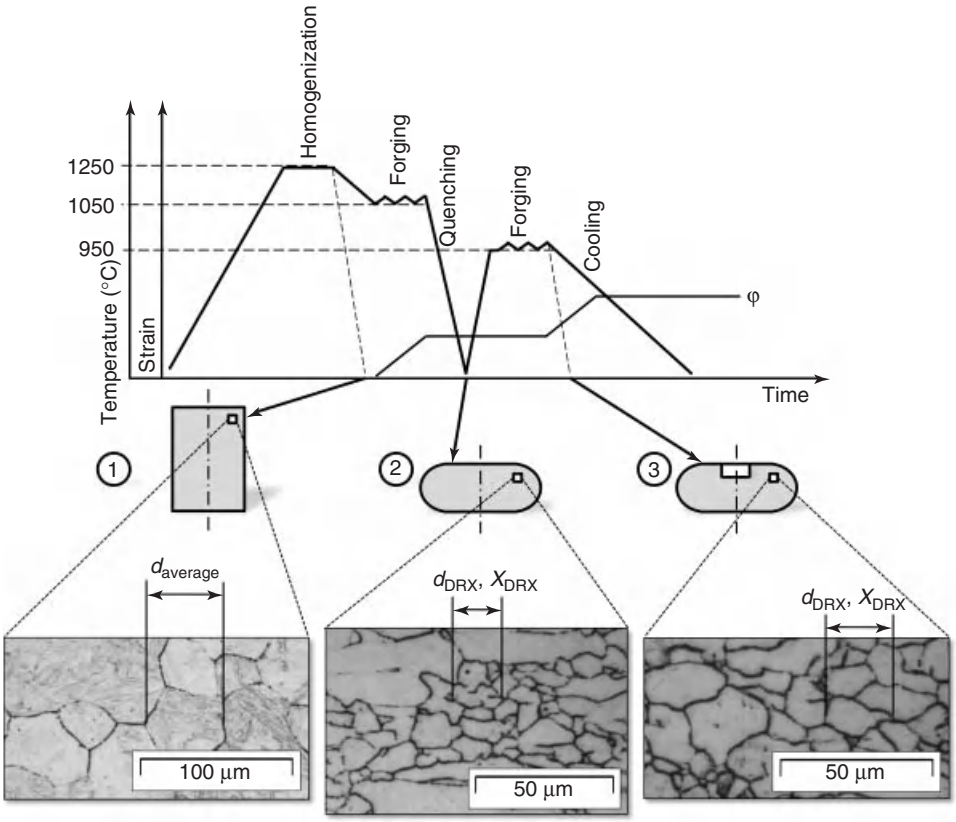

Figure 9.5 Strain–temperature evolution in the process chain comprising two hot compression steps; after quenching, the austenite grain structure has been analyzed using light optical metallography.

9.4.3
Characterization of Phase Transformations

Phase transformations were investigated on the principle gearing component as well as on small samples with a size of $9 \times 4 \times 1\,mm^3$ after heat treatment using a dilatometer for an optimized temperature control. The dilatometer samples were cut from the principle gearing component after each process step and treated using process parameters of the next step. The phase transformation and grain size evolution were separately investigated for each phase using light optical metallography and different etching methods. Using automatic image analysis of the micrographs, the phase fraction, nucleation density, and grain size of individual phases were identified and used for setting up and validating simulation parameters and results.

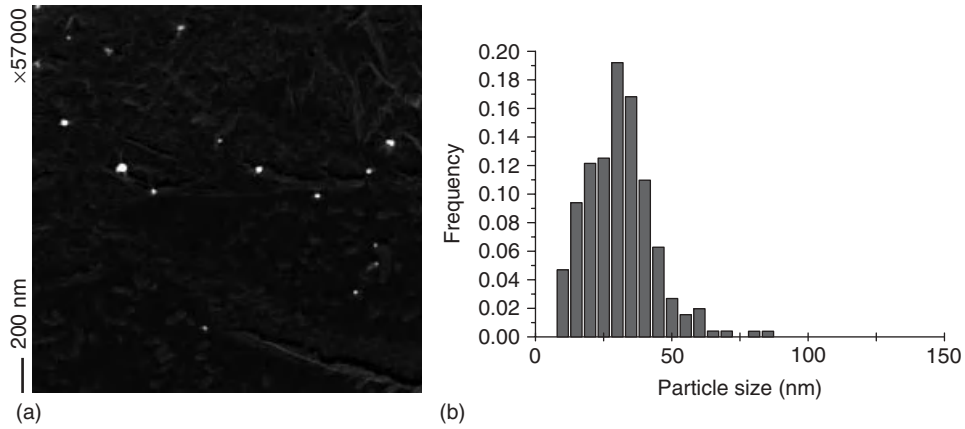

Figure 9.6 Example of dark field image of the sample "as received" after dissolving the (Fe,Cr)-carbides (a) and particle size distribution after particle analysis (b).

9.4.4
Investigation of the Particle Evolution along the Process Chain

Particle evolution was investigated by STEM (scattering transmission electron microscopy). The samples were selected from different process steps. It was important to ensure that no (Fe,Cr)-carbides were present, which would hinder the identification of the microalloying (Al,Ti,Nb)-carbonitrides. In situations in which (Fe,Cr)-carbides are assumed to exist, an additional heat treatment of the sample has been carried out to dissolve these (Fe,Cr)-carbides without modifying microalloying precipitates remarkably. This additional solution treatment consisted of heating with 10 K s^{-1} up to 1000 °C and a dwell time of 30 s at that temperature followed by quenching with maximum rate. The solid (Ti,Nb)-carbonitrides and Al-nitrides can be identified in the dark field image (Figure 9.6) as bright spots with a sharp surface, while impurities are gray in homogeneously distributed spots without a clear surface.

Thus, the evolution of (Ti,Nb)-carbonitrides and Al-nitrides can be monitored, which are essential to calculate the particle pinning Zener force during annealing and to control grain size stability. The composition of the particles was independently investigated by energy dispersive x-ray (EDX) and the results show that (Ti,Nb)-carbonitrides are round particles, while most Al-nitrides appear as elongated tubes. This information can be used for the rough separation of Al-nitrides and (Ti,Nb)-carbonitrides quantitatively. For this analysis, the particles were analyzed and counted individually with respect to their elongation factor. Here, the Al-nitrides reveal an elongation factor exceeding the value of 2, while (Ti,Nb)-carbonitrides show a factor between 1 and 2 [5].

The summary of the experimental results provides the particle evolution along the entire process chain (Table 9.3). The analysis of the results shows that

Table 9.3 Experimental results after transmission electron microscopic (TEM) investigation for particle size evolution along the process chain.

	Mean particle size (nm)		
	All particles	**Elongation factor <2, (Nb,Ti)-(C,N)**	**Elongation factor >2, AlN**
Initial (as received)	28	27	34
After first forging	50	49	52
After second forging	25	24	33
After austenitization during FP annealing	26	23	44
After carburizing (1 h)	41	39	53

Al-nitrides tend to a higher growth rate in comparison to (Ti,Nb)-carbonitrides during dwelling at different temperatures. The particle size changes along the process chain with a decreasing mean particle size after nucleation of new particles and with increasing size during growth and particle coarsening. The number of detected Al-nitrides (particles with elongation factor >2) is considerably smaller than that of (Ti,Nb)-carbonitrides (particles with elongation factor <2).

9.4.5 Characterization of Welding Depth

To characterize the weld, cross sections of the welded part were prepared (Figure 9.7). The cut edges are cleaned by Nital etching (3 % nitric acid) and analyzed by optical microscopy. In the heat-affected zone, the microstructure

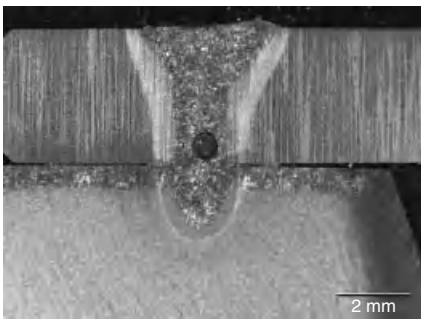

Figure 9.7 Macrosection of a laser weld. Upper region: ring welded to component. Lower region: part of component after processing. The resulting weld shows a depth of $d = 5.5$ mm.

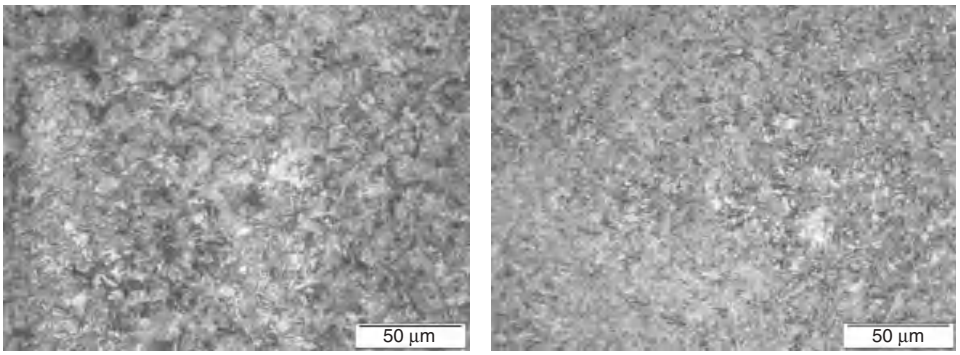

(a) (b)

Figure 9.8 Microsections of heat-affected zones. Upper ring with ferrite–bainite structure (a) and lower component with ferrite-bainite-retained austenite structure (b).

of the upper ring consists of ferrite–bainite, while the component itself shows ferrite-bainite-retained austenite structure (Figure 9.8).

9.5 Simulation Chain and Results

9.5.1 Overview of Simulation Chain

To simulate the entire process chain, the universal platform AixViPMaP was used. This platform allows different software tools to be mutually connected and to communicate with each other using a bus-type Internet-based architecture. The main design of the simulation chain (Figure 9.9) is directly related to the industrial typical process chain and basically consists of the same sequence of steps. The simulation of different phenomena is carried out for precipitates and microstructure (nano-/microscale) and for the component (macroscale).

Various simulation software tools and models are used, in particular different metallurgical-enriched finite element method (FEM) tools on the macroscale of the component, the multi-phase-field software MICRESS [6] on the scale of microstructure and MatCalc [7] for the nanoscale of the precipitates. On the macrolevel, the simulation software allows analyzing the heat distribution, phase transformation, metal deformation, carbon diffusion, and welding process within the entire gear component. On the microlevel, the evolution of the microstructure is simulated only at some selected points, tracking the time temperature evolution on the macroscale and applying it as boundary conditions for microscopic simulations addressing phase transformation or precipitation evolution. Some phenomena, such as phase transformations, have been calculated on both levels simultaneously: on macroscale as effective quantities and on microscale with full spatial resolution.

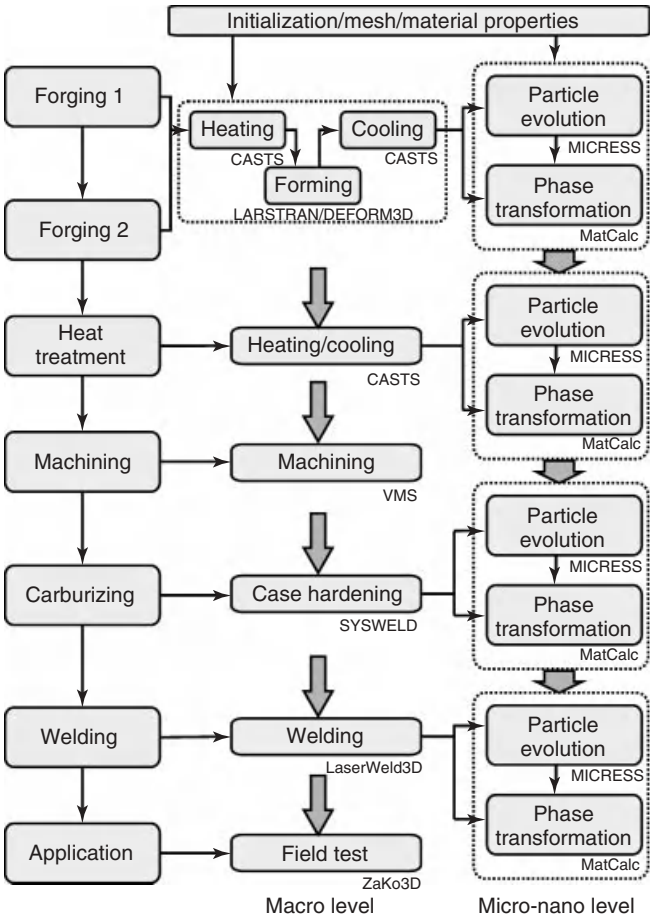

Figure 9.9 Simulation chain of the process steps for exemplarily gear manufacturing chain on macro- and micro-/nanolevel by coupling of different simulation tools.

The simulation chain started with the identification and the setting up of the initial state and the determination of materials parameters and properties. Respective initial conditions and materials parameters and properties have been stored in a universal format and could be applied by all of the simulation tools using suitable data converters. After the initialization, the generated mesh and materials properties are read by CASTS [8] for the calculation of the heating of the gear component in a furnace and the subsequent phase transformation. The furnace parameters and environment properties have been stored in the CASTS script file for setting up of the simulation. The results of the simulation are saved directly in the platform standard format VTK (Visualization Tool Kit) for use in the FEM software LARSTRAN/SHAPE [9], simulating the subsequent hot materials deformation in austenite. After calculating the sample's compression, the

simulation results are also converted to VTK format for interpretation, visualization, and for the next simulation step. The simulation results are then used again by either CASTS or SYSWELD [10] to calculate the cooling or quenching of the samples, and the results of these calculations are again saved in the universal VTK format. The same type of simulation flow, although with different parameters, has then been applied to the forging step.

Subsequent heat treatment of the samples was simulated out by CASTS, taking into account phase transformations with formation of austenite during heating or perlite–ferrite formation during cooling and holding after typical FP annealing. The carburizing step was easily simulated using SYSWELD, which contains convenient models. The simulation of the low-pressure carburizing was modeled as carburizing under atmosphere pressure with constant carbon flow.

The welding simulation LaserWeld3D requires a tetrahedral mesh with very fine elements along the weld line to resolve large temperature gradients near the laser welding capillary. To obtain such a mesh, the surface meshes of both parts to be joined were extracted and merged using the VTK Merge filter service (Chapter 6). This surface mesh acts as input for a tetrahedral Delaunay mesher, with additional refinement constraints along the weld line. The LaserWeld3D simulation maps the materials properties from upstream hexahedral meshes to the generated tetrahedral mesh and also maps back temperature values to the hexahedral mesh for further processing steps.

Operational and noise behaviors of gear components are commonly analyzed by using tooth contact analyses (TCAs). Within a TCA simulation, a gear set is meshed, and by applying defined loads, the operational behavior of this gear set can then be determined.

The TCA tool ''ZaKo3D'' enables such an analysis of the running and noise behaviors of beveloid, cylindrical, bevel, and face gears [11]. The software calculates the transmission error, the gear stiffness, the tooth root stresses, as well as the flank pressure. The transmission error and the change in the contact stiffness give a conclusion regarding the excitation behavior of the gear set. Furthermore, the influences of manufacturing-related deviations or the assembly process can be analyzed for the different gear types. Hence, a simulation chain is realized, enabling the analysis of a gear from the first manufacturing step via heat treatment to the application (Figures 9.9 and 9.10).

The principle of simulation interaction and structure is shown in detail for the two simulation steps – heating and rolling – in Figure 9.10. The same principle holds for each pair of calculation steps: transfer first step results to the next process simulation tool using the universal VTK data format and/or a suitable data converter.

During initialization stage, input data such as the geometry of the gearing component, chemical composition, and initial microstructure as well as the materials data and input parameter are converted into a format that can be used by the particular simulation tool. Materials data such as specific heat or heat conductivity can be, for example, determined using Thermo-Calc [12], MatCalc [7], or JMatPro

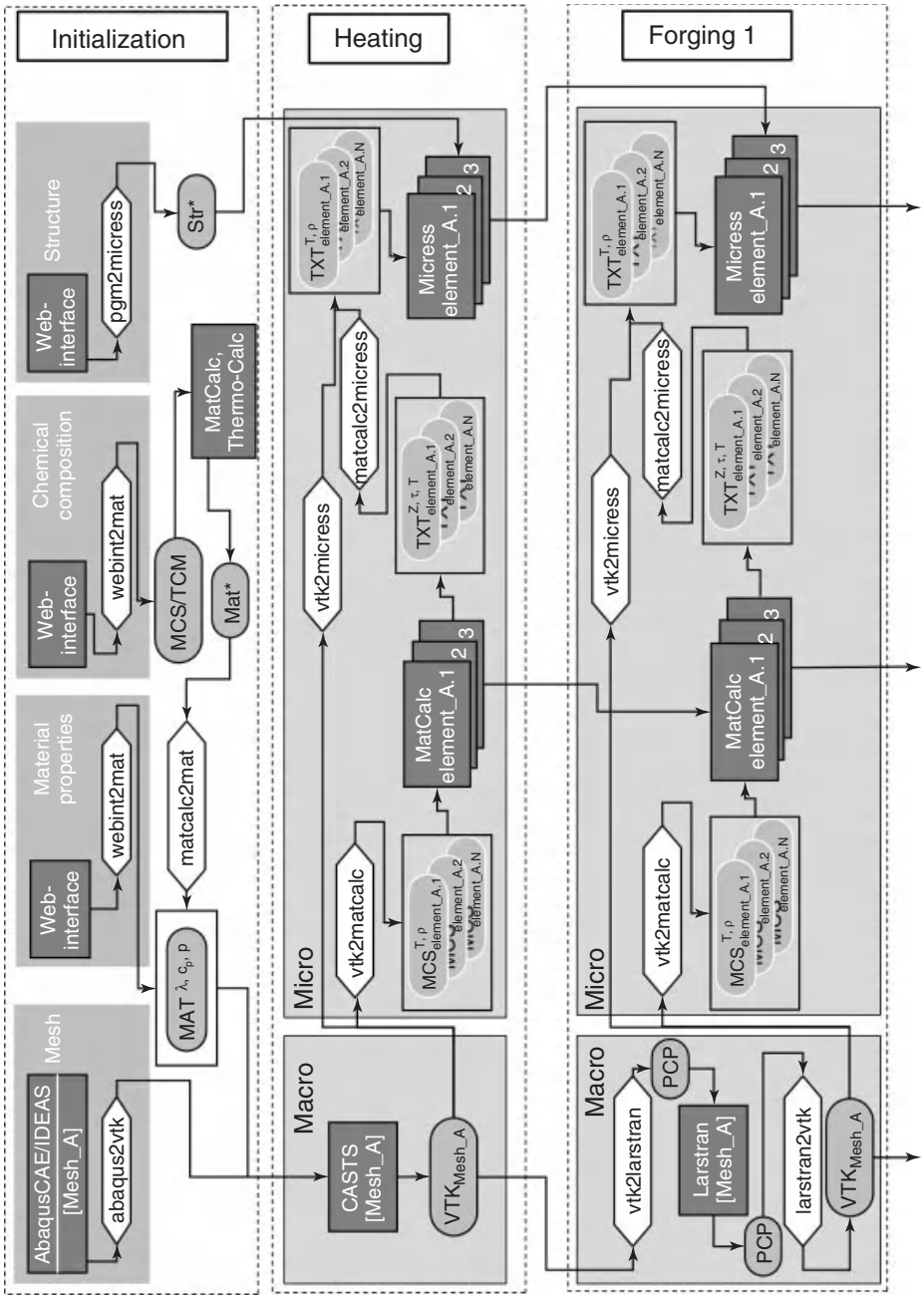

Figure 9.10 Detailed simulation flowchart with principle of simulation tool structure, connections, and data exchange for initialization and calculation of heating and forging.

[13]. For the calculation of heating during the hot forging operation, the materials data are converted in a *.mat-file (Chapter 4), which contains, for example, materials properties required for the heating simulation. In addition, the initial microstructure is provided in a suitable format for MICRESS.

After initialization, the component geometry and the microstructure were imported into CASTS for simulating the heat distribution and phase transformation on the process level. The simulation results are stored in the universal VTK format and time–temperature profiles are extracted for MatCalc and MICRESS for selected points of the component. In the next step, the particle size evolution is calculated by MatCalc using the time–temperature history and information about current matrix phase, mean grain size, and dislocation density from simulation results on the macrolevel for several points in the gearing component, which are tracked along the entire simulation chain.

9.5.2 Macroscopic Process Simulations

Hot Forging The simulation of forging on the macroscopic level was split into three separated simulations because the commercial simulation tools can treat either (i) deformation with consideration of form changing, dynamic, and static recrystallization but without any phase transformation or (ii) heat treatment including phase transformations, however, without any deformation effects. In the first step, the meshed geometry was imported into CASTS, allowing for simulation of sample heating in a muffle furnace using materials parameters from thermodynamic calculations and heat treatment conditions from experiment settings. The final state of this heating process was a sample with homogeneous austenitic structure revealing a defined grain size. This result was then used for a forging simulation with consideration of deformation effects using LARSTRAN/SHAPE. Eventually, quenching of the sample was again calculated by CASTS (Figure 9.11). This scheme allows the consideration of a maximum number of different effects occurring during forging. In addition, the results of the previous calculation can be used in subsequent simulations or transferred through different simulation steps using, for example, point tracking to save the information for later use.

Dynamic Recrystallization The microstructure produced during processing, especially the grain size, has a decisive influence on the final transmission components properties. Dynamic recrystallization (DRX) highly affects the grain size evolution on the one hand and the flow stress on the other hand. Therefore, a correct understanding and a quantitative description of DRX is absolutely meaningful for designing processes in terms of maximal forces, and so on, and estimating the final products properties.

To characterize DRX, a series of compression tests was conducted in which cylindrical specimens of 10 mm in diameter and 15 mm in height were compressed. To guarantee a homogeneous strain distribution during the compression, two pockets

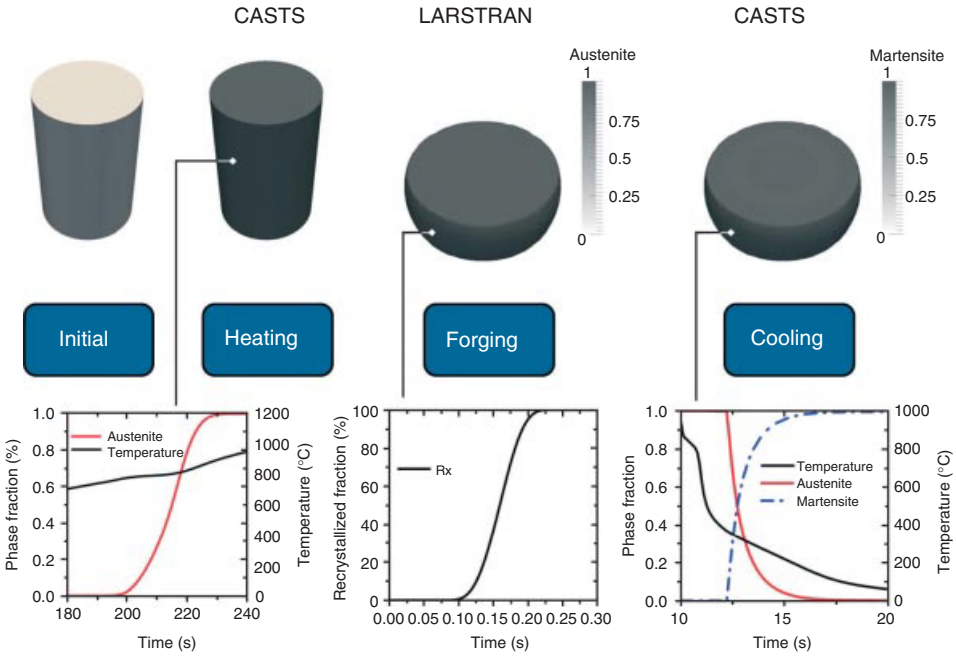

Figure 9.11 Simulation flow for a hot forging process using different simulation tools. The tracked point is located in the centerline at the surface on the outer diameter.

for the lubricant (glass powder) on both plane surfaces of the specimens were machined. An initial grain size of about 34 µm was determined metallographically.

During this series, the specimens were heated and homogenized at a temperature of 1250 °C for 10 min. This homogenization procedure was applied in an external furnace. After this procedure, the specimens were placed into the compression furnace, which was heated to forming temperature. Under contact with the dies, the specimens were cooled down as fast as possible to the respective forming temperatures (750–1250 °C). The specimens were compressed nearly isothermally in a single stroke to the strain of 0.75 at constant true strain rates varying from 0.01 to 100 s^{-1}. In order to investigate the microstructure evolution under the conducted hot working conditions, each specimen was quenched immediately after compression. All specimens were analyzed in terms of the recrystallized volume fraction and its corresponding grain size metallographically. Figure 9.12a illustrates the flow curves from 800 to 1200 °C at various strain rates including their scattering obtained by multiple testing (black).

The empirical, phenomenological microstructure model StrucSim, which is used to model the materials flow behavior and microstructure evolution in combination, is based on the work of Luton and Sellars [14]. The equations used are summarized in Table 9.4. The model was implemented as a FORTRAN subroutine coupled with

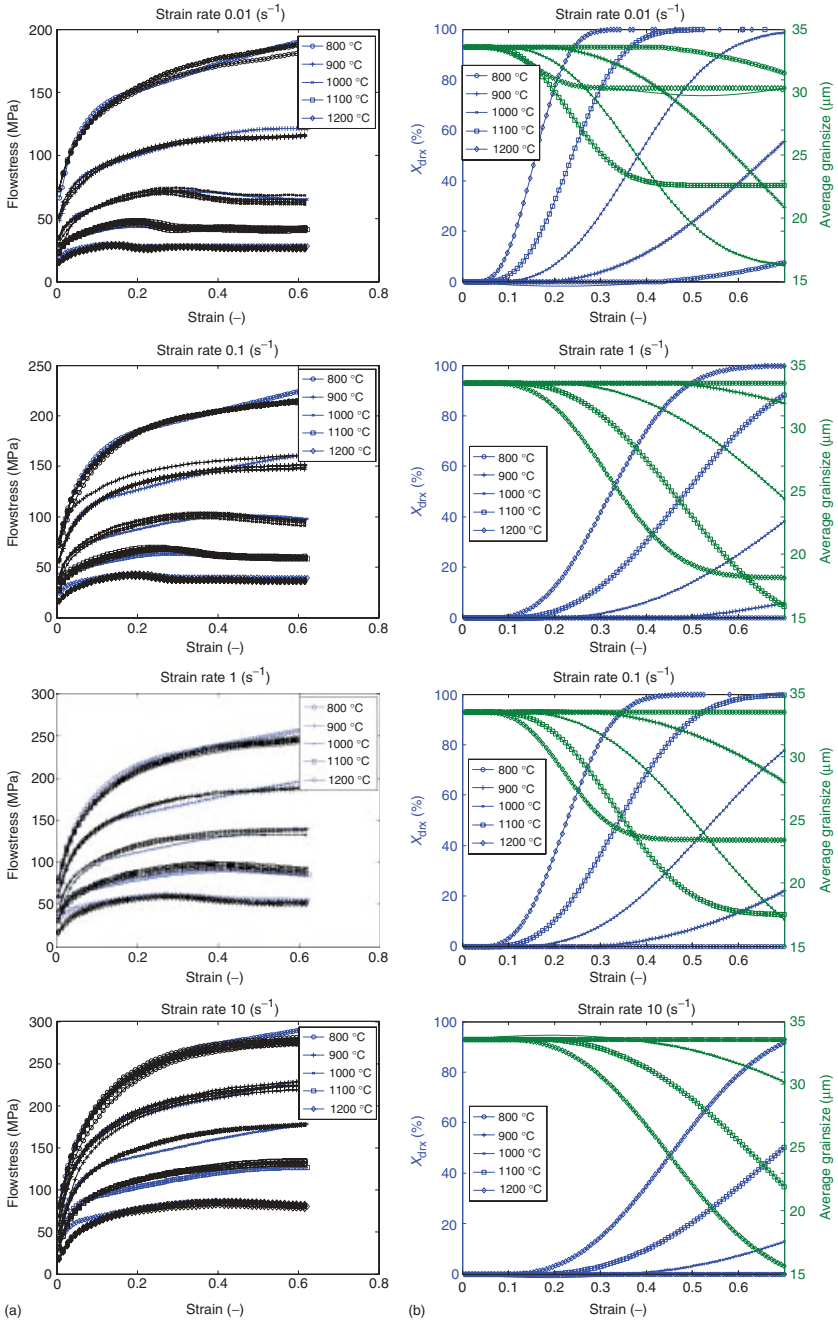

Figure 9.12 Experimental flow curves (black) and results calculated by StrucSim (blue, green) for the microalloyed case hardening steel 25CrMo4(Nb/Ti).

Table 9.4 Equations to describe DRX; the values a_i, e_i, f_i, and Q_w (see text) are material-dependent model coefficients to be identified with respect to experimental data.

Phenomenon	Equation	
Zener–Hollomon Parameter	$Z = \dot{\varepsilon} \cdot \exp\left(\frac{Q_w}{R \cdot T}\right)$	(9.1)
Peak strain	$\varepsilon_p = a_1 \cdot d_0^{a2} \cdot Z^{a3}$	(9.2)
Critical strain	$\varepsilon_c = a_4 \cdot \varepsilon_p$	(9.3)
Steady-state strain	$\varepsilon_{ss} = e_1 \cdot \varepsilon_p + e_2 \cdot d_0^{e3} \cdot Z^{e4}$	(9.4)
Work hardening	$\frac{\sigma}{\sigma_p} = \left[\frac{\varepsilon}{\varepsilon_p} \cdot \exp\left(1 - \frac{\varepsilon}{\varepsilon_p}\right)\right]^C$	(9.5)
Maximum flow stress	$\sigma_p = \frac{f_1 \cdot Z^{f2}}{\sin h\,(f_2)}$	(9.6)
Fraction of dynamic recrystallization	$X_{DRX} = 1 - \exp\left[d_1 \left(\frac{\varepsilon - \varepsilon_c}{\varepsilon_{ss} - \varepsilon_c}\right)^{d_2}\right]$	(9.7)
Dynamic recrystallized grain size	$d_{DRX} = b_1 \cdot Z^{b2}$	(9.8)

the FEM-Code LARSTRAN/SHAPE on the one hand and the numerical computing environment Matlab on the other hand.

Figure 9.13 illustrates the concept of the model. In a finite element (FE) model, the macroscopic equivalent strain, strain rate, and temperature are supplied at each integration point. Initially, the entire volume of an FE represents a homogeneous structure S1. As soon as the strain in the element exceeds the critical value necessary to initiate DRX during deformation, a substructure S2 develops, whose volume fraction is determined by a rate formulation (Eq. (9.7) in Table 9.4). Strain hardening in S2 is reset to the undeformed value, and strain hardening and grain size are then tracked individually for S2. As deformation continues, further substructures develop, which evolve independently and are characterized by their own set of variables characterizing strain hardening and grain size. At the end of each increment, the new overall flow stress is calculated as the volume-weighted sum of flow stress values characterizing each substructure. The macroscopic flow stress is then fed back to the FE main program, and the different substructures are stored for the next time increment.

As a first step, the activation energy Q_w is experimentally determined according to [15]. For this purpose, only the peak flow stresses and their corresponding true strains were determined from temperature-compensated flow curves. Thermal materials properties were considered using CALPHAD methods [16]. The exact

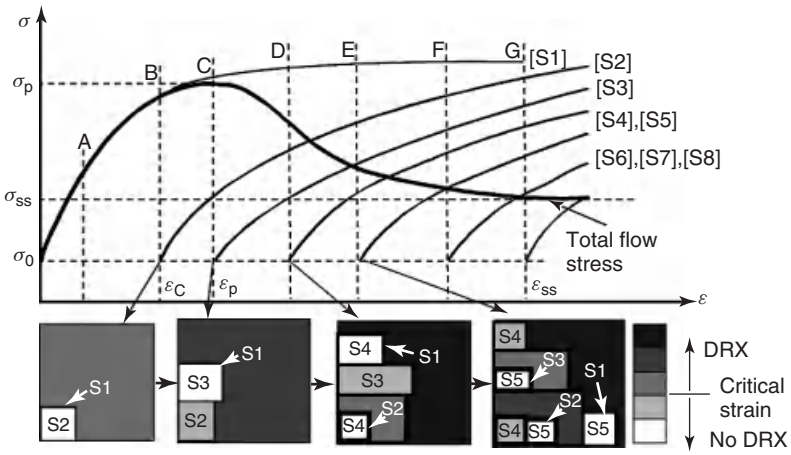

Figure 9.13 StrucSim concept for managing the DRX as a set of substructures. S1, initial microstructure; S2–S5, recrystallized substructures; A–G, time steps (supporting points).

procedure to compensate for the softening during compression is again described comprehensively in Ref. [15]. Applying a simple linear regression fit, the optimum f_3 value was calculated as 0.0072 N mm^{-2} and the value of Q_w was determined as 442 078 kJ mol^{-1}.

One common procedure to determine the model parameters of the Eq. (9.1–9.8) is the application of single regressions using compensated, isothermal flow curves and/or the determined microstructure as input data for each equation. The disadvantages of this procedure can be summarized as follows:

1) As seen in Table 9.4, some of the parameters appear in several equations, for example, the critical strain and steady-state strain given by Eqs. (9.2) and (9.3), respectively, are used in Eq. (9.7). In view of this interdependence in the model, all the parameters identified should work together to optimally predict both flow curves and DRX kinetics.
2) Owing to dissipation effects, the specimen's temperature increases during compression, especially at higher strain rates. This effect is taken into account in terms of flow stresses by the application of compensation strategies. But its influence on the microstructure evolution is neglected. Consequently, the final DRX fraction and grain size at the end of the process are not determined for the desired constant testing temperature and thus also not for a constant Zener–Hollomon parameter Z.
3) Comparing the quality of the measured force–displacement curves and the resulting flow curves with the quality of the measured recrystallized volume fraction and corresponding grain size, metallographic measurements provide less accuracy and reproducibility. As some of the equations exclusively rely

on metallographic measurements as input for the parameter fit, the resulting parameters of a single regression can be highly inaccurate.

Hence, the parameter set as a whole needs to be optimized in a second step using an inverse analysis. For this purpose, the compression tests performed experimentally are simulated using an FE model to which the microstructure model is coupled. The parameter values determined through regression are used as starting values for the optimization. It has to be mentioned that this procedure is time consuming and laborious.

To shorten the procedure for the determination of the other parameters, the microstructure model StrucSim was directly implemented into a Matlab-based routine that allows for calculating nonisothermal flow curves and its corresponding microstructure evolution ($X_{DRX}(t), d_{DRX}(t)$) with high computation speeds. On a 3.0 GHz AMD, Athlon 64 X2 Dual system and 2.0 GB RAM running a 32 bit Matlab version 150 flow curves including microstructure evolution per second can be calculated. It is worth mentioning that the inhomogeneous strain distribution due to friction during the compression tests and its effect on the flow curve can be neglected as shown in [17]. Its effect on the microstructure is neglected as well as the metallographic results reveal only poor reproducibility.

Applying the developed routine on experimental flow curves reaching from 0.01 to 100 s^{-1} in terms of strain rate and from 750 to 1250 °C in terms of temperature, the nonlinear least-square problem considering all parameters at the same time was solved within an acceptable optimization time.

The determined parameters are listed in Table 9.5.

Figure 9.12 shows a comparison between the calculated and measured flow stresses of various parameter combinations at strain rates varying from 0.01 to 10 s^{-1} and different temperatures for 25CrMo4(Nb/Ti). Very good agreement is obtained between the calculation and measurement in view of the shape of the flow curves and the absolute level of the calculated flow stress. In addition, the predicted recrystallized volume fractions and the resulting average grain sizes are illustrated (Figure 9.12b). The comparison of calculated grain size and recrystallized fraction with metallographically determined values yields fair agreement (Table 9.6).

Table 9.5 DRX parameters using automatic, inverse parameter identification procedure.

Parameters			
$Q_w = 442\,078\,\text{kJ mol}^{-1}$	–	–	–
$A_1 = 0.7367\text{E}3$	$a_2 = 0$	$a_3 = 0.1287$	$a_4 = 0.69$
$B_1 = 1017.49$	$b_2 = -0.1116$	–	–
$D_1 = -2.3064$	$d_2 = 2.7234$	–	–
$E_1 = 0.5916$	$e_2 = 0.4131\text{E}3$	$e_3 = 0.34489$	$e_4 = 0.15891$
$f_1 = 0.1621\text{E}2$	$f_2 = 0.1493$	$f_3 = 0.7239\text{E}2$	–
$C = 0.3727$	–	–	–

Table 9.6 Comparison of microstructural parameter grain size d_{avg} and recrystallized fraction X_{DRX} from metallographic analysis after compression test (exp) with calculated (cal) values.

Temperature (°C)	Strain rate	$d_{avg,exp}$ (μm)	$X_{DRX,exp}$ (%)	$d_{avg,cal}$ (μm)	$X_{DRX,cal}$ (%)
1200	0.01	37	100	31	100
1200	0.1	36	100	23	100
1200	1	24	100	18	100
1200	10	20	100	16	90
1000	0.01	24	94	17	98
1000	0.1	21	92	17	80
1000	1	24	64	24	38
1000	10	34	32	30	16

Heat Treatment and Carburizing For heat treatment simulations before and after forging as well as during FP annealing and carburizing, two different tools were used. The first one is CASTS, which allows calculation of heating and heat distribution in the sample. The second tool is the commercial software SYSWELD, which can be used for simulation of case hardening and distortion in addition to heating. However, the conversion of simulation results to the universal VTK platform standard as well as the consideration of thermodynamic and thermomechanical materials data requires a higher effort. In this study, individual simulation steps were calculated using CASTS for heat treatment and SYSWELD for case hardening.

In the simulation chain for this test case, the heat treatment simulation starts with heating of the cylindrical sample. For the calculation of heat distribution and phase transformation, various materials properties must be evaluated or calculated. The commercial software JMatPro provides values for thermodynamic properties such as heat conductivity, density, or specific heat of possible phases. For the calculation of phase transformation, the Avrami parameters (Eq. (9.9)) were defined from dilatation experiments for reheating and from calculated time temperature precipitation (TTP) diagrams for cooling, assuming that the Avrami parameters are constant for a certain temperature and independent of the cooling rate for small time steps. The parameter determination was carried out using the Avrami approach for one temperature with consideration of a small temperature increment, which has two different phase fractions (Eq. (9.10)).

$$x_i = 1 - \exp\left(-bt^n\right) \tag{9.9}$$

where x_i is phase fraction of the phase i at time t for a constant temperature T, Avrami factor b, and Avrami exponent n.

It should be noted that the Avrami exponent n depends on phase fraction and time values only while Avrami factor b needs evaluation of the Avrami exponent n

additionally.

$$n(T_i) = \frac{\ln\left[\frac{\ln(1-x_i)}{\ln(1-x_{i-1})}\right]}{\ln\left(\frac{t_i}{t_{i-1}}\right)} \tag{9.10}$$

$$b(T_i) = -\frac{\ln(1-x_i)}{t_i^n}$$

Once a materials data set is available, the simulation of heat treatment can be performed using generated meshes or meshes exported from preceding calculation step and heating conditions. For the calculation of case hardening close to the surface, a mesh with edge sizes smaller than one-tenth of case hardening depth is needed. As the case hardening depth is usually small compared to the size of the component, this yields an increasing number of elements for the whole volume. In this case, the initial mesh has to be selected as a compromise between calculation accuracy and calculation time. The surface should have small elements in defined depth and the mesh in the core can be generated using large elements.

Thus, the fine initial mesh, even if only at the surface, can lead to a large number of elements causing high computational effort for the preceding forging simulation. In addition, after a forging simulation, the element shape may change because of deformation. Thus, an alternative solution is seen in remeshing of the entire volume before the case hardening simulation. The result of the remeshing depends on the shape of the calculated component and the remeshing methods being applied. In case of complicated component shapes, automatic remeshing may, however, fail and then has to be performed manually.

By point tracking of the simulation results, the evolution of the phase transformation can be observed along the entire process chain at a predefined point of the component (Figure 9.14). The point tracking procedure is used for extraction of local process parameters to provide boundary conditions such as temperature or dislocation density for simulation of phase transformation and particle evolution on the microscale.

Laser Welding The LaserWeld3D [18, 19] simulation is based on the so-called hybrid model. In case of LaserWeld3D, the term *hybrid* refers to the coupling of numerical FEM models to calculate the evolution of heat inside the part and further models with a strongly reduced number of degrees of freedom to display the motion of the welding capillary.

Conventional welding simulations such as SYSWELD or Ansys depict the thermal heat coupling by an equivalent volumetric heat source being parameterized by a small number of constant heat source parameters that have to be determined experimentally, for example, by thermal couples and macrosections.

The motivation to create a model that uses a free moving capillary boundary as heat source is to reflect the physical process of laser welding and to gain a model that does not require experimentally determined heat source parameters. Eventually,

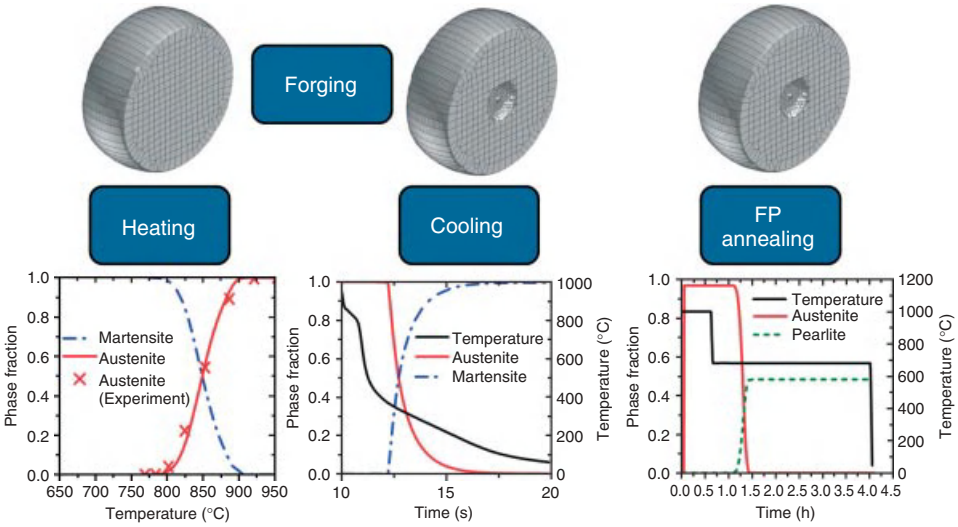

Figure 9.14 Results of calculation on the macroscale for heat treatment of the sample with consideration of phase transformation using point tracking. The tracked point is located in the centerline at the surface on the outer diameter.

models using constant heat source parameters cannot consider conditions in which the process affects the heat source itself. During laser welding, an interdependency of process and heat source may occur if conditions in front of the laser beam are not constant but have to be resolved temporally and spatially. An example of such a condition is a component with varying materials properties along the weld path. Another example is welding of a closed contour with multiple passes. In this case, the temperature in advance of the laser beam will rise with the number of passes, which leads to larger weld depth in most cases.

The hybrid model approach used in LaserWeld3D considers these conditions by solving the heat conduction equation (HCE) inside the part numerically using spatially resolved materials properties (Figure 9.15) and a free moving boundary inside the part with a temperature boundary condition. The shape of this boundary has the physical meaning of the welding capillary surface and is part of the solution of the welding model. To drastically reduce the numerical effort for the motion of this boundary, the partial differential equation (PDE) for the HCE is delegated to an equivalent variational equation. By using an approximate attempt for the temperature as solution quantity, which is parameterized by a small number of characteristic dynamical variables, the PDE is transferred to a system of ordinary differential equations (ODEs) for the characteristic variables [20]. The time-dependent values of these variables are used to reconstruct the shape of the capillary.

The main advantage of this approach is to avoid a complicated attempt to describe the motion of the capillary boundary using a numerical method such as Level-Set,

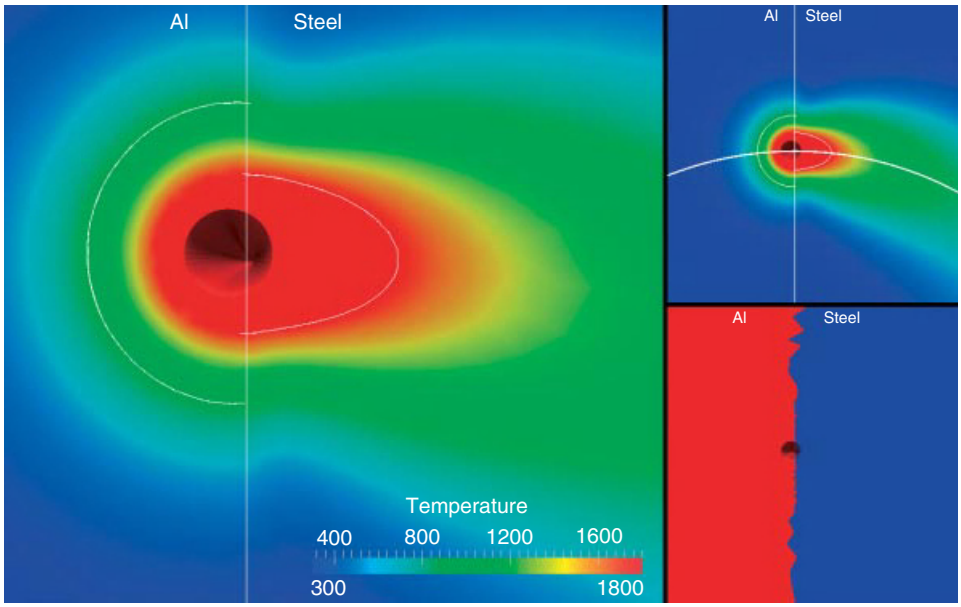

Figure 9.15 Solution for temperature while welding two materials with different materials properties.

which leads to a strongly increased computation time. As long as the conditions for the variational approach are met, the ODE solution [21] offers a good approximation for the shape of the capillary, which can be calculated with very low numerical effort. As the variational approach uses long-term characteristics of the fast variables in the PDE system, the variational approach offers good results if the timescales of external perturbations of the system (e.g., caused by modulation of laser beam parameters) are slower than that of the ODE solution. For continuous-wave laser welding, this condition is met. The variation in materials properties is a very slow process compared to the timescales of the capillary surface and can be considered by recalculation of the ODE system. In the LaserWeld3D simulation, recalculation of the capillary shape is performed if temperature or materials properties in advance of the laser beam change.

The second part of the hybrid model is described by the HCE inside the component, whereby spatially resolved materials properties have to be taken into account. LaserWeld3D uses a standard FEM approach to solve the HCE. The combination of both models leads to a fast simulation that solves the free boundary problem of laser welding with varying materials properties where the motion of the free boundary is performed by a reduced model with very low computational effort.

To simulate the welding of the gearing component, the resulting geometry of the joint part has to be merged. LaserWeld3D uses this merged geometry as calculation domain for the welding simulation. The required materials property data is provided by JMatPro [27]. Later, inhomogeneous and anisotropic materials

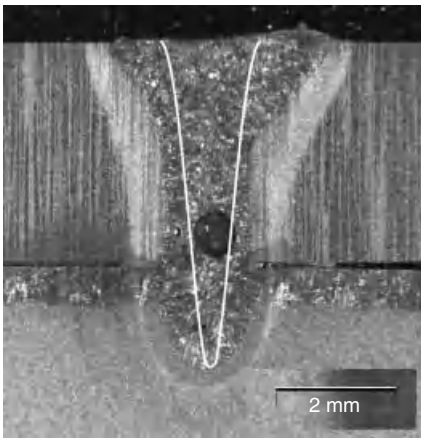

Figure 9.16 Macrosection of gearing component and simulated weld line (white solid line). The experimental and simulated weld depths have a value of $d = 5.5$ mm.

properties from upstream simulations may be taken into account; at present, materials properties are assumed as constant.

As seen in Figure 9.16, there is a good match with the simulated weld depth. The width of the weld is underestimated by the simulation. The strong deviation between simulated and experimental weld seam width may be related to anisotropic materials properties in the real part. Refinements in the welding model and consideration of materials properties from upstream simulations should lead to a better match between simulated and experimental results.

Application The TCA software ''ZaKo3D'' uses the approach according to [22], requiring input of the tooth geometry in Cartesian coordinates with the normal vectors of each considered tooth flank point (Figure 9.17). This geometry can be obtained, for example, from a manufacturing simulation, such as ''Gear Generator'', [23] or via measured results. Along with the input of the tooth geometry, the mutual positioning of the gears has to be defined. Furthermore, pitch deviations, flank modifications, and positioning variations can be considered in the simulation. Thus, parameter variations are possible to identify, for example, the sensitivity of the gear set against manufacturing or mounting errors. While generating the flank grid of the gear for the simulation under load, it is important to generate not only the tooth flanks but also the tooth root. The tooth root is necessary for the mesh generation for the FE-based approach in ZaKo3D in order to calculate tooth flank and root stresses.

In the next step, each node of the FE mesh on the flank, which might come into contact, is loaded with unit forces in the x-, y-, and z-directions. For each of these loads, the displacement of all nodes is obtained using an FE solver. For linear elastic materials behavior, these reactions can be superpositioned in the

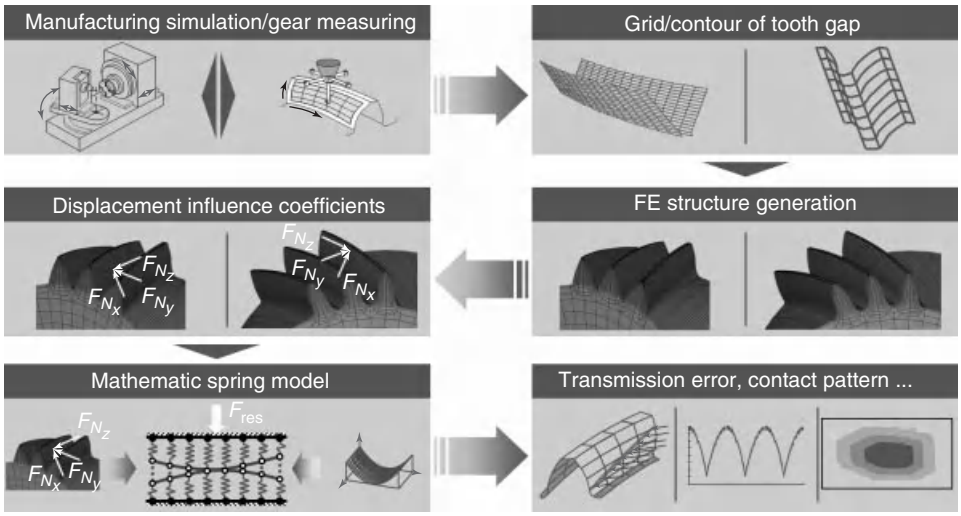

Figure 9.17 Features of the 3D tooth contact analysis.

mathematic spring model [11], which is used for the description of the contact characteristics under load. At first the contact distances between the mating flanks are determined by calculating the distances from all points of one flank to the mating flank. This approach is the three-dimensional component of the TCA, since now the contact search (collision detection) is not limited to the theoretical line of contact as in common software. If only a load-free analysis is needed, such as the tangential composite inspection test in industrial applications, the FE part can be skipped and the contact simulation is directly realized for all pitch positions. In this case, the FE model is not required. Here, the load-free transmission error, contact pattern, and ease off are calculated. Hence, the TCA enables the analysis of the running and noise behaviors of different types of gears. The deviations from the manufacturing as well as the influence of the assembly of the gears can be considered.

In order to close the gap between the different simulation software for rolling, forging, carburizing, machining, and application for the gear part, a data interface is needed. Thus, the data format *.vtk is chosen to transfer the data from one simulation to another. This interface enables the simulation to consider the calculated geometry as well as the local materials properties of the gear as resulting from the prior simulation chain.

9.5.3 Microscopic Simulations

Microstructure Evolution during FP-Annealing For the calculation of pearlite formation during FP annealing, the phase field method was used. The calculation was carried out using the commercial software MICRESS, and for a better

Table 9.7 Activation energy for interface mobility [25].

	Austenite–austenite	Austenite–ferrite	Austenite–pearlite	Ferrite–ferrite	Ferrite–pearlite	Pearlite–pearlite
Q (kJ mol^{-1})	185	150	150	150	215	215

consideration of volumetric carbon distribution the simulation was performed in 3D. The thermodynamic data for the austenite to ferrite transformation was calculated by using MICRESS-Thermo-Calc-coupling and the TCFE5 database. The thermodynamic interaction data for austenite to pearlite transformation were calculated using linearization of the Fe–C diagram with the bulk composition of Mn under paraequilibrium condition. The metastable pearlite phase was taken as a stoichiometric phase with a eutectoid carbon content in the paraequilibrium diagram. The calculation for diffusion of carbon and manganese in ferrite and austenite was performed using the Thermo-Calc coupling and the mobility database MOB2. The values for interfacial energy between ferrite–austenite–pearlite were taken from literature [24]. The interfacial mobility was calculated depending on temperature, according

$$\mu_{ij} = \mu_{ij}^{0} \exp\left(-\frac{Q_{ij}}{kT}\right) \tag{9.11}$$

where μ is the interfacial mobility proportional to the preexponential factor μ^0 and depended on activation energy Q, Boltzmann constant k, and temperature T.

For the interfacial mobility, the activation energy was taken constant for all interfaces from Table 9.7, and the preexponential factor μ^0 was fitted using experimental dilatometer results. The nucleation kinetics was also calibrated according to the experimental results.

The simulation results are shown in Figure 9.18. At the temperature of 1000 °C, only austenite is stable and carbon is homogeneously distributed. During cooling to 680 °C, ferrite grains were first formed on triple junctions between austenite grains. The solubility of carbon in ferrite is much lower than that in austenite. Thus the carbon diffuses from the ferrite–austenite interface into the austenite grains during growth of the ferrite grains. When reaching the carbon solubility limit in austenite, pearlite nuclei were first formed on the ferrite–austenite interface. The remaining austenite forms pearlite. An inconsiderably small redistribution of Mn can be observed during the transformation until all austenite is transformed to pearlite. The reason for that is a very small mobility of Mn in ferrite or austenite in comparison with the process time and temperature. Thus, the pearlite transformation occurs under paraequilibrium condition [25].

Precipitation Evolution along the Process Chain In order to calculate the grain size stability during high-temperature carburizing, the evolution of precipitate size and fraction has to be calculated along the entire process chain. On the

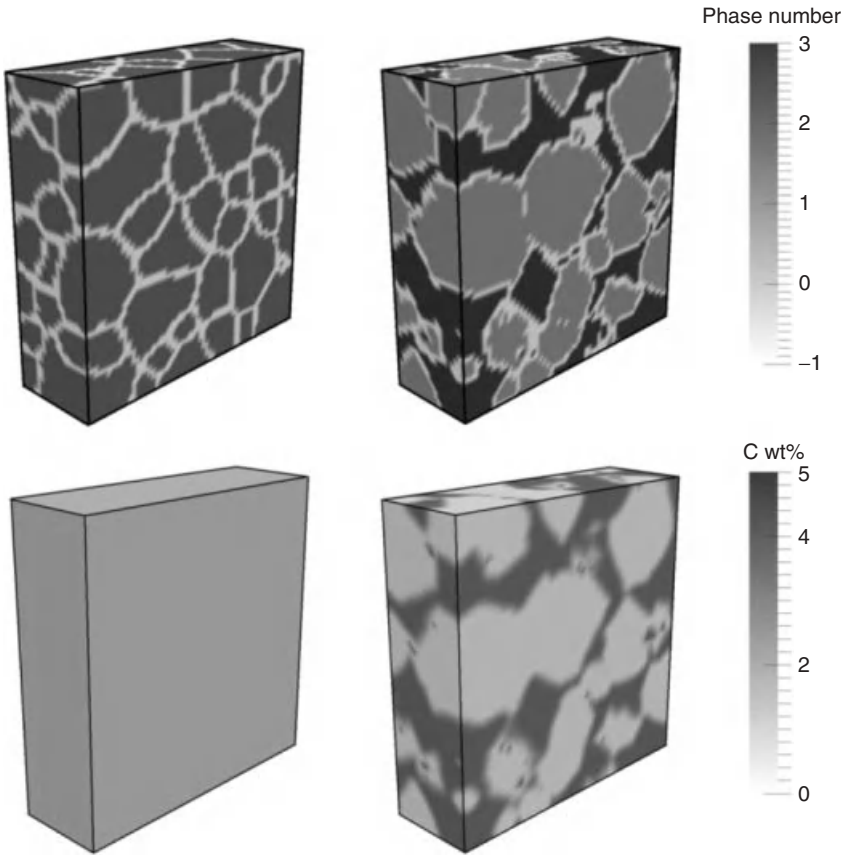

Figure 9.18 Results of a 3D MICRESS simulation of ferrite–pearlite formation from austenite using the phase field method: phase (a: 1, ferrite; 2, austenite; 3, pearlite) and related carbon distribution (b).

basis of the evolution of the process parameter as tracked by the macrocalculation in terms of temperature, strain, grain size, and recrystallized fraction, the precipitation evolution has been simulated along the processes of hot compression, forging, FP annealing, and eventually high-temperature carburizing. On the basis of the calculation of the Zener pinning force as a function of precipitate size and amount during carburizing, the fine grain stability can be calculated [4].

Besides the macroscopic process parameters in terms of temperature, holding time, heating and cooling rates, and deformation degree, the main influencing microstructural factors on particle evolution are the grain size of the matrix and the dislocation density in the respective process time step. During the process chain, these parameters change continuously in time, controlling the evolution of both particle amount and size. For setting up a MatCalc calculation, several simplification assumptions were made:

- Grain size and dislocation density were kept constant during precipitation evolution calculation.
- The initial volume fraction of particles was set to an equilibrium amount according to Thermo-Calc results as initial condition.
- A diffusion correction factor has been introduced to be 100 for (Ti,Nb)-carbonitrides and 10 for Al-nitrides following the procedure described in [5].

For this simulation, the case hardening parameters were set to 5 h at 1000 °C, which corresponds to a carburizing depth of 1 mm. The evolution of the maximal pinning force was calculated using the Gladman approach [26] for Al-nitrides and (Ti,Nb)-carbonitrides separately:

$$Z = \frac{3 \cdot \gamma \cdot f}{2 \cdot r} \tag{9.12}$$

where Z is the pinning force (J cm^{-3}) proportional to surface energy γ (J cm^{-2}), particle volume fraction f, and inversely proportional to mean particle radius r (cm).

The total Zener pinning force for all particles was calculated as the sum of Zener pinning forces for each Al-nitrides and (Nb,Ti)-carbonitrides:

$$Z = Z^{\mathrm{AlN}} + Z^{(\mathrm{Ti,Nb})-(\mathrm{C,N})} \tag{9.13}$$

The evolution of mean particle size along the process chain is compared with experimental results in Figure 9.14. The comparison shows a good agreement with small deviation of mean particle size after rolling. This deviation can be caused by the assumption that initial particle amount is equal to equilibrium amount and nucleation of particle on existing particles is not taken into account. The coarsening rate of (Ti,Nb)-carbonitrides before case hardening is much lower than that of Al-nitrides. During the case hardening at carburizing temperature, (Ti,Nb)-carbonitrides show the same coarsening rate than Al-nitrides, but Al-nitrides have larger size.

The evolution of particle fraction along the process chain can be observed in Figure 9.19a. Al-nitrides were completely dissolved during the hot rolling at 1250 °C and (Ti,Nb)-carbonitrides were only partially dissolved at the same temperature because of the high stability of Ti-nitrides. In the second heat treatment step, new Al-nitrides were formed and grew by reheating and soaking during the forging process. The fraction of (Ti,Nb)-carbonitrides and Al-nitrides increased at this time but did not reach the maximum equilibrium value. Thus, during the next austenitization and holding in ferrite–pearlite area, a further increase in particle fraction can be observed.

When reaching the case hardening temperature, the amount of (Ti,Nb)-carbonitrides is higher in comparison to Al-nitrides. Coarse Al-nitrides and their lower amount are reasons for smaller pinning force as compared to (Ti,Nb)-carbonitrides (Figure 9.19c). The (Ti,Nb)-carbonitride contribute the larger part of the total pinning force and thus are more efficient for grain size control for this material at this carburizing temperature.

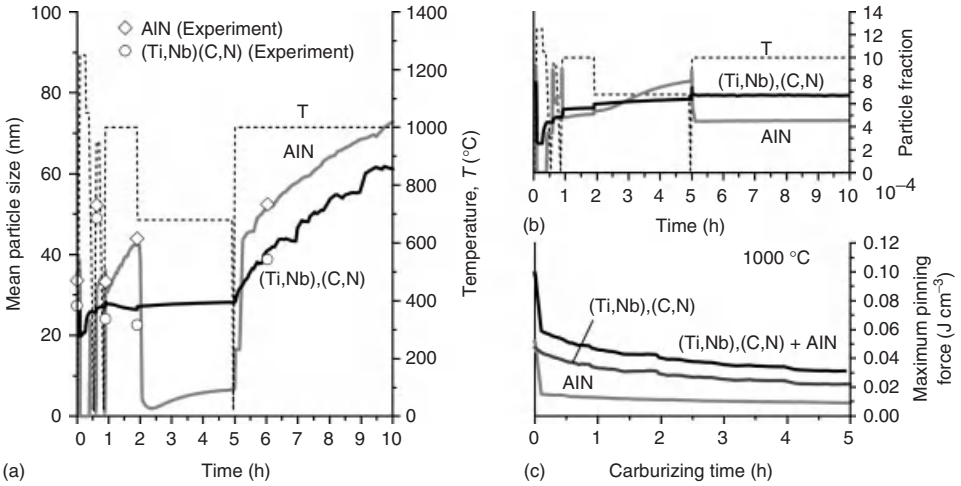

Figure 9.19 Simulation results of particle mean size compared with experimental results (a), particle fraction (b) evolution along the process chain (hot rolling, forging, FP annealing, carburizing), and calculated maximal pinning force during the case hardening at 1000 °C (c).

Influence of Process Chain Variation The above approach has been applied to calculate the influence of a variation in the process chain and parameters on the pinning force [5]. This study focuses on variation of FP annealing and carburizing process. Four process chains have been compared numerically concerning their effect on Zener pinning force during carburizing (Figure 9.20):

- **Process chain 1**: This is the reference process chain as presented in the section titled Precipitation Evolution along the Process Chain; the austenitization of FP annealing is carried out at 1000 °C for 1 h.
- **Process chain 2**: It is characterized by an extra high-temperature carburizing process at 1100 °C, while the FP annealing is same as process variation 1.
- **Process chain 3**: It is characterized by a high austenitization temperature 1200 °C during FP annealing, while the carburizing conditions are same as for variation 1.
- **Process chain 4**: It is characterized by decreased FP annealing 0.5 h at 1000 °C, while the carburizing is same as in variation 1.

In Figure 9.20, the results of the calculation are compared with respect to the reference process chain:

1) Increasing the austenitization temperature up to 1200 °C during the FP annealing can be used with the aim of maximizing the dissolved particle amount and renucleation of fine particles. The process chain calculation, however, shows that in this case, the pinning force remarkably decreases. This process variation thus will not lead to grain size stability during high-temperature carburizing.

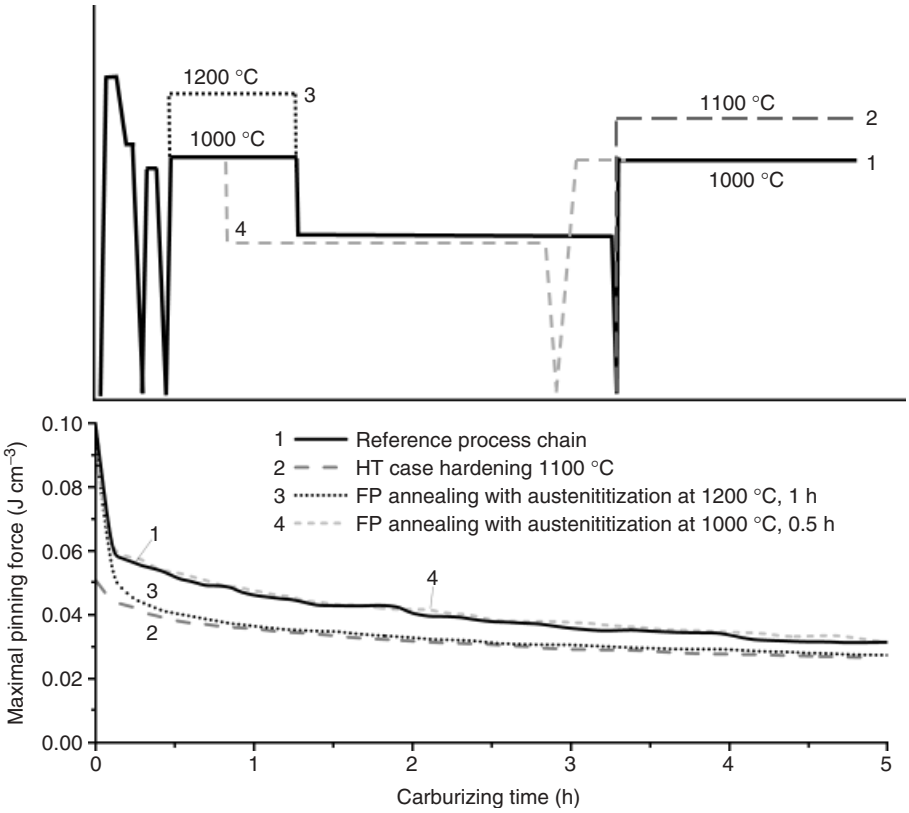

Figure 9.20 Results of pining force calculation for holding at different temperatures and for different process chains (see text).

2) An increase in the carburizing temperature up to 1100 °C shows the same decrease in pinning force evolution. This process chain also will not ensure grain size stability, as the Zener force is too small.
3) The reduction in soaking time for austenitization during the FP annealing leads to the same value of pinning force as the reference process. This variation will have no negative effect on the grain stability and thus a more energy- and time-efficient FP annealing can be chosen.

9.6 Conclusions

Case hardening at high temperatures above 950 °C requires the optimization of materials concepts using selective additions of microalloying elements. The addition of elements such as niobium, titanium, or/and aluminum in a defined relation to nitrogen forms stable particles of nanometer size at this temperature,

which allows to obtain control on grain growth for high temperature of more than 1050 °C. In addition to these chemical arguments, the grain size of austenite during the carburizing process depends on the particle state as well as on the initial austenite grain size. Former work has shown that all previous process steps such as heat treating and deformation may influence both particle state and initial austenite grain size, thereby affecting grain stabilization.

Thus, for design of optimized materials and processes, it is necessary to consider the entire process chain in order to reach optimal fine grain stability. The virtual platform AixViPMaP was used for the exchange of the simulation results between different simulation tools along the virtual process chain and across all relevant length scales. Using the example of the production of a gearing component, the exchange is realized by a universal data format for taking into account all factors influencing the mechanical behavior of a component in an integrative, multiscale simulation approach. By comparison of simulation and experimental results, the predictions were validated successfully.

Finally, the influence of variations in process steps and process parameters on the evolution of Zener pinning force has been shown. This parameter quantifies the effect of process history in terms of precipitation state, and it helps to predict the stability in grain size during high-temperature carburizing as a function of the process chain. The next steps will be the investigation of robustness of process chains against variations due to production errors, the application to large components such as for wind energy and the design of an Al-reduced concept aiming cleanliness optimization.

References

1. Hippenstiel, F., Bleck, W., Clausen, B., Hoffmann, F., and Kohlmann, R. (2002) Innovative Einsatzstähle als maßgeschneiderte Werkstofflösung zur Hochtemperaturaufkohlung von Getriebekomponenten. *HTM Z. Werkst. Waermebeh. Fertigung*, **27** (4), 290–298.
2. Klenke, K. and Kohlman, R. (2005) Einsatzstähle in ihrer Feinkornbeständigkeit, heute und morgen. *HTM Z. Werkst. Wärmebeh. Fertigung*, **60** (5), 260–270.
3. Konovalov, S., Clausen, B., Prahl, U., Bleck, W., and Zoch, H.-W. (2009) Entwicklung einer Prozesskette zur Herstellung von Schmiedebauteilen für die Hochtemperaturaufkohlung, Final report of research project AiF 14841 N.
4. Rudnizki, J., Zeislmair, B., Prahl, U., and Bleck, W. (2010) Prediction of abnormal grain growth during high temperature treatment. *Comput. Mater. Sci.*, **49** (2), 209–216.
5. Konovalov, S., Prahl, U., Kohlmann, R., Kozeschnik, E., and Bleck, W. (2011) Simulation der Ausscheidungsentwicklung entlang der Prozesskette für das Hochtemperatur-Aufkohlen. *J. Heat Treat. Mater.*, **66** (4), 217–229.
6. Microstructure Evolution Simulation Software (MICRESS) (2009) User's Manual, Release 5.3, October 2009, *http://www.micress.de* (accessed 2011).
7. MatCalc – The Materials Calculator (2011), *http://www.matcalc.tuwien.ac.at*
8. STAR -Cast Casting and Solidification Simulation Software, (2010) *http://www.starcast.org* (accessed 2011).
9. LARSTRAN (1994) User's Manual (Revision F), LASSO Ingenieurgesellschaft, Leinfelden Echterdingen.

10. ESI Group (2011) SYSWELD Release Notes, *http://www.esi-group.com/products/welding* (accessed 2011).
11. Brecher, C., Gorgels, C., and Röthlingshöfer, T. (2010) Simulation and measurement of the running behaviour of beveloid gears. International Conference on Gears, Düsseldorf, 2010, pp. 1349–1360.
12. Thermo-Calc Software AB (2010) Database TCFE6, *http://www.thermocalc.com*
13. JMatPro (2010) User's Guide, Sente Software Ltd., Guildford, *http://www.thermotech.co.uk/jmatpro.html* (accessed 2011).
14. Luton, M.J. and Sellars, C.M. (1969) Dynamic recrystallization in Ni and Fe-Ni alloys during high temperature deformation. *Acta Metall.*, **17**, 1033–1043.
15. Xiong, W., Wietbrock, B., Saeed-Akbari, A., Bambach, M., and Hirt, G. (2011) Modeling the flow behavior of a high-manganese steel Fe-Mn23-C0.6 in consideration of dynamic recrystallization. *Steel Res. Int.*, **82** (2), 127–136.
16. Thermo-Calc AB TCFE4-TC Steels/Alloys Database, Sweden.
17. Henke, T., Bambach, M., and Hirt, G. (2011) Experimental uncertainties affecting the accuracy of stress-strain equations by the example of a Hensel-Spittel approach. The 14th International Esaform Conference on Material Forming: ESAFORM 2011, Belfast, Northern Ireland, 27–29 April 2011.
18. Jansen, U. (2009) *Simulation des Schweißens kleiner Bauteile*, RWTH Aachen University, Aachen.
19. Pfeiffer, S. (2010) *Hybrides Prozessmodell für das Tiefschweißen mit Laserstrahlung*, RWTH Aachen University, Aachen.
20. Schulz, W. *et al.* (2009) Simulation of laser cutting, in *The Theory of Laser Materials Processing*, Series in Materials Science, Vol. **119** (ed. J.M. Dowden), Springer.
21. Schulz, W. *et al.* (1997) A free boundary problem related to laser beam fusion cutting: ODE approximation. *Int. J. Heat Mass Transfer*, **40** (12), 2913–2928.
22. Hemmelann, J. (2007) *Simulation des lastfreien und belasteten Zahneingriffs zur Analyse der Drehübertragung von Zahnradgetrieben*, Shaker Publisher, Aachen.
23. Brecher, C., Gorgels, C., and Röthlingshöfer, T. (2009) Manufacturing simulation of beveloid gears for the use in a general tooth. Contact analysis software. *Prod. Eng. Res. Dev.*, **3** (1), 103–109.
24. Savran, V. (2009) Austenite formation in C-Mn steel. PhD thesis. Delft University of Technology.
25. Tewari, S.K. and Sharma, R.C. (1985) The effect of alloying elements on pearlite growth. *Met. Mater. Trans. A*, **16** (4), 597–603.
26. Gladman, T. (2004) *Grain Size Control*, Maney Publishing, London.
27. Saunders, N., Guo, Z., Li, X., Miodownik, A.P., and Schillé, J.-Ph. (2003) Using JMatPro to model materials properties and behavior. *JOM*, **55/12**, 65.

10
Test Case: Technical Plastic Parts

Walter Michaeli, Christian Hopmann, Thomas Baranowski, Gottfried Laschet, Barbara Heesel, Tim Arping, Kirsten Bobzin, Tatyana Kashko, and Mehmet Öte

10.1
Introduction

Plastic parts are being used more and more in technical applications where they especially have to fulfill various mechanical requirements. Hence, the material-oriented design and dimensioning of technical plastic parts is a key technology. The great number of available materials, in addition to complex part geometries due to a high degree of functional integration, increases the effort for a proper evaluation of a design concept. On top of that, polymers show a nonlinear mechanical behavior that is affected by the so-called inner properties of the plastic materials. Especially for semicrystalline thermoplastics, inner properties such as crystalline morphology and molecular orientations vary strongly with the processing conditions and their processing history. Thus, the integrated computational materials engineering (ICME) approach appears to be successfully applicable to this materials class to improve the quality of computer-aided engineering of technical plastic parts.

In this test case, the integrative simulation approach is applied to the injection molding process, which is mostly used for the production of technical plastic parts. The aim of this investigation is to enhance the prediction of the mechanical part behavior regarding the microstructure of the examined specimens. For this, a simulation tool that is able to predict the local microstructure evolution in an injection-molded part is developed. This microstructure information is transferred into effective mechanical properties on the macroscale via homogenization approaches [1, 2]. This locally variable effective materials behavior is finally incorporated in the structural simulation of the considered specimen.

This simulation chain should be understood as an example of the advantage of considering the influence of the inner properties on the macroscopic behavior of plastic parts. Besides the mechanical behavior, the microstructure of thermoplastics influences numerous part characteristics such as its chemical resistance, its optical properties, or its shrinkage and warpage behavior. Therefore, the presented simulation technologies can still be employed for many other applications.

Integrative Computational Materials Engineering: Concepts and Applications of a Modular Simulation Platform,
First Edition. Edited by Georg J. Schmitz and Ulrich Prahl.

As thermoplastic materials have a completely different structure and behavior compared to metals, in the following section some details on the examined plastic material are given.

10.2 Material

Plastic materials are macromolecular materials that are composed of a multitude of monomeric elements, leading to the name polymer (from Greek ''poly meros'' meaning ''many parts''). The materials behavior of polymers is totally controlled by their molecular structure [3]. Macromolecules mostly consist of a carbon backbone with optional side groups leading to various materials with differing properties. If its macromolecules are linear or branched but not cross-linked, a plastic material is referred to as a *thermoplastic*. Besides the covalent bonds in the backbone in this materials class, cohesion is maintained by intermolecular (van der Waals) forces that strongly vary with the distance between the molecules. As between the macromolecules, there are no cross-link thermoplastics that can be melted and processed very easily. In practice, plastics are applied comparatively close to their melting temperature. In combination with the molecular structure, this evokes high dependencies on time and temperature of the materials behavior.

The processing conditions and the molecular structure influence the alignment of the molecules in the materials and therefore have an impact on the materials behavior. If the macromolecules in a polymer reveal a very uniform configuration, superordinate structures are built during cooling, in which the macromolecules are arranged very closely to each other, leading to high intermolecular forces. Between these crystalline structures, amorphous areas always exist in which the macromolecules are not ordered. Hence, these materials are called *semicrystalline thermoplastics*. Also, shearing of polymer melts during processing leads to an alignment of the molecule chains in the direction of flow. These orientations relax in time at temperatures in the area of the melting temperature. In industrial plastic processing, the material is cooled so fast that the molecular orientations are maintained in the solid plastic product, leading to an anisotropic materials behavior.

10.2.1 Polypropylene

The material analyzed in this study is an unreinforced polypropylene (PP), SABICPP 505 P, manufactured by Saudi Basic Industries Corporation (SABIC), the Netherlands [4]. PP is polymerized from propylene ($H_3C–CH=CH_2$), resulting in a nonpolar hydrocarbon-based polymer. The low density of the material is in the range of 0.905–0.915 g cm^{-3}, and the melting temperature of the crystalline structures is about 160–165 °C. Isotactic PP is processed with melt temperatures of

Table 10.1 Basic properties of polypropylene SABIC 505 P.

	Density	Melt flow rate (MFR) at 230 °C and 2.16 kg	Flexural modulus	Stress at yield
Values	905	2.0	1450	41
Unit (SI)	kg m^{-3}	g per 10 min	MPa	MPa

220–270 °C. The service temperature is limited to 140 °C for short-term and 100 °C for long-term loadings.

On the basis of quantity, PP is one of the most processed plastic materials. The low costs and the favorable materials properties such as good chemical resistance, minimal water absorption, and adequate mechanical performance lead to a further penetration of the market. Examples of technical applications of PP can be found in automotive interiors, ventilation systems, tool cases, functional parts with integral hinges, or white goods.

In Table 10.1, some basic properties of SABICPP 505 P are listed.

10.3 Process Chain

The injection molding process is the most important manufacturing process for technical plastic parts. The main advantages of this one-step primary shaping process are a high reproducibility, a full automation, and no necessity for finishing. With this advanced technology, a direct transformation of the raw material into a finished, highly integrated component is possible. Hence the process chain for injection molding parts is very short and mostly consists of just the one process step. Besides the manufacturing process, the resulting mechanical part behavior during the service life is also of interest for this test case. As the focus in this study lies on the first realization of an integrative materials modeling for unreinforced plastics, possible subsequent processing steps such as coating or welding are not regarded here. This leads to the process chain shown in Figure 10.1.

During the injection molding process, the granulated thermoplastic material is melted by a plasticizing unit. For this, a rotating screw conveys and plasticizes the material. After closure of the mold, which contains the cavities for the manufactured parts, the plasticized material is injected into the mold via an axial movement of the screw. Inside the cavities, the thermoplastic material is cooled until a solid state that allows a damage-free demolding of the parts is reached. The inner properties of the processed material in the manufactured parts can be influenced strongly by varying the temperature and flow conditions of the process. Hence, a variation in process parameters as mold and melt temperature or injection velocity affects the

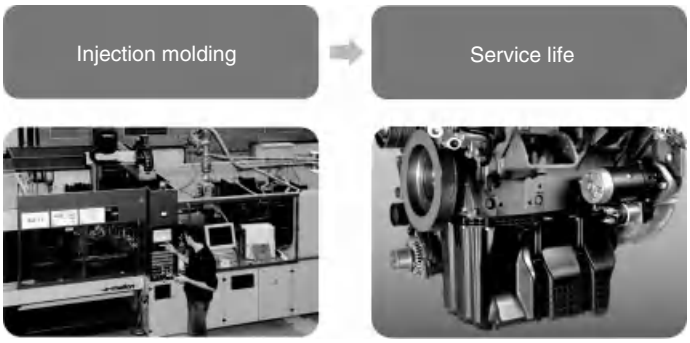

Photo: Wincany/IKV, BASF

Figure 10.1 Process chain for technical plastic parts.

useful properties of the finished parts. This effect on the service life performance of a plastic part is modeled in this test case.

10.4 Modeling of the Phenomena along the Process Chain

10.4.1 Crystallization of Semicrystalline Thermoplastics

The crystallization of polymers has been investigated and modeled for more than 50 years by many scientists, resulting in a broad variety of different models. This phenomenon can be divided into two main processes, *the nucleation and the growth*. Nucleation describes the development of seeds that function as an origin for the growth of polymer crystals, leading to a specific morphology in the solid state. Different investigations show that the evolution of morphology in injection-molded parts depends on the thermal and rheological boundaries in the cavity. Typically, three different main layers of morphologies are distributed over the wall thickness in injection-molded parts. At the boundary of the parts, a very fine, almost amorphous, microstructure develops because of the high temperature gradient resulting from the contact of hot melt and relatively cold mold wall. Near this boundary layer, the shear stresses during part filling are very high and in many cases lead to a specific flow-induced crystallization, resulting in yet another different morphology. Toward the center of the part, the low temperature gradient leads to coarse structures the so-called spherulites (Figure 5.13) [5].

10.4.1.1 Modeling of Crystallization in Injection-Molded Parts

Although extensive research has been conducted on the modeling of microstructure evolution, no integrative approach has been made to transfer the information of polymer microstructure into structural analysis. To achieve an integrative simulation and to predict the 3D microstructure evolution during the injection

molding process, the software SphäroSim was developed at the Institute for Plastics Processing (IKV), Aachen, in the past four years [6, 7]. This software uses the results of the macroscale injection molding simulation as input data and is based on a cellular automat for calculation. Such a cellular automat can assign cells one of two different states, melt state or solid state. The decision whether and when a cell in melt state crystallizes is mainly dependent on its temperature and the relation to its neighboring cells. For the described investigations, three different nucleation models and a spherulite growth model were implemented and validated in SphaeroSim. Those models are listed in the following sections. Further information can be found in the referenced literature.

10.4.1.2 Implemented Models

Nucleation To describe the macromolecular nucleation phenomenon, the well-known model of Hoffman *et al.* [8] is implemented in SphaeroSim (Eq. (10.1)).

$$\dot{N} = \dot{N}_0 \bullet \exp\left(\frac{-U^*}{R \bullet (T - T_\infty)}\right) \bullet \exp\left(\frac{-7.55 \bullet \sigma_s^2 \bullet \sigma_e \bullet \left(T_\mathrm{m}^0\right)^2 \bullet \left(T_\mathrm{m}^0 + T\right)^2}{k \bullet \Delta h_f^2 \bullet T^3 \bullet \Delta T^2}\right) \tag{10.1}$$

In this expression, $\dot{N}$ describes the nucleation rate and $\dot{N}_0$ stands for a material-dependent parameter. T_∞ is the temperature where no chain movement takes place anymore, R is the gas constant, k the Boltzmann constant, Δh_f specifies the heat of fusion, σ_s and σ_e are surface energies, and U^* is the activation energy of a molecular segment necessary to crystallize. Furthermore, ΔT is defined as $\Delta T = T_\mathrm{m}^0 - T$, where T_m^0 is the equilibrium melting temperature. Besides this macromolecular model, two empirical models are also implemented in SphaeroSim. In the first model, according to Moneke [9], the parameters A_N, B_N, and T_C were determined by using experimental data (Eq. (10.2)).

$$\dot{N}(T) = \frac{A_\mathrm{N}}{\sqrt{2\pi \bullet B_\mathrm{N}^2}} \bullet \exp\left(-\frac{(T - T_\mathrm{C})^2}{2 \bullet B_\mathrm{N}^2}\right) \tag{10.2}$$

The second empirical model for nucleation is based on the work of Janeschitz-Kriegl [10] (Eq. (10.3)).

$$N(T) = N_\mathrm{ref} \bullet \exp\left(c_\mathrm{N}(T - T_\mathrm{N,ref})\right) \tag{10.3}$$

In this equation, N_ref is the amount of spherulites referring to a reference temperature $T_\mathrm{N,ref}$ and c_N is a material-dependent parameter.

Spherulite Growth For the spherulite growth, again a macromolecular model from Hoffman *et al.* [8] is adopted:

$$G = G_0 \bullet \exp\left(-\frac{U^*}{R(T - T_\infty)}\right) \bullet \exp\left(-\frac{K_\mathrm{g}}{T \bullet \left(T_\mathrm{m}^0 - T\right)}\right) \tag{10.4}$$

In this model, G_0 stands for a material-dependent value and K_g is the nucleation exponent of the secondary nucleation, the other parameters are the same as in Eq. (10.1).

10.4.1.3 **Validation**

Spherulite Growth To validate the implemented growth model working in a cellular automat, a specific scenario is created. A single nucleus is set in an element with 10^6 cells, then the spherulite growth is calculated with SphaeroSim, and its growth rate is determined (Figure 10.2).

These results are compared to the experimental data from Janeschitz-Kriegl [10] and the material-specific parameters G_0 and K_g are adapted. The results of calculated spherulite growth with the modified parameters ($G_0 = 0.44\,\mathrm{m\,s^{-1}}$ and $K_g = 350\,000\,\mathrm{K}$) and the measurements are shown in Figure 10.3.

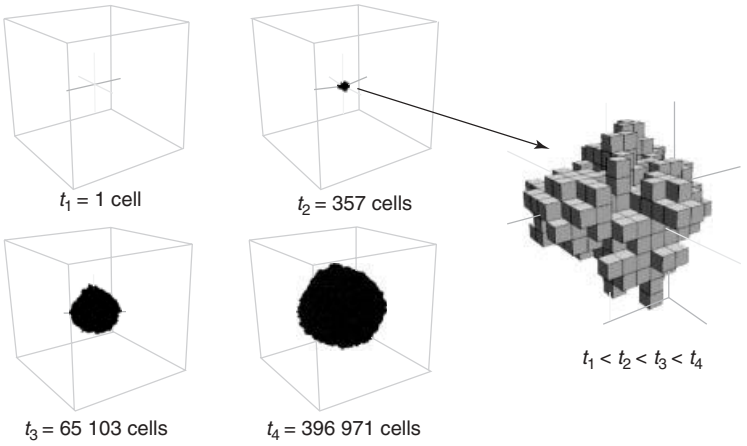

Figure 10.2 Calculated spherulite growth in one element.

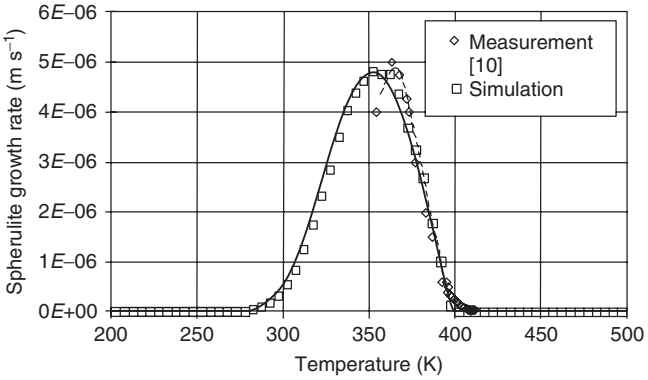

Figure 10.3 Calculated and measured spherulite growth rate depending on temperature.

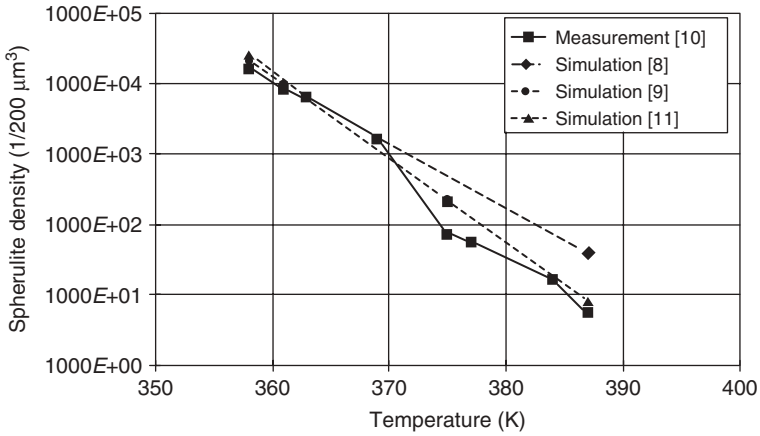

Figure 10.4 Influence of crystallization temperature on spherulite density.

This comparison shows that the cellular automat is able to predict the spherulite growth correctly for temperatures between 420 and 360 K. Toward lower temperatures, the simulation outlines a difference in the measurements. Yet, as the crystallization of isotactic PP takes place, in most cases between 420 and 370 K, this difference has only a small impact on the calculated results.

Nucleation For the validation of the nucleation models, experimental data from Janeschitz-Kriegl [10] containing a measured amount of spherulite depending on the crystallization temperature are used. Therefore, the modified spherulite growth algorithm with the parameters explained above ($G_0 = 0.44\ \mathrm{m\ s^{-1}}$ and $K_g = 350\,000\ \mathrm{K}$) is used to validate the implemented nucleation models. The results of a calculated element (with an edge length of 200 µm) under isothermal boundary conditions are shown in Figure 10.4 for the three nucleation models.

The parameters used for all models are listed in Table 10.2.

These results show a very good accordance with reality by using the models from Housmans [11] and Moneke [9] and good results with the model from Hoffman *et al.* [8]. As the calculation is correlated under isothermal conditions, the results must be validated for all models on realistic, nonisothermal conditions (Section 10.7)

10.4.2 Formation of Molecular Orientations

Molecular orientations result from the flow behavior of thermoplastic melts during processing and have a distinct distribution in injection-molded plastic parts. Owing to shear stresses in the flow channel, molecular chains are stretched during part filling and can, if cooled down rapidly, solidify in an oriented state. If stressed melts are in a state of shear and are not cooled down or are cooled down at low temperature gradients, those molecular orientations can also disappear by

Table 10.2 Modified parameters for the calculation of nucleation.

Parameter	Value	Unit	Model
$\dot{N}_0$	10^{23}	1 (m^3 s^{-1})	[8]
U^*	418.7	Cal	[8]
R	8314	J (mol K)$^{-1}$	[8]
T_∞	220	K	[8]
T_m^0	483	K	[8]
σ_s	0.0118	J m^{-2}	[8]
σ_e	0.09	J m^{-2}	[8]
Δh_f	2.8×10^8	J m^{-2}	[8]
k	1.38×10^{23}	W (m^2 K^4)$^{-1}$	[8]
A_N	2×10^{18}	K (m^3 s)$^{-1}$	[9]
B_N	10	K	[9]
T_C	330	K	[9]
N_{ref}	10^{10}	1 m^{-3}	[11]
c_N	0.4	–	[11]
$T_{N,ref}$	383	K	[11]

molecular relaxation. In most cases, high orientations occur in injection-molded parts and can be found near part boundaries, where high stresses and temperature gradients occur. In addition, there is a dependence on the wall thickness and also one on the flow length. Along the flow path, the temperature, velocity, and shear profiles change and lead to a variation in molecular orientations. Therefore, process parameters as mold temperature and injection velocity also have a strong influence on molecular orientations [10, 12, 13]. The amount of orientation can indirectly be analyzed by birefringence of Fourier transform infrared (FT-IR) measurements, as was shown in [9] for different samples.

10.4.2.1 Modeling of Molecular Orientations in Injection-Molded Parts

In the research work described in the following, molecular orientations are predicted by using the results of the injection molding simulation software SigmaSoft as input. The results of this simulation include the temperature, velocity, and shear fields and their histories, all influencing factors in the development of molecular orientations. Using Eq. (10.5) proposed by Pantani [27, 28] these calculated values can be used to predict a local distribution of the relaxation time.

$$\lambda\,(T, \dot{\gamma}) = \frac{\lambda_0\,(T)}{1 + \left[\frac{\lambda_0(T)}{k}\dot{\gamma}\right]^{1-m}} \tag{10.5}$$

with

$$\lambda_0\,(T) = \lambda^* 10^{\frac{-A(T-T_0)}{B+T-T_0}} \tag{10.6}$$

Table 10.3 Determined parameters of PP 505 P.

Parameter	Value	Unit
A	66.85	–
B	1000	K
T_0	513	K
K	0.1590	–
Λ^*	500	S
M	0.2885	S

Equation (10.5) describes the relaxation time depending on the processing parameters. These are the temperature T and the shear rate $\dot{\gamma}$. The other parameters listed in Eq. (10.5) are material-dependent constants that were determined at IKV for the used PP (Table 10.3).

With the information about the relaxation time, the conformation tensor $\langle \underline{RR} \rangle$ is calculated according to Eq. (10.7):

$$\frac{D}{Dt}\langle \underline{RR} \rangle - \underline{\underline{\nabla v}} \times \langle \underline{RR} \rangle - \langle \underline{RR} \rangle \times \underline{\underline{\nabla v^T}} = -\frac{1}{\lambda}\left[\langle \underline{RR_0} \rangle - \langle \underline{RR} \rangle\right] \tag{10.7}$$

with $\langle \underline{RR_0} \rangle$ as a structural tensor, which is assumed to be the unit tensor at the simulation begin. Equation (10.8) describes the deformation tensor

$$\underline{\underline{A}} = \frac{3}{\langle R_0^2 \rangle}\left[\langle \underline{RR} \rangle - \langle \underline{RR} \rangle_0\right] \tag{10.8}$$

where $\langle R_0^2 \rangle$ is the trace of the conformation tensor. The eigenvalues of the deformation tensor are then determined and set in correlation with the birefringence, the stress optical coefficient C, and the shear modulus G in Eq. (10.9).

$$\Delta n = \phi \bullet C \bullet G \tag{10.9}$$

The optical coefficient is assumed to be 5×10^{-9} for thermoplastic materials [14, 15], while the shear modulus is calculated with the correlation of viscosity and relaxation time (Eq. (10.10)).

$$G(T, \dot{\gamma}) = \frac{\eta(T, \dot{\gamma})}{\lambda(T, \dot{\gamma})} \tag{10.10}$$

As the last step of the calculation, birefringence is projected onto one layer perpendicular to the flow direction (and perpendicular to the cross section of the calculated part).

10.4.3 Effective Mechanical Properties of Semicrystalline Thermoplastics

The spherulite microstructure of an injection-molded PP part is complex and heterogeneous. Its effective elastic properties can be predicted by the asymptotic

homogenization method, outlined in Section 5.2. As it is not possible to produce test specimens of both involved phases of a semicrystalline thermoplastic, the amorphous and crystalline ones, the derivation of their effective properties is delicate. The amorphous phase is assumed to be in a rubbery state [16] and its properties are deduced from this assumption, whereas the mechanical properties of the monoclinic crystalline phase can be determined either by theoretical molecular dynamic simulations [17] or by X-ray diffraction measurements [18].

In this chapter, we present two different homogenization approaches and compare their accuracy. First, *a simple direct homogenization scheme* is introduced by assuming that each spherulite is homogeneous and isotropic. Uniaxial tensile tests have been performed on PP specimens with different crystallization degrees (Section 10.6) in order to deduce the dependency of the Young's modulus on the spherulite diameter of PP. A linear regression was applied to the results (Figure 10.5) and leads to following empirical relationship:

$$E(\Phi_S) = 21.611\ \text{MPa} \bullet \Phi_S + 1053\text{MPa with } 5\ \mu\text{m} \leq \Phi_S \leq 55\ \mu\text{m} \qquad (10.11)$$

where Φ_S is the spherulite diameter.

As it is difficult to accurately measure the dependence of the Poisson ratio with the spherulite diameter, a linear variation with the crystallization degree κ is assumed: $\nu(\kappa) = 0.42 \bullet \kappa + (1 - \kappa) \bullet 0.4993$, where 0.4993 and 0.42 are the values of the amorphous [16] and crystalline phases, respectively. As interface elements are generated between domains with different mechanical properties and in order to reduce the representative volume element (RVE) model, *classes of spherulites* have been specified. In order to be as accurate as possible, a class regroups all spherulites having their diameter in a small specified range: for example, $\left[\Phi_{S,\text{m}-0,6\ \mu\text{m}}, \Phi_{S,\text{m}+0,6\ \mu\text{m}}\right]$, where $\Phi_{S,\text{m}}$ is the mean spherulite diameter of the considered class.

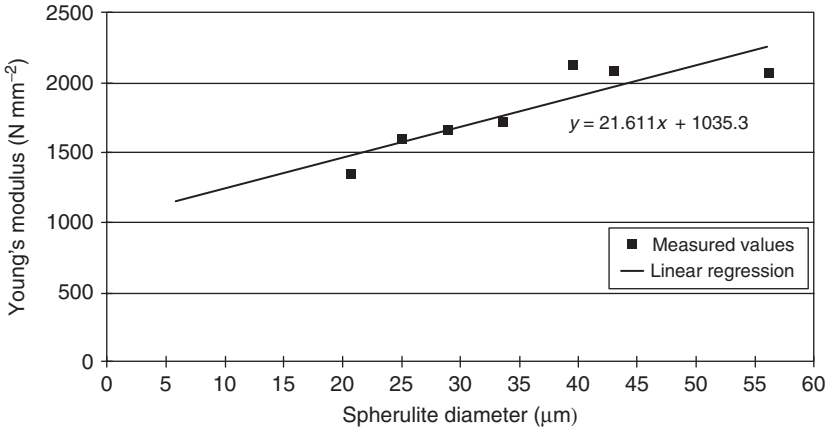

Figure 10.5 Experimentally measured Young's modulus as function of the spherulite diameter and the corresponding linear regression equation.

In order to overcome the assumption of isotropy of the spherulite and the linear variation of Poisson's ratio with spherulite diameter, a second, more sophisticated model is developed. The spherulite is no longer assumed to be isotropic, but a radial distribution of crystalline lamellae and of amorphous molecules growing from the monocrystalline nucleus is assumed there (Figure 5.13). This leads us to define a new two-level homogenization scheme:

- **Nanoscale**: homogenization of the bilamina formed by the crystalline lamella and the amorphous layer;
- **Microscale**: homogenization of the spherulite by assuming *a radial distribution of equivalent bilamina* around its monocrystal center.

This two-level homogenization scheme is detailed in Section 5.7. Three bilamina designs have been introduced there. Note that the resulting Hooke matrix is anisotropic with strain extension coupling terms. At the microscale, a 3D spherulite model with a radial distribution of bilamina is developed. Normal to this radial direction, the bilamina are assumed to be distributed randomly. The same notion of spherulite classes as for direct homogenization scheme has been introduced in order to reduce the size of the RVE model. Indeed, interface elements with double nodes are now only generated between two different spherulite classes and not between two individual spherulites. Moreover, the number of different bilamina designs, function of the crystallinity degree of the spherulites and subsequently of their spherulite diameter, is further reduced by the definition of *groups of spherulite classes* having their crystallinity degree in a defined range: for example, $[\kappa_{G,\mathrm{m}-0{,}6\%}, \kappa_{G,\mathrm{m}+0{,}6\%}]$, where $\kappa_{G,\mathrm{m}}$ is the mean degree of crystallization of the considered group of spherulite classes.

10.4.4
Macroscopic Mechanical Materials Behavior

The challenge on the macroscale is to develop an appropriate materials model for semicrystalline thermoplastics, which takes their inner properties, in an averaged manner, into account. The inner properties dominating the materials properties are the morphological structure, degree of crystallinity, spherulite diameter, and molecular orientation. Furthermore, unlike for metals and ceramics, the service temperature of thermoplastics is very close to their melting temperature. Owing to this fact, thermoplastics show a mixture of solid and liquid, or, more precisely, of elastic and viscous materials behavior. This mechanical behavior is also referred to as *viscoelasticity* and means that the mechanical materials behavior is highly dependent on the duration of the loading period and on the surrounding temperature. Thus, the stress–strain behavior of thermoplastics is highly nonlinear, even at small deformations.

Extensive research has been conducted in the past concerning the correlations between inner polymer structure and mechanical materials behavior [19–22]. *Inter alia*, it was shown that the degree of crystallinity and the spherulite diameter can have a significant influence on the mechanical properties of thermoplastic

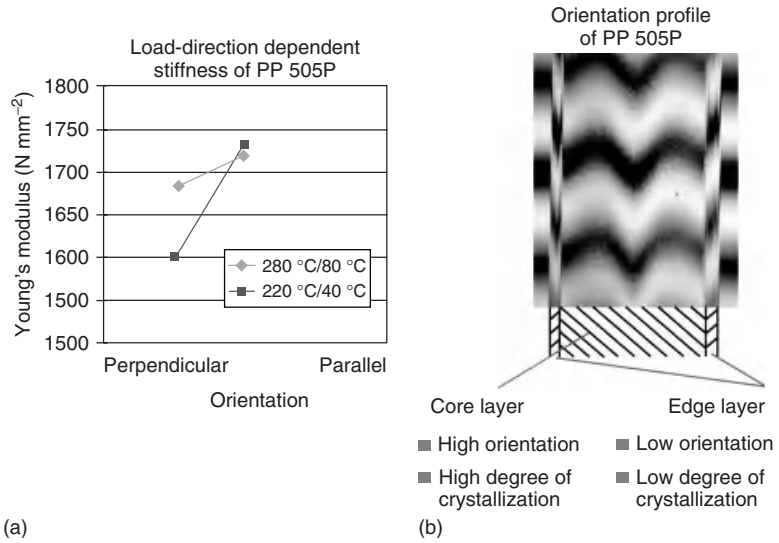

Figure 10.6 Molecular orientation-based anisotropy of PP.

parts. An increasing degree of crystallinity leads to an increase in tensile stiffness, whereas the decrease in the spherulite diameter leads to a better fracture behavior. Besides the state of crystallization, molecular orientations also have an influence on materials behavior. According to a molecule-theoretical approach, the Young's modulus in the molecular main chain direction is dependent on the molecule conformation and the chemical bonding forces between the atoms [23]. Thus, molecular orientations induce anisotropy into the mechanical behavior, as shown in Figure 10.6, where the comparison of the Young's modulus is shown for tensile specimens milled out of PP plates in different orientation directions. It can clearly be seen that the processing temperatures have a significant influence on the mechanical materials behavior. The orientation profile can be made visible by use of polarization microscopy. The measured birefringence is proportional to the orientation profile and therefore allows a qualitative determination of the state of orientation. Figure 10.6b shows such a birefringence profile of a specimen cross section. Further studies concerning the relation between state of molecular orientation and mechanical properties have been performed by Michaeli *et al.* [24].

10.4.4.1 Multilinear Elastic Model for the Crystallization Influence

The development of a macroscopic material model for the crystallization influence needs to take two essential effects into account. For one, local effective materials properties must be assigned to each element separately, according to the spherulite diameter predicted in the microstructure simulation. Next, a nonlinear macroscopic model for these materials is required; even the homogenization scheme provides currently only elastic properties. Indeed, such nonreinforced thermoplastics present

significant nonlinear behavior even at small strains. Owing to this constraint, a novel local multilinear elastic materials model has been developed.

In general, Hooke's law can be specified for linear elastic materials behavior as follows [25]:

$$\begin{pmatrix} \sigma_{11} \\ \sigma_{22} \\ \sigma_{33} \\ \sigma_{12} \\ \sigma_{13} \\ \sigma_{23} \end{pmatrix} = \begin{pmatrix} K+\frac{4}{3}G & K-\frac{2}{3}G & K-\frac{2}{3}G & 0 & 0 & 0 \\ K-\frac{2}{3}G & K+\frac{4}{3}G & K-\frac{2}{3}G & 0 & 0 & 0 \\ K-\frac{2}{3}G & K-\frac{2}{3}G & K+\frac{4}{3}G & 0 & 0 & 0 \\ 0 & 0 & 0 & 2G & 0 & 0 \\ 0 & 0 & 0 & 0 & 2G & 0 \\ 0 & 0 & 0 & 0 & 0 & 2G \end{pmatrix} \begin{pmatrix} \varepsilon_{11} \\ \varepsilon_{22} \\ \varepsilon_{33} \\ \gamma_{12} \\ \gamma_{13} \\ \gamma_{23} \end{pmatrix} \tag{10.12}$$

In order to describe the nonlinearity of the mechanical materials behavior even at small deformations, a piece-wise linear elastic formulation is adopted here. Therefore, the tangential stiffness is defined dependending on the occurring strain. This strain-dependent formulation of the tangential modulus is not continuous, but *discrete*, defined for n strain levels. Within each strain level, the tangential modulus remains constant. The desired number of strain levels can be specified by the user. The local tangential modulus is formulated depending on an equivalent strain according to [26]:

$$E = f\left(\varepsilon_V^{\text{Mises}}\right) \tag{10.13}$$

with

$$\varepsilon_V^{\text{Mises}} = \frac{1}{1+\nu}\sqrt{\frac{1}{2}\left[(\varepsilon_{11}-\varepsilon_{22})^2+(\varepsilon_{22}-\varepsilon_{33})^2+(\varepsilon_{33}-\varepsilon_{11})^2\right]+3\left[\varepsilon_{12}^2+\varepsilon_{13}^2+\varepsilon_{23}^2\right]} \tag{10.14}$$

This leads to the stress/strain relationship defined by the strain-dependent stiffness matrix $\left[E\left(\varepsilon_V^{\text{Mises}}\right)\right]$:

$$\begin{pmatrix} \sigma_{11} \\ \sigma_{22} \\ \sigma_{33} \\ \sigma_{12} \\ \sigma_{13} \\ \sigma_{23} \end{pmatrix} = E\left(\varepsilon_V^{\text{Mises}}\right) \begin{pmatrix} \frac{(1-\nu)}{(1+\nu)(1-2\nu)} & \frac{\nu}{(1+\nu)(1-2\nu)} & \frac{\nu}{(1+\nu)(1-2\nu)} & 0 & 0 & 0 \\ \frac{\nu}{(1+\nu)(1-2\nu)} & \frac{(1-\nu)}{(1+\nu)(1-2\nu)} & \frac{\nu}{(1+\nu)(1-2\nu)} & 0 & 0 & 0 \\ \frac{\nu}{(1+\nu)(1-2\nu)} & \frac{\nu}{(1+\nu)(1-2\nu)} & \frac{(1-\nu)}{(1+\nu)(1-2\nu)} & 0 & 0 & 0 \\ 0 & 0 & 0 & \frac{0.5}{(1+\nu)} & 0 & 0 \\ 0 & 0 & 0 & 0 & \frac{0.5}{(1+\nu)} & 0 \\ 0 & 0 & 0 & 0 & 0 & \frac{0.5}{(1+\nu)} \end{pmatrix} \begin{pmatrix} \varepsilon_{11} \\ \varepsilon_{22} \\ \varepsilon_{33} \\ \gamma_{12} \\ \gamma_{13} \\ \gamma_{23} \end{pmatrix} \tag{10.15}$$

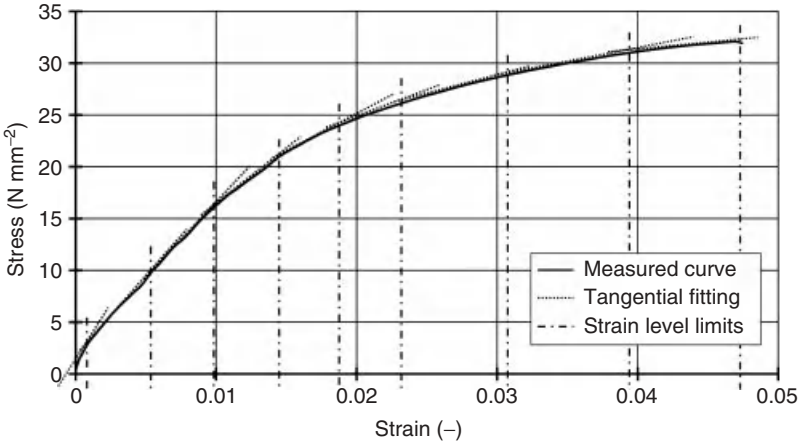

Figure 10.7 Approximation of measured stress–strain curve for the calibration of the multilinear elastic materials model (PP 505P).

The influence of the local microstructure is taken into account by defining the tangential modulus for each element separately depending on its morphology. Thus, for a number of n elements in an finite element (FE) model and m strain levels up to (n × m), tangential moduli are defined. The homogenization described in Section 10.4.3 provides the Young's modulus (=initial tangential modulus) for each microstructure. The decrease in the tangential modulus with increasing deformation can be calibrated by approximation of measured tensile stress–strain curves. The procedure is shown in Figure 10.7.

On the basis of an experimentally determined stress/strain curve, n strain levels are defined. Subsequently, a linear regression of the measured stress/strain behavior is conducted for each strain level. Thus, the decrease in the tangential modulus can be expressed as a percentage of the initial tangential modulus.

10.4.4.2 Linear Elastic Model for Molecular Orientation Influence

To include the local molecular orientations into structural analysis, a second user-defined materials model has been developed. Assuming three planes of symmetry within the material, an orthotropic formulation was chosen. This implies that, referring to the principle axes, normal stresses can only lead to normal strains, while shear stresses can only lead to shear strains. The calculation of the stress/strain behavior is based on nine independent materials values [25]. These values are the tensile moduli E_1, E_2, and E_3; the shear moduli G_{12}, G_{13}, and G_{23}; and the Poisson's ratios ν_{12}, ν_{13}, and ν_{23}, respectively. Generally, ν_{ij} and ν_{ji} are not equal. Yet, the two elastic constants are coupled by Eq. (10.16):

$$\frac{\nu_{ij}}{E_i} = \frac{\nu_{ji}}{E_j} \tag{10.16}$$

Furthermore, a local coordinate system that describes the position of the orthotropic axes in the three-dimensional state is defined. By utilization of this orthotropic

materials model, the strains within a material can be calculated according to Eq. (10.17):

$$\begin{pmatrix} \varepsilon_{11} \\ \varepsilon_{22} \\ \varepsilon_{33} \\ \gamma_{12} \\ \gamma_{13} \\ \gamma_{23} \end{pmatrix} = \begin{pmatrix} \frac{1}{E_1} & \frac{-\nu_{21}}{E_2} & \frac{-\nu_{31}}{E_3} & 0 & 0 & 0 \\ \frac{-\nu_{12}}{E_1} & \frac{1}{E_2} & \frac{-\nu_{32}}{E_3} & 0 & 0 & 0 \\ \frac{-\nu_{13}}{E_1} & \frac{-\nu_{23}}{E_2} & \frac{1}{E_3} & 0 & 0 & 0 \\ 0 & 0 & 0 & \frac{1}{G_{12}} & 0 & 0 \\ 0 & 0 & 0 & 0 & \frac{1}{G_{13}} & 0 \\ 0 & 0 & 0 & 0 & 0 & \frac{1}{G_{23}} \end{pmatrix} \begin{pmatrix} \sigma_{11} \\ \sigma_{22} \\ \sigma_{33} \\ \sigma_{12} \\ \sigma_{13} \\ \sigma_{23} \end{pmatrix} \tag{10.17}$$

The nine materials parameters can be determined either by a combination of calibration data from mechanical tests and the prediction of the state of orientation at the microscopic level or by applying the homogenization scheme. At the moment, the information about direction and degree of orientation is used and inserted into the materials model by using the orientation tensor proposed in the above-mentioned papers by Pantani *et al.* [27, 28]. This orientation tensor combines the information about the mean direction of the molecules with that about the stretch of the molecules. The orientation is indicated by using the mean direction of end-to-end vectors of the molecular chains. It is combined with the stretch of the molecules in the second-order conformation tensor and its state of rest as shown in Eq. (10.18):

$$\underline{\underline{A}} + \underline{\underline{I}} = \frac{\langle \underline{\underline{RR}} \rangle}{\langle R_0^2 \rangle} \tag{10.18}$$

On the basis of Eq. (10.8), Eq. (10.18) describes the normalized conformation tensor with respect to its rest state. $\underline{\underline{A}} + \underline{\underline{I}}$ now defines the orientation tensor. The orientation tensor can then be examined. The orientation of the materials coordinate system can easily be derived from the eigenvectors. In addition, the eigenvalues lead to the local amount of stretch in the material.

$$\underline{\underline{A}} + \underline{\underline{I}} = \begin{pmatrix} \lambda_1 & 0 & 0 \\ 0 & \lambda_2 & 0 \\ 0 & 0 & \lambda_3 \end{pmatrix} \tag{10.19}$$

Thus, the orientation tensor allows a full description of the state of molecular orientation. The mechanical values depending on this state of orientation are measured in calibration tests. By the measurement of mechanical values for totally nonoriented materials and materials with three increasing degrees of stretch, a set of data that allows a full calibration of the simulation is determined. So, the orientation tensor in Eq. (10.19) is linked to the orthotropic stiffness in Eq. (10.17).

10.5 Implementation of the Virtual Process Chain

10.5.1 SigmaSoft

As the first step in the integrative simulation chain, the injection molding process of a 2 mm PP plate is simulated on the macroscale. For this simulation, the heat and fluid flow simulation program SigmaSoft is used. This software enables the modeling of injection-molded parts and molds including cooling system or hot runner and so on. A database includes different polymer and mold materials and can be extended easily by the user. For polymer materials, rheological, thermal, and mechanical materials data can be used for calculations. The software calculates flow velocities, shear flow velocities, temperature distributions, pressures, and so on on the macroscale and is also able to predict shrinkage and warpage. The results of the simulation are visualized via an internal postprocessor. To transfer data to structural analysis software, a special tool is also included in SigmaSoft. As the Visualization Toolkit (VTK) format is not supported by this tool, the simulation results are transferred into this universal data format via an in-house developed tool Sigma2VTK using the included API (application programming interface) of SigmaSoft.

10.5.2 SphaeroSim

The next step toward an integrative multiscale simulation of thermoplastic materials is the calculation of the microstructure and molecular orientations that develop during the injection molding process under nonisothermal conditions. The output data from SigmaSoft in the VTK format serve as input for this microscale simulation. The calculation of the microstructure is operated via a control file. This file includes all information that is necessary for the calculation such as the input data directory, the nucleation and growth models, and the amount of calculation results to be written. These results can be saved in the VTK format for further transfer to the homogenization tool (morphology) or directly to the macromodel (molecular orientation).

10.5.3 HOMAT

The steady-state 3D spherulite microstructures, predicted by SphaeroSim, are transferred to HOMAT via the preprocessor tool Mesh2Homat. This program automatically detects the interfaces between adjacent spherulite classes and generates new nodes and interface elements and the periodic boundary conditions. It also rewrites the present solutions onto the new unstructured mesh, stores the geometrical information in a *.hgeo file, of Abaqus FEA input type and writes a template

of the HOMAT command file. As outlined in more detail in Section 7.1.2, HOMAT evaluates, for example, the effective mechanical properties of the spherulite microstructure. These effective materials properties are written in a *.mat file that can be directly used by the developed macroscopic materials models in Abaqus FEA.

10.5.4 Abaqus FEA

The last link in the simulation chain is the structural analysis of a semicrystalline thermoplastic part on the macroscale. The commercial FE-solver Abaqus FEA [29] is used for this purpose. Abaqus FEA has an implicit and an explicit solver and offers the possibility of implementing user-defined materials models programmed in Fortran. The native input data format for Abaqus FEA is INP, while the output data are provided in ODB format. For the realization of the simulation chain described above, the materials models described in Section 10.4.4 are implemented as UMATs for Abaqus FEA.

10.5.5 Simulation Chain

The developments described in this chapter aim at enabling a more precise prediction of the mechanical behavior of semicrystalline thermoplastics by taking into account the local inner properties. As shown, microstructure features such as spherulite diameter and degree of crystallization have a significant influence on the mechanical materials properties as well as molecular orientations. Yet, the interaction between these influencing factors is very complex and can currently not be described sufficiently. Therefore, in the first step, the microcoupling–macrocoupling of the consideration of crystallization effects on the one hand and molecular orientations on the other hand are examined separately. Thus, two simulation chains have been implemented: one chain for the integrative modeling of crystallization effects and the second for the modeling of molecular orientation effects in the mechanical materials behavior of semicrystalline thermoplastics.

10.5.5.1 Integrative Modeling of Crystallization Effects

The implemented simulation chain for the integrative modeling of crystallization effects in the mechanical materials behavior of semicrystalline thermoplastics is shown in Figure 10.8.

The process simulation is modeled in SigmaSoft where the results in the form of temperature and the used mesh (Mesh_A) are transferred into VTK format using the Sigma2VTK tool. This information is used by SphaeroSim for the microstructure calculation on the microscale level. Microstructure evolution is evaluated for each macroscopic SigmaSoft element (Element_A.N), and the results are also written in VTK format. Then, these microstructures are transferred

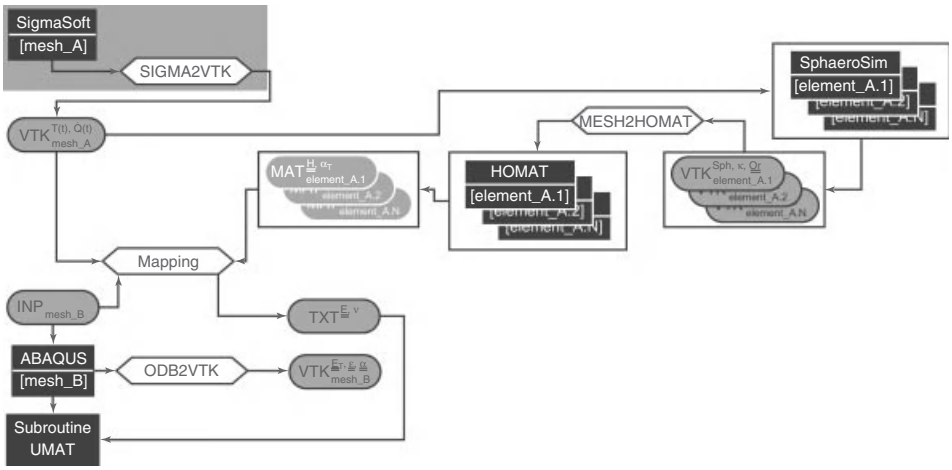

Figure 10.8 Implemented simulation chain for the modeling of crystallization effects.

via Mesh2Homat to HOMAT in order to evaluate their effective mechanical properties.

The element types used in the microstructure simulation and structural analysis differ as well as the discretization levels of the simulation models. The results from HOMAT, which are calculated for each element of the fine microstructure mesh, are therefore transferred to the FE mesh for the structural analysis by means of a mapping algorithm. The input data needed for this mapping algorithm are the microstructure mesh in VTK format (source Mesh_A), the structural analysis mesh in INP format (target Mesh_B), and the results of HOMAT in MAT format. The output data of the mapping step are given in a user-defined text format and used directly by the UMAT of the multilinear materials model. This text format contains an initial Young's modulus and Poisson's ratio for each element. The results of the analysis are given in the binary output format ODB. In order to view these results by ParaView, a conversion of the results into VTK format is carried out with the convertor tool ODB2VTK. The results stored in the ODB file are extracted and written to the new VTK file using a Python script.

10.5.5.2 Integrative Modeling of the Molecular Orientation Effects

The second implemented simulation chain for the integrative modeling of molecular orientation effects in the mechanical materials behavior of semicrystalline or amorphous thermoplastics is shown in Figure 10.9.

For the calculation of molecular orientations, more information is required than for the microstructure simulation. Therefore, the velocity and shear rates are also exported to the VTK format as results of the macroscopic SigmaSoft calculation. SphaeroSim uses these data to calculate currently a time-discrete orientation tensor for every element directly on the macroscopic level and writes the results in VTK format.

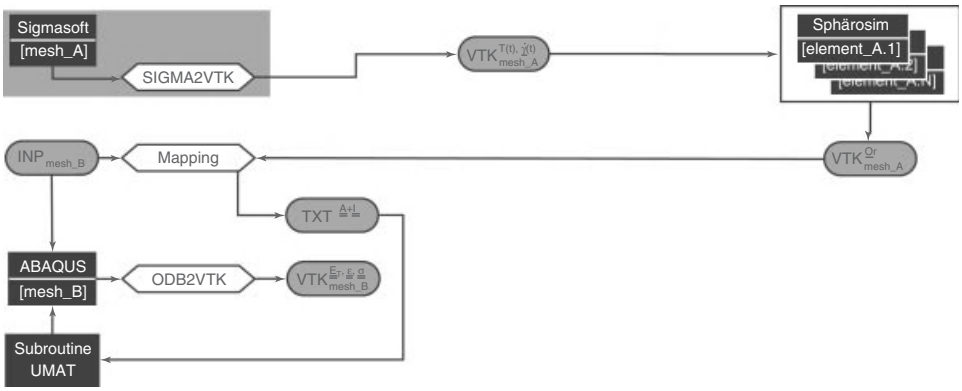

Figure 10.9 Implemented simulation chain for the modeling of molecular orientation effects.

Yet again, the element types used in the microstructure simulation and structural analysis differ as well as the discretization levels of the simulation models. The calculated birefringence values are therefore again transferred to the FE mesh for the structural analysis by means of a mapping algorithm. The input data needed for this mapping algorithm are the microstructure mesh in VTK format (source mesh), this time containing not only the geometry information but also the results of the birefringence calculation, and the structural analysis mesh in INP format (target mesh). The output data of the mapping step are again written in a user-defined text format, which contains the orientation tensor $\underline{\underline{A}} + \underline{\underline{I}}$ for each element. This information is then read by the linear orthotropic model (second UMAT subroutine). Finally, the structural analysis is performed using Abaqus FEA and either the multilinear model for crystallization effects or the orthotropic linear model in order to take molecular orientation effects into account is applied.

10.6 Experimental Methods

As described in Sections 10.4.1 and 10.4.2, the developing microstructure within an injection-molded part is strongly dependent on the processing conditions during injection molding. In order to determine the Young's modulus of the PP depending on the spherulite diameter, PP plates with a thickness of 4 mm were manufactured by injection molding. The processing parameters were varied according to Table 10.4 in order to obtain specimens with different microstructures.

For the uniaxial tensile testing program, specimens with geometries according to DIN 53504, type S3 [30] and DIN EN ISO 527-2, type 1BA [31] were

Table 10.4 Process parameters used for the manufacturing of specimens.

	A	*B*	*C*	*D*	*E*	*F*	*G*
T_{melt} (°C)	190	240	240	240	270	280	280
T_{mold} (°C)	45	40	50	60	80	80	90
$\dot{V}_{injection}$ ($cm^3\ s^{-1}$)	84	80	25	40	10	10	20

milled out of the plates. In addition, tensile bars according to DIN EN ISO 527-2 type 1B were directly injection molded. For all specimens, the thickness of the boundary layers and the morphological structure were determined via transmitted light microscopy (TLM) and subsequently milled off the specimen, leaving the core layer of a mostly homogeneous spherulitic structure for the determination of their Young's modulus. According to DIN EN ISO 527-1, tensile tests were performed at a quasi-static deformation rate of approximately 1%-strain min^{-1}. With this technique, the average spherulite diameter of the central part of the specimen's microstructure is directly correlated to the measured materials stiffness. Exemplarily, an image of the edge layer-to-core layer ratio and the determination of the average spherulite diameter are shown in Figure 10.10. The determined average spherulite diameters and the corresponding measured values of Young's modulus are given in Table 10.5. It can be concluded that the materials stiffness increases with rising average spherulite diameters of semicrystalline polymers.

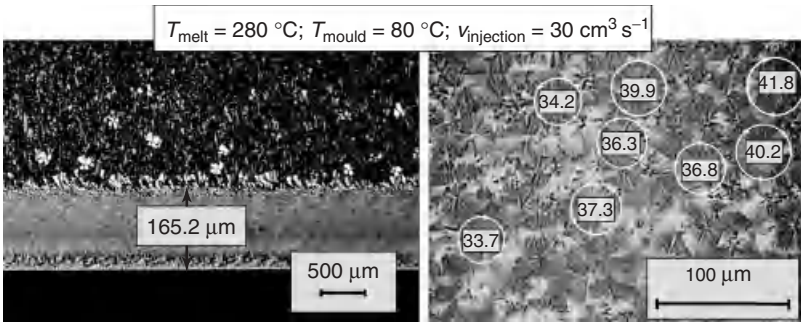

Figure 10.10 Spherulite diameter and thickness of edge layers and core layer in injection-molded PP plates.

Table 10.5 Measured spherulite diameter and corresponding Youngs's modulus.

	A	B	C	D	E	F	G
Spherulite diameter (µm)	39.6	25.05	20.70	43.10	29.01	33.62	56.20
Young's modulus (N mm^{-2})	2120	1595	1349	2084	1656	1717	2068

10.7 Results

The results of the single simulation tools on the microscale, macroscale, and transmission scale are discussed separately in this chapter and in [2]. The course of action for the targeted integrative simulation chain and the acquired results are discussed for the modeling of crystallization effects by the example of a tensile bar according to DIN EN ISO 527-2, type 1BA, which is milled out of an injection-molded, plate-shaped demonstration part processed at two different parameter sets (''warm'' and ''cold''). Hence, the simulation chain begins with the macroscopic simulation of the plate filling, followed by the calculation of the developing microstructure for a representative cross section. Subsequently, these representative cross-section elements are homogenized for both parameter sets. At last, tensile tests are simulated for both warm and cold processed parts, and a conclusion is drawn from the gained results.

10.7.1 Macroscopic Process Simulation

The discretization of the plastic part for the simulations with SphaeroSim is achieved using hexahedral volume elements. As the calculation of the morphology takes place on the microscale level and that of the molecular orientation is restricted at the moment to the macroscale level, different meshes are used for both simulations to gain a high resolution for each calculation. For the microstructure simulation, five elements over the wall thickness are specified. The injection molding simulation is performed for two combinations of process parameters, as shown in Table 10.6.

The calculated filling and cooling of the plate-type molding is illustrated in Figure 10.11.

For the molecular orientation calculation, a finer mesh with 20 elements over the cross section is adopted in order to have a more precise variation over the wall thickness. As the discretization of the whole part with such a fine mesh is not possible for reasons of time and computer storage, only a small region in the center of the molding is used for this refined calculation.

Table 10.6 Process parameters used for the injection molding simulation.

Parameter	T_{melt} (°C)	T_{mold} (°C)	$\dot{V}_{injection}$ $(cm^3\ s)^{-1}$
Warm	280	80	30
Cold	240	40	80

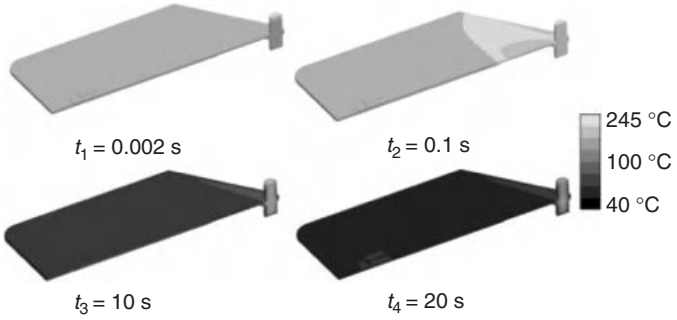

Figure 10.11 Calculated part filling and cooling on macroscale level.

10.7.2 Microstructure Simulation

10.7.2.1 Crystallization

For this calculation, five elements in the center of the molding defining its cross section are selected. These elements have been discretized by a fine mesh of 10^6 cells, and their microstructure evolution is predicted with SphaeroSim (Figure 10.12). For this simulation, the validated nucleation model of Housmans [11] and the spherulite growth model of Hoffman *et al.* [8] are used.

A growth sequence of the microstructure for one element near the part's surface is shown in Figure 10.13.

Owing to the cooling of the melt and the relation to its neighbor cells, spherulites develop subsequentlyout of these nuclei near the mold surface. The growth of a spherulite continues until two or more spherulites collide or the borders of an element are reached. It can be seen clearly that the cellular automat that is used for the probability calculation of the crystallization process leads to the typical spherulitic structures as they appear in reality.

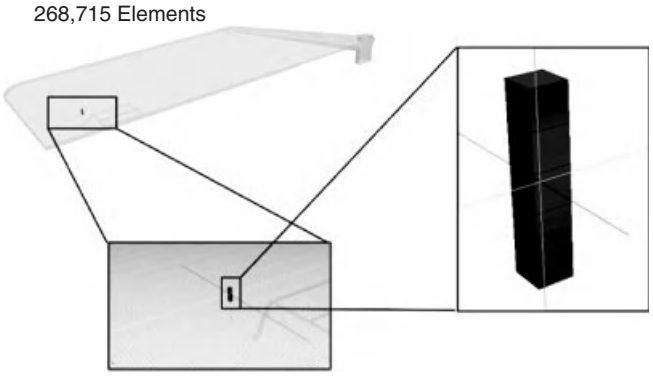

Figure 10.12 Mesh of 2 mm PP molding with the chosen five elements over the thickness.

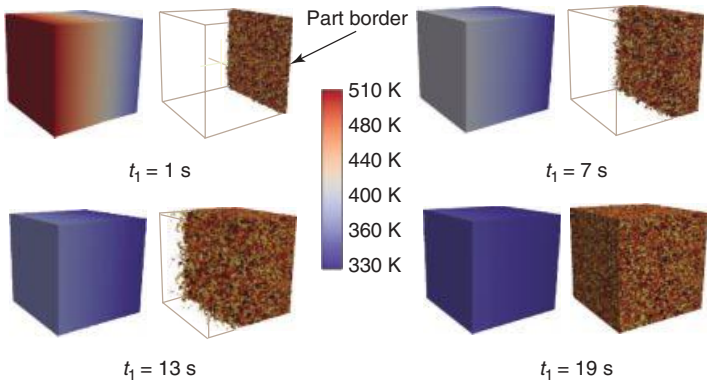

Figure 10.13 Predicted microstructure evolution in an element at the part surface.

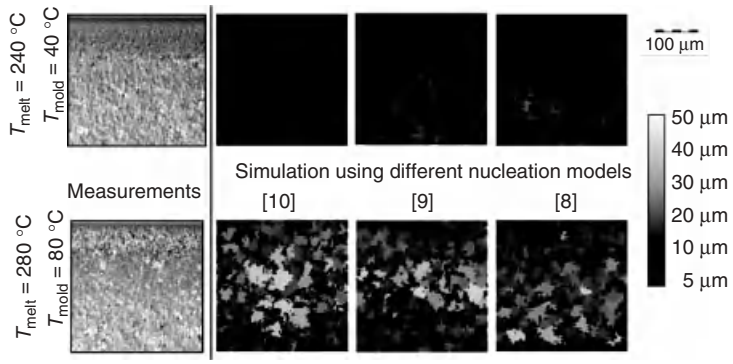

Figure 10.14 Calculated results using different nucleation models compared with measurements.

The comparison of those three nucleation models with measured microstructure of one element depending on process parameters is shown in Figure 10.14.

All models show qualitatively good results, with a typical fine microstructure at the edge of the part and coarse morphology to the center of the part. The results reveal the best prediction for the nucleation model according to Hoffman *et al.* [8]. For all five elements, the microstructure evolution is shown in Figure 10.15.

The low temperatures lead to a layer with fine microstructure at the part's surface and to an almost homogeneous microstructure in the part's core.

The results of the whole part, using a low discretization in every element of 8000 cells, are shown in Figure 10.16. The coarsest microstructures are predicted in the thicker gate.

10.7.2.2 **Molecular Orientation**

For predicting the molecular orientation, the same plate geometry with a thickness of 2 mm, as for the morphology prediction, is used. Figure 10.17 shows the results of the injection molding simulation over the plate's cross section. In the figure, the

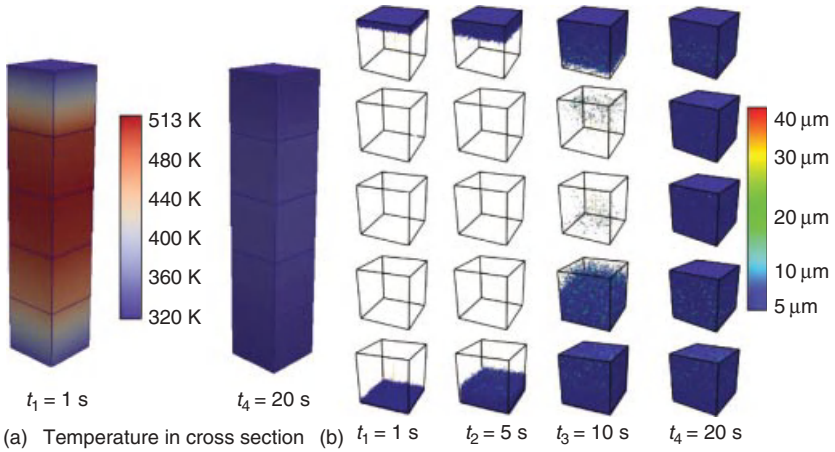

Figure 10.15 Microstructure evolution in five elements over the cross section: temperature profile (a) and spherulite diameter (b).

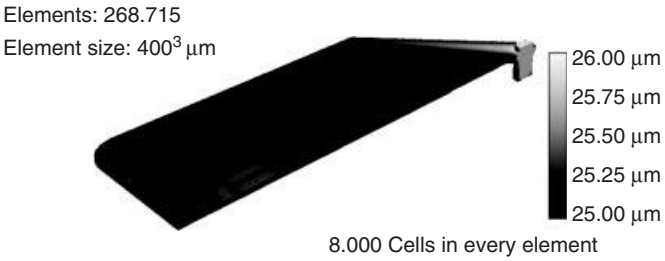

Figure 10.16 Calculated results of the average spherulite diameter for the part.

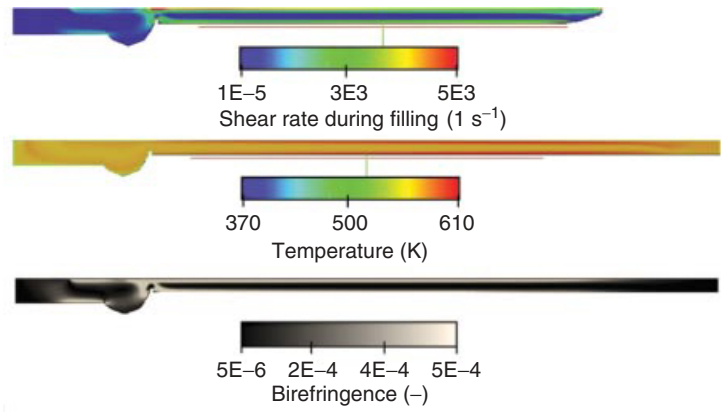

Figure 10.17 Calculated shear rate, temperature, and birefringence in cross section.

local values for the shear rate (during filling) and temperature (shortly after filling) are visualized during the filling process.

Figure 10.17 also shows the derived distribution of birefringence after the completion of the filling and cooling process. One can see the high birefringence in the outer layers and the very small values in the center area of the molding. Also, the decrease in the birefringence along the flow path is clearly noticeable. Figure 10.18 reveals the influence of the flow path for half a cross section.

A comparison to the visualized birefringence (dark deflection in samples) by means of optical polarization microscopy in Figure 10.19 shows a qualitative agreement between simulation results and the experiment. The high birefringence in the edge layers of the sample is calculated as well as the decrease in birefringence down to a minimum value in the middle of the cross section.

Overall, the simulation correctly predicts the characteristics of the distribution of birefringence in the direction of thickness as well as along the flow path.

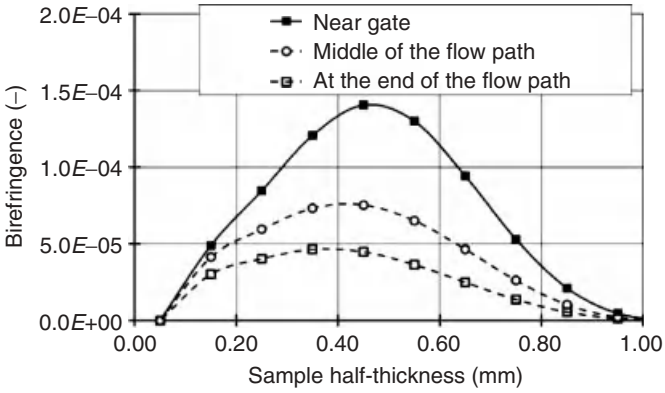

Figure 10.18 Calculated birefringence profile in cross section depending on flow path.

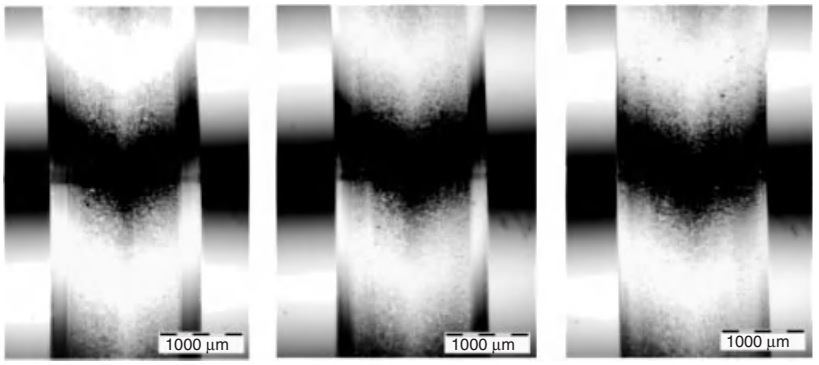

Figure 10.19 Measured orientation allocation depending on flow path.

10.7.3 Effective Mechanical Properties

The determination of the effective mechanical properties is only conducted for the results of the microstructure simulation concerning the prediction of crystallization effects. Results are presented for both homogenization schemes, described in Section 10.4.3.

10.7.3.1 Direct Homogenization Results

For the cold and warm process parameters, 15 and 40 classes of spherulite diameters, respectively, have been specified. This corresponds to a range of 1.2 µm per class. In Table 10.7, the effective Young's moduli in the three structural directions are outlined for the warm process conditions and for two RVEs located at the edge and in the center of the molding. The mean and volume averaging values are also given in the table.

Independent of the RVE localization, the rather simple homogenization scheme predicts an *isotropic* equivalent behavior of the polyspherulite microstructure. It neglects completely the experimentally observed anisotropy with higher Young's moduli in the flow direction than transverse to it (Figure 10.6). A relative difference $\Delta E_{1,\mathrm{m}} < 0.05\%$ is noted for both RVEs. Moreover, this first-order homogenization scheme improves only a little the volume averaging Young's modulus according to Eq. (5.14). Indeed, only small Hooke matrix discontinuities exist between the spherulite classes at their interfaces, thus leading only to small implicit forces and subsequently to small microscopic displacements on the RVE (Figure 10.20). This result differs from the large corrections noted in unidirectional composites or effusion cooled materials [32, 33].

In Figure 10.21, the effective mechanical properties of the five selected elements over the part's thickness are given for both couples of process parameters.

The effective Young's and shear moduli of the cold processed parts are quasi constant: maximum relative variation of 0.1% at position 0.6 mm ($E_{\mathrm{m}} = 1191.84$ MPa) and the Poisson coefficient is constant there: $\nu = 0.4667$. The warm processed plate has not only a significant larger stiffness than the cold one but also presents larger variations of the effective elastic properties over the thickness. Indeed, compared to the cold processed plate, the Young's and shear moduli of the warm one increase by 15%, and at its boundary, the Young's and shear moduli

Table 10.7 Effective orthotropic Young's modulus for the warm process parameters, the mean and the volume averaging value, and the relative difference between the last two values.

Position (mm)	E_1	E_2	E_3	E_{m}	E_{va}	$\Delta E_{1,\mathrm{m}}$	$\Delta E_{\mathrm{m,va}}$
0.2	1391.0	1390.2	1391.3	1390.8	1393.2	−0.043	0.173
1	1362.6	1361.9	1362.95	1362.5	1364.4	−0.045	0.139

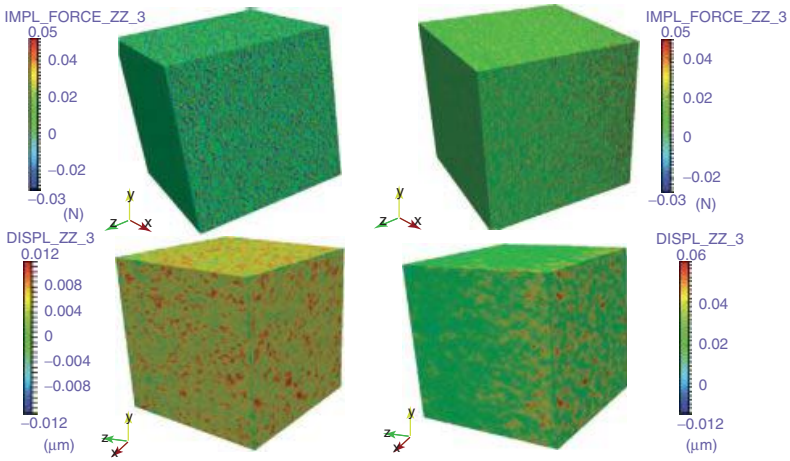

Figure 10.20 Implicit force component in the thickness direction z generated under warm process conditions (80/280 °C) by the macrostrain E^0_{xx} (above) and the corresponding microscopic displacement component (below) on the border RVE for direct homogenization (left) and the two-level homogenization scheme (right) respectively.

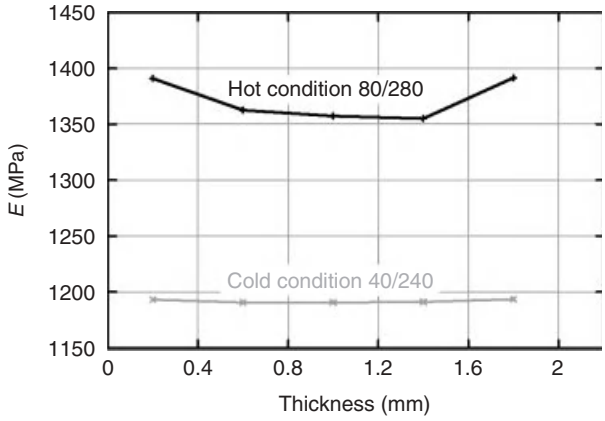

Figure 10.21 Influence of the process parameters on the Young's modulus variation over the thickness of a 2 mm PP molding.

are larger by 2.7 and 2.6%, respectively, than in its center. This behavior can be explained by analyzing the spherulite microstructures. In fact, both extremal RVEs present after small spherulites at their boundary several larger spherulites, generated by a local temperature variation suitable for spherulite growth and not nucleation. These effective mechanical properties are then transferred to the FE-program Abaqus FEA for the stress/strain analysis on the macroscale.

10.7.3.2 Two-Level Homogenization Results

As a larger variation of the effective Young's moduli over the thickness can be expected under warm process conditions, the more complex two-level homogenization scheme has been performed only for these process conditions. To reduce the number of required bilamina designs, the 40 classes have been segmented in 7 groups. Each group corresponds to a range of degree of crystallinity of 1.2%.

Homogenization Results of the Bilamina at the Nanoscale For the mean Sawatari model and the classical bilamina design (details are outlined in Section 5.5), we obtain following effective Hooke matrix (in MPa) in the local axis system $\vec{e}_1, \vec{e}_2,$ and $\vec{e}_3$ (Figure 5.15):

$$H_{bila}^{eff} = \begin{bmatrix} 2796 & 1890 & 1807 & -0.25 & -2.86 & -135 \\ 1890 & 2158 & 1902 & -3.1 & -0.91 & 74.2 \\ 1807 & 1902 & \mathbf{10728} & 2.27 & -1.24 & -158.7 \\ -0.25 & -3.1 & 2.27 & 176.6 & -11.3 & -3.4 \\ -2.86 & -0.91 & -1.24 & -11.3 & 689.1 & -0.5 \\ -135 & 74.2 & -158.7 & -3.4 & -0.5 & 723.8 \end{bmatrix} \quad (10.20)$$

This homogenization result is meaningful: the effective Hooke matrix of the bilamina is *full anisotropic* with a high Young's modulus in the transverse chain direction. The in-plane shear modulus is low compared to the transverse ones and there exists also extension-shearing coupling terms.

Next, the homogenization results of the three introduced bilamina designs in Section 5.5.1.2 and the mean Sawatari model are reported in Table 10.8. The variation compared to the classical design without the surrounding amorphous phase is also given there. The stiffness H_{11} decreases because of the additional implicit forces generated in direction e_1. This result is analogous with Doyle's [34] decrease in the Young's modulus with the aspect ratio b/L. The H_{22} component increases slightly because of the reduction of the implicit forces in e_2 induced by their interruption in the RVE center. As no discontinuity acts in chain direction e_3, stiffness H_{33} is simply given by volume averaging. Note that design VAR2 induces

Table 10.8 Terms of the effective Hooke matrix (MPa) of the three bilamina designs and their relative variation in terms of the reference one.

Design		H_{11}	H_{22}	H_{33}	H_{12}	H_{23}
Bilamina		2796.4	2157.6	10 728.4	1890.0	723.8
VAR1	Value	2583.7	2148.2	10 707.6	1877.2	524.9
	variation	−6.92	−0.43	−0.19	−0.68	−27.48
VAR2	Value	2194.0	2063.6	9826.6	2301.0	809.5
	variation	−20.9	−4.36	−8.41	21.71	11.84

Note that the local axis system ($e_1, e_2,$ and e_3) is shown in Figure 5.15.

Table 10.9 Effective Young's modulus in the structural axis system, the corresponding mean value, and the relative difference of E_Z from the mean one.

Design	Materials model	E_X (MPa)	E_Y (MPa)	E_Z (MPa)	E_m (MPa)	$\Delta E_{Z,m}$ (%)
Bilamina	Sawatari mean	1938.7	1372.4	2837.3	2049.4	38.4
	Sawatari min	1755.1	1306.9	2526.7	1862.6	35.7
VAR1	Sawatari mean	1766.9	1177.6	2254.9	1733.1	30.1
	Sawatari minimum	1431.1	1018.6	1727.4	1392.4	24.1
VAR2	Sawatari mean	1742.5	773.7	2317.3	1611.2	43.8
	Sawatari minimum	1278.1	462.1	1788.1	1176.1	52.0
Direct homogenization		1391.0	1390.2	1391.3	1390.8	0.04

a strong increase of in-plane shear stiffness H_{12} and of the transverse one H_{23}, whereas design VAR1 reduces this last stiffness drastically.

Homogenization Results at the Microscale First, the effective elastic properties of the border element at $z = 0.2$ mm are analyzed in detail. In Table 10.9, the effective properties in the structural directions X, Y, and Z; the corresponding mean value; and the relative deviation of E_Z from the mean one are reported for the three bilamina designs at the nanoscale and for the two variants of the Sawatari and Matsuo [18] chain Young's modulus. Note that the X direction is parallel to flow, Y corresponds to the transverse direction, and Z to the thickness direction.

Independent of the design and materials model, *the two-level homogenization scheme predicts a pronounced orthotropic effective behavior with* $E_Y < E_X < E_Z$. *The direct homogenization scheme is, however, not able to predict this observed anisotropic equivalent behavior* (Figure 10.22). In order to explain this significant accuracy increase of the two-level homogenization scheme compared to the direct one, a detailed analysis on the RVE of the implicit forces and of the corresponding periodic displacements in the thickness direction Z is performed (Figure 10.20). First, note that no further assumption of equivalent isotropic behavior of a spherulite is made in the two-level homogenization scheme. In addition to implicit forces generated at the class boundaries, which are rather constant over the RVE thickness (Figure 10.20 left), only the two-level homogenization scheme generates implicit forces due *to the orientation variation of effective bilamina in each spherulite*. The total implicit forces are now larger for the bigger spherulites directly under the boundary layer than elsewhere. Thus, large positive displacements occur there on the RVE. Thus, the direct homogenization is not able to predict these displacement gradients over the RVE thickness and subsequently its anisotropy.

Independent of the adopted materials model, the standard bilamina model without surrounding amorphous molecules predicts a too stiff effective behavior. The classical bilamina and the VAR1 designs predict an orthotropy of E_Z of nearly 30%, whereas the minimum Sawatari model predicts slightly less orthotropy than

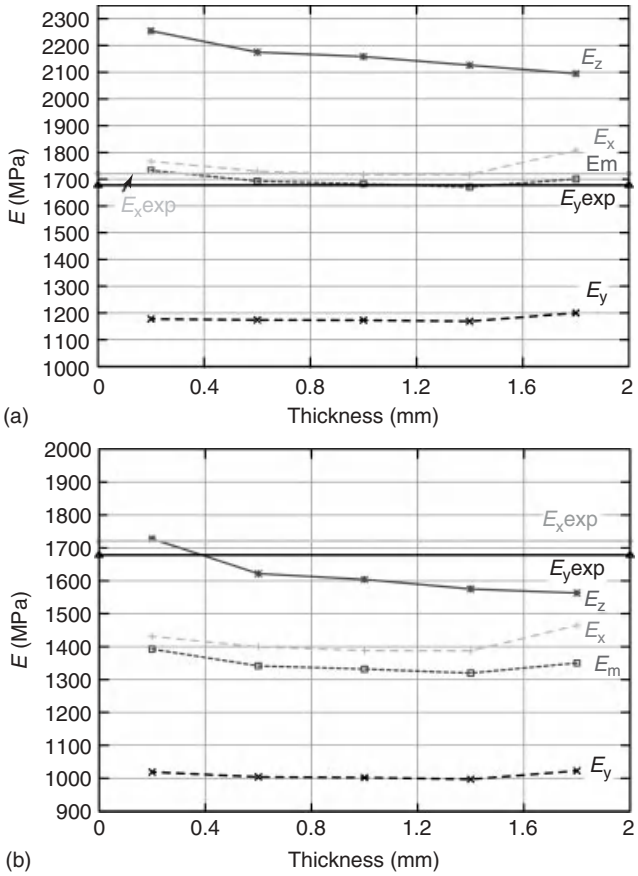

Figure 10.22 Variation of the effective orthotropic Young's moduli over the PP plate thickness and comparison of experimental values for bilamina design VAR1 and the mean Sawatari model (a) and for minimum Sawatari model (b).

the mean one. Note that design VAR2 provides unrealistic results with an extremely low transverse Young's modulus and a very large orthotropy.

In Table 10.10, the effective shear moduli, the corresponding mean value, the relative deviation of the in-plane shear modulus G_{XY} to the mean one, and the mean Poisson's ratio are reported. Independent of the adopted bilamina design and materials model, the two-level homogenization model also predicts orthotropic effective shear moduli of the border element with $G_{XY} < G_{XZ} \approx G_{YZ}$. Designs Bilam and VAR1 predict a rather similar reduction of the in-plane shear modulus G_{XY} compared to the mean one: ≈15.5%. But, design VAR2 provides more than 35%. Moreover, this model also predicts a high mean effective Poisson's ratio because of a too large influence of the incompressible amorphous phase surrounding the crystalline one. All these results indicate clearly that the design

Table 10.10 Effective shear modulus in the structural axis system, the corresponding mean value, the relative difference of G_{xy} to the mean one, and the effective poisson coefficient.

Design	Materials model	G_{XY} (MPa)	G_{XZ} (MPa)	G_{XZ} (MPa)	G_m (MPa)	$\Delta G_{XY,m}$ (%)	ν_m
Bilamina	Mean	561.1	696.2	732.9	663.4	−15.4	0.4404
	Minimum	524.5	663.1	707.9	631.9	−17.0	0.4410
VAR1	Mean	487.7	625.1	530.6	547.8	−11.0	0.4446
	Minimum	379.0	560.5	450.0	463.1	−18.2	0.4514
VAR2	Mean	459.3	776.2	797.9	677.8	−32.2	0.4738
	Minimum	374.6	730.7	740.0	615.1	−39.1	0.4897
Direct homogenization		478.5	478.7	478.9	478.7	−0.04	0.4536

These results are provided for both Sawatari materials models and the three bilamina designs.

VAR2 is not accurate enough *and the aspect ratio b/L* (Figure 5.15) *must be defined smaller than 0.1, whereas the bilamina design VAR1 provides the most promising effective properties*.

In Figure 10.22, the variation of the effective orthotropic Young's moduli E_X, E_Y, and E_Z and the corresponding mean one, E_m, over the PP plate thickness are drawn for the retained bilamina design VAR1 and both materials models. These numerical predictions are compared with experimental Young's moduli parallel, E_{Xexp} (1721 MPa) and transverse to the flow direction, E_{Yexp} (1678 MPa). Note that no experimental values are available in the thickness direction. For the mean Sawatari model, the predicted Young's modulus E_X in the flow direction and also the mean value are in excellent agreement with the experimental ones. Only the transverse modulus E_Y is significantly lower than its experimental one, leading to a more pronounced in-plane orthotropic behavior. Further investigations are required to reduce this to large in-plane orthotropy, but the predicted tendency is correct: $E_X > E_Y$. Note that the minimum Sawatari variant predicts lower effective Young's moduli, and its discrepancy to the experimental values increases substantially. Thus, *the minimum Sawatari variant is less accurate than the mean one*.

Otherwise, independent of the materials model, the Young's modulus E_Z decreases over the plate thickness, whereas the Young's moduli E_X, E_Y, and consequently E_m are lower in the plate center and higher at its edge because of the larger spherulites there.

10.7.4 Macroscopic Part Behavior

On the basis of the results of the direct homogenization, various structural analyses on the macroscale are performed by using the multilinear elastic materials model and calibration technique described earlier. For reasons of comparison, each parameter variation is additionally carried out with a linear elastic materials model

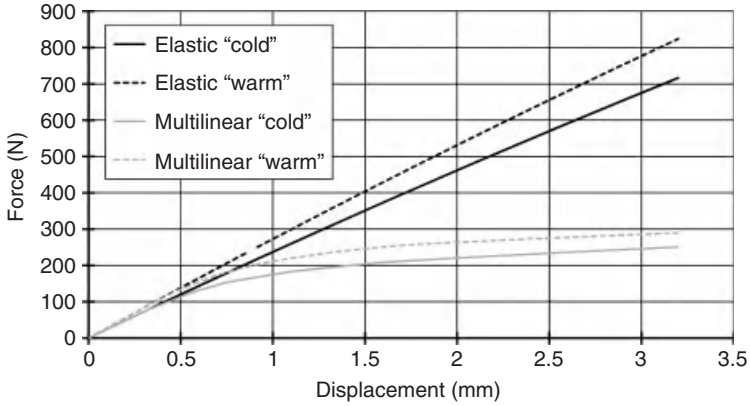

Figure 10.23 Comparison of simulated force–displacement curves using a linear elastic and a multilinear elastic materials model.

as well. As test specimen, a tensile bar of 2 mm thickness and corresponding to the DIN EN ISO 527-2, type 1BA norm is used. An overall uniaxial extension of 3.2 mm is applied to this specimen in a quasi-static manner at a constant haul-off speed of 20 mm min^{-1}. In order to minimize the simulation effort, the symmetry of the specimen is used and only a quarter of the geometry is modeled. The effective properties determined for the warm and cold processing parameters are mapped onto the tensile bar geometry. Hence at both parameter sets, the tensile bar is modeled using five layers of different effective properties, for example, Young's modulus and Poisson's ratio. The comparison of force/displacement curves calculated using either a linear or multilinear elastic materials model is shown in Figure 10.23. It can be seen that when using a linear elastic materials formulation, the calculated forces are significantly higher than when adopting the multilinear one. Owing to the fact that thermoplastics show a highly nonlinear mechanical behavior even at small deformations, the bearable forces at an applied displacement are highly overestimated by the linear elastic materials model.

The comparison with the experimental force/displacement curve obtained by using warm process parameters (Figure 10.24) shows a good performance of the multilinear model, and corroborates the conclusion that a pure elastic model does not predict the materials behavior accurately.

The influence of the heterogeneous materials data is demonstrated in Figure 10.25. When defining the same Young's modulus for each element, disregarding the influence of the local microstructure within the bar, the calculated stress in the highest loaded cross section of the tensile bar is homogeneous (Figure 10.25(a)). Taking into account the results of the multiscale simulation, it is shown in Figure 10.25(b) that the calculated stress in the same cross section varies depending on the microstructure stiffness: owing to higher Young's modulus in the boundary layers than in the plate center (Figure 10.21), the stress response increases slightly there.

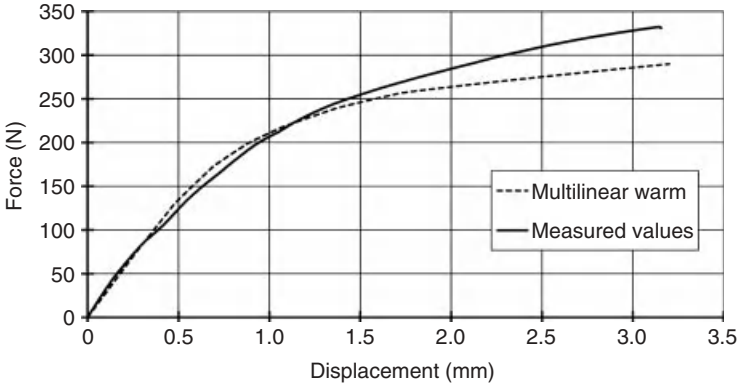

Figure 10.24 Comparison of simulated and measured force–displacement curves of PP tensile bars processed with 280/80 °C.

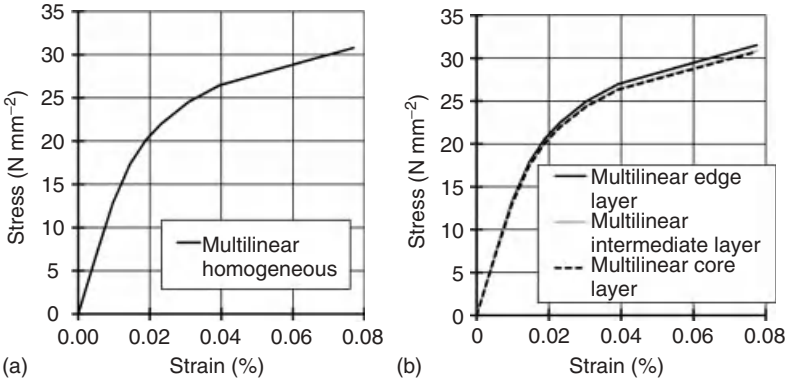

Figure 10.25 Influence of the microstructure properties on the local part stiffness in the highest loaded cross section.

10.8 Summary and Conclusion

For the realization of an integrative simulation chain for a microstructure-based structural analysis of semicrystalline thermoplastic parts, several software tools were developed, modified, or extended by additional models. In order to transfer the results of the macroscale heat and fluid flow simulation to the microstructure simulation software SphaeroSim, a tool Sigma2VTK has been developed. Besides that, based on the existing program SphaeroSim 2D, a 3D version was developed [6] enabling the prediction of a local microstructure evolution under the temperature conditions extracted from the linked heat and fluid flow simulation of the injection molding process on the macroscale. Different nucleation and spherulite growth models were validated with experimental data. This software tool was furthermore

extended for the prediction of molecular orientations due to shear deformation of the melt in the mold cavity. The homogenization software HOMAT [32] and its specific preprocessor tool Mesh2Homat were extended to treat semicrystalline thermoplastic materials. Indeed, as the amorphous and the crystalline phase are not available separately, two different homogenization schemes – a direct one where the spherulite is assumed to be isotropic and a more complex two-level scheme – have been implemented and compared. Classes of spherulites have been introduced in order to reduce the computational costs of the homogenization step. In order to predict the mechanical part behavior precisely depending on the inner properties of a thermoplastic part, two user-defined materials descriptions were developed and implemented in Abaqus FEA. Here, a multilinear elastic formulation has been chosen for the consideration of crystallization effects, while a linear elastic orthotropic formulation has been adopted to handle the molecular orientation effects.

Furthermore, the virtual process chain regarding crystallization effects was validated on a simple specimen. The application to 2 mm PP plate-type molding shows that SphaeroSim is able to predict the effect of process parameters on the spherulites morphology and their diameter correctly under qualitative aspects. The direct homogenization results for the PP plate show that under warm process parameters, the effective Young's and shear moduli present slightly higher values at the plate edge than in its center. A dedicated two-level homogenization scheme has been successfully developed for semicrystalline thermoplastics. First, this scheme predicts the correct tendency of the observed anisotropy of the injection-molded PP plate. It outperforms the direct scheme and indicates clearly that the assumption of an isotropic spherulite is inaccurate. Moreover, it allows the accurate determination of the influence of the bilamina design and of the crystalline properties, deduced from *ab initio* calculations [17] and X-ray diffraction measurements [18], on the effective properties of spherulitic microstructures. It shows also that the classical bilamina is too stiff, and the surrounded amorphous phase has to be modeled with an aspect ratio lower than 0.1. The calibration of the isotropic multilinear materials model for the structural analysis requires effective elastic properties for each element as well as the specification of the decreasing tangential stiffness with increasing strain. For this purpose, the multilinear model operates with various user-defined strain levels. Stress/strain simulations of a multilayer PP bar with local variable stiffness due to the inhomogeneous microstructure lead to more accurate results. Nevertheless, the difference in the local stiffness is rather small in the present application; one can estimate the accuracy increase in the structural analysis of complex thermoplastic parts with varying wall thicknesses by taking the microstructure-related inner properties into account.

Future work on the microscale shall be dedicated to the inclusion of effects of shear-induced crystallization and its influence on the resulting mechanical part properties. In order to take into account the effective anisotropic behavior of the semicrystalline thermoplastics predicted by the two-level homogenization scheme in the macrosimulation, the isotropic multilinear model shall be extended in the near future to include anisotropic materials behavior. Moreover, the predicted

average molecular orientation over an element shall be also transferred to the 3D spherulite model of the two-level homogenization scheme in order to improve this model and to achieve first a link between both inner properties, the crystallization and the molecular orientation, at the microscale and subsequently on the macroscale.

References

1. Michaeli, W., Bobzin, K., Parkot, D., Kashko, T., Heesel, B., and Baranowski, T. (2009) Skalenübergreifende simulation teilkristalliner thermoplaste. *Werkstoffe Fertigung*, **5**, 33–34.
2. Michaeli, W., Hopmann, Ch., Bobzin, K., Arping, T., Baranowski, T., Heesel, B., Laschet, G., and Öte, M. (2012) Development of an integrative simulation method to predict the microstructure influence on the mechanical behaviour of semi-crystalline thermoplastics. *Int. J. Mater. Res.*, **103** (1), 120–130.
3. Osswald, T.A. and Hernández-Ortiz, J.P. (2006) *Polymer Processing – Modeling and Simulation*, Carl HanserVerlag, Munich.
4. N.N. (2010) SABIC PP 505P. Datasheet, SABIC Europe, Sittard, Netherlands.
5. Hoffmann, S. (2003) Berechnung von kristallisationsvorgängen in kunststoffformteilen. Dissertation. RWTH Aachen.
6. Michaeli, W. and Baranowski, T. (2010) Simulation of the microstructure formation in injection molded semi-crystalline thermoplastic parts. *J. Polym. Eng.*, **30** (1), 29–43.
7. Michaeli, W., Bobzin, K., Arping, T., Bagcivan, N., Baranowski, T., Heesel, B., and Kashko, T. (2010) Integrative materials modelling of semi-crystalline thermoplastics parts in 3D. Proceedings of the Polymer Processing Society 26th Annual Meeting, Banff.
8. Hoffman, J.D., Davis, G.T., and Lauritzen, J.I.J. (1976) *Treatise on Solid State Chemistry*, Plenum Press, New York.
9. Moneke, M. (2001) Die kristallisation von verstärkten thermoplasten während it der schnellen abkühlung und unter druck. Dissertation. TU Darmstadt.
10. Janeschitz-Kriegl, H. (2010) *Crystallization Modalities in Polymer Melt Processing*, Springer-Verlag, Wien.
11. Housmans, J.W. (2008) Flow induced crystallization of isotactic polypropylenes. Dissertation. Technische Universiteit Eindhoven.
12. Hoffman, J.D. and Miller, R.L. (1997) Kinetics of crystallization from the melt and chain folding in polyethylene fractions revisited: theory and experiment. *Polymer*, **38**, 3151–3212.
13. Mandelkern, L. (1964) *Crystallization of Polymers*, McGraw-Hill, New York.
14. Nakamura, K., Katayama, K., and Amano, T. (1973) Some aspects of nonisothermal crystallization of polymers. II. Consideration of the isokinetic condition. *J. Appl. Polym. Sci.*, **17**, 1031–1041.
15. Zinet, M., Otmani, R.E., Boutaous, M., and Chantrenne, P. (2010) Numerical modeling of nonisothermal polymer crystallization kinetics: flow and thermal effects. *Polym. Eng. Sci.*, **50**, 2044–2059.
16. Bédoui, F., Diani, J., Regnier, G., and Seiler, W. (2006) Micromechanical modeling of isotropic elastic behavior of semicrystalline polymers. *Acta Mater.*, **54** (6), 1513–1523.
17. Tashiro, K., Kobayashi, M., and Tadokoro, H. (1992) Vibrational spectra and theoretical 3-D elastic constants of isotactic polypropylene crystal: an important role of anharmonic vibrations. *Polym. J.*, **24** (9), 899–916.
18. Sawatari, C. and Matsuo, M. (1986) Elastic modulus of isotactic polypropylene in the crystal chain direction as measured by X-Ray diffraction. *Macromolecules*, **19** (7), 2653–2656.
19. Wübken, G. (1976) Einfluß der verarbeitungsbedingungen auf die innere struktur thermoplastischer

spritzgußteile unter besonderer berücksichtigung der abkühlverhältnisse. Dissertation. RWTH Aachen.
20. Backhaus, J. (1985) Gezielte qualitätsvorhersage bei thermoplastischen spritzgießteilen. Dissertation. RWTH Aachen.
21. Meijer, H.E.H. and Govaert, L.E. (2005) Mechanical performance of polymer systems: the relation between structure and properties. *Progr. Polym. Sci.*, **30**, 915–938.
22. Kech, A., Ludwig, H.-C., Möginger, B., Eyerer, P., and Christiansen, J.D.C. (2000) Mechanical properties of isotactic polypropylene with oriented and cross – hatched Lamellae Structure. *Int. Polym. Proc.*, **15** (2), 202–206.
23. Tashiro, K. and Kobayashi, M. (1996) Molecular theoretical study of the intimate relationships between structure and mechanical properties of polymer crystals. *Polymer*, **37** (10), 1775–1786.
24. Michaeli, W., Gutberlet, D., and Glißmann, M. (2000) Determination of mechanical characteristics of semi-crystalline thermoplastics in dependence on molecular orientation. *Macromol. Mater. Eng.*, **279**, 19–25.
25. Altenbach, J. and Altenbach, H. (1994) *Einführung in die Kontinuumsmechanik*, Teubner, Berlin.
26. Gutberlet, D. (2002) Ansätze zur verbesserten werkstoffbeschreibung für die dimensionierung von Thermoplastischen kunststoffen. Dissertation. RWTH Aachen.
27. Pantani, R., Sorrentino, A., Speranza, V., and Titomanlio, G. (2004) Molecular orientation in injection molding: experiments and analysis. *Rheol. Acta*, **43**, 109–118.
28. Pantani, R. (2005) Validation of a model to predict birefringence in injection molding. *Eur. Polym. J.*, **41**, 1484–1492.
29. Abaqus FEA (2011) Analysis User's Manual 6.10., Dassault Systèmes Simulia Corp., Providence, RI.
30. DIN (2009) 53504. *Prüfung von Kautschuk und Elastomeren – Bestimmung von Reißfestigkeit, Zugfestigkeit, Reißdehnung und Spannungswerten im Zugversuch*, Beuth, Berlin.
31. DIN (2010) DIN EN ISO 527-2. *Kunststoffe – Bestimmung der Zugeigenschaften -- Teil 2: Prüfbedingungen für Form- und Extrusionsmassen*, Beuth, Berlin.
32. Laschet, G. (2002) Homogenisation of the thermal properties of transpiration cooled multi-layer plates. *Comput. Methods Appl. Mech. Eng.*, **191** (41–42), 4535–4554.
33. Laschet, G. and Rex, S. (2008) Effective Thermoelastic Properties of Flat and Curved Transpiration Cooled Multilayer Systems Via Homogenisation, ASME Paper No: GT2008-50590.
34. Doyle, M.J. (2000) On the effect of crystallinity on the elastic properties of semi-crystalline polyethylene. *Polym. Eng. Sci.*, **40** (2), 330–335.

11
Textile-Reinforced Piston Rod

Britta Kuckhoff, Josef Klingele, Markus Linke, Thomas Gries, Kirsten Bobzin, Thomas Schläfer, Tatyana Kashko, and Mehmet Öte

11.1
Introduction

Textile-reinforced metal matrix composites (MMCs) are a very innovative class of materials. This class of materials opens up new applications and more efficient design options as compared to nonreinforced lightweight metallic materials. The development objectives for light metal composites in general and especially for textile-reinforced MMCs are [1]

- increase in yield strength and tensile strength at and above room temperature while maintaining the toughness;
- increase in creep resistance at higher temperatures;
- increase in fatigue strength, especially at higher temperatures;
- improvement of thermal shock resistance;
- improvement of corrosion resistance;
- increase in Young's modulus;
- reduction of thermal expansion.

One of the main characteristics of fiber-reinforced MMCs and especially of textile-reinforced composites is the anisotropy of their properties essentially evoked by the anisotropy of the fibers, the textile structures and their orientation in the metal matrix, respectively. This anisotropy can be tailored for dedicated applications at the local scale of the material and especially at the scale of the entire component. This anisotropy makes textile-reinforced components a highly interesting test case to verify the concept of the simulation platform depicted in this book, and a textile-reinforced aluminum piston rod was thus selected to verify the developed simulation technologies (Figure 11.1).

Another peculiarity of textile-reinforced composites is the multiple length scales relevant to both the processing and the properties of components ranging from the size of a component, via the scale of the textile structure, with size and distance of rovings down to the size of the diameter of an individual filament within a roving (Figure 11.2).

Integrative Computational Materials Engineering: Concepts and Applications of a Modular Simulation Platform,
First Edition. Edited by Georg J. Schmitz and Ulrich Prahl.

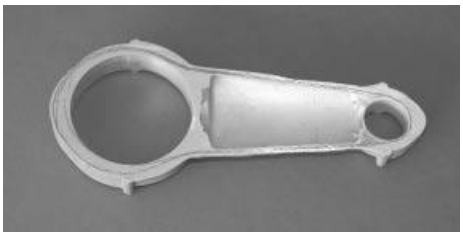

Figure 11.1 Section of a textile-reinforced aluminum piston rod. Especially, the locally anisotropic mechanical properties of the material and of the entire component are in the focus of this test case scenario. Anisotropic permeabilities relevant to the production of this component by investment casting are investigated as well.

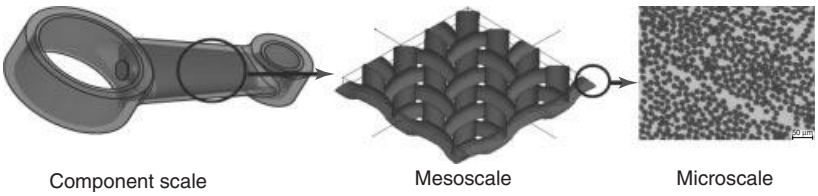

Figure 11.2 Different scales relevant to the manufacture and properties of a textile-reinforced metal matrix components: the macroscopic scale of the component, the mesoscale of the braided roving structure, and the microscale of the individual filaments constituting an individual roving.

11.2 Experimental Process Chain

The basic process chain for the manufacture of textile-reinforced MMCs is based on investment casting [2], which, in general, comprises the following steps:

- creation of a wax model/wax pattern;
- repeatedly coating this wax pattern with suitable ceramic slurries, including intermediate drying steps leading to a shell mold;
- removal of the wax pattern once the shell mold reveals a sufficient green strength;
- firing of the green shell mold to obtain a ceramic mold;
- casting the molten metal into this mold; and
- removal of the ceramic shell after solidification of the metal.

The peculiarities of the production of a textile-reinforced piston rod are essentially in (i) the process of creating a combined gypsum/wax pattern overbraided with ceramic fibers (called "*textile preform*" in the following text), (ii) the fixation of the ceramic textile in the ceramic shell mold, and (iii) infiltrating the ceramic textile with the molten melt.

For the production of the textile preform, a radial braiding process on the combined gypsum/wax pattern acting as a braiding mandrel is used. The wax mandrel is overbraided with ceramic Al_2O_3 fibers to form the textile preform for the subsequent investment casting process. These fibers reveal excellent thermal stability, but typically are very brittle, making it difficult to process them on textile machinery.

The special scopes of this test case [3] are the numerical investigation of the processes for creating different textile preforms, identification of their permeability in view of their infiltration by the metallic melt, evaluation of the mechanical properties of textile-reinforced metallic alloys, and eventually simulation of the anisotropic behavior of textile-reinforced components.

The entire experimental process chain for AluTex has been developed in a separate project [4]. In combining two state-of-the-art manufacturing techniques, a new manufacturing route was created, which allows the production of complex-shaped components with a braided reinforcement custom tailored to the operating loads. Furthermore, the process is cost efficient and can be easily integrated into existing investment casting facilities.

11.2.1 The Braiding Process

For the production of the textile preform, an overbraiding process is used. Compared to other preforming technologies such as multiaxial warp-knitting or weaving, overbraiding can be used to create tubular structures with adjusted properties regarding fiber material, fiber orientation, and textile structure. While the braiding process itself is very efficient and reproducible, setting up the machine and identifying suitable process parameters is time consuming and costly.

Yarns are placed on bobbin carriers that are moved in two independent groups on opposing sinusoidal orbits. Owing to the intertwining of the yarns, a predetermined pattern is created. The result is a tubular braid formed and laid down on the braiding mandrel, which is moved through the braiding eye. The withdrawal of the braid is realized by the movement of the mandrel. For complex shapes, the withdrawal of the mandrels is best realized using robots. The ratio between the movement of the bobbin carriers (i.e., the speed of the braiding machine), the withdrawal speed of the robot, and the diameter and shape of the braiding mandrel determine the *braiding angle* in which the yarns are oriented on the mandrel.

Uniaxial fibers can further be integrated into the braid in addition to the braiding yarns, leading to *triaxial textile* structures. Moreover, *multiple layers* can be produced by moving the mandrel through the braiding eye multiple times. The braiding angle can be adjusted independently for each layer and ranges from 10 to 80° being measured against the direction of production.

Braiding of the Textile Preform Owing to the brittleness of the ceramic Al_2O_3 fibers, processing of these fibers is rather challenging. One reason for damage to the fibers is the interaction between the ceramic rovings and the machine

parts guiding the rovings. Yarn damage also occurs in the middle of the braiding machine, where the fibers interact with each other and the braiding eye. In order to achieve a well-compacted braid on the braiding mandrel, the yarn tension has to be sufficient. However, the yarn damage also increases with increasing yarn tension because of the increased forces between yarns and machine elements. This eventually may lead to yarn breakage.

The yarn tension can be altered by selecting different types of coil springs within the bobbin carrier. For the described test case, the yarn tension was adjusted carefully to achieve good braid properties regarding low filament breakage and good compaction of the braid.

Variation of the Textile Structure The infiltration of the textile preform, the solidification of the metal matrix, and the mechanical properties of the composite are largely influenced by the structure of the textile preform. Moreover, the overall yarn fraction of the composite depends on the textile structure. Different textile structures such as, for example, ''closed'' and ''open'' structures (Figure 11.3), have been created with the overbraiding technology, mainly by altering the distribution of the bobbins over the horngears of the machine. Note the different geometrical features of the braided textile such as, for example, the

- shape of the individual rovings (round to flat cross-sections, untwisted to twisted);
- distance between different rovings (open to closed textile structures); and
- contact angles between the different rovings (varying with the position on the wax surface).

These features, to some extent, can be controlled by selecting adequate process parameters.

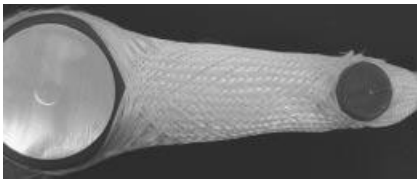

(a)

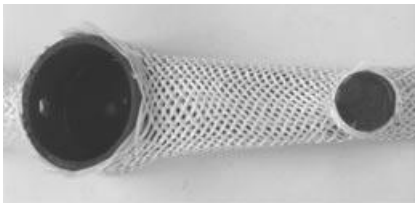

(b)

Figure 11.3 Braiding mandrel and textile preform with a (a) closed and (b) open textile structure.

11.2.2
The Investment Casting Process

For the casting of the test component, an investment casting process has been selected. Typically, investment casting allows the manufacture of parts with complex geometries or thin walls with high accuracy. Subsequent machining of the cast part can often be omitted in view of the high quality of the as-cast geometry. Many metals and alloys can be used for this process as long as the flow behavior is sufficient to ensure complete filling of the mold [2].

For manufacture of the textile-reinforced piston rod, a pattern that comprises two different materials is used. Where there is wax in the pattern, the latter part will be of unreinforced aluminum and the gypsum parts will be hollow. The gypsum areas also serve for the later positioning of the textile within the ceramic shell mold. The pattern is used as a braiding mandrel for the production of the textile perform, with the overbraiding technology as described above. The resulting wax pattern covered with textile is shown in Figure 11.3.

This textile preform is used to create an investment shell mold as described above. After the creation of this shell mold, the wax parts are removed by heating the assembly. The shell mold is then fired to result in a ceramic mold with sufficient mechanical properties. During casting, the original wax-filled areas of this mold and the textiles are filled and infiltrated with the aluminum alloy, while the gypsum parts are removed after the solidification of the metal. The resulting textile-reinforced aluminum piston rod is shown in Figure 11.1.

11.3
Simulation Chain

11.3.1
Overview

The simulation chain can be structured according to the different scales essential for the process and the properties of the textile-reinforced component.

On the *macroscale*, the simulation of the *braiding process* proceeds using PAM-Crash [5, 6] as detailed in Section 11.3.2. The essential result parameters are the braiding angles on the surface of the braiding mandrel and the distances between the yarns. These parameters are saved and used later (i) for the determination of permeabilities affecting the infiltration process simulated using CASTs [7], as detailed in Section 11.3.4, (ii) for the determination of locally anisotropic materials properties, as described in Section 11.3.6, and later for (iii) the overall anisotropy of the component revealing a range of angles for the reinforcing textile. This geometric information is complemented by local information about the local materials properties extracted from the micro- and mesoscales and then provided to a structural simulation using Abaqus [8], as outlined in Section 11.3.7.

The *mesoscopic level* correlates the microscopic level that describes the influence of the filaments on the properties of an individual roving and the macroscopic scale that defines the geometry of the braided structure. At the mesocale, different unit cells for different macroscopic braiding structures (varying, e.g., in braiding angle, distance of rovings, thickness, etc.) are modeled using WiseTex [9]. WiseTex results for individual unit cells are then geometrically arranged to a multilayer and transformed to a finite-volume-model using T-Grid [10]. This multilayer unit cell is then used as the basis for the determination of the properties of the textile-reinforced material in Section 11.3.6 and to investigate, for example, the permeabilities during the infiltration (Section 11.3.4).

The *microscale* is the scale of the individual filaments constituting the individual mesoscale roving. The individual filaments play an important role in the evolution of the solidification microstructure as they influence (i) the infiltration of melt into the spaces between the filaments, (ii) the nucleation conditions for the solidifying melt, and (iii) the thermal conditions for growing grains. Simulations of microstructure evolution in infiltrated textiles were performed using MICRESS® [11] and are detailed in Section 11.3.5. The resulting microstructures along with digitized experimental cross sections were then used to elaborate the mechanical properties of the infiltrated roving (Section 11.3.6).

The individual simulations are detailed in the following sections and a schematic overview is given in Figure 11.4.

11.3.2
Simulation of the Braiding Process

The simulation of the braiding process has been developed based on the PAM-Crash finite elements software (ESI Group) [5, 6]. PAM-Crash is usually used for the dynamic analysis of the crash behavior of structures. It provides interfaces for creating and exporting grids, changing model parameters, calculating the crash process, and analyzing the results (Figures 11.5 and 11.6).

The main scope of the PAM-Crash simulations is the description of the position and orientations of the yarns in the braided structure covering the mandrel. Correct positioning of the yarn is most important for both the later application of the component as well as for the infiltration and subsequent machining processes.

A PAM-Crash-compatible setup thus is used to simulate the braiding process. The spool pattern is modeled using CABRUN, a software developed to generate a series of movements on a 3D rotary braiding machine [6]. A rotational movement was mapped in order to use this software as the basis for the simulation of the braiding process. In the second step, the orientation of the bobbin carriers with respect to the direction of the braiding point was taken into account; the orientation of the braided fibers corresponding to a radial braiding machine with 144 bobbin carriers. The model is adaptable to various other braiding machines. The software output is the coil carrier paths. These can be imported into PAM-Crash. A track function is thereby assigned to each fiber. The user in PAM-Crash defines materials, components, boundary conditions, and 3D-forces in accordance with the actual

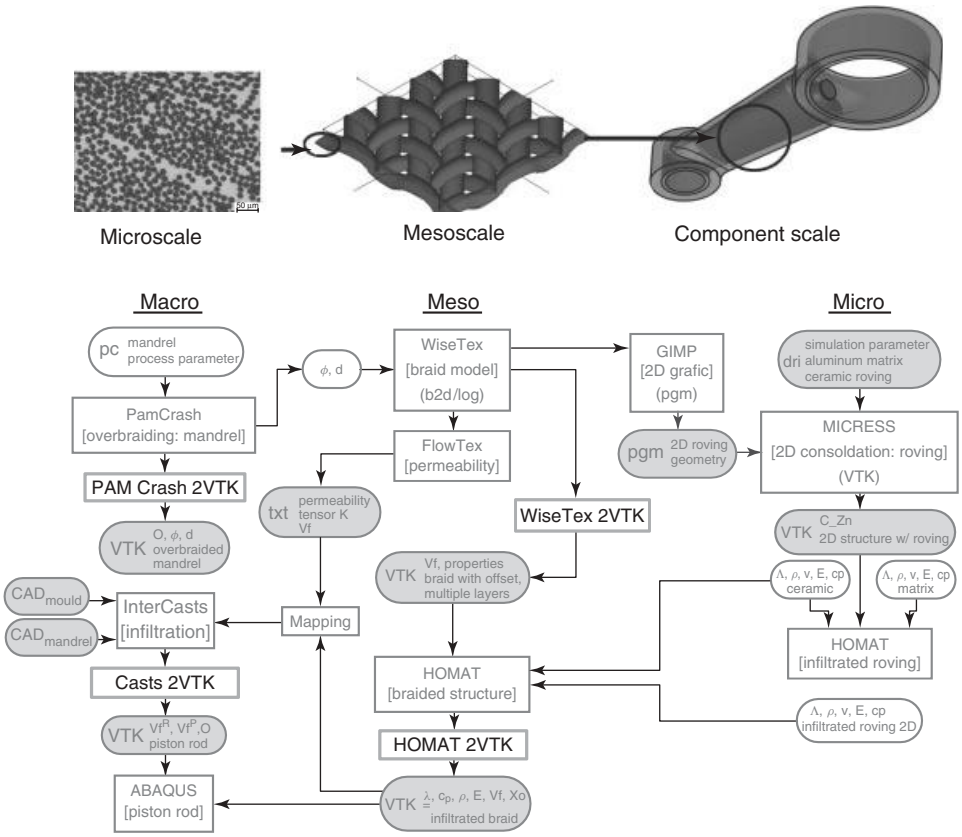

Figure 11.4 Simulation flowchart for the test case of a textile-reinforced piston rod indicating the different simulation tools interacting across different length scales.

braiding setup. This enables a description of complex braiding setups in which different machine parts such as braiding rings and a braiding core including its travel path are taken into account in the simulation. All fibers and machine parts can be assigned to different material models.

The braiding process is simulated with PAM-Crash by calculating all collisions between the core and the fibers as well as the mutual collisions of the fibers along their paths. Braid fibers are modeled in PAM-Crash in three sectors: the lower part corresponds to the carrier and is modeled elastic, the central part of each fiber represents the inelastic fibers, and the upper part of the fiber is located at the extraction point. This categorization enables different material properties to be assigned to each part of the fiber. The upper and lower parts of the fibers comprise a single 1D element, whereas the central section of the fiber comprises an interlinked chain of various short 1D elements that are connected at their ends via node points

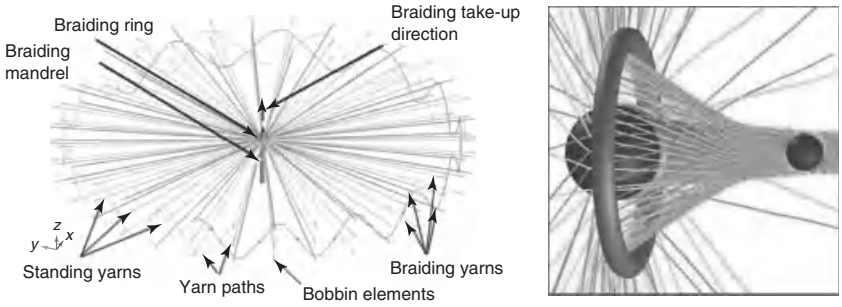

Figure 11.5 The braiding process. The individual yarns follow complex paths, being essentially defined by the motion of the bobbin elements. Different yarn sections are assigned to different properties to model their mutual collisions as well as their interaction with the braiding ring and the mandrel (see text).

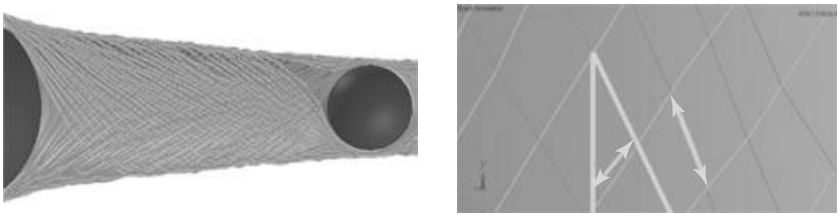

(a) (b)

Figure 11.6 (a) Overbraided mandrel for the piston rod. (b) Important parameters being extracted from this simulation are the locally varying braiding angles and the mutual distance between adjacent yarns.

to which the force is coupled. The length of these elements ranges from 1 to 5 mm and is set by the user. A simulation may include 0° fiber orientations and can take different fiber materials in the braid into account (Figure 11.7).

The material model used for the fibers can be interpreted as a general Kelvin mechanism (Figure 11.8). The properties of the spring and of the damping element can be set as linear or defined as nonlinear functions wherein this type of elements can be allotted forces but no torque (Eq. (11.1)):

$$F(\sigma, \dot{\sigma}) = k * \sigma + c * \dot{\sigma} \tag{11.1}$$

The fiber tension is taken into account in the carrier model. It behaves like a spring that applies a constant force to the fiber, resulting in a constant tension. The parameters being varied for the central portion of the fiber include mass (m), density (ρ), linear stiffness (k), and the viscous damping coefficient (c).

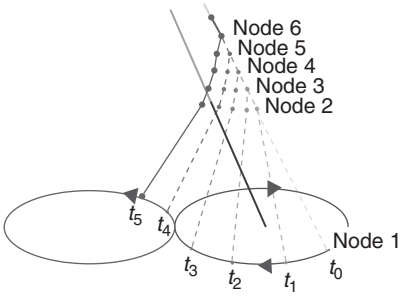

Figure 11.7 Node and rod elements at different time points t_i.

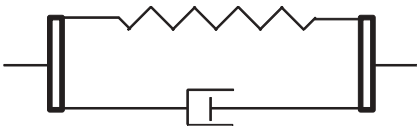

Figure 11.8 Kelvin model comprising spring and damping modules.

The boundary conditions describe the mechanical degrees of freedom of all components in the simulation. To create the boundary conditions and to determine the forces for the newly added bodies, the components are assumed as ''rigid bodies.'' A ''rigid body'' comprises a set of nodes. In PAM-Crash, for instance, the relevant center of the mass, local coordinates, total mass, and the components of the inertia tension are calculated in the global frame of reference.

Friction is described in the simulation from the perspective of the contact plane. The friction between fibers and wax mandrel (''core'') are treated separately from the mutual friction of the fibers among one another. A master/slave contact is selected for the core/fiber friction. While the master is compressed, the slave applies force to the master. This differentiation is made to reduce the computing time for the contact search algorithms. In this case, the core is the master and all fiber node points are the slaves. The overall friction force is divided into three components:

- damping-dependent component;
- constant friction-coefficient (μ)-dependent component ; and
- contact thickness depending on contact force.

The contact thickness corresponds to a distance from the master surface, which is used in the search algorithm to determine expected impacting slave-node points. If an impacting node point is discovered, a force is applied to it in the normal direction with respect to segment surface such that the node point does not penetrate the ''rigid body.'' Reality and simulation can be calibrated with the aid of a factor. A lot of effort had to be taken in order to eliminate oscillations in the simulations, which could eventually be avoided by a suitable model for the rode and well-defined contact conditions.

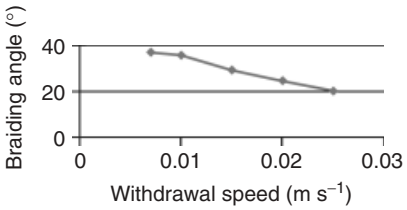

Figure 11.9 Exemplary result for the variation of the braiding angle with increasing withdrawal velocity for a specific position on the mandrel.

On the basis of the above model description and assumptions, a computer-aided design (CAD) model of the mandrel/core has been enmeshed and PAM-Crash simulations were performed, including varying process parameters such as

- withdrawal speed of the core;
- bobbin velocity;
- bobbin track;

and/or varying material parameters such as

- different material models and
- different assumptions for friction between the yarns and between yarns and mandrel.

An exemplary result is the variation of the braiding angle with the withdrawal speed for a given location on the mandrel (Figure 11.9). The braiding angle is one of the key geometrical parameters for further processing and eventually for determining the properties of the reinforced component.

11.3.3 Simulation of the Braiding Structure

The collisions between the yarns are simulated assuming mathematically sharp line elements in above PAM-Crash simulations. The resulting braiding parameters such as angles and distances are thus used to create a planar 3D CAD model of the braiding structure using the software WiseTex (developed at KU Leuven, Belgium [9]).

On the basis of these data, WiseTex calculates, for example, the total height of one layer or the shape of the braided roving (Figure 11.10). The elementary structural data of such a braided structure, such as coordinates of the knots, boundary surfaces of the geometry, number of the surfaces and knots, and so on, is stored in a StereoLithography-file (STL-file). This information can then be further processed, for example, using T-Grid [10] (Figure 11.11).

The distance and orientation of the layers depend on the braiding process and the machine settings. In this case, it was assumed that these parameters are fixed and only a defined braid was used. In practice, several layers are generally used for a textile preform. These layers are frequently randomly displaced with respect to each other (Figure 11.12).

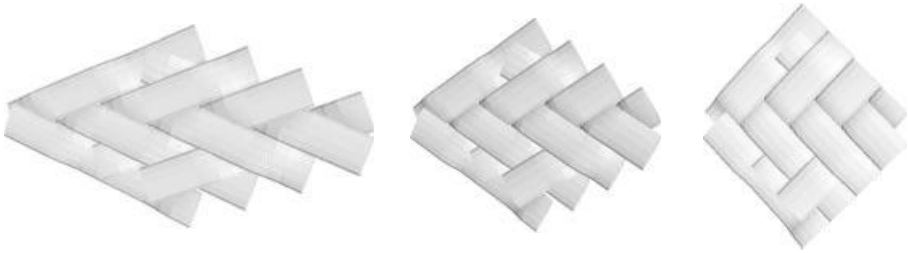

Figure 11.10 Braid structures being generated using WiseTex on the basis of different geometrical data for braid angles (angle between roving and withdrawal direction of mandrel) of 20, 30, and 45°.

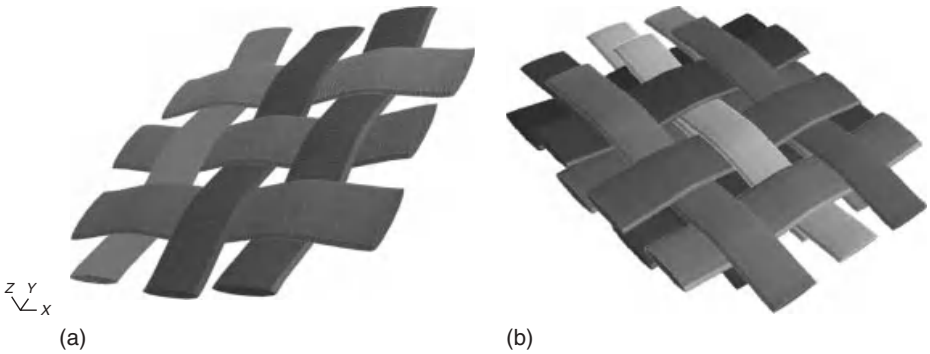

Figure 11.11 Braided structure in T-Grid. The surface meshes of the individual braid layers as provided by WiseTex are first converted into volumetric data (a) and can then be arranged into multilayer structures (b) on the basis of adjustable orientation relations (Figure 11.12).

11.3.4
Simulation of the Infiltration Process

In FLUENT [12], the melt flow through a unit cell of a braid structure is simulated to estimate the pressure drop across the braid structure. The braid structure represents an obstacle for the melt flow during infiltration. It contributes to friction and/or dissipation losses in the flow and therefore corresponds to a restriction in the flow field.

The objective of the simulation is to estimate the pressure loss throughout the braid structure under the conditions of a stationary, incompressible, and laminar flow. The pressure loss depends on the free volume of the textile. The free volume of the braid, is in turn, dependent on

- distance and mutual orientation of the rovings in a single layer;
- the number of layers of braid being stacked on top of each other; and
- the mutual orientation and/or offset between the different layers.

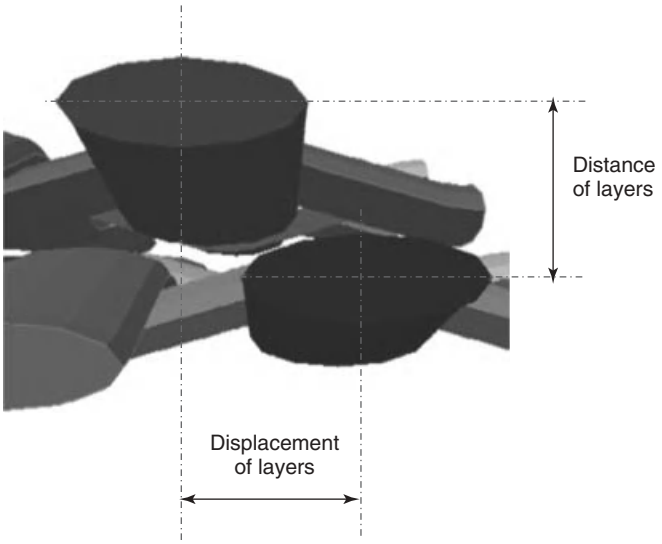

Figure 11.12 Geometrical arrangement of multiple braid layers as generated using T-Grid.

The influence of several layers on the pressure loss is thereby simulated at different flow speeds, while the influence of the offsetting is simulated at a constant speed (Figure 11.13). The basic findings are

- the more layers that are present, the greater is the pressure loss;
- the greater the offset between the layers, that is, the greater the packing density of the braid, the greater is the pressure loss.

Pressure losses and loss coefficients were identified for a single-layer and an eight-layer structure. For the eight-layer structure, a simple relationship between infiltration velocity and pressure loss could be established in the form $\Delta p = f(v)$.

As the major result, the full permeability tensor is exported in ASCII format (out) for each of the unit cells of the multilayer braiding.

11.3.5
Simulation of the Solidification Microstructure

Several simulation scenarios to describe microstructure evolution during the solidification process of a textile-reinforced aluminum alloy were developed using MICRESS [11]. 2D simulations now cover the scales from individual filaments up to a single roving and will be extended to 3D braided textile structures in future. Different conditions during the casting process (temperature–time profiles, concentration of alloying element (Zn), undercooling ratio, temperature gradients, etc.) were taken into account. The simulated material comprises ceramic filaments (Al_2O_3) infiltrated by a binary aluminum alloy ($AlZn_6$). The infiltration process itself is not taken into account and the simulations thus start from a melt already

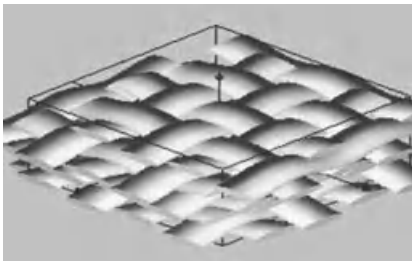

(a)

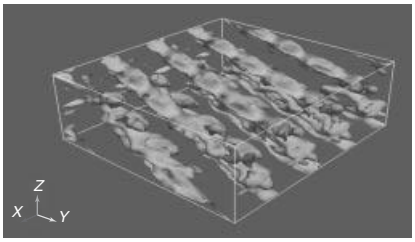

(b)

Figure 11.13 Gradient of the flow velocity (b) during infiltration of a 3D textile multilayer (a) braid.

infiltrated into the textile structures and assume absence of any flow within the melt as an initial condition.

The different initial distributions of the individual Al_2O_3 filaments being simulated were

- a single fiber surrounded by the melt;
- a regular, periodic arrangement of a few fibers (Figure 11.14a,b);
- an irregular distribution of filaments at the scale of a roving (Figure 11.14c).

Several assumptions for the properties of the different materials in the process were made: the ceramic filaments were modeled as an isotropic phase and reactions between the ceramic filaments and any of the other phases (melt and solid aluminum) were not considered. The solid aluminum grains were treated as an anisotropic phase with cubic crystal symmetry. Thermophysical data such as, for example, heat conductivities of both phases were taken from literature and/or estimated. Thermodynamic data for the phase transformation (i.e., solidification) were modeled by means of a linearized phase diagram. The driving force for both nucleation and solidification was assumed to purely depend on the local conditions of temperature and concentration. Influences of internal material stress and latent heat on microstructure formation were neglected.

The simplest model of an aluminum melt around a *single ceramic filament* served to identify parameters affecting the solidification process of such materials. Geometry and spatial arrangements of *several ceramic fibers in a regular array* were then varied to investigate their effect on the solidification phenomena such as nucleation and grain growth. For this purpose, periodical boundary conditions

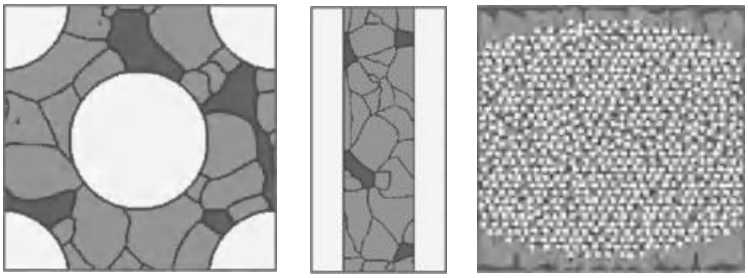

Figure 11.14 2D simulations of nucleation and growth of Al-grains being constrained by filaments (bright). Residual liquid is displayed dark in the cross-section of a few filaments (a), the longitudinal section along two filaments (b), and in an entire roving consisting of many statistically distributed filaments (c).

were selected. The initial condition was a mere liquid melt between the Al_2O_3 fibers. Nucleation was then allowed to occur both at interfaces with the Al_2O_3 fibers and in the bulk melt regions. The latter type of nucleation sites allowed modeling of heterogeneous nucleation as occurring in the Ti_2B-grain-refined experimental reference samples. The crystallographic orientation of the new nuclei was considered as random.

The necessary condition for a nucleation event was exceeding a nucleation threshold – a ''critical undercooling'' – which was compared to the actual local undercooling derived from local conditions of temperature and alloy composition in reference to the thermodynamic equilibrium as determined from the phase diagram.

In summary, microstructure evolution simulations of infiltrated rovings show reasonable qualitative agreement with experimental observations (Figure 11.15). In order to obtain a more quantitative predictability, careful calibration of the simulations is required, especially with respect to nucleation phenomena. In the long term, the developed approach for infiltrated textiles may be applied also to

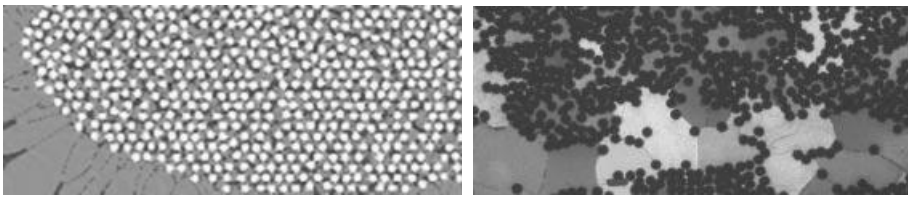

Figure 11.15 Qualitative comparison of simulated and experimental AluTex grain structures in textile fibers being infiltrated with an $AlMg_6$ alloy. Different types of nucleation mechanisms either on filament interfaces or on intentionally added nucleants determine the eventual grain size. The microstructure simulations have to be calibrated in this context. Slightly larger grains are observed outside the roving section in both experiment and simulation.

more complex alloy system of technical relevance [13] and the crystallographic texture of the infiltrated compound may be considered as well.

As a benefit of the platform standard VTK format, realistic 3D geometries of stacked roving structures resulting from WiseTex and T-Grid simulations can now directly be used as initial geometry for microstructure simulations at the scale of the textile.

11.3.6 Effective Anisotropic Material Properties

As the aluminum-infiltrated rovings and textile structures are not directly accessible for mechanical testing, a two-stage homogenization procedure covering two different length scales was developed in order to determine the effective, anisotropic properties of the textile-reinforced piston material. The two different scales being considered are (i) the *microscopic* scale of an individual roving consisting of multiple filaments embedded in the Al-matrix and (ii) *mesoscopic* braided structures consisting of a number of rovings braided into a defined geometry (Figure 11.16). This geometry eventually has been varied, especially with respect to the braiding angle. Asymptotic homogenization, described in detail in Chapter 5, was used in this work on both scales.

In view of the simultaneous development of microstructure simulations for infiltrated fibers, the development of the homogenization schemes was proceeded on the basis of experimental cross sections serving as the basis for the application of the homogenization methods. In future, homogenization may directly act on full 3D-simulated microstructures including also the orientations of the grains using the standardized platform format.

Homogenization allows the determination of the effective properties of non-homogeneous materials based on the microstructure of the material and the properties of the individual constituents by using the homogenization methods comprehensively described in Chapter 5. The ''classic'' direct homogenization was initially developed for the microstructures with optically distinguishable constituents (the so-called phases). Direct homogenization, schematically represented

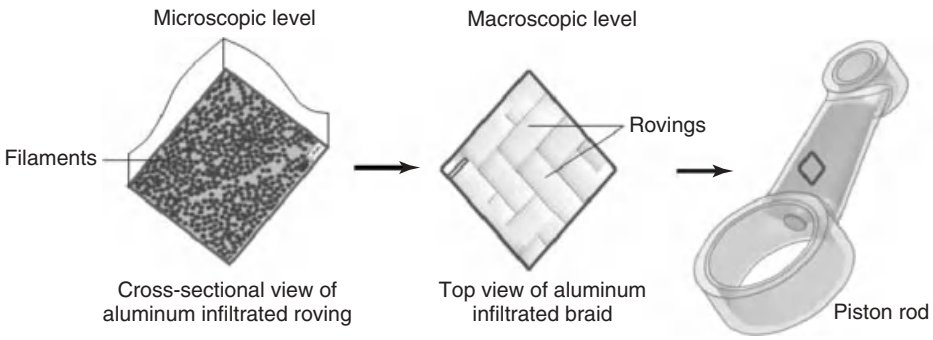

Figure 11.16 States and scales of homogenization procedure for the piston rod.

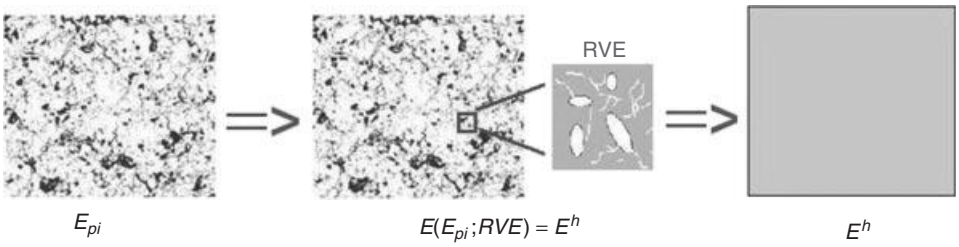

Figure 11.17 Schematic representation of the direct homogenization for the example of Young's modulus computation (see text).

in Figure 11.17, requires the material microstructure/topology and the properties (e.g., the Young's moduli) of the individual phases as input and delivers the homogenized, effective property of the material as output. As a result, it becomes possible to develop computationally effective numerical models at the macroscopic level by disregarding the geometries of the individual phases and modeling the structure as if it were a homogeneous continuum revealing an effective property, for example, the Young's modulus.

At the *microscopic* scale of an individual roving consisting of multiple filaments infiltrated by the Al-matrix, the effective Young's modulus and Poisson ratio were calculated using the material properties of the optically distinguishable constituents of the composite – the ceramic filaments and the aluminum matrix (Figure 11.18). In accordance with the experimental observations, a 100% infiltration of the roving by the aluminum has been assumed. The classical formulation of asymptotic homogenization methods (AHMs), as detailed in Section 5.2, requires a periodicity of the microstructure to be homogenized. In case of textile-reinforced composites, the periodicity of the structure on the ''microscopic'' level is not obvious (Figure 11.16). Since it was shown that the use of periodic boundary conditions for the determination of the mean effective properties of heterogeneous materials with *random microstructure* is more accurate than the use of either stress or strain boundary conditions [14, 15], the presented investigations were performed with periodic boundary conditions applied on the representative volume element (RVE) microstructure. Although the anisotropic characteristic of the fibers within the roving is well known, for the sake of simplicity the mechanical properties of the fibers in the aluminum-infiltrated roving are considered to be isotropic [16].

In this test case, spectral analysis (Section 5.3.1) was used for definition of the RVE size. The so-called ''windowing'' technique, as described in [17] (see also Section 5.3.2), was used to define the geometry of the RVE. Within this approach, 50 windows were cut from the original cross-sectional geometry of the aluminum-infiltrated roving in order to determine the distributions of the filament fractions (A_f) and the Young's moduli (E) across the geometry. The procedure [16] is illustrated in the example of two ''windows'' being cut from the geometry in Figure 11.18.

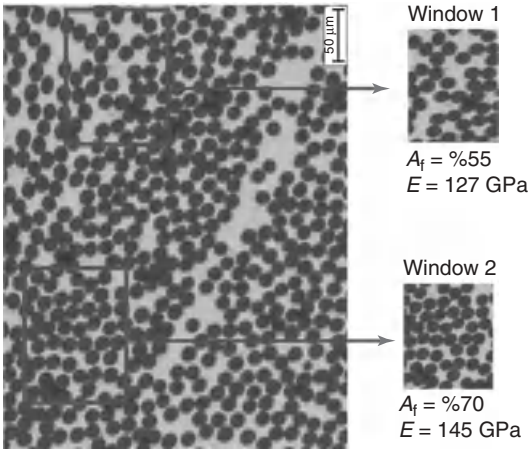

Figure 11.18 Windowing procedure for the example of two windows cut from the cross-sectional geometry of the aluminum infiltrated roving. Round, dark gray points are the ceramic filaments while the light gray areas correspond to the aluminum matrix.

The coordinates of the windows were generated randomly. The distribution of the filament fraction (Figure 11.19) is characterized by a mean value of 0.624, while the standard deviation is 0.0433 or approximately 6% of the mean value [18].

On the basis of the extracted RVE windows, effective Young's moduli were calculated. When interpolated as a function of the RVE coordinates within the specimen, they can be considered as a distribution of the effective Young's modulus over the roving cross section (Figure 11.20). The mean value of the effective Young's moduli, calculated by means of asymptotic homogenization, amounts to 136.9 GPa and the standard deviation of the distribution is 5.51 GPa (corresponding to approximately 4% of the mean value). Owing to this small variation in the distribution of the Young's modulus, there is no need to enlarge the RVE, and thus the mean value derived from this RVE can be taken as ''the'' effective Young's modulus of the aluminum-infiltrated roving [18].

The anisotropic properties of the aluminum-roving composite have been calculated for a fully infiltrated roving using the cross-sectional roving geometry (Figure 11.18) and the results are summarized in Table 11.1.

As to be expected, the Young's modulus in the longitudinal direction of the aluminum-infiltrated roving (z-direction) is significantly higher than the Young's moduli in the perpendicular directions. The difference between the Young's moduli in the different cross-sectional directions itself is not significant.

Since the aluminum infiltrated rovings constitute the structural components of the braided textile structure, which is itself embedded in an aluminum matrix, the calculated mechanical properties of the aluminum-infiltrated roving in combination with the properties of the embedding aluminum matrix were used in the mesoscopic

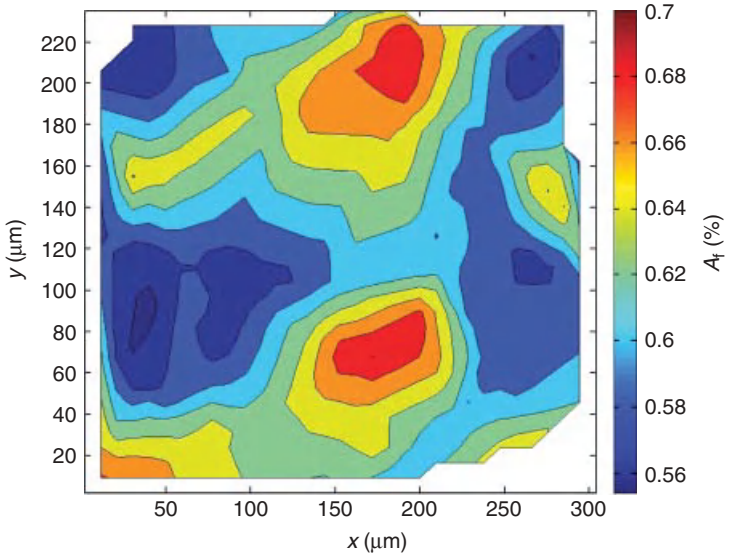

Figure 11.19 Distribution of filament fraction across the roving cross section.

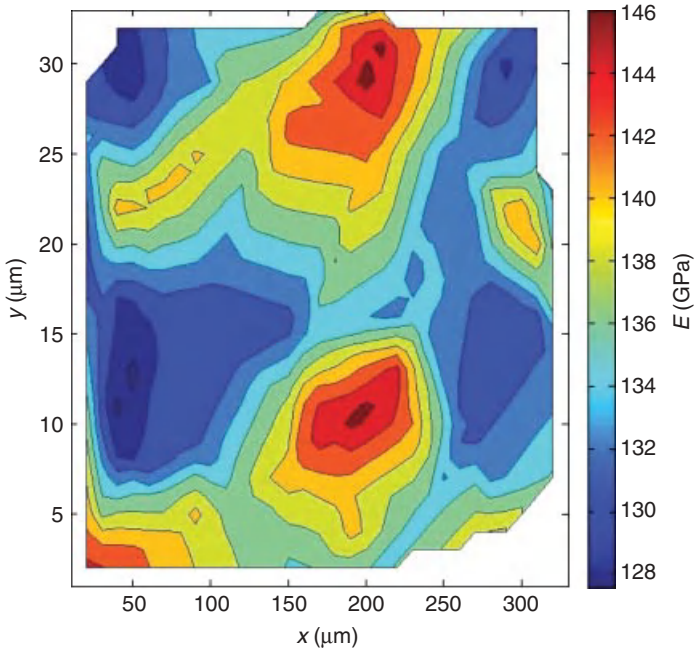

Figure 11.20 Distribution of effective Young's modulus over the roving cross section.

Table 11.1 Young's moduli of an infiltrated roving in different directions.

E_x	E_y	E_z
143.81 GPa	142.16 GPa	168.53 GPa

The *z*-direction corresponds to the longitudinal direction parallel to the individual fibers, while the *x*- and *y*-directions are perpendicular to the fiber.

level to calculate the effective mechanical behavior of the aluminum-infiltrated braid on the mesoscopic scale.

The geometry of the RVE on the *mesoscopic* level of the braided textile is defined by the periodic structure of the 3D braided textiles, which depends not only on the geometrical properties but also on the process parameters such as, for example, withdrawal speed. The size and geometry of the RVE on the "mesoscopic" level thus are defined by the period of the braid unit cells being simulated using the software WiseTex, as detailed in Section 11.3.3. Different unit cells revealing, for example, different orientations/braiding angles of the rovings were thus obtained (Figure 11.21).

The results of the asymptotic homogenization for the aluminum-infiltrated braids with different roving orientations are illustrated in Figure 11.22. The Young's moduli in the *x*- and *y*-directions obviously do not differ significantly as might be expected because the anisotropic characteristic of the roving material have

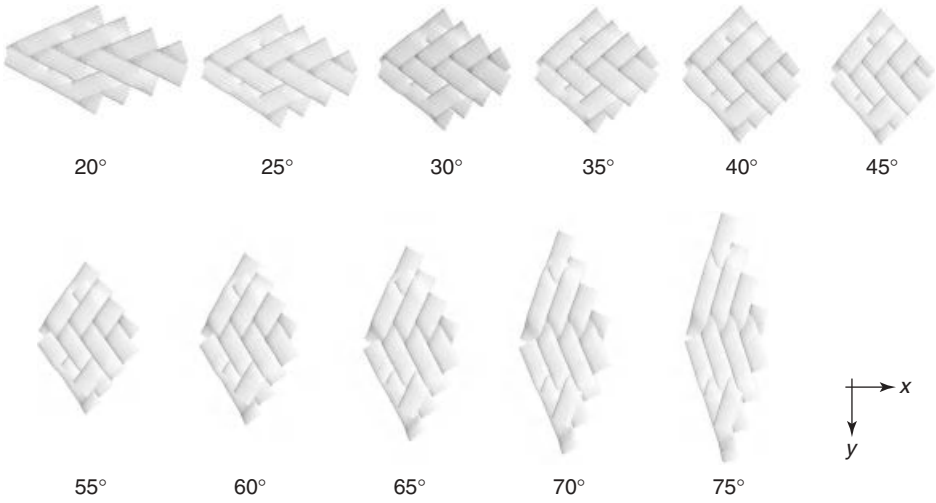

Figure 11.21 Unit cells of the braided textile with different roving orientations on the *x*–*y* plane. The braiding angle indicated below the pictures is defined as the angle between the withdrawal direction of the mandrel (here: the *x* direction) and the direction of the roving itself.

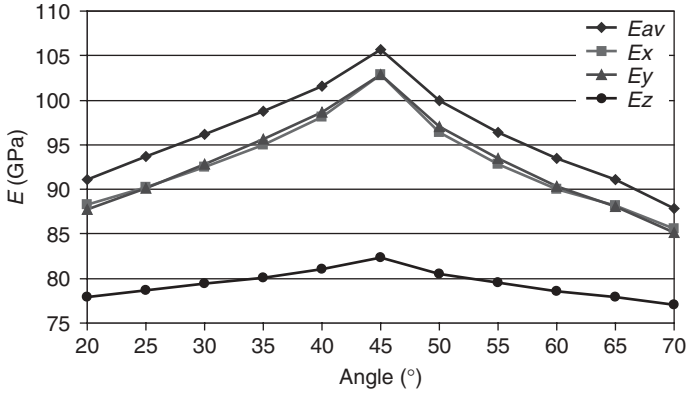

Figure 11.22 Young's moduli of different braids made from fully infiltrated rovings with respect to different roving orientations and braiding angles.

not been taken into consideration. Further, the Young's modulus in the z-direction is quite low in comparison to the x- and y-directions because the braid has only a small reinforcing effect on the load transfer in this particular direction. Remarkable is the variation of the Young's modulus with respect to different braiding angles. Since the braided rovings stick together most strongly for a braiding angle of 45°, the Young's modulus of this particular braid reveals a maximum as compared to other braid angles.

Depending on the process parameters, the infiltration process might lead to fully infiltrated rovings or only partial or even no infiltration might occur. In order to investigate the influence of different degrees of matrix infiltration on the mechanical properties of the braid, simulations with theoretical rovings being considered as aluminum-free (i.e., the spaces between the filaments being filled with air) were performed. The results of the Young's modulus are compared with the results of the simulations for fully infiltrated rovings in Figure 11.23.

The infiltration of the ceramic filaments with the softer matrix obviously reduces the stiffness of the overall material over the entire range of braiding angles. The difference between the Young's moduli of infiltrated versus noninfiltrated roving constituents reaches a maximum value of almost 45 GPa for a braiding angle of 45°.

11.3.7
Effective Properties of the Component

Feeding back micro- and mesoscopic anisotropic properties to the simulations on the process scale still remains an open task for future activities.

In particular, the anisotropic, effective permeabilities of the multilayer braid can be used to model fluid flow and melt infiltration at the process scale, where all detailed geometrical information is lost and the thickness of the braided structure corresponds to the size of just a few numerical cells.

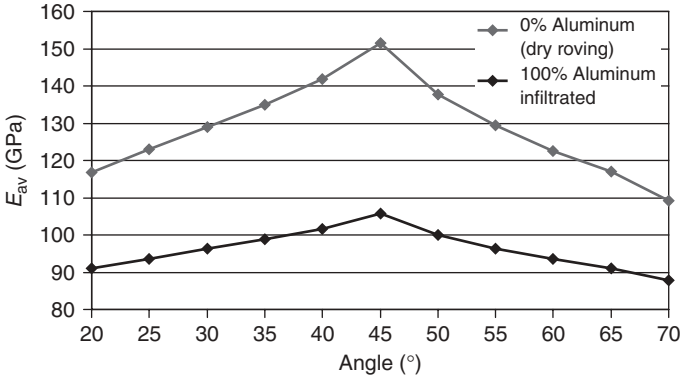

Figure 11.23 Average Young's moduli of different braids and braiding angles for (i) fully infiltrated and (ii) noninfiltrated roving materials.

In view of describing the mechanical properties of the entire component, the combination of the simulated distribution of braiding angles across the component surface with the knowledge about braiding-angle-dependent mechanical properties will be most beneficial. For this purpose, the full anisotropic properties of the infiltrated braid – as determined by the procedures outlined in this chapter – may be saved, for example, in an Abaqus materials file according to the platform standard, and then be made available for further detailed finite element method (FEM) analysis of the properties of the entire component.

11.4 Conclusion/Benefits

The major focus of this test case was the investigation of ''anisotropy'' in the context of the simulation platform and the determination of anisotropic materials properties using mathematical homogenization methods. In view of an apparent periodicity of textile structures, AHMs especially had a priori been envisaged for this purpose. Owing to the anisotropic properties and the complex production processes of textile-reinforced metals and components, material and process simulations are essential to manage this class of materials and products. A textile-reinforced aluminum piston rod thus was chosen to exploit the simulation tools and the results to some extent could be validated against experimental data available from another project. A particular challenge of this test case was the adaptation of the results of *several commercial* software tools to the standardized information exchange on the platform.

The test case scenario aimed at predicting the mechanical properties of a textile-reinforced piston rod as a function of the microstructure being described over several scales, starting at the individual infiltrated roving via the mesoscopic scale of the braid and eventually covering scale of the component.

By now, a concept model enabling the determination of the effective, anisotropic material properties has been developed and applied to evaluate differences in the materials properties for braids with different braiding angles. In the future, the anisotropic characteristics of the rovings must also be taken into consideration in the asymptotic calculations at the mesoscopic level in order to determine the effective properties of the braid precisely. For this purpose, individual materials properties will be assigned to each of the individual rovings in future. The mechanical properties of the textile-reenforced component vary over its body, for example, with respect to the different braiding angles and different infiltration grades of the braids. These local material properties can be evaluated by the methods outlined in this chapter and then become the input for finite element (FE) simulations aiming at the prediction of the anisotropic component behavior.

References

1. Kainer, K.U. (Hrsg.) (2006) *Metal Matrix Composites. Custom-Made Materials for Automotive and Aerospace Engineering*, 1. Auflage, Wiley-VCH Verlag GmbH, Weinheim.
2. Fachausschuß Feinguß im Verein Deutsche Gießerei-Fachleute e.V. (Hrsg.), (1964) Feinguß, Ausgabe, Düsseldorf 1964.
3. Kuckhoff, B., Stüve, J., Gries, T., Benke, S., and Schmitz, G.J. (2007) Simulation of textile reinforced cast parts, in *Proceedings Aachen Dresden International Textile Conference, Aachen, November 29–30, 2007* (ed. B. Küppers), DWI an der RWTH Aachen e.V., Aachen.
4. Kuckhoff, B. and Fettweis, D. (2009) AluTex – A new aluminum matrix composite featuring a braided 3D continuous fiber reinforcement ICAA11, in *11th International Conference on Aluminum Alloys, Aachen, 22–26 September, 2009, Mitteilungen des Institutes für Textiltechnik der Rheinisch-Westfälischen Technischen Hochschule Aachen*, Band **55/2008** (hrsg. T. Gries), Institut für Textiltechnik der RWTH Aachen, Aachen.
5. Stüve, J., Gries, T., and Tolosana Enrech, N. (2006) 3D-braided textile preforms: from virtual design to high-performance-braid. *Society for the Advancement of Material and Process Engineering (Hrsg.): SAMPE Fall Technical Conference: Global Advances in Materials and Process Engineering, Dallas, 06–09 November, 2006*, Society for the Advancement of Material and Process Engineering, Covina, CA.
6. Stüve, J.; Gries, T. (2009) Advances in the simulation of the overbraiding process using FEM In: Erath, Mark A. (Ed.): *Composites – innovative materials for smarter solutions : SEICO 09 ; SAMPE Europe 30th International Jubilee Conference and Forum ; March 23–25th 2009, Paris ; Proceedings 2009. – Riehen : SAMPE Europe Conferences, S.* 618–625.
7. *http://www.starcast.org*
8. Abaqus (2011) Analysis User's Manual 6.10, Dassault Systèmes Simulia Corp.
9. Lomov, S.V., Bernal, E., Koissin, V.E., and Peeters, T. (2006) Integrated Textile Preprocessor, WiseTex, Version 2.5, User's Guide, Leuven.
10. ANSYS, Inc. (2008) *TGrid Documentation 5.0*, ANSYS, Inc., Canonsburg, PA, *http://www.ansys.com/Products/Other+Products/TGrid* (accessed 18 May 2011).
11. The Microstructure Evolution Simulation Software (2011) User's Manual Release 5.3., Aachen, 2011, *http://www.micress.de* (accessed 18 May 2011).
12. ANSYS, Inc. (2006) *FLUENT Documentation 6.3*, ANSYS, Inc., Canonsburg, PA.
13. Schmitz, G.J., Böttger, B., Eiken, J., Apel, M., Viardin, A., Carré, A., and Laschet, G. (2011) Phase-field

based simulation of microstructure evolution in technical alloy grades. *Int. J. Adv. Eng. Sci. Appl. Math.*, doi: 10.1007/s12572-011-0026-y.

14. Trias, D., Costa, J., Turon, A., and Hurtado, J.E. (2006) Determination of the critical size of a statistical RVE for carbon reinforced polymers. *Acta Mater.*, **54** (13), 3471–3484.
15. Kanit, T., Forest, S., Galliet, I., Mounoury, V., and Jeulin, D. (2003) Determination of the size of the representative volume element for random composites: statistical and numerical approach. *Int. J. Solid Struct.*, **40**, 3647–3679.
16. Bobzin, K., Bagcivan, N., Kashko, T., Kuckhoff, B., and Gries, T. (2010) Advances on an integrative simulation chain of textile reinforced aluminum. Aachen Dresden International Textile Conference, ADITC-10.
17. Torquato, S. (2002) *Random Heterogeneous Materials: Microstructure and Macroscopic Properties*, Springer-Verlag, New York.
18. Bobzin, K., Bagcivan, N., Parkot, D., and Kashko, T. (2010) Calculation of the effective properties of textile reinforced aluminum alloy by two-step homogenization procedure. *Comput. Mater. Sci.*, **47** (3), 801–806.

12
Test Case Stainless Steel Bearing Housing

Stephan Freyberger, Stefan Benke, Hendrik Quade, and Jenny Rudnizki

12.1
Introduction

The permanently increasing complexity of products and their manufacturing processes combined with the demand for high-quality products with tight dimensional and material quality tolerances lead to the use of integrative simulation techniques in product and manufacturing design. Especially, high precision cast components have a dimensional tolerance in the range of a few millimeters and strict tolerances regarding the material properties. The stainless steel bearing housing treated in this chapter is such a highly precise manufactured component.

In general, any product is made in a series of production steps. Each production step in turn may influence the material properties being determined by the microstructure of the material and change the deformation state and the residual stresses of the product. A sound prediction of materials properties therefore is highly important. Such a prediction requires tracking of microstructure and properties evolution along the entire lifecycle of the component starting from a homogeneous, isotropic, and stress-free melt and eventually ending in failure under operational load.

Machine components made from highly alloyed austenitic stainless steels are manufactured by sand casting. During solidification from the liquid melt, the basic characteristics of the microstructure such as grain size and macrosegregation pattern are already defined. During the solidification process, because of varying cooling conditions and thermal shrinkage, residual stresses in the component start to build up, and its shape starts to change, that is, distortions of the original geometry as defined by the cast mold arise. After solidification and subsequent cooling down to room temperature, gating and feeder systems are removed and the cast component again deforms by the release of elastic energy of the residual stresses, which are partly released. In a second production step, the component is heat treated in a homogenization procedure at 1150 °C for 3 h followed by quenching in water. During this homogenization treatment, precipitates are partly dissolved and residual stresses vanish by inelastic creep processes. By quenching in a water bath, the component is then rapidly cooled down, freezing the homogenized

Integrative Computational Materials Engineering: Concepts and Applications of a Modular Simulation Platform,
First Edition. Edited by Georg J. Schmitz and Ulrich Prahl.

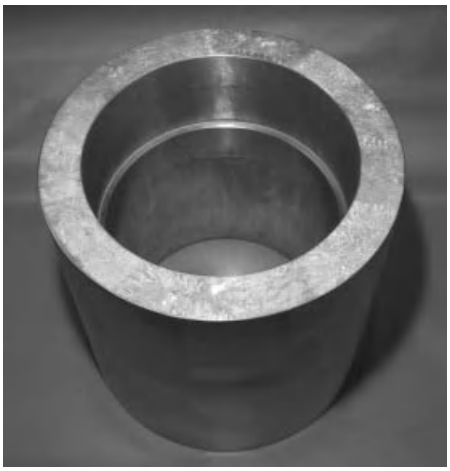

Figure 12.1 Bearing housing made from highly alloyed stainless steel.

microstructure. Locally varying cooling conditions result in locally varying thermal shrinkage, leading to residual stresses building up and further deformation of the component. The residual stresses easily exceed the elastic limit of the material and lead to large plastic deformations, especially in regions close to the outer surface of the component. In a final step of the manufacturing process, the component is machined by removing the cast oversize. The residual stresses are again relocated and decreased in value because of the release of elastic energy in the machined material. The removal of surface material, being primarily in a state of compression during machining, reduces the internal tensile stresses in the component. The majority of the newly exposed surface is still in compression, albeit with a reduced magnitude.

The lifetime behavior of the component is intrinsically determined by its alloy composition, microstructural features, and the presence and size of defects. Extrinsic factors such as residual stress and in-service loads also influence the lifetime behavior as the stress state in the material is a result of the cyclic service loads and residual stresses originating from manufacture.

The scope of this test case is the integrative simulation of the production process of a bearing house made from the high-alloyed austenitic stainless steel GX5CrNiMoNb19-11-2, as shown in Figure 12.1. The picture shows a pilot casting of the component being investigated. The pilot casting has a diameter of 450 mm, a height of 450 mm, and a wall thickness of 60 mm. In a small series, some of these components shrank on the bearing during operation, leading to its destruction. After a remachining process, the bearing housings did not reveal any further problems. The failure in operation cannot be explained as being due to quality problems in an isolated production step or by an inadequate mechanical layout.

The scope of this test case is to identify whether a combination of effects can explain the failures observed. The scientific hypothesis in this context is that effects in each process step, each being well within specification, in their combination lead

to the problem being described: microsegregations stemming from casting locally lower the stability of austenite. In combination with residual stresses from the heat-treatment process, redistributed by machining, the operational load leads to local transformation of austenite into martensite and a respective volume increase.

12.2 Materials

12.2.1 Overview

The cast component being produced is made out of the highly alloyed austenitic stainless steel 1.4581 or GX5CrNiMoNb19-11-2 with a nominal composition, as listed in Table 12.1.

Throughout the production process, the component is in contact with several other materials that must be considered in the numerical simulation in order to create appropriate boundary conditions for the simulation of the component. These materials comprise

- the molding material made of furane-bound silica sand;
- the steel chills in the casting process;
- water for quenching after the heat treatment.

12.2.2 Thermophysical Properties

Properties of GX5CrNiMoNb19-11-2 The properties of the material used in a macroscopic casting simulation are components of the database of the commercial simulation tool MAGMAsoft. These properties especially are the density, specific heat, heat of fusion, and the liquidus and solidus temperatures.

The relevant thermophysical material properties for the simulation of heat treatment are the specific heat and the density as a function of the temperature. Both are taken from the TCFe 6 database of Thermo-Calc. The relevant mechanical material parameter for the simulation of residual stresses and distortions are the Young's modulus and the stress–strain curves of the material as a function of the temperature. These parameters are taken from experimental tensile

Table 12.1 Nominal composition of the highly alloyed stainless steel GX5CrNiMoNB19-11-2.

C	Si	Mn	Cr	Ni	Mo	Nb	S	P
<0.06	<1.50	<1.50	18.00–20.00	10.50–12.50	2.00–2.50	$\geq 8 \times C \leq 1.00$	≤ 0.03	<0.045

tests performed at several temperatures on samples taken from the coarse grain area as well as from the fine grain regions of the pilot casting.

Properties Related to the Molding Material and to the Chills The properties of the molding materials and the chills are automatically set in the simulation tool used. This data is proprietary and therefore not discussed in detail here.

12.3 Processes

12.3.1 Overview of the Process Chain

The bearing housing's process chain comprises three steps before shipping it to the customer, as illustrated in Figure 12.2. Basic microstructural properties such as grain size and segregations originate from the solidification process. Throughout the 3-h heat treatment at 1150 °C, undesired precipitates such as the sigma phase are dissolved and the residual stresses stemming from solidification are released. Quenching the component in water after the heat treatment leads to new residual stresses. These residual stresses are partly released and redistributed during the machining of the component. Cyclic mechanical load during service is essentially concentrated in the bearing seat.

Lifecycle properties of the bearing housing thus are determined by each step of its production history. Therefore, lifecycle simulation vitally needs pieces of information from all steps in production.

12.3.2 The Casting Process

The first production step in the process chain is the pouring of the steel melt at 1500 °C into a furane-bound sand mold at ambient temperature. The filling time is about 20 s. During solidification, the initial microstructure with micro-

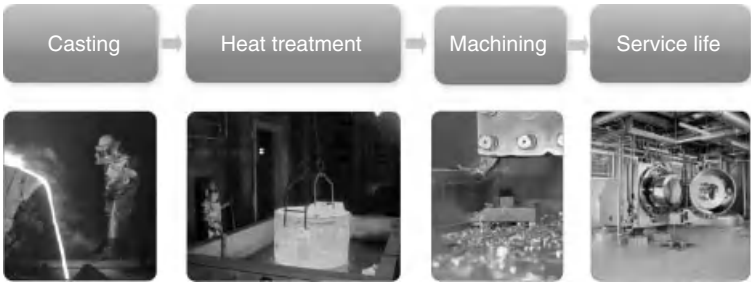

Figure 12.2 Production process chain of the high-precision machined cast component.

Figure 12.3 Immersion of the quarter model into the water bath: symmetry surfaces and surfaces covered by air are light gray, immersed surfaces are dark gray.

and macrosegregations is formed. After solidification and during further cooling, the cast component shrinks and exhibits inner tensions, eventually leading to distortion buildup.

After removing the part from the sand mold, the casting system and the feeders are removed. At this stage, the microstructure exhibits undesired precipitates such as the sigma phase due to slow cooling as a result of the sand casting process. Austenitic steel grades are therefore usually heat treated after casting.

12.3.3 The Heat Treatment Process

In the second step of the production process, the cast component is reheated to a temperature of 1150 °C in order to generate a homogeneous austenitic microstructure comprising some delta ferrite. The component is tempered for a period of 3 h. During this tempering procedure, the residual stresses, originating from solidification, are mostly released by time-dependent creep processes. On the microscale, some minor grain growth may take place and most dislocations anneal. Owing to the compact shape and the considerable wall thickness, newly introduced distortions are negligible.

Quenching of the component is realized by immersing it into a water bath, as shown in Figure 12.3. During the transport from the heat treatment furnace to the water bath, heat dissipation is determined by diffuse radiation. The heat extraction due to convection and advection in the water bath is determined by an effective heat extraction rate being a function of the local surface temperature of the component. This heat extraction rate takes into account the occurrence of boiling effects, leading to a change in the heat transfer coefficient. During this step, new residual stresses build up because of large temperature gradients in the component.

12.3.4 The Machining Process

After the heat treatment and the quenching procedure, the component is machined on a turntable. On each turn, an amount of material is removed from the casting, leading to a change in mechanical properties of the surface and the overall stress state. As the component is large compared to the amount of material removed during one turn, the influence of a change in surface properties on the overall

properties is negligibly small. Thus, the influence of the tool on the component is currently neglected and only the removal of the stressed material volume is taken into account.

12.3.5 The Application

During its application, the bearing housing experiences a cyclic load, imposed by a rotating mass. In the beginning of their service life, some cast components showed shrinkage, rendering the bearings defective. The phenomenon could neither be tracked to overload nor to inaccurate machining. After remachining, the components could be used without any more problems.

For confidentiality reasons, no detailed information on the actual load situation during the application is available. For that reason, the production conditions under which the scientific hypothesis can be proved are explored, leaving the final assessment to the industrial partner.

12.4 Phenomena

12.4.1 Overview of Phenomena to Be Modeled

The scientific hypothesis for this test case is that effects in each process step, each of them being well within specification, in their combination may lead to the failure of the system. Microsegregations stemming from casting locally lower the austenite stability. In combination with residual stresses from the heat treatment process, redistributed by machining, the load in service leads to local transformation of austenite into martensite along with a volume increase. Figure 12.4 gives an overview of the phenomena to be modeled on both the micro- and the macroscale.

12.4.2 Description of the Individual Phenomena

Macrosimulation of Casting Simulation of the process chain starts with simulation of mold filling. This simulation is performed with MAGMAsoft [1]. Prediction of time-dependent temperature, cooling rate, temperature gradient, and local chemical composition in the cast component, as well as microstructural characteristics such as grain size, the amount of delta ferrite, and macrosegregation of the species are of primary interest in this first simulation step. This information determines the component's microstructure and the corresponding mechanical properties for the next two simulation steps of heat treatment and machining. The residual stresses induced by solidification and subsequent cooling to room temperature are of minor interest in the solidification step as they are entirely released during the heat treatment.

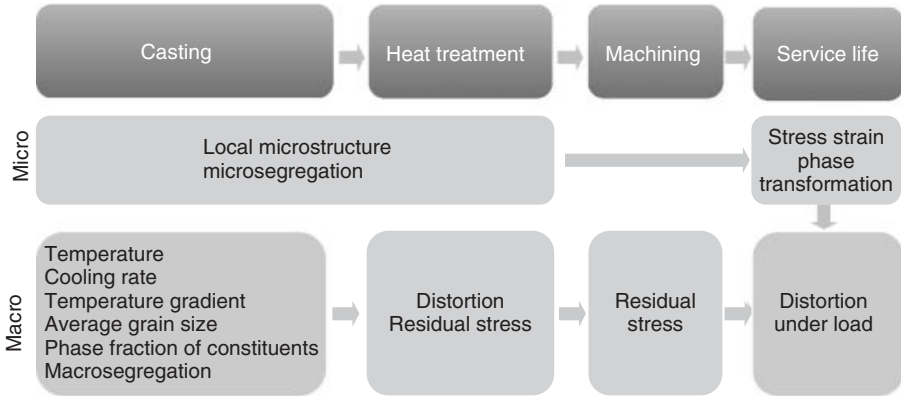

Figure 12.4 Overview of the phenomena to be modeled in the test case stainless steel bearing housing.

The calculation of the macrosegregation pattern is based on the material data of the likewise austenitic steel GX5CrNiMo18-12, which lacks the carbide-former niobium. An exactly fitting data set is not yet available. Results should nevertheless be comparable to GX5CrNiMoNb19-11-2, which exhibits a niobium content of about 0.6 wt%, depending on carbon content. A description of the underlying model can be found in Schneider, M.C. *et al.* [9]

The calculation domain consists of five million finite difference cells with about 690 000 cells in the actual cast component. The casting setup to be numerically simulated is shown in Figure 12.5.

Figure 12.5 Calculation domain consisting of the actual casting, the feeders, the runner system, the chills, and the mold. Mold and FDM cell structure are omitted for clarity reasons.

The casting temperature was set to 1500 °C. Filling time of the mold was set to 20 s. Both values correspond to the known industrial process parameters.

Microsimulation of Casting Microsegregation of chromium in austenite grains leads to locally different stability of this phase at room temperature. With mechanical load exceeding a certain critical limit, martensite is formed depending on the local chromium content. This transition goes along with an increase in volume leading to elastoplastic strain.

Microstructural properties are strongly correlated to the local cooling rate. This local cooling rate at certain areas of interest, calculated by macrocode, is transferred to a microsimulation tool as a boundary condition.

Simulations are performed in a 250 × 400 μm^2 calculation domain, with the alloying elements considered intentionally limited to C, Cr, Mn, Mo, Nb, and Ni.

Simulation of Heat Treatment The mechanical material behavior for the heat treatment and machining simulation depends on the grain size resulting from casting simulation.

The heat extraction during the transport from the heat treatment furnace to the water bath is modeled as diffuse radiation. The heat extraction from the immersed surface of the component is modeled using an effective heat transfer coefficient, which includes steam at high temperatures, the boiling state between 400 and 200 °C, and convection coding below 100 °C at the surface of the component [2].

Since the mechanical properties of metals largely depend on grain size, this effect is taken into account during the simulation of heat treatment. The calculation of the grain size is based on the solidification time provided by MAGMAsoft

$$d_{\text{Grain}} = a t_{\text{S}}^{n} \tag{12.1}$$

where a and n are material-dependent parameters and t_{S} is the solidification time. Both parameters a and n have been fitted according to the grain size measurements.

Using this calculated grain size, the local stress–strain curves are interpolated between the values measured by compression tests at various temperatures on samples taken from the fine and large grain areas.

The number of constituents and the phase fractions in equilibrium state at 1150 °C are calculated by Thermo-Calc.

Simulation of Machining The simulation of machining is modeled by the stepwise removal of the material starting at the outer surface of the cast component, similar to the real machining process. For each time step, the new static mechanical equilibrium of the remaining material volume is calculated. The influence of the tool on the component is neglected. This assumption seems reasonable as the material region being influenced by the tool is located within a thin layer near the surface of the component and is small compared to the total cross section of the component. For the same reason, simulations on the microscale in this step are not mandatory.

Microsimulation of Application The expected microsimulation results for this process step are local stress–strain curves depending on the local composition for areas of interest in the component where an austenite–martensite transformation is anticipated.

The model presented here is based on the work of Sierra and Nemes, who assumed that martensitic nuclei emerge at shear-band intersections consisting of epsilon martensite [3]. The *plastic strain rate* is defined as the sum of the plastic strain rate that is induced by slip deformation in austenite and martensite and the transformation strain that is induced by phase transformation. The overall plastic strain rate tensor is thus given by the following expression:

$$\dot{\varepsilon}_{ij}^{\mathrm{p}} = \dot{\varepsilon}_{ij}^{\mathrm{pslip}} + \dot{\varepsilon}_{ij}^{\mathrm{ptrans}} = \dot{\varepsilon}_{ij}^{\mathrm{pslip}} + \dot{\varepsilon}_{ij}^{\mathrm{pshape}} + \dot{\varepsilon}_{ij}^{\mathrm{pdilat}} \tag{12.2}$$

where the slip deformation plastic strain rate tensor is given by

$$\dot{\varepsilon}_{ij}^{\mathrm{pslip}} = \dot{\overline{\varepsilon}}^{\mathrm{pslip}} \frac{\partial F}{\partial \sigma_{ij}} \tag{12.3}$$

with the equivalent plastic strain rate induced by slip deformation $\dot{\overline{\varepsilon}}^{\mathrm{pslip}}$ and the yield condition $F = \overline{\sigma} - \overline{\sigma}_{\mathrm{am}}$, where $\overline{\sigma} = \sqrt{3J_2}$ is the equivalent von Mises stress and $\overline{\sigma}_{\mathrm{am}}$ is the effective stress of the austenite–martensite constituent. The shape change plastic strain rate tensor is defined as follows:

$$\dot{\varepsilon}_{ij}^{\mathrm{pshape}} = R\dot{f}^{\mathrm{m}} \frac{\partial F}{\partial \sigma_{ij}} \tag{12.4}$$

with the magnitude of shape change

$$R = R_0 + R_1 \left(\frac{\overline{\sigma}}{\sigma_{\mathrm{ya}}} \right) \tag{12.5}$$

and the yield stress of the parent austenitic phase σ_{ya}. The increase in martensite volume fraction $\dot{f}^{\mathrm{m}}$ is determined by plastic strain in the austenite and is written in the following form:

$$\dot{f}^{\mathrm{m}} = A\left(1 - f^{\mathrm{m}}\right) \dot{\overline{\varepsilon}}_{\mathrm{a}}^{\mathrm{pslip}} \tag{12.6}$$

with the equivalent plastic strain rate in austenite because of slip deformation $\dot{\overline{\varepsilon}}_{\mathrm{a}}^{\mathrm{pslip}}$, and A being defined as follows:

$$A = \alpha\eta \left(f^{\mathrm{sb}}\right)^{n-1} \left(1 - f^{\mathrm{sb}}\right) \tag{12.7}$$

with the volume fraction of shear bands f^{sb} and the hardening exponent n. α is a temperature-dependent coefficient and η, the driving force for martensite formation. Finally, the dilatational plastic strain rate tensor is expressed by

$$\dot{\varepsilon}_{ij}^{\mathrm{pdilat}} = \frac{1}{3}\Delta\upsilon\dot{f}^{\mathrm{m}}\delta_{ij} \tag{12.8}$$

where $\Delta\upsilon$ accounts for the volume change and is in a range between 0.02 and 0.05 and δ_{ij} is the well-known Kronecker delta. By substituting Eqs. (12.3), (12.4), and

(12.8) into Eq. (12.2), the plastic strain rate tensor can be expressed in a simplified form

$$\dot{\varepsilon}_{ij}^{\mathrm{p}} = \frac{\partial F}{\partial \sigma_{ij}} \dot{\bar{\varepsilon}}^{\mathrm{p}} + s_{ij} \Delta \upsilon \dot{f}^{\mathrm{m}} \tag{12.9}$$

with

$$s_{ij} = -\frac{\partial F}{\partial \sigma_{ij}} \Sigma + \frac{\delta_{ij}}{3}$$

and the equivalent plastic strain rate

$$\dot{\bar{\varepsilon}}^{\mathrm{p}} = \dot{\bar{\varepsilon}}^{\mathrm{pslip}} + R\dot{f}^{\mathrm{m}} + \Sigma \Delta \upsilon \dot{f}^{\mathrm{m}}$$

The effective stress of the M/A constituent is calculated by using a rule of mixture which assumes the same effective plastic strain in austenite and martensite. Eventually, the constitutive law describing the behavior of the effective material is given by

$$\dot{\sigma}_{ij} = D_{ijkl}^{\mathrm{e}} \dot{\varepsilon}_{kl} - P_{ij} \dot{\bar{\varepsilon}}^{\mathrm{p}} - Q_{ij} \Delta \upsilon \dot{f}^{\mathrm{m}} \tag{12.10}$$

with

$$P_{ij} = \frac{E}{1+\upsilon} \frac{\partial F}{\partial \sigma_{ij}}$$

and

$$Q_{ij} = -P_{ij} \Sigma + \frac{1}{3} \delta_{ij} \frac{E}{1-2\upsilon}$$

$\dot{\sigma}_{ij}$ is the rate of Cauchy stress, D_{ijkl}^{e} is the elastic stiffness tensor, E is the Young's modulus, and ν is the Poisson's ratio.

In order to be able to simulate the microstructural influence on phase transformation under mechanical load with nonconserved volume and thus going along with distortions, experimental microstructures from etched samples were used as initial conditions for the simulation (Figure 12.6). Different cooling rates lead to differences in grain size and fraction of delta ferrite.

Macrosimulation of Application The simulation of the cyclic load in the service life of the steel component was carried out with Abaqus®. The necessary material

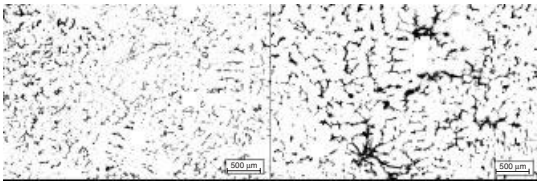

Figure 12.6 Microstructure of two samples. Sample GKM, representing an area of medium cooling rate, on the left corresponds to faster cooling as compared to sample GZI, representing an area of slow cooling on the right. White is the austenite phase, black represents the delta ferrite phase.

parameters are taken from microsimulations in the form of homogenized flow curves being derived from virtual tests. The problem was simplified to a point load representing the ball bearing's load on the component.

12.5 Simulation Chain

12.5.1 Simulation Tools

The simulation tools used in the test case stainless steel bearing housing are represented in Figure 12.7. All are commercially available, and except for MAGMAsoft, all have been integrated in the Aachen (Aix) Virtual Platform for Material Processing (AixViPMaP).

12.5.2 Simulation Flowchart

An overview of the simulation flow is given in Figure 12.8. Calculations start on macroscale with MAGMAsoft on a finite difference method (FDM) mesh, referred to as "*Mesh_A*." As mentioned, the package is not integrated into the AixViPMaP platform as it cannot run in a batch mode on the grid. The resulting information is mapped from the FD Mesh_A onto an Abaqus-compatible tetrahedron mesh by MAGMAsoft. The exported results are then converted to the platform-compatible

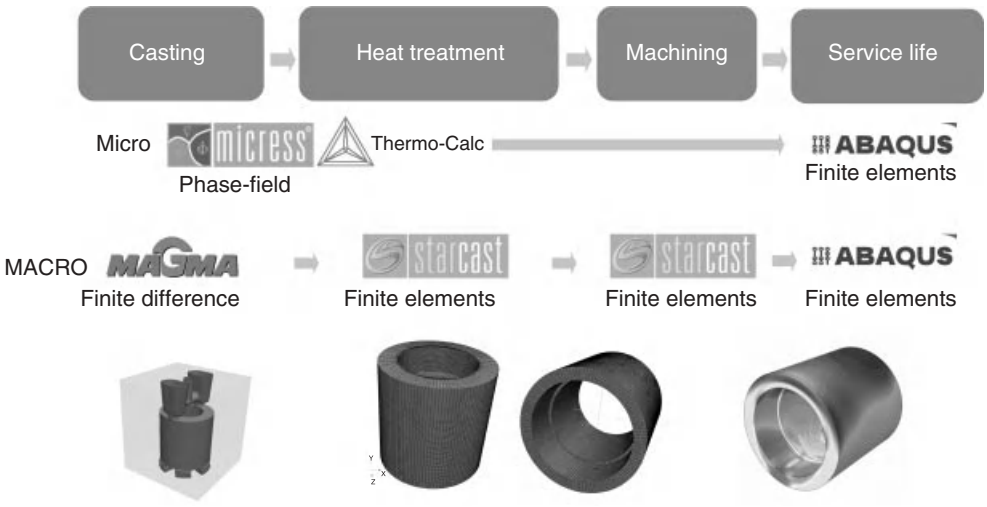

Figure 12.7 Simulation tools used in the testcase stainless steel bearing housing.

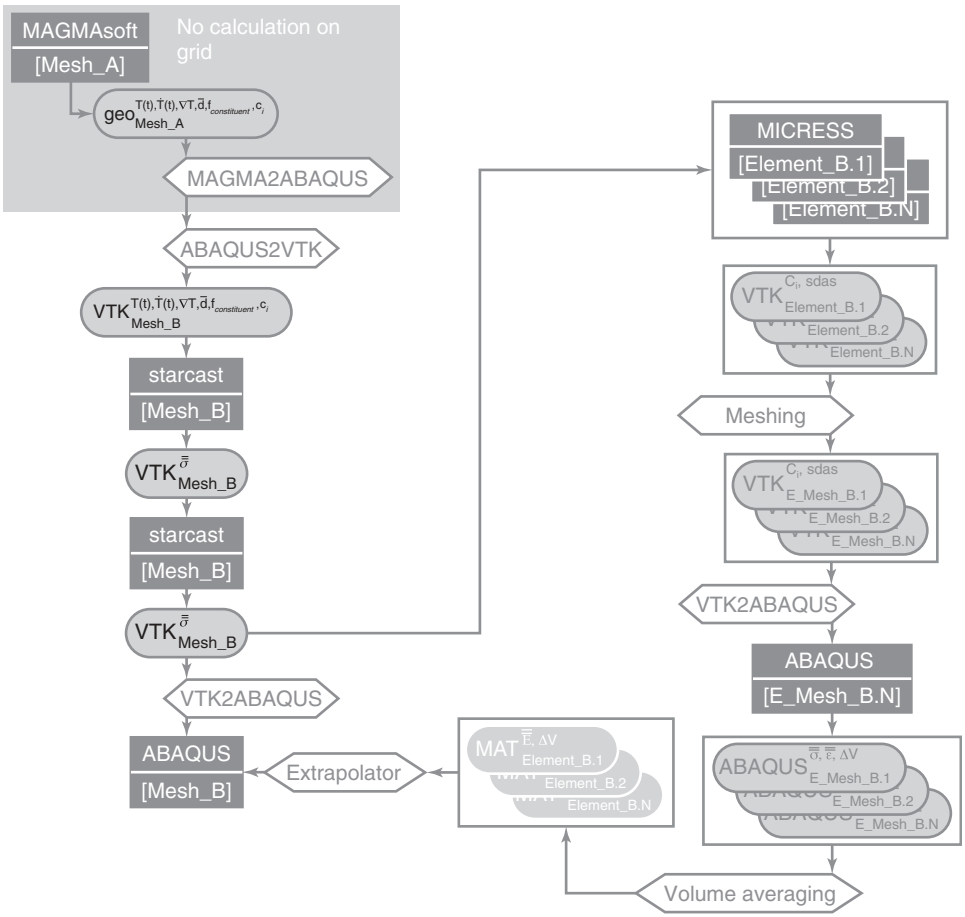

Figure 12.8 Simulation flowchart of the testcase stainless steel bearing housing. Improved coupling between micro- and macrocode is still in progress.

Visualization Tool Kit (VTK) file and are in turn mapped on a hexahedral finite elements (FE) Mesh_B used for the simulation of the heat treatment and machining operations. After this step, the areas of interest in the component are selected and the time–temperature history is passed to MICRESS as a thermal boundary condition. After calculation of the microstructure and microsegregations, the FDM cells of MICRESS are meshed and transferred to Abaqus for microsimulations, generating flow curves and information about the transformed fraction of austenite by volume averaging. This information serves as parameters for the distortion simulation along with the information of the macrobranch in the flowchart.

12.6
Results

12.6.1
Macroscopic Process Simulations

Casting Some results of the macrosegregation calculations are shown in Figures 12.9 and 12.10. Energy-dispersive X-ray spectroscopy (EDX)-spot composition analytics on sample castings from production are in quantitative agreement with simulation findings for silicon, chromium, and manganese. Nickel and molybdenum content, in contrast, are not well predicted. This is most probably due to the missing niobium in the dataset being used. Liquid diffusion of nickel and molybdenum are presumably different in the absence of niobium.

The average cooling rate during solidification determines the grain size. As to be expected, short solidification times are observed close to the chills, as displayed in Figure 12.11. Already in short distance from the chills, the solidification time strongly increases. The slowest solidification leading to the largest grains is observed in the inner region of the casting.

Three main results from macrocasting simulation are passed on to subsequent simulation processes. These are the austenite grain size (Figure 12.12), fraction of delta ferrite (Figure 12.13), and local cooling conditions. These three parameters represent the major influence on local mechanical properties during the subsequent production steps and in service life. In addition, temperature–time profiles are conveyed to microsimulation tools for selected areas.

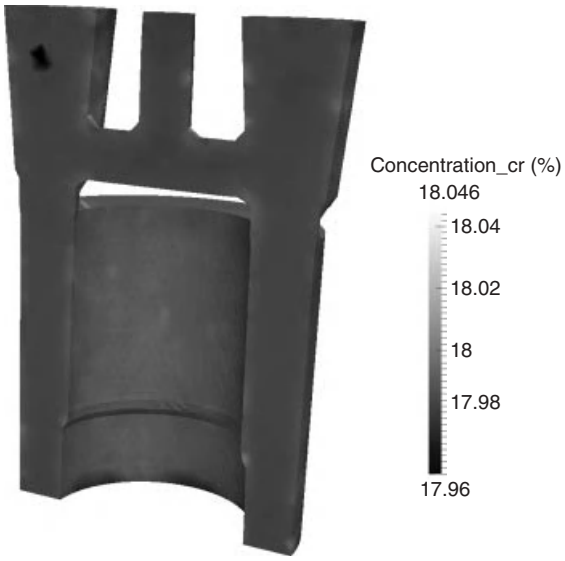

Figure 12.9 Macrosegregation of chromium.

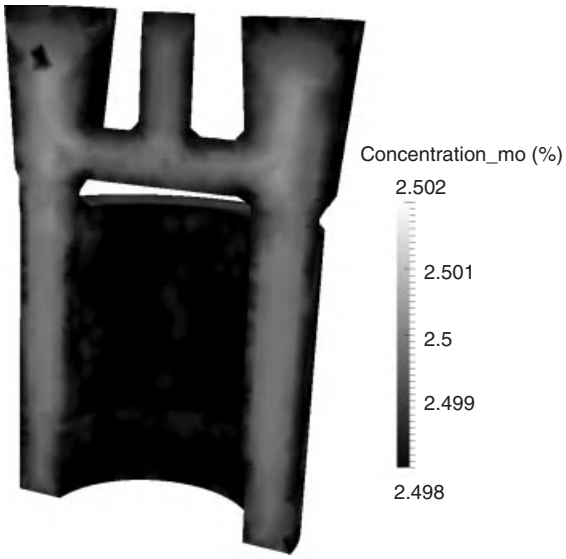

Figure 12.10 Macrosegregation of molybdenum.

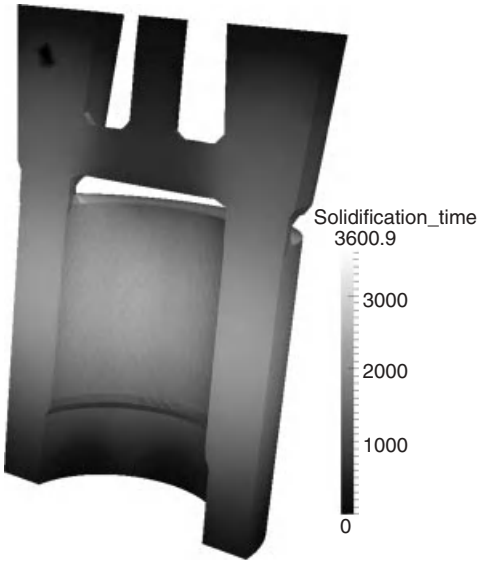

Figure 12.11 Local solidification time in seconds.

Heat Treatment After the heat treatment at 1150 °C for 3 h, the component is quenched in water resulting in formation of stresses and distortion. Evolution of the temperature and, therefore, the formation of the residual stresses can be split into three stages (Figure 12.14). In the first stage, the outer jacket of the component cools down, shrinks, and builds up tensional stresses. These

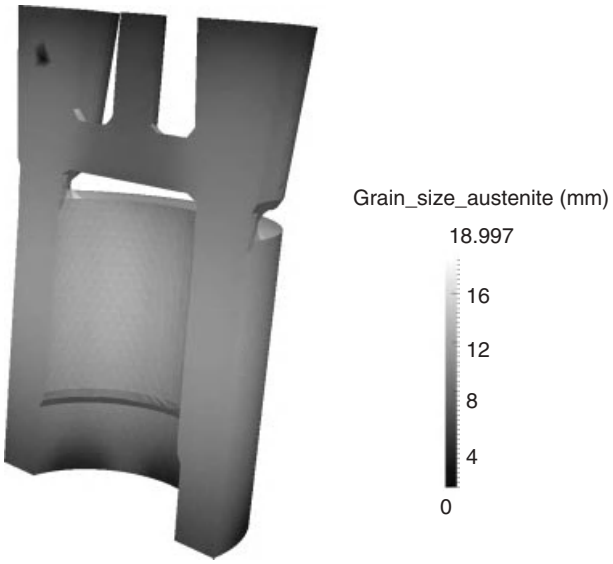

Figure 12.12 Austenite grain size in millimeters.

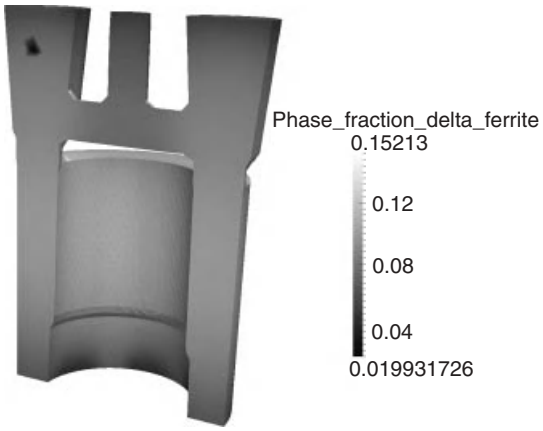

Figure 12.13 Phase fraction of delta ferrite.

stresses exceed the elastic limit of the material and thus lead to local plastic stretching of the outer jacket. Stresses and the inelastic deformation increase until the temperature difference between the center and the outer region reaches its maximum. In the second stage of the quenching procedure, the inner region starts to cool down and the temperature difference between the center and the outer surface becomes smaller. The residual stresses decrease and at some point reach their minimum. In the third stage, the center region cools down further and shrinks. The outer region, being inelastically stretched in the first phase, now gets compressed. This leads to tensile stresses in the center region

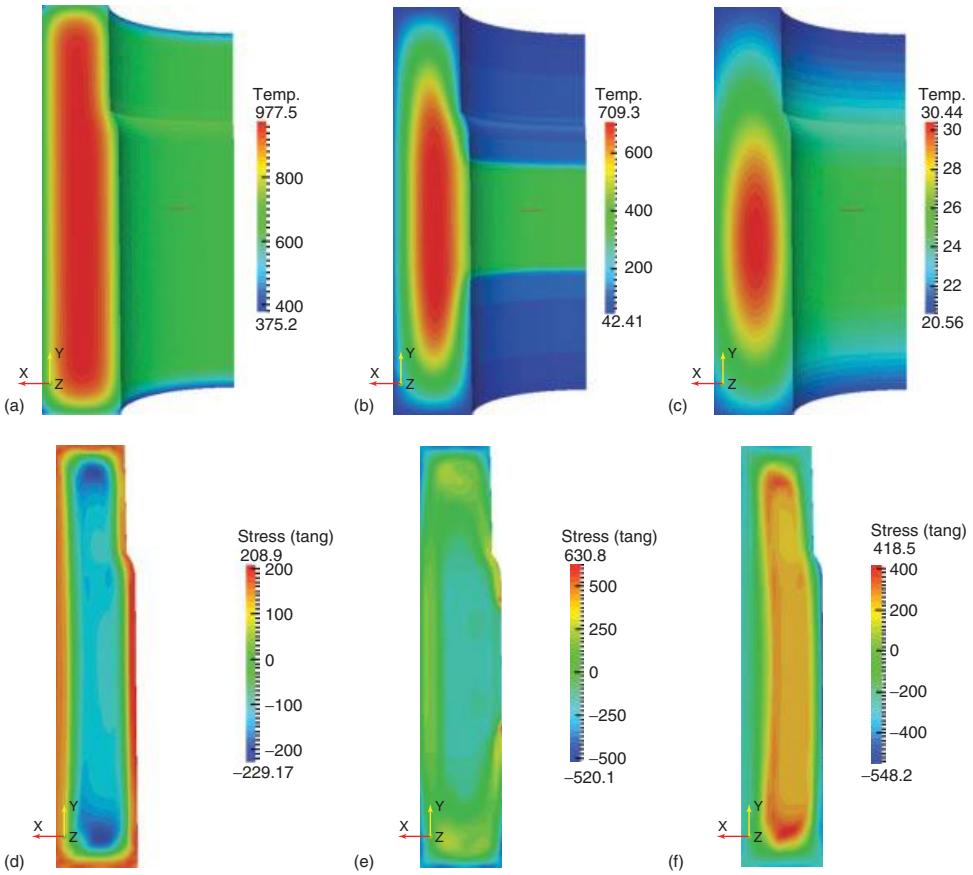

Figure 12.14 Stages of the temperature evolution during the quenching process (°C) (a–c) and stages of the evolution of the hoop stresses during the quenching process (MPa) (d–f).

of the component and compressive stresses in the outer jacket. Thus, a change in the sign of the residual stresses as compared to the first stage of cooling takes place. At the end of the quenching process, the residual stresses reach a maximum. The predicted residual stress distribution in the bearing house after the quenching operation is compressive over most of the surface with balancing tensile stresses occurring in the center region, as shown in Figure 12.14. The highest compressive residual stresses exist at the edges of the cross-section and the highest balancing tensile stresses occur in the center section because of the thermal gradients and the corresponding plastic strains in these sections during the quenching.

A full coupling was realized between the heat treatment simulation and the machining step by exchanging all mechanical results.

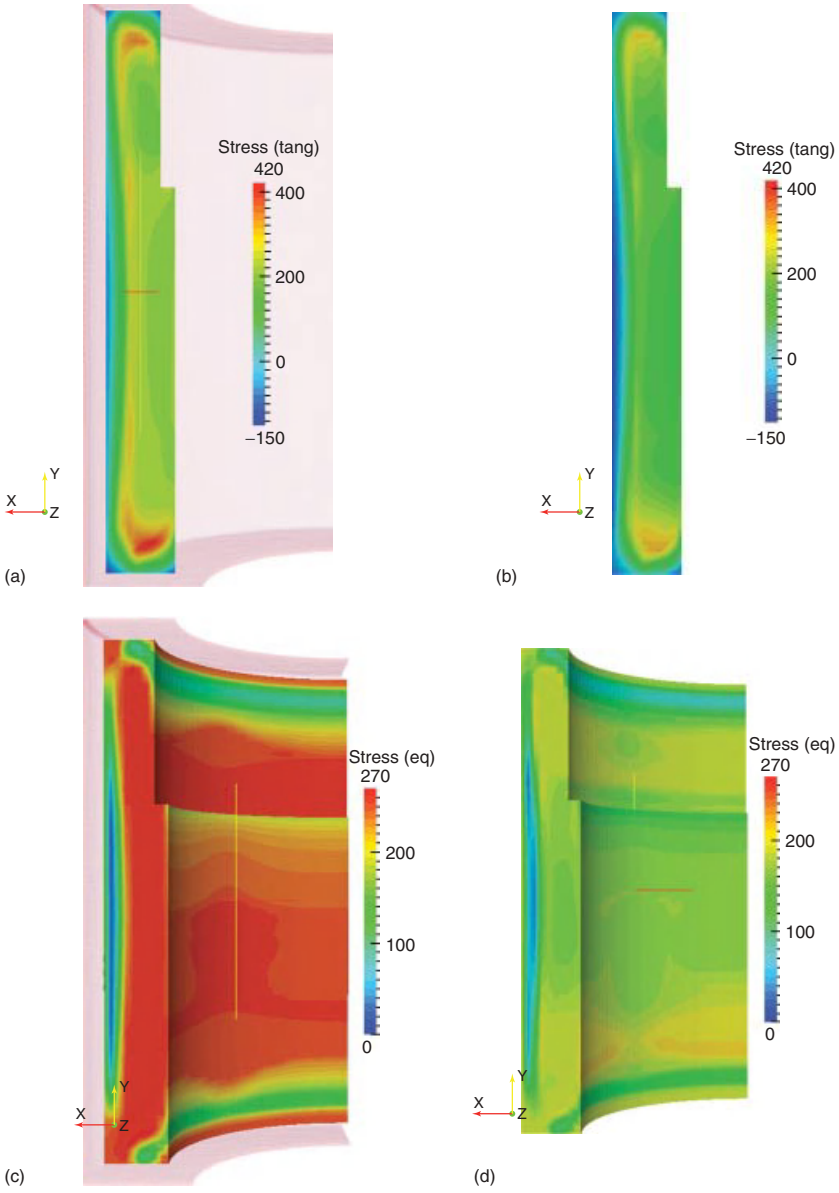

Figure 12.15 Hoop stresses (MPa) in the cross section (a) before and (b) after machining and equivalent stresses (MPa) in the component (c) before, and (d) after machining.

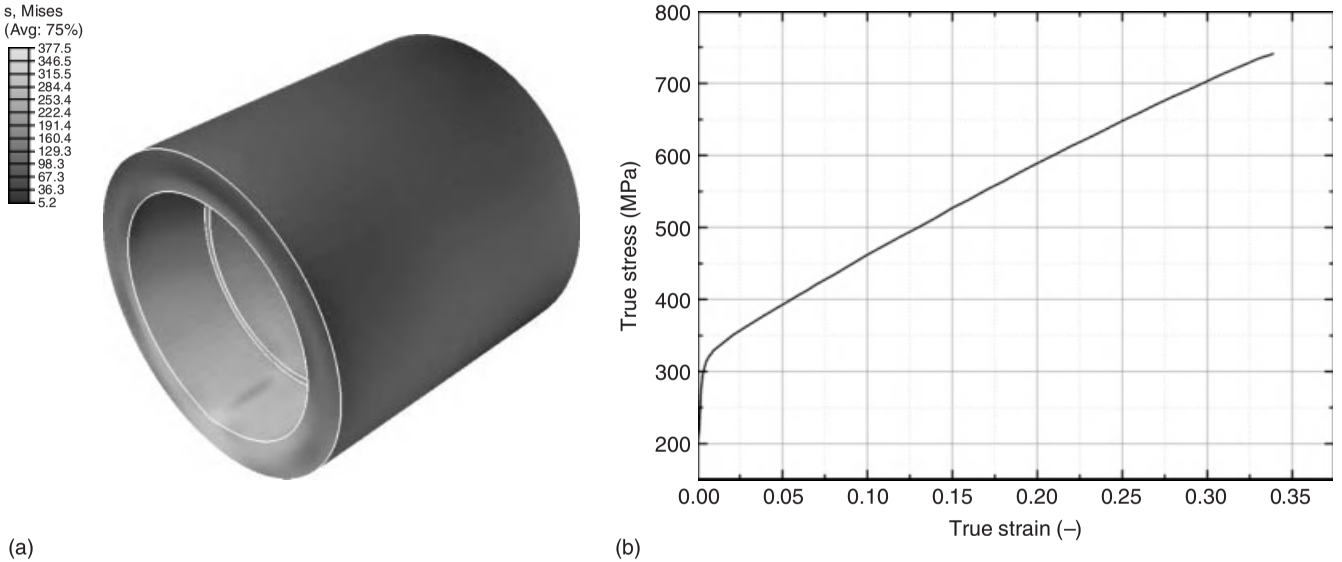

Figure 12.16 Locally increased stress in the component due to Hertzian stress during application (a) and homogenized flow curve from microstructural calculations (b).

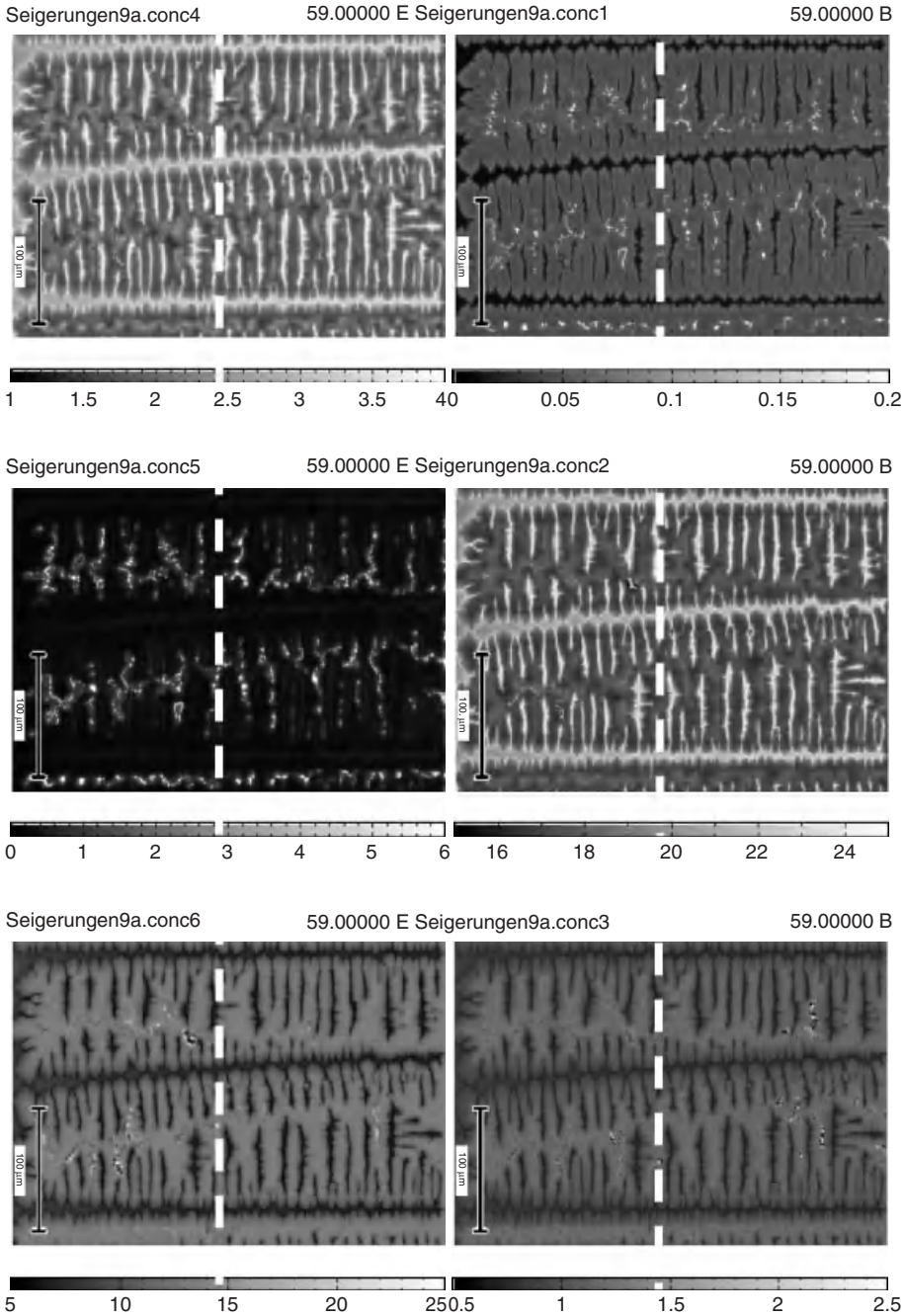

Figure 12.17 Concentration distribution of C, Cr, Mn, Mo, Nb, and Ni (from top left to bottom right).

Machining Machining was modeled by removal of surface material, which is at first in a state of compression. In this process step, the internal tensile stresses are reduced by 10–20%. The majority of the newly exposed surface is still in compression (Figure 12.15), albeit with a reduced magnitude. Experimental verification of the simulated thermomechanical data was carried out by destructive testing. Results show a very good qualitative agreement. Quantitative mismatch of about 40% between numerical and experimental data is probably due to numerical reasons and inaccuracy in material data for the heat treatment [4].

Application The macroscopic simulation of the working load was performed with the finite element program Abaqus. As materials description, the homogenized flow curve resulting from microstructure simulations was used (Figure 12.16).

12.6.2 Microstructures

Casting Delta ferrite is the first crystal modification to solidify from the melt in this peritectic-type solidification process. At lower temperatures, austenite forms on the delta ferrite (Figures 12.17 and 12.18). The simulation was carried out down to a temperature of 1090 °C corresponding to the heat treatment parameters. Coming from the liquid phase, there is a liquid fraction of 0.2% because of a high carbon and niobium content caused by microsegregation. On this basis, the niobiumcarbide content in this interdendritic area was calculated to 0.018 wt% by using Thermo-Calc.

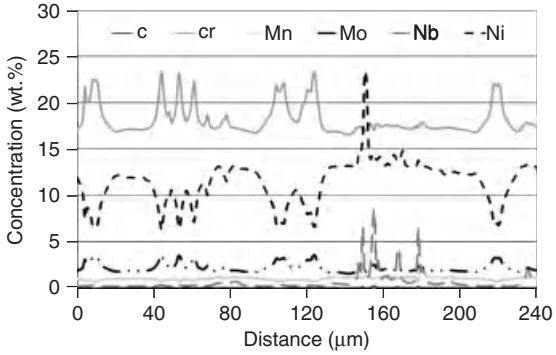

Figure 12.18 Concentration of C, Cr, Mn, Mo, Nb, and Ni along the dashed line through the center of the simulated domain.

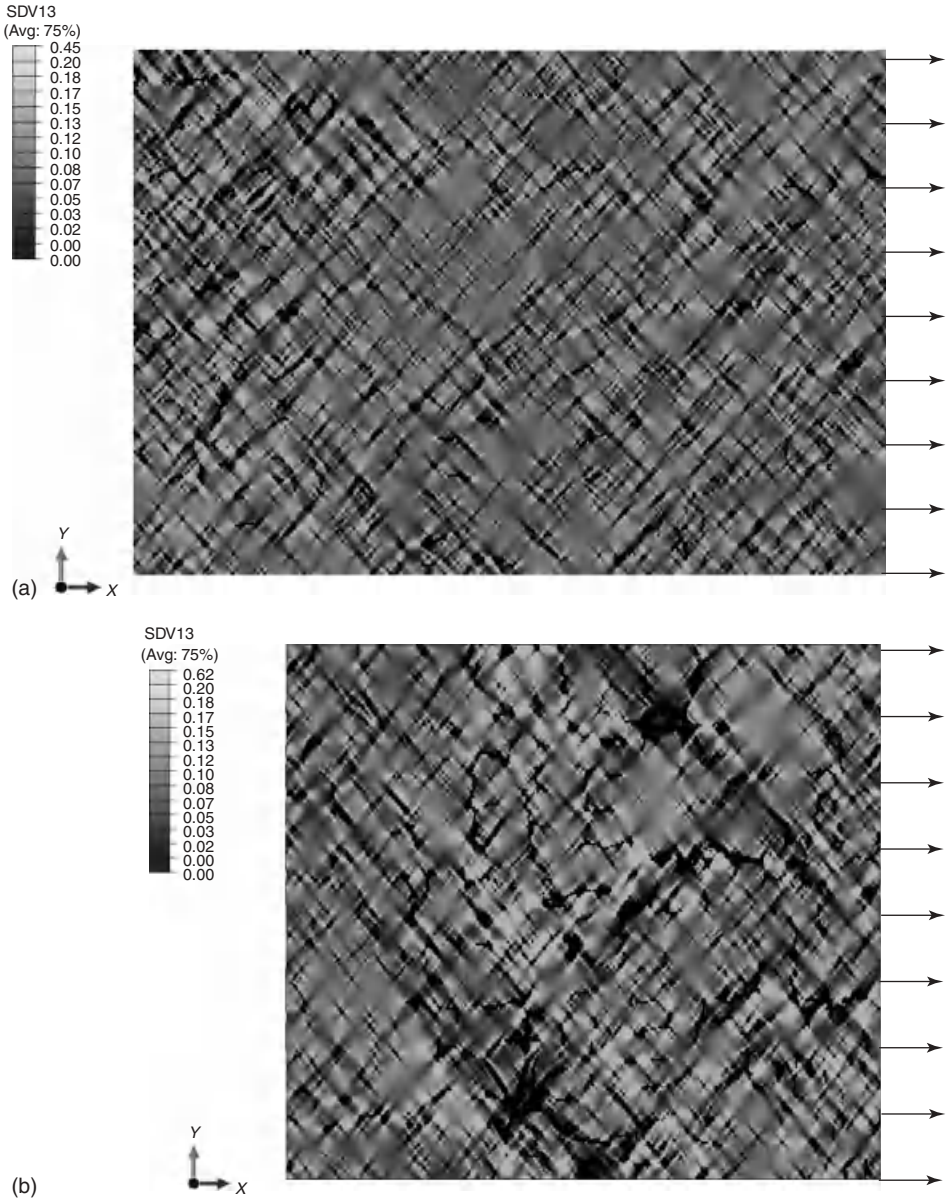

Figure 12.19 Martensite volume fraction in the microstructure GKM (a) and GZI (b) after 2.5% deformation in the *x*-direction (light gray: martensite, dark gray: austenite, and white: delta ferrite).

Application The simulation of stress imposed on the microstructure leads to partial transformation of austenite into martensite depending on the initial morphology, as shown in Figure 12.19. It occurs preferentially in close vicinity to these areas. The phenomenon can be explained by the concentration of stress close to areas with delta ferrite. The effect is even amplified by the volume increase due to the transformation. Figure 12.20 gives a good example of the stress concentration and its dependence on delta ferrite fraction.

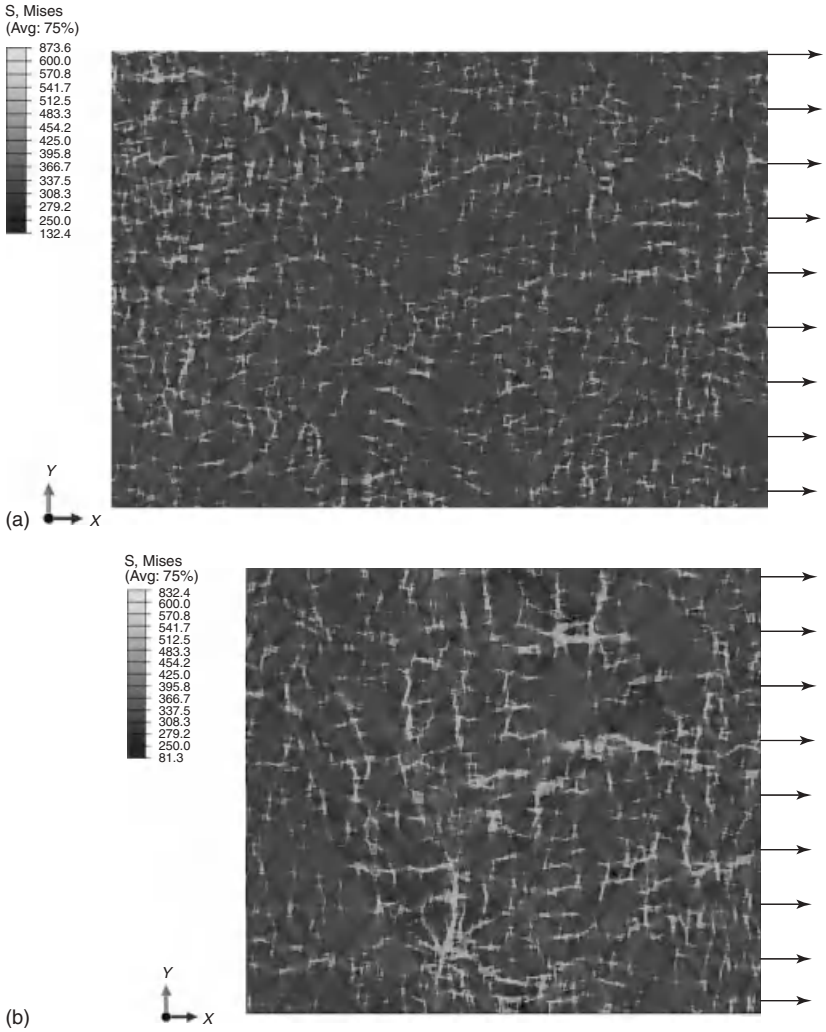

Figure 12.20 Equivalent stress according to von Mises in the microstructure GKM (a) and GZI (b) after 2.5% deformation in *x*-direction.

The microstructure on the left represents a sample taken from a component with a faster solidification and therefore a lower delta ferrite content than the one on the right side.

12.7 Conclusions/Benefits

The methodology of the open integrative scale-bridging process modeling platform AixViPMaP described in this book was applied to a bearing housing cast from the austenitic stainless steel grade GX5CrNiMoNb19-11-2. Microstructural parameters and the distribution of inner tensions after the production process were determined and the evolution of inner tensions and distortion throughout production, and service up to failure were predicted.

The findings comprise the development of microstructure, residual stress, and distortion in each production step and reveal the influence on mechanically induced local martensite formation under service load. Verification of the simulated thermomechanical data was carried out by destructive testing. Results show a very good qualitative agreement. A quantitative mismatch of about 40% between numerical and experimental data is attributed to numerical reasons and inaccuracy in material data especially for the heat treatment.

Owing to the local phase transformation, especially in the interior of the component, the maxima of inner stresses in the cast component are highly localized. The evolution of the phase transformation is not evenly distributed throughout load history. From a microstructural point of view, a morphological influence on the austenite–martensite transformation was verified.

A combination of residual stresses, service load, and local microsegregation patterns originating from solidification has been shown to result in martensitic solid-state transformation. This leads to deformation of the bearing housing due to volume increase in service and thus to system failure.

References

1. *http://www.magmasoft.com* (accessed 23 February 2012).
2. Brooks, B.E. *et al.* (2007) Prediction of heat treatment distortion of cast steel C-rings. Proceedings of the 61st Technical and Operating Conference, SFSA, Chicago, IL.
3. Sierra, R. and Nemes, J.A. (2008) Investigation of the mechanical behaviour of multi-phase TRIP steels using finite element methods. *Int. J. Mech. Sci.*, **50**, 649–665.
4. Benke, S. *et al.* (2009) Prozessübergreifende Simulation der Herstellung von hochpräzisionsbearbeiteten Bauteilen aus hochlegiertem Edelstahl, NAFEMS Conference Multidisciplinary Simulations-The Future of Virtual Product Development, Wiesbaden.
5. Bathe, K.-J. (2007) *Finite Element Procedures*, Prentice-Hall.
6. Eiken, J. *et al.* (2006) Multiphase-field approach for multicomponent alloys with extrapolation scheme for numerical application. *Phys. Rev. E*, **73**, 066122.

7. Lipinski, D.M. (1996) Mold filling simulation for casting processes. Dissertation. RWTH Aachen.
8. Schäfer, W. (2002) Formfüllungs- und Erstarrungssimulation von Gußteilen auf Rechnerarchitekturen mit verteiltem Speicher. Dissertation. RWTH Aachen.
9. Schneider, M.C. *et al.* (1995) Formation of macrosegregation by multicomponent thermosolutal convection during the solidification of steel. *Met. Mater. Trans. A*, **26A**, 2373–2388.

13
Future ICME

Ulrich Prahl and Georg J. Schmitz

13.1
Imperative Steps

Computer simulation has established itself as an own discipline within – or even bridging – natural and engineering sciences and complementing classical theory and experiments. This especially holds for materials science and technology in a remarkable manner. Integrated computational materials engineering (ICME) extends computational materials science in a way that it integrates horizontally along the history of a material with respect to components as well as vertically across different length scales in order to develop materials and properties being designed to the specific product demands. In that sense, ICME is an emerging field that promises (and really offers) a tremendous potential for acceleration and cost reduction within the design process for advanced materials, production processes, and process chains and components/products as compared to classical trial-and-error approaches.

In 2008 it was stated, that for ICME to succeed three things must happen. [1] The relevance of these three statements has in no way decreased since the publication of this study and now can be formulated with even more emphasis:

1) **''ICME must be embraced as a discipline in the materials science and engineering community, leading to changes in education, research, and information sharing.''**
   This statement is reflected in the actually emerging efforts spent in the education of high-quality materials scientists to become familiar with modeling and numerical methods. Several university courses on computational engineering science (e.g., at RWTH University as a cross faculty Bachelor and Master programs) or the PhD programs at Imperial College [2] or at NorthWestern University [3] have been established recently. Even more effort has to be spent in this kind of interdisciplinary education in future. However, the modeling and simulation activities are still disincentive to most metallurgical scientists, in particular, in the early stages of their education. A statement being assigned

Integrative Computational Materials Engineering: Concepts and Applications of a Modular Simulation Platform,
First Edition. Edited by Georg J. Schmitz and Ulrich Prahl.

to Bo Sundman (one of the founders of Thermo-Calc) ''I decided to study metallurgy because I thought that this topic would be too complicated to be ever put on a computer'' seems to still hold in the minds. A more experimentally based approach is often more favorable for many engineers. It is no secret that a remarkably high number of chairs in materials sciences are presently given to physicists.

With respect to postgraduate and industrial *research*, there are more than enough open topics for the next-generation scientists to spend remarkable effort on. Some of the huge challenges are, for example, (i) the quantitative prediction of mechanical properties, in particular the prediction of failure and fatigue as a function of microstructure and chemical composition, (ii) the quantitative predictability of *ab initio* methods and their incorporation into a holistic ICME approach, and (iii) the development of methods for inverse engineering and even more.

With respect to *information sharing*, procedures to convey information have to be largely facilitated. Information in this context explicitly also comprises models and algorithms. As a first step to facilitate information exchange, modeling programs require a common language for an intense communication of data and results. This book contributes to respective efforts by offering a first concept for a simulation platform based on a common language for data and control parameters. However, even if sharing of information is highly beneficial for future ICME, it should be noted that a reasonable degree of confidentiality and secrecy is most important as well. This is due to the fact that especially problems to be tackled by ICME, in general, will reveal a competitive character as one of the major benefits associated with ICME is to reduce efforts and the time spent for the development of new products (i.e., to ''provide a competitive advantage'').

2) **''Industrial reluctance to accept ICME must be overcome. This acceptance is hindered by the slow conversion of science-based computational tools to engineering tools, a lack of awareness and investment, and by a shortage of trained computational materials engineers.''**
When discussing *industrial reluctance* to accept ICME, it seems meaningful to discuss different types of industry: (i) companies providing infrastructure for ICME, (ii) users of ICME in large-scale companies, and (iii) small and midsize enterprises (SMEs).

Companies providing ICME infrastructure – especially software and modeling tools – feel uncomfortable only in case ICME concepts are successfully provided by their competitors. Most of the major software companies already have own concepts to integrate their different proprietary models and tools. However, exchange of results with tools from other providers or from academia often still is not easy.

Typically, industry reports to spent more than 50% and up to 80% of their engineering capacity within typical, own ICME projects into data conversion and data management even between different commercial tools. Thus, software

producers have to be convinced that opening their input and output formats toward one single common ''language'' represents a benefit in the sense that all their tools can be daisy chained into one holistic approach. This will largely foster the acceptance and application of ICME in industrial settings. Besides an increasing number of licenses, most probably being sold in the wake of a holistic software application, new business models might be envisaged, such as ''Simulation as a Service'' or ''Computational On- Demand.'' These again will create new markets and income for software development and service companies.

Several *large-scale companies* maintain own research and development departments with highly skilled scientists working on ICME. One example is the VIR* projects of the European Aluminum Industry, which have been realized in a multi-industrial consortium with participation of several research departments and now are implemented as daily working and decision supporting tools at Hydro Aluminum [4].

For *SMEs* the situation is quite different. Here, typically no capacity is available to spend major effort in computational and scientific methods at all. Offering a publicly available platform for ICME with a ''Simulation as a Service'' concept guaranteeing confidentiality will offer a path also to SME to benefit from the rapidly developing ICME approach.

Major efforts still have to be spent by the producing industry for the further development of ICME as the industry will benefit the most from this innovative design approach. Nevertheless, it cannot be expected that the producing industry will contribute to a public and open development strategy, as typically producers will concentrate on their own materials, processes, and tools in view of intellectual property rights. Thus, support from the production industry may mainly be expected in the field of specification of precompetitive foundational engineering problems and benchmark tests for model validation. Such contributions are, however, most important as they ensure that the ICME approach – being very successful at present – will have an increasing number of success stories in the future. Successes will spread the news about the benefits of ICME and thus help overcome the lack of awareness. A continuous publication of relevant success stories will be the most effective support for the discussion on further public and industrial funding.

In view of the individual interest from industrial ICME users and of commercial software providers, probably only the open research community and/or governmental bodies will be willing and able to define a common data exchange and program communication standard, that is, a common ICME standard.

The definition and supervision of standards often is a ''public task,'' and frequently is the duty of special government authorities such as the National Institute of Standards and Technology (NIST) in the United States or the Physikalisch-Technische Bundesanstalt (PTB) in Berlin, Germany. As the topic of ICME is rather wide and the contributions from research and science are global, standardization in ICME seems not to be optimally tackled by a

single national, governmental authority. Thus, a self-organization within the ICME community based on a scientific, public ethic could be the answer to create, maintain, and to further develop such a standard. In this sense, this book may serve as a first proposal to be discussed within this community.

Besides a general lack of acceptance by industry of the ICME approach, the shortage of specifically trained computational engineers is especially a key obstacle. This clearly underlines the need for coordinated training and education programs, which have to be designed and even financed from the side of university education and research, not only during study but also as training-on-the-job programs within a lifelong learning approach.

3) **The government must give coordinated support to the initial development of the ICME tools, infrastructure, and education. These are currently inadequate, yet are critical for ICME's future.**
The government – as stated in the original formulation [1] – should be reformulated into each government as ICME activities are not only global but also in the vital interest of any country. While coordination of the support for the individual countries is a matter of the individual governments, there is moreover a need to support and coordinate international efforts for an effective, standardized exchange of data. At this early stage, there is a chance to avoid the situation known from traveling, where different adaptor plugs are needed to connect to the power in different countries. Instead, a much better situation known, for example, from .mpeg or .jpg standard formats being nowadays accepted worldwide for both software and hardware applications is still possible for simulations in research and development.

The further development of ICME into an industrially accepted, comprehensive, and adaptable approach, eventually leading to a holistic production theory by incorporating the field of production and logistics management, definitely will need more activities to be supported from governments as well as from industry. Here, it is necessary to focus on the role of materials within production technologies for high-value products for the welfare of modern societies. Relevant success stories have to be published in a way that not only specialists but also society will realize the need for modern design tools such as ICME.

Support is especially requested in the initial phases of model development and model integration. It should, however, be clearly noted that ICME tools and infrastructure once developed still require a substantial and sustainable funding to ensure operational simulation environments especially at universities.

13.2 Lessons Learned

A number of lessons learned from the early applications of ICME are documented in the National Research Council (NRC) report [1]. In the meantime, first steps in

the direction of a generic ICME approach have been realized. By evolving individual approaches, summarizing current scale bridging activities toward homogenization, coupling a remarkable number of codes on a virtual platform, and showing the potential of this approach within test cases, a nucleus that might serve as a concept for further development of an applicable tool set for industrial and scientific developments and research tasks in the area of ICME has been offered. About three years later, it seems worth to discuss how the ''10 lessons learned,'' documented in the NRC report [1], have been considered in the framework documented in this book.

1) **ICME is an emerging discipline, still in its infancy**
   By defining a modular, comprehensive, and adaptable platform as infrastructure based on a common data and communication format in horizontal (along the simulation chain) as well as in vertical (scale bridging) direction, the first steps in the direction of adulthood have been realized. Such a common format might be accepted as the first schoolbook for the ''primary school'' learning of the meaning of the first characters. The definition of the main ingredients (''I,'' ''C,'' ''M,'' and ''E'') and the definition how to speak (output), how to listen (input), how to call and serve (bridging the scales), how to interact with others, as well as the common visualization standard (vtk) now offer communication between programs as well as between various processes and disciplines.

   The next steps toward ''secondary school'' will be to concentrate on filling the knowledge gaps in the model chain. Once a standardized ICME platform format has been established and widely accepted, it will provide even more options to solve problems that could not be tackled before. Such topics might, for example, be the optimization of process parameters, process chains, or even entire production scenarios including an assessment of their robustness. Further topics may be an inverse design of processes for the manufacture of ''fit for purpose'' materials/products or the prediction of failure/fatigue based on chemical composition and microstructure as a result of production history.

2) **There is clearly a positive return on investment in ICME**
   It has been stated that ICME has the potential to reduce the time for development of a new material from the classically 10- to 20-year time frame down to 2–3 years [5]. The ICME potential for return on investment is announced to be 3 : 1 and in some cases it reaches 9 : 1 [6]. In view of time to market, a value significantly exceeding 9 : 1 has been reported [7]. Some problems can only be tackled and solved using ICME approaches. Large companies and, increasingly, also larger SME-sized companies are actively investing in modeling capabilities in order to understand and to optimize their processes and products. Almost all steel producers presently draw on thermodynamic databases based on the CALPHAD approach; in many cast-houses, fluid flow solvers are available and most forging companies use finite element (FE)-based forming simulation tools. In automotive production and supply chain industry, FE calculations are state of the art for forming as well as for crash simulations. The increasing use of computational tools in automotive and many other producing industries

clearly demonstrates the needs and benefits of materials modeling and ICME in an industrial frame.

Most product design and mechanical engineering tasks are still based on a global view of a material as being homogeneous and isotropic while neglecting its history and its microstructure determining its local properties. A future consideration of local and anisotropic properties offers a huge potential for energy and materials optimization. Even a more general view of production processes and associated planning efforts is detailed in this book. Such a holistic view will shorten design times, decrease production and materials cost, and consume fewer resources in terms of materials and energy.

3) **Achieving the full potential of ICME requires sustained investment**
This statement is more than true. And the current variety of ongoing activities and achievements in this young field [8] still underlines the need for further investment and additional support. In view of competitive issues, the full potential of ICME can only be raised if national and international authorities and also nonprofit organizations are involved. Standardization, in this context, is commonly in the hands of public bodies such as the NIST or the PTB, but the discussion about standards has to be global under the leadership of the ICME community. National and international support is required for establishing a sustainable institution taking the responsibility for further defining, maintaining, and developing standards for ICME and for fostering communication of the different parties in the field by arranging regular meetings with global participation.

In addition to such a sustainable political ICME infrastructure, there is still a strong need for the further development of the tools used in ICME. Future activities have to address, for example, (i) closing the gaps in the model chain, (ii) furthering sustainable individual model development, (iii) scientific exploitation of the benefits of a holistic description, and (iv) an eventual commercialization, for example, of platform concepts in the long term.

Classical funding schemes, at least in universities, do not put any effort into a sustainable algorithm and computational tool development or into user friendliness. As a consequence, model and tool development in many university departments works in periods of a PhD thesis, a generation of students, or the duration of an individual project. Instead of a sustainable model framework, in many cases individual and stand-alone computational algorithms are the result written by scientists typically spending most of their efforts in the development of dedicated models but not into a general framework. In this context, support in building up a professional and sustainable software development frame with professional, technical, and permanent IT staff would be most helpful especially for university departments.

The sustainability of the ICME approach will strongly depend on a continuous model and approach development in universities and research centers in combination with a transfer into applications in an industrial environment.

4) **ICME requires a cultural shift**
The present engineering culture is categorized by a number of disciplines scarcely interacting with each other. Mechanical engineers typically understand the material as a homogeneous, isotropic mass that can be procured with desired properties being specified according to standardized rules. To accept and calculate the material as a history-dependent, locally varying, and anisotropic object surely is a change in paradigm for mechanical engineering design concepts.

Current qualification procedures for materials and components have to be redesigned carefully. Material innovations for demanding applications are hindered or even blocked by time and costs to pass the qualification scheme for new materials. As structural designers use FE analysis to optimize structures and components, materials designers in future will be able to realize new alloy concepts and process optimization in short design times. Aiming to introduce ICME as an ''FE approach for materials design'' and to couple it with classical FE approaches requests a paradigm change. The classical FE method has convinced engineers and is nowadays included in qualification schemes. Exactly this paradigm shift has to be triggered for ICME in future, allowing the qualification of new materials by virtual design and testing.

The project ''Integrative Production Technologies for High-Wage Countries,'' being funded by the German Government, might serve as an example of the first step in the direction of a cultural shift. For the first time, production engineers and materials scientists jointly worked on a holistic theory of production, giving a special focus to integrating materials science and production engineering.

5) **Successful model integration involves distilling information at each scale**
The microstructure reflects the entire materials history and eventually determines the components' properties. Thus, neither the process nor the application parameters are the ''state variables'' determining the behavior of the components. Instead, the microstructure has to be taken into account, and all process or application parameters represent boundary conditions for further microstructure development. Accepting this point of view requires a paradigm change in the simulation of materials and components as it underlines the need for not only taking all relevant microstructural changes *during loading* into account but also all prior processes determining the initial microstructure *before loading*. This can be realized either by using effective material evolution laws or by zooming into the microstructure and calculating microstructure evolution incrementally on the microscale and feeding back effective properties to the larger process scale based on a homogenization scheme. This clearly underlines the need for consistent homogenization approaches (Chapter 5) distilling effective properties from the scale of the microstructure, which then can easily be incorporated into the multiscale approach. However, distilling information to obtain effective properties is only one essential part of information flow in an ICME context. Others are (i) consideration of local effects in larger scale simulation, that is, making real use of effective properties and (ii) well-defined

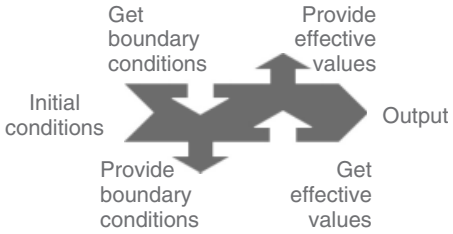

Figure 13.1 Basic structure of a simulation module in a platform concept (Chapter 2).

boundary conditions provided by larger scale models to smaller scale models in a self-consistent way and – most important – well-defined initial conditions on each scale (Figure 13.1).

An instructive example of distilling information at different scales has been given in Chapter 9, where a nanoscale precipitate distribution was used to extract an effective force for grain boundary pinning at the mesoscale. Grain growth simulations at the mesoscale then served for the extraction of information on stability regions during a macroscopic carburization processes. An important point to conclude is that not always does a strong coupling in the sense of distilling information at each scale for *each time step* of simulation codes interacting at different length scales seem mandatory. Frequently, the determination of materials laws and materials parameters eventually entering the process simulations can be developed and/or calibrated by microscopic and mesoscopic simulations before performing the process simulation in a sense of weak coupling. Also, it does not seem to be mandatory to calculate, for example, microstructures for each point of a macroscopic component. Distilling effective information from the microscale may thus proceed only for a few points, while for the effective properties of the other points suitable interpolation schemes may already be sufficient.

6) **Experiments are the key to the success of ICME**
In general, any model development has to be validated by suitable experiments. The validated model can then be considered as true until it is falsified by other experiments or it fails to predict the experimental data with sufficient accuracy. The model then has to be replaced by other models or it has to be refined in order to match the precision of the experimental findings. Besides supporting model development and contributing data to identify model coefficients, experiments will increase the confidence in computational methods, serve as the benchmark, and provide feedback for the further development and improvement of ICME models and approaches.

A very special situation, however, is present for ICME. Any result of a simulation in a process chain strongly depends on the initial conditions, which themselves are the result of the preceding model. In an ICME setting, therefore, well-defined experiments especially with respect to their initial conditions and the components microstructure are mandatory. Simulation chains in ICME

therefore must be accompanied and complemented by respective chains of experiments tracking the entire production history of the components.

In many cases, simulations, however, cannot offer the required information as not all necessary models to mimic the entire model chain may exist. Experiments then may or even have to serve to bridge these gaps. This raises a strong demand for experimental data for the respective steps. The future use of a single, common data format for experimental data and simulation results will be most beneficial and strongly support the feedback of experimental data into an ICME approach.

In summary, ICME inherently needs experiments. The quality of experiments will probably shift from screening-type approaches, for example, to determine properties of a specific material toward well-documented, dedicated, and very detailed experimentation chains for model development and model validation.

7) **Databases are the key to capturing, curating, and archiving the critical information required for the development of ICME**

Data and models are the fundamental ingredients of any virtual production system. Data (information, knowledge, and experience) on all scales – ranging from atomistic values defining materials properties to global data such as availability of resources – are most important for a holistic design and optimization of production processes. Data may reveal a socioeconomical or technological character and may comprise not only pure numbers but also complex process scenarios originating from real production or from virtual investigations. Thus, ICME will eventually require a ''virtual production intelligence (VPI),'' which will focus on creating effective information structures for data aggregation, retrieval, and exploitation using dedicated models and visualization methods. Such structures may be used for industrial R&D and especially for training and education of next-generation engineers.

The best simulation is the one that has not to be performed, because a solution is already readily available or can be easily obtained by minor modifications of an existing scenario. Setting up a complex chain of simulations to describe or predict the properties of a product in an ICME-type approach takes significant efforts. A well-performing simulation scenario thus represents a value of its own worth being saved in a retrievable manner. However, not only simulations should be part of such a VPI system but also any type of experimental knowledge and experience. If there are experimental records for a specific problem, they can be used as a solution directly avoiding a simulation or act as experimental background for setting up a simulation.

A change of paradigm seems meaningful: from results published in articles to results published in databases. Again, especially a standardized data format will be most useful in this context. Beyond merely reading an article, the reader may become a user of the published results by directly entering a result file into his own simulation.

8) **ICME activities are enabled by open-access data and integration-friendly software**
This statement surely holds, but it seems hard to judge and realize. Concerning open-access data, the interest and effort spent by those who created, collected, and implemented the data should not be underestimated or be neglected. Accordingly, the access to such datasets being regularly maintained, updated, and extended, in general, has to be associated with costs. Origin, quality, and actuality of freely available, open-access data in contrast are not always obvious, and their respective documentation is often poor. Industry thus frequently relies on commercial software and commercial datasets in view of quality assurance and respective certifications for their products. ''Open access'' in this context thus should probably be distinguished from ''freely available.'' Most software providers have special conditions for universities, offering their products at lower prices.

To exploit the full potential of ICME, it must be possible to integrate especially verified/validated commercial software and data as black boxes into the framework. This can be realized by a standardized and modular concept as described in this book. In particular, this concept accounts for the intellectual rights of those having developed and implemented the model/software and continue to care about its further, sustainable evolution. Commercial accounting schemes as ''Simulation as a Service'' or ''Calculation on Demand'' may be an option to bridge the interest of both sides.

9) **In applying ICME, a less than perfect solution may be good enough**
In modern design processes, numerical simulations frequently provide remarkable contributions. Nevertheless, simulation itself needs capacity in terms of simulation tools, hardware, CPU time, and work time of trained engineers, being able to control the simulation code and to interpret the results. The degree of accuracy has to be balanced with the costs and efforts needed to create highly precise simulation results. Some applications might already profit from the availability of rough estimators. Future concepts thus will aim at offering different models providing a dedicated degree of accuracy. Such an approach will help to estimate the calculation costs in relation to the return on investment before setting up an entire ICME system. This will enable faster simulations acting as ''estimators'' for the systems behavior, which might be the ideal solution for many ICME applications. Nevertheless, accepting ICME as an approach not necessarily providing quantitative results being correct ''up to the last digit,'' a scheme that estimates not only the costs/efforts for a simulation but also its eventual precision and predictive capabilities along several process steps is needed.

10) **Development of ICME requires cross-functional teams focused on common goals or ''foundational engineering problems''**
Further development and application of ICME needs a strong focus on advanced method development spanning several disciplines. Relevant

contributions are needed from materials science, chemistry, physics, information technology, and mathematics as well as application engineering sciences.

To strengthen cross-discipline motivation in such multidisciplinary teams, strong application problems have to be defined as a common objective. In the definition of such ''test cases'' or ''foundational engineering problems,'' several conditions should be taken into account:

a. The test case needs the potential for quick and high return on investment.
b. Its solution needs interdisciplinarity.
c. It requires a multiscale approach spanning multiple processes.
d. A strong need to solve this problem not only quickly and holistically but also pragmatically.
e. Clear commitment of all participants
f. Sustainable funding.

In view of these considerations, the interdisciplinary Aachen team – consisting of physicists; chemists; mathematicians; IT engineers; materials scientists in metals, alloys, and polymers; foundry engineers; welding and forging engineers; textile engineers; and others – focused on the five test cases with respect to foundational engineering problems, described in detail in Chapters 8–12. These tasks could only be tackled by such an interdisciplinary group. It seems worthwhile to note that some of the research teams were later complemented by mechanical engineers to include, for example, machining and application of the product into the model chain.

13.3 Future Directions

Currently, the concept of an expandable platform for virtual materials processing comprising commercial and noncommercial software packages, databases, and models has been designed, implemented, and built up. It includes the definition of an open, well-documented, and standardized format for exchange of information. During the start phase, a number of software packages related to materials processing available at the RWTH University were installed and harmonized as an initial platform nucleus. A distributed grid and middleware were used to direct communication between the different software packages installed at various places. This concept has been tested for various test cases, published at conferences and in international journals (especially in this book), and offers access via an Internet platform *www.aixvipmap.de*. In future, various topics have to be addressed for a sustainable installation and application of this concept, and bringing it into a continuous use for both science and applications. These topics are detailed in the following sections.

13.3.1 Education and Training

Teach Materials Engineering Students to Think "Integrative" and "Computational" Classical education of materials and production engineers is based on trial-and-error approaches and gives detailed qualitative knowledge of mechanisms and cause–effect correlations. In particular, for technical alloy systems including 10 and more components, quantitative correlations typically are based on empirical equations from many tests and examples. Nowadays, thermomechanical approaches grow in maturity, applicability, and predictability even for complicated and real-world industrial boundary conditions. The combination of these models in several process steps and their integration into various multiphysics approaches clearly needs people being trained to think integrative and computational. To ensure that engineers are ready to use ICME, the training on modeling approaches and computational tools have to be included in a lifelong learning scheme.

In various universities, new courses that support the idea of computational engineering have been introduced, where students are trained to think integrative, for example, the program "Computational Materials Science" at RWTH Aachen University or the Doctoral Training Centre (DTC) on "Theory and Simulation of Materials (TSM)" at Imperial College London. In addition, a new TSM conference was started on ICME in 2011 in Seven Springs, Pennsylvania. The next step toward spreading ICME into application will be to offer summer schools and special courses. Also, the application of these tools in classrooms for under ages is needed in order to inspire pupils.

Provide a Platform for Integrated Teaching of Materials Science The presented platform idea itself offers applications within teaching and training programs if challenging success stories are available to attract young students. Courses and classes may connect their own tools with those of other groups. In many situations, software suppliers offer training and education licenses with reduced data, models, or opportunities, which can be implemented in the platform for education or training and used for easy and reduced case studies.

13.3.2 Internationalization, Professionalization, and Commercialization

ICME as a Global Topic In summer 2011, the First World Congress on ICME took place in Seven Springs, USA, providing a forum for presentations and discussions on various ICME-related topics [8]. ICME is an international issue as reflected by participants coming from industry and research centers in the United States, Europe, and Asia. Its further development will be realized efficiently and effectively only if it is treated from a global point of view. As this topic is more than a national one, the participating researchers

and applicants need a frame to discuss and agree on common approaches standards and interfaces. A series of international conferences and workshops has to be set up focusing on ICME, including not only discussion and presentation but also exchange of standards, algorithms, and approaches from all over the world. The presented AixViPMaP concept can serve as a first example of how the discipline spanning design and definition of platforms for ICME can be realized.

Implementation of an Accounting Scheme for Commercial Providers Commercialization of ICME is an important step toward a sustainable professionalization of this approach. Long-term development will be possible only if industrial investment is explored.

A relevant increase in application of ICME will only be realized if the use and linking of various simulation tools and approaches are realized not only by single model experts but also by engineers in various R&D departments of both large-scale companies and also SMEs. User-friendly interfaces and instructive calculation examples offering all relevant model data have to be provided for this purpose. Typically, this is a contribution of commercial software houses and will be financed only if the ICME approach includes commercialization strategies.

Software providers in this context can market ''Calculation on Demand'' or ''Software as a Service'' strategies in case suitable accounting systems are available and implemented.

Confidential Platform Use The second important condition for professionalization is ensuring confidentiality for all participants as there are software suppliers, data suppliers, and industrial users. As simulation tools may be offered on machines within the software houses and be called via Internet, confidentiality for the software supplier is obvious. For data suppliers (e.g., thermodynamic data), reliable strategies have already been developed and are available for integration in this platform concept. The industrial user of such a system expects confidentiality with respect to process parameters and materials specifications being, in general, company specific knowhow and the key to commercial success. Till now, there are no specific safety strategies available, beyond what is used on standard Internet communication such as, for example, in online banking. Especially for SMEs not maintaining own IT and simulation expertise, the step into a network-based ICME approach to this issue may represent a high threshold.

The future development of hidden or crypted data transfer strategies is mandatory, as also a professional and transparent policy for ICME users and developers. For many situations and industries, a reasonable compromise may be to build up an own simulation expertise for proprietary key processes and only to link respective input and output data with external software codes complementing uncritical parts of the process chain.

13.3.3 Platform Development

Extension of the Platform The modular AixViPMaP concept at the present stage offers a simulation platform for ICME including a multiscale approach spanning from nanoscale to the scale of machines and manufacturing processes. The incorporated simulation tools can describe and optimize processes starting from liquid homogeneous state and ending at application and properties of components. On the basis of this partial integration of individual model areas within a modular simulation platform, the objective of future research is their further development and integration into a comprehensive integrative computational materials and production engineering (ICMPE) platform combining materials and machining simulation with factory and production planning. Such an approach will bring this platform – based on quantitative and knowledge-driven simulations – into application toward an efficient and effective scheme for the design of materials and processes. For this purpose, the following extension directions have to be addressed (Figure 13.2):

- Extension of the available materials and process simulation platform to production planning approaches and to real process control data within a VPI approach, which will provide concepts for information aggregation, retrieval, exploration, and visualization.
- Extension of *ab initio* approaches being able to provide thermodynamical, mechanical, metallurgical, and energetic data needed on nanoscales and microscales in order to evaluate continuum field model coefficients.
- Implementation of failure and fracture models including fatigue toward lifetime prediction as well as repair to realize a lifetime balance of materials in application. This will enable calculation of the production costs in relation to the use and maintenance costs and, thus, will offer the optimization of full costs per time in use. Eventually, this quantity is the most relevant to estimation and decision making on new materials and manufacturing processes.
- Incorporation of design tools taking into account not only the structural integrity and geometrical optimization but also the materials and manufacturing optimization. Special focus is laid on materials inherent inhomogeneities or anisotropies on the microstructural scale.

Tailored Accuracy In the long term – once a comprehensive model map covering all processes at all scales has been established – an option to indicate the quality in terms of quantitative predictability of a model may be included. In case different models are available for a specific process at a specific length scale, these models might differ in the level of detail, precision of results, underlying assumptions, and so on. Such differences should be known before design and application of models and models chains in order to judge the costs of modeling in relation to the expected profit by improvement or optimization of processes and/or materials.

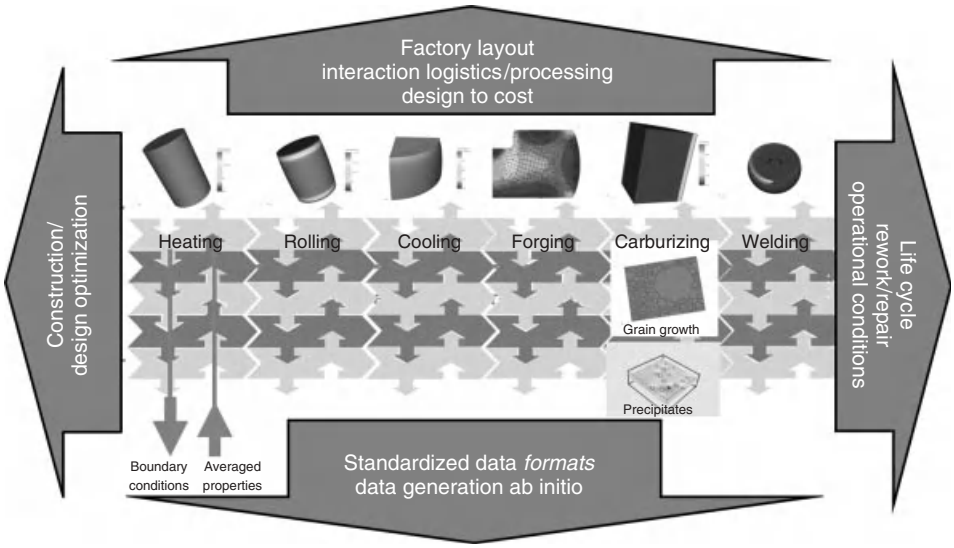

Figure 13.2 Schematic view of present status and future extension direction of the AixViPMaP.

A possible approach might be to classify models by superscript indices from 1 to 9, indicating the degree of approximation and accordingly the degree of reliability of the results. The index ''1'' in this context could mean ''first-order approximation'' and – as in Taylor expansions – the degree of precision increases with increasing order. An increase in precision in general will go along with an increase in computational effort, which affects the time and price of calculations. Depending on the nature of the problem and the desired precision of the results it may be interesting and appropriate to go for type ''1'' models for some of processes, while obtaining a deeper view with higher order accuracy at other process steps.

In this context, type ''0'' models may also be defined. Such models represent simple assumptions being made, where no suitable models are available at all. Type ''9'' models could be related to experimental information. A preliminary approach to a model categorization is given in Table 13.1.

Predicting Robustness Once an entire simulation chain has been created and adapted to the desired degree of accuracy, it may be interesting to investigate the robustness of the real process chain against disturbances in the production process. One important condition in this context is the robustness of the individual simulation models and tools against major variations in their initial and boundary conditions. This is particularly important for ICME as the output of an upstream calculation may contain unexpected results, which then have to be digested by the downstream models and tools.

Table 13.1 A preliminary approach to a model categorization.

Degree of accuracy	Model characterized by
0	minimum accuracy, only estimates of field values, or other conditions
1	constant, isotropic, and homogeneous field values
2	temperature-dependent, isotropic, and homogeneous field values
3	. .to be done . . .
4	. .to be done . . .
5	anisotropic models, etc.
6	. .to be done . . .
7	. .to be done . . .
8	. .to be done . . .
9	experimental data

Open Gaps There are still many open gaps to close before the scenario depicted in this book enters the everyday life of process and production engineers. Many of these gaps and challenges are related to the improvement of the individual models used to compose an ICME setting such as, for example, quantitative predictive power of models and *ab initio* data for technical alloys. Quantitative *ab initio* prediction of mechanical properties has made progress in case of elasticity, while inelastic, generalized anisotropic properties and the dependence of chemical composition for technical systems are still an open topic. With regard to plasticity, an approach similar to the thermodynamic Gibb's energy functional and CALPHAD method, which can be handled based on appropriate energy databases, is needed. Besides plasticity, the investigation of damage, failure, and fatigue mechanisms in a quantitative, predictive sense is another open topic.

Other gaps are directly related to coupling different models across different scales and coupling with reality. Examples are the loss of accuracy during scale bridging or the need for standards to link experimental results with simulation, in particular, for 3D metallography on all relevant scales at different resolution.

Eventually, a large number of gaps and challenges are expected to arise when actually performing coupled simulations as experienced and when composing the test case scenarios described in this book and getting them operational.

13.4 Closing Remark

''There's plenty of room at the bottom.'' This sentence by Richard P. Feynman in 1959 marked the beginning of nanosciences and nanoengineering.

''There are plenty of options along the process chain.'' This might become the future paradigm for ICME. Exploiting all these options can effectively proceed on

the basis of a holistic view spanning all length scales on the evolution of materials from their initial liquid state up to final properties in application. This eventually leads to a new paradigm:

"History matters engineers!"

References

1. National Research Council (2008) *Integrated Computational Materials Engineering: A Transformational Discipline for Improved Competitiveness and National Security*; National Academic Press, Washington, DC, ISBN: 0-309-12000-4.
2. Sutton, A. (2011) The Doctoral Training Centre (DTC) on Theory and Simulation of Materials (TSM) at Imperial College London. 1st World Congress on ICME, Pittsburgh PA, June 11–14, 2011.
3. Olson, G. (2011) ICME education. 1st World Congress on ICME, Pittsburgh PA, June 11–14, 2011.
4. Hirsch, J. (2011) History of ICME in the European aluminium industry. 1st World Congress on ICME, Pittsburgh PA, June 11–14, 2011.
5. Pollock, T. and Christodoulou, J. (2011) Presentation given at the 1st World Congress on ICME, Pittsburgh PA, June 11–14, 2011.
6. IDC (2004) White paper on Modeling and Simulation: The Return on Investment in Materials Science, July 2004; sponsored by Accelrys Inc.
7. Piegert, S. (2011) Benefits of thermodynamics and kinetic calculations in an industrial setting. Thermo-Calc Users Meeting 2011, Aachen, Germany, *http://www.thermocalc.de* (accessed 8-9 September 2011).
8. Allison, J., Collins, P., and Spanos, G. (eds) (2011) *Proceedings of the 1st World Congress on ICME*, John Wiley & Sons, Inc., pp. 223–228, ISBN: 978-0-470-94319-9.

Index

Integrative Computational Materials Engineering: Concepts and Applications of a Modular Simulation Platform,
First Edition. Edited by Georg J. Schmitz and Ulrich Prahl.